A COMPARISON AND EVALUATION OF DIFFERENT SOIL-STRUCTURE-INTERACTION APPROACHES FOR BRIDGES

by
Oytun İnci
B.S., Civil Engineering, Midde East Technical University, 2013

Submitted to the Kandilli Observatory and Earthquake Research Institute
in partial fulfillment of the requirements for the degree of
Master of Science

Graduate Program in Earthquake Engineering
Boğaziçi University
2019

A COMPARISON AND EVALUATION OF DIFFERENT SOIL-STRUCTURE-INTERACTION APPROACHES FOR BRIDGES

APPROVED BY:

Prof. Dr. Erdal Şafak (Thesis Supervisor)	……
Dr. Göktürk Önem (Co-Thesis Supervisor)	……
Assoc. Prof. Dr. Ufuk Hancılar	……
Asst. Prof. Dr. Özden Saygılı (Yeditepe University)	……

DATE OF APPROVAL: 01.08.2019

ACKNOWLEDGEMENTS

I am deeply indebted to my supervisors Erdal Şafak and Göktürk Önem for their guidance and constant encouragement. I would like to express my gratitude to Erdal Şafak for his endless patience and support for my study. I cannot overstate how Göktürk Önem's inspiring ideas and invaluable suggestions and supports improved my visions in all aspects, and I am extremely grateful to him for sharing his knowledge and experiences generously.

I would also like to express my appreciation to the faculty of Earthquake Engineering for their precious assistance, theoretical and practical knowledge and passion.

I would like to express my special thanks to my dear colleagues Arif Kıvanç Yılmaz and Sedat Mavuzer for their contribution both morally and mathematically at every stage.

I would like to express my deepest gratitude to my beloved partner Sümeyra for her love and extreme supports of me throughout this entire process, none of this would have been possible without her.

Last but not least I am extremely grateful to my mother and father for all the love and unconditional support they provided to me all through my life.

ABSTRACT

A COMPARISON AND EVALUATION OF DIFFERENT SOIL-STRUCTURE-INTERACTION APPROACHES FOR BRIDGES

During the last fifty years, bridge construction has increased extensively throughout the world, including on areas with bad soil conditions, to meet the transportation needs of expanding urban areas. Although Soil-Structure-Interaction (SSI) procedures for performance-based design of buildings have been introduced in design guidelines, seismic provisions are not clearly stated for bridges. There are two main approaches to include SSI in performance-based design of the bridges; direct method and substructure method. In the direct method, bridge and soil systems are analyzed as a single system under seismic shaking, defined at bedrock. As an alternative, the substructure method is introduced to solve the system as substructures in two stages, called kinematic interaction and inertial interaction. The nonlinear response of piled foundation systems of bridges are subjected to kinematic interaction; whereas, the nonlinear response of superstructure is subjected to inertial interaction.

In this study, first, he linear design of two different bridges are introduced by considering their geometry and the number of spans. Bridge-I has three spans with uneven pier heights, and Bridge-II has four spans with identical piers and the geometry. Both bridges are designed based on a response spectrum created according to site response analysis and used in the performance-based design of the bridges. 19 different records are selected and scaled according to the criteria given in AASHTO LRFD Bridge Design Specifications Article 4.7.4.3.4 (AASHTO, 2012) Seismic Design Guidelines. Seismic records are categorized with respect to soil parameters, chosen for both strength-based and performance-based design of bridges.

Secondly, using the direct method, the Nonlinear Time History (NTH) analyses are performed for both bridges to investigate the behavior of structural elements. The nonlinear responses of the bridges are re-calculated by using the substructure method, including the kinematic and inertial interactions. Responses of the structural elements are combined according to commonly-used combination rules.

Finally, results of these methods are compared with each other, as well as the linear response of the structures, to underline how the behavior of the structures vary according to different analysis methods.

ÖZET

KÖPRÜLER İÇİN FARKLI YAPI-ZEMİN-ETKİLEŞİM YAKLAŞIMLARININ DEĞERLENDİRİLMESİ VE KARŞILAŞTIRILMASI

Geçtiğimiz son elli yılda, genişleyen yerleşim alanlarının ulaşım ihtiyacını karşılayabilmek için zemin koşullarına bakılmaksızın köprü inşası oldukça artmıştır.

Yönetmeliklerde uzun zamandır Yapı-Zemin-Etkileşim prosedürleri binaların performansa dayalı tasarım için açıkça tanımlanmış olmasına rağmen, köprüler için açıkça belirtilmemiştir. Performansa dayalı köprü tasarımlarında Yapı-Zemin-Etkileşim problemlerini çözmek için direkt metot ve altyapı metodu olmak üzere iki ana yaklaşım bulunmaktadır. Direkt metotta, köprü ve zemin sistemleri ana kayada tanımlanan sismik etkiler altında tek bir sistem olarak analiz edilmektedir. Direkt metoda alternatif bir yaklaşım olan alt-sistem metodunda ise problemi çözmek için kinematik etkileşim ve eylemsizlik etkileşimi olarak adlandırılan iki aşamalı sistem kullanılır. Kinematik etkileşimde kazıklı temel sistemine sahip köprülerin doğrusal olmayan davranışı incelenirken; eylemsizlik etkileşimi üstyapının doğrusal olmayan davranışını incelemek için kullanılır.

Bu çalışmada, iki farklı köprünün doğrusal tasarımı, geometri ve açıklık sayısı açısından tanıtılmıştır. Köprü-1 eşit olmayan kolon yüksekliklerine sahip üç açıklıklı iken Köprü-2 aynı geometrili kolonlara sahip dört açıklıklı bir köprüdür. Her iki köprü de performansa dayalı köprü analizlerinde kullanılan sismik kayıtların serbest-zemin analizine göre oluşturulmuş elastik davranış spektrumuna göre tasarlanmıştır. AASHTO LRFD Sismik Tasarım Rehberi Madde 4.7.4.3.4 (AASHTO, 2012)'de verilen kriterlere göre 19 farklı kayıt seçilip ölçeklendirilmiştir. Köprülerde kuvvete ve performansa dayalı tasarım kriterlerine göre zemin parametreleri seçilerek sismik kayıtların serbest-zemin analizi gerçekleştirilmiştir.

İkincisi, bu çalışmada köprüleri oluşturan yapıların davranışını araştırmak için zaman tanım aralığında doğrusal olmayan analizler yapılmıştır. Her iki köprünün de doğrusal olmayan davranışı alt-sistem metodunun kinematik ve eylemsizlik etkileşimi ile elde edilmiştir. Yapıların davranışı belirtilen kombinasyon kurallarına göre birleştirilmiştir.

Son olarak, bu yöntemlerin sonuçları ve farklı analiz metotlarına göre yapıların doğrusal davranışları bu çalışmada karşılaştırılmıştır.

TABLE OF CONTENTS

ACKNOWLEDGEMENTS iii
ABSTRACT iv
ÖZET vi
LIST OF FIGURES x
LIST OF TABLES xix
LIST OF SYMBOLS / ABBREVIATIONS xx
1. INTRODUCTION 1
1.1. Motivation of the Study 2
1.2. Summary and Scope 2
2. LITERATURE REVIEW 4
3. STRUCTURAL SYSTEM, SOIL PROPERTIES, GROUND MOTIONS AND DESIGN 8
3.1. Geometric Properties 8
3.2. Soil Properties 11
3.3. Ground Motion Selection and Scaling 14
3.4. Design of Bridges 27
3.4.1. Loads Considered for Design 28
3.4.2. Response Spectrum analysis 29
3.4.3. Capacity Estimation 30
4. COMPERATIVE STUDY OF NONLINEAR TIME HISTORY AND SUBSTRUCTURE SSI ANALYSIS 34
4.1. Modelling 34
4.1.1. Models for Structural Analysis 34
4.1.2. Site Response Analysis Model 55
4.2. Direct Method 66
4.2.1. Application of Soil Displacement to Structural System 66
4.3. Substructure Method 69
4.3.1. Kinematic interaction 69
4.3.2. Inertial Interaction 73
5. ANALYSIS RESULTS 77

5.1. Direct Method Analysis Results 77
5.2. Substructure Method Analysis Results 85
5.2.1. Kinematic Interaction Analysis Results 85
5.2.2. Inertial Interaction Analysis Results 100
6. CONCLUSIONS 114
REFERENCES 129
APPENDIX A: DETERMINATION OF NON-LINEAR *p-y* CURVES 132
A.1 *p-y* Springs for Sand Under Static and Cyclic Loading 132
A.2 *p-y* Springs for Soft Clay Under Static Loading 133
A.3 *p-y* Springs for Soft Clay Under Cyclic Loading 135
A.4 *p-y* Springs for Stiff Clay with free water Under Static Loading 136
A.5 *p-y* Curves for Stiff Clay with Free Water Under Cyclic Loading 140
A.6 *p-y* Curves for Stiff Clay without Free Water Under Static Loading 141
A.7 *p-y* Curves for Stiff Clay without Free Water Under Cyclic Loading 142
A.8 Effect of Group Action 144

LIST OF FIGURES

Figure 3.1. Section drawings of the pier and the superstructures. 9

Figure 3.2. Bridge-I and the soil profile. 10

Figure 3.3. Bridge-II and the soil profile. 10

Figure 3.4. SPT N - depth graph. 13

Figure 3.5. San Fernando 02/09/71 14:00, La Hollywood Stor Lot, 090 (USGS station 135). 16

Figure 3.6. Friuli, Italy 05/06/76 2000, Tolmezzo 16

Figure 3.7. Imperial Valley 10/15/79 2316, Delta, 262 (UNAM/UCSD station 6605) 17

Figure 3.8. Imperial Valley 10/15/79 2316, El Centro Array #11, 140 (USGS station 5058). 17

Figure 3.9. Superstition Hills 11/24/87 13:16, El Centro Imp Co Center. 18

Figure 3.10. Superstition Hills 11/24/87 13:16, POE, 270 (USGS station temp). 18

Figure 3.11. Superstition Hills 11/24/87 13:16, POE, 270 (USGS station temp). 19

Figure 3.12. Loma Prieta 10/18/89 00:05, Gilroy Array #3, 000 (CDMG station 47381). 19

Figure 3.13. Cape Mendocino 04/25/92 1806, Rio Dell overpass FF, 270 (CDMG station 89324). 20

Figure 3.14. Landers 06/28/92 1158, Yermo fire station, 270 (CDMG station 22074). 20

Figure 3.15. Northridge EQ 1/17/94, 12:31, Beverly Hills - 14145 Mulh, 009 (USC station 90013). 21

Figure 3.16. Northridge EQ 1/17/94, 12:31, Canyon Country - W Lost Canyon, 000 (USC station 9)..... 21

Figure 3.17. Kobe 01/16/95 2046, Nishi-Akashi, 000 (CUE). 22

Figure 3.18. Kobe 01/16/95 2046, Shin-Osaka, 000 (CUE). 22

Figure 3.19. Kocaeli 08/17/99, Arcelik, 000 (KOERI). 23

Figure 3.20. Kocaeli 08/17/99, Duzce, 180 (ERD). 23

Figure 3.21. Chi-Chi 09/20/99, CHY101, E. 24

Figure 3.22. Duzce 11/12/99, Bolu, 000 (ERD). 24

Figure 3.23. Hector Mine 10/16/99 02:47, HEC, 000. 25

Figure 3.24. Target spectrum. 25

Figure 3.25. %5 Damped response spectrum of raw data with target spectrum..... 26

Figure 3.26. %5 Damped response spectrum of matched data with target spectrum. 27

Figure 3.27. H30-S24 truck live load. 28

Figure 3.28. Design spectrum. 30

Figure 3.29. Cross-section of the pier. 31

Figure 3.30. Pier 14.00 m pier strong direction moment-curvature diagram. 32

Figure 3.31. Pier 14.00 m pier weak direction moment-curvature diagram. 32

Figure 3.32. Pier 28.00 m pier strong direction moment-curvature diagram. 33

Figure 3.33. Pier 28.00 m pier weak direction moment-curvature diagram. 33

Figure 4.1. Modelling of superstructure – pier connection. 36

Figure 4.2. Pier structural model. 37

Figure 4.3. Pile system analysis model. 39

Figure 4.4. Mander unconfined concrete model for piles, f_{ck}=25 MPa. 40

Figure 4.5. Mander unconfined concrete model for piers, f_{ck}=35 MPa. 41

Figure 4.6. Reinforcing steel S420 stress-strain curve, f_{yk}=420Mpa. 42

Figure 4.7. 2D yield surface and elasto-plastic moment-plastic hinge relationship. 43

Figure 4.8. Typical P-M interaction diagram for piers. 44

Figure 4.9. Typical P-M interaction diagram for piers. 44

Figure 4.10. Typical P-M interaction diagram for piles. 45

Figure 4.11. Pier foundation geometry. 46

Figure 4.12. Pile layout and α factors for the *p-y* springs. 46

Figure 4.13. The *p-y* curves for soft clay layers 2.5 to 11.5 m depth from surface. 47

Figure 4.14. The *p-y* curves for sand layers 12.5 to 31.5 m depth from surface. 48

Figure 4.15. Typical *t-z* curves (API 2A, 2000). 50

Figure 4.16. *t-z* curves for each soil layer. 52

Figure 4.17. Typical *Q-z* curve. 53

Figure 4.18. Pile tip load-displacement (*Q-z*) curve for the bottom soil layer. 54

Figure 4.19. Record 68_090 site response analysis summary diagrams. 56

Figure 4.20. Record 125_000 site response analysis summary diagrams. 57

Figure 4.21. Record 169_352 site response analysis summary diagrams. 57

Figure 4.22. Record 174_11230 site response analysis summary diagrams. 58

Figure 4.23. Record 721_000 site response analysis summary diagrams. 58

Figure 4.24. Record 725_270 site response analysis summary diagrams. 59

Figure 4.25. Record 752_000 site response analysis summary diagrams. 59

Figure 4.26. Record 767_000 site response analysis summary diagrams. 60

Figure 4.27. Record 829_360 site response analysis summary diagrams. 60

Figure 4.28. Record 900_270 site response analysis summary diagrams. 61

Figure 4.29. Record 953_279 site response analysis summary diagrams. 61

Figure 4.30. Record 960_270 site response analysis summary diagrams. 62

Figure 4.31. Record 1111_000 site response analysis summary diagrams. 62

Figure 4.32. Record 1116_000 site response analysis summary diagrams. 63

Figure 4.33. Record 1148_000 site response analysis summary diagrams. 63

Figure 4.34. Record 1158_270 site response analysis summary diagrams. 64

Figure 4.35. Record 1244_101n site response analysis summary diagrams. 64

Figure 4.36. Record 1602_090 site response analysis summary diagrams. 65

Figure 4.37. Record 1787_090 site response analysis summary diagrams. 65

Figure 4.38. Superstructure – pile – soil mutual system schematic figure. 68

Figure 4.39. Max. envelope lateral soil displacements relative to bedrock. 70

Figure 4.40. Total lateral displacements of the soil profile at the instant of maximum 71

Figure 4.41. Relative lateral displacements of the soil profile with respect to bedrock 71

Figure 4.42. Total lateral displacements of the soil at the instant of maximum drift along the pile length. 72

Figure 4.43. Relative lateral displacements of the soil with respect to bedrock at the 72

Figure 5.1. Bridge I record 68_090 / 174_11230 / 767_000 / 829_360 plastic hinge formation. 77

Figure 5.2. Bridge I record 960_270 / 1148_000 / 1244_101n / 1602_090 plastic hinge formation. 78

Figure 5.3. Bridge I displacement time history envelope moment diagram. 79

Figure 5.4. Bridge I displacement time history plastic hinge rotation. 80

Figure 5.5. Bridge I displacement time history deck lateral displacement. 81

Figure 5.6. Bridge II record 68_090 / 174_11230 / 767_000 / 829_360 plastic hinge formation. 82

Figure 5.7. Bridge II record 960_270 / 1148_000 / 1244_101n / 1602_090 plastic hinge formation. 82

Figure 5.8. Bridge II displacement time history envelope moment diagram. 83

Figure 5.9. Bridge II displacement time history plastic hinge rotation. 84

Figure 5.10. Bridge II displacement time history deck lateral displacement. 85

Figure 5.11. Bridge-I kinematic interaction envelope moment diagram. 86

Figure 5.12. Bridge-I kinematic interaction plastic hinge rotation. 87

Figure 5.13. Bridge-I kinematic interaction deck lateral displacement. 88

Figure 5.14. Bridge-I 14.00 m pier envelope shear force diagram. 89

Figure 5.15. Bridge-I 14.00 m pier envelope moment diagram. 90

Figure 5.16. Bridge-I 28.00 m pier envelope shear force diagram. 91

Figure 5.17. Bridge-I 28.00 m pier envelope moment diagram. 92

Figure 5.18. Bridge II kinematic interaction envelope moment diagram 93

Figure 5.19. Bridge II kinematic interaction plastic hinge rotation. 94

Figure 5.20. Bridge II kinematic interaction deck lateral displacement. 95

Figure 5.21. Bridge-II edge pier envelope shear force diagram. 96

Figure 5.22. Bridge-II edge pier envelope moment diagram. 97

Figure 5.23. Bridge-II middle pier envelope shear force diagram. 98

Figure 5.24. Bridge-II middle pier envelope moment diagram. 99

Figure 5.25. Bridge-I inertial interaction pile envelope moment diagram. 100

Figure 5.26. Bridge-I inertial interaction plastic hinge rotation. 101

Figure 5.27. Bridge-I inertial interaction deck lateral displacement. 102

Figure 5.28. Bridge-I inertial interaction 28.00m pier envelope shear force diagram. 103

Figure 5.29. Bridge-I inertial interaction 28.00m pier envelope moment diagram. 104

Figure 5.30. Bridge-I inertial interaction 14.00m pier envelope shear force diagram. 105

Figure 5.31. Bridge-I inertial interaction 14.00m pier envelope moment diagram. 106

Figure 5.32. Bridge II inertial interaction pile envelope moment diagram. 107

Figure 5.33. Bridge II inertial interaction plastic hinge rotation. 108

Figure 5.34. Bridge II inertial interaction deck lateral displacement. 109

Figure 5.35. Bridge-II inertial interaction middle pier envelope shear force diagram. 110

Figure 5.36. Bridge-II inertial interaction middle pier envelope moment diagram. 111

Figure 5.37. Bridge-II inertial interaction edge pier envelope shear force diagram. 112

Figure 5.38. Bridge-II inertial interaction edge pier envelope moment diagram. 113

Figure 6.1. Bridge-I pile envelope moment diagram comparison. 115

Figure 6.2. Bridge-I corner pile plastic rotation comparison. 116

Figure 6.3. Bridge-I deck lateral displacement comparison. 117

Figure 6.4. Bridge-I 14.00 m pier envelope shear force diagram comparison. 118

Figure 6.5. Bridge-I 14.00 m pier envelope moment diagram comparison. 119

Figure 6.6. Bridge-I 28.00 m pier envelope shear force diagram comparison. 120

Figure 6.7. Bridge-I 28.00 m pier envelope moment diagram comparison. 121

Figure 6.8. Bridge-II corner pile envelope moment diagram comparison. 122

Figure 6.9. Bridge-II corner pile plastic rotation comparison. 123

Figure 6.10. Bridge-II deck lateral displacement comparison. 124

Figure 6.11. Bridge-II edge pier envelope shear force diagram comparison. 125

Figure 6.12. Bridge-II edge pier envelope moment diagram comparison. 126

Figure 6.13. Bridge-II middle pier envelope shear force diagram comparison. 127

Figure 6.14. Bridge-II middle pier envelope moment diagram comparison. 128

Figure A.1. C1, C2, C3 coefficients according to angle of internal friction (API 2A,2000). 133

Figure A.2. p-y springs for soft clay in the presence of free water, (a) static; (b) cyclic; (c) after cyclic loading (Matlock, 1970). 136

Figure A.3. Ac and As (Reese and Van Impe, 2001). 139

Figure A.4. p-y springs under static loading in stiff clay in the presence of free water (Reese and Van Impe, 2001). 139

Figure A.5. p-y springs under cyclic loading in stiff clay in the presence of free water (Reese and Van Impe, 2001). 141

Figure A.6. p-y springs under static loading in stiff clay without free water (Reese and Van Impe, 2001). 142

Figure A.7. p-y springs under cyclic loading in stiff clay without free water (Reese and Van Impe, 2001). 144

Figure A.8. Reduction factors for piles in group action. 145

LIST OF TABLES

Table 3.1. Properties of the bridges. 9

Table 3.2. Section properties of the superstructures. 11

Table 3.3. Soil properties. 12

Table 4.1. Effective flexural stiffness of 14.00 m pier section. 36

Table 4.2. Effective flexural stiffness of 28.00 m pier section. 37

Table 4.3. Effective flexural stiffness of pile section. 38

Table 4.4. Strength classes for concrete. 40

Table 4.5. Mechanical properties of reinforcing steel. 41

Table 4.6. Recommended *t-z* curves for clays (API 2A, 2000). 49

Table 4.7. Recommended *t-z* curves for sands (API 2A, 2000). 49

Table 4.8. Design parameter table for cohesionless siliceous soil 51

Table 4.9. *Q-z* curves for clays and sands (API 2A, 2000) 53

Table 4.10. Bridge I & II seismic demand. 76

Table A.1. ε_{50} for normally consolidated clays (Reese and Van Impe, 2001). 135

Table A.2. K_{py} for overconsolidated clays (Reese and Van Impe, 2001). 138

Table A.3. ε_{50} for overconsolidated clays (Reese and Van Impe, 2001). 138

LIST OF SYMBOLS / ABBREVIATIONS

c_u	Undrained shear strength
C_s	Seismic response coefficient
I_e	Importance factor
d_b	Diameter of the longitudinal reinforcement
E	Modulus of elasticity
f_{ck}	Characteristic strength of concrete
f_i	*i*-th frequency
f_n	Natural frequency of the oscillator
f_{yk}	Characteristic yield strength of reinforcement
$\bar{h}$	Effective height of the structure
I	Moment of inertia
K	Stiffness matrix
K_y	Lateral stiffness of the foundation
$\bar{k}$	Stiffness of the fixed base structure
L_p	Plastic hinge length
M	Mass matrix
M_p	Plastic moment capacity
N	Axial load
p_0'	Effective overburden pressure(kPa)
R	Response modification factor
RRS_{bsa}	Ratio of response spectra for base slab averaging
RRS_e	Ratio of response spectra for embedment
S_{DS}	Design spectral response acceleration of the design response spectra
S_s	Spectral acceleration coefficient at period 0.2 sec
S_1	Spectral acceleration coefficient at period 1.0 sec
T	Fundamental period of the structure
V	Base shear
$\tilde{V}$	Base shear of SSI system
V_s	Shear wave velocity
$\bar{W}$	Effective weight of the structure

$\tilde{\beta}$	Fraction of critical damping for the structure-foundation system
ɣ	Soil unit weight
Ø	Live load impact factor
ϕ_y	Yield curvature
$(EI)_e$	Effective flexural stiffness
η	Mass-proportional damping coefficient
δ	Stiffness-proportional damping coefficient
ξ	Damping ratio
ξ_n	Critical damping ratio
w_n	Natural frequency

AASHTO	American Association of State Highway and Transportation Officials
ADRS	Acceleration-Displacement Response Spectra
API	American Petroleum Institute
ASCE	American Society of Civil Engineers
ATC	Applied Technology Council
BSSC	Building Seismic Safety Council
CQC	Complete Quadratic Combination
FAS	Fourier Amplitude Transform
FEMA	Federal Emergency Management Agency
NEHRP	National Earthquake Hazard Reduction Program
NTH	Nonlinear Time History
LRFD	Load Resistance Factor Design
MDOF	Multiple Degree of Freedom System
PGA	Peak Ground Acceleration
SDOF	Single Degree of Freedom System
SPT	Standard Penetration Test
SRSS	Square Root of the Sum of Squares
SSI	Soil Structure Interaction

1. INTRODUCTION

Early bridges were mostly arch bridges because of the lack of tension members. Compressional members used were too large and heavy compared to today's modern bridges. Due to the rigidity of structural members used, bridges behaved in linear elastic range under seismic loading. Developments in construction technology in later years, made it possible to build slender and lighter bridges. In order to design these bridges, it is important to understand such concepts as ductility and collapse mechanisms. Observations after destructive earthquakes and laboratory tests clearly show that structural damage is controlled mostly by deformation rather than strength.

Seismic response of a structure depends not only on the properties the structure but also the properties of seismic shaking. Source effects, path effects, local soil conditions, and soil-structure interaction are the main parameters affecting the response. Source effects cover the fault mechanism, distance to fault, and the magnitude of the earthquake; whereas, field effects cover the filtering of seismic waves by different soil strata that seismic waves pass through. Local soil conditions near the surface can strongly modify the waves' amplitude and frequency content.

The term Soil-Structure Interaction (SSI) defines the alterations in the dynamic response of the structure created by the interaction between the soil surrounding foundation and the foundation itself. For soft soils and heavy structures, such as bridges, SSI is an important factor affecting the response of the structure.

In this study, the influence of SSI on the seismic response of two bridge structures are investigated by using two different approaches. First one includes both structure and soil models together and is called the direct approach. Second one is the substructure approach; where the bridge structure is divided into two segments as the superstructure and the foundation system, accounting for both inertial and kinematic interactions.

1.1. Motivation of the Study

Although, SSI has a significant role on seismic response of structures, most of the design guidelines and common practices throughout the world have a tendency to ignore it. SSI is accounted for in design in an approximate way by simply applying modification factors to design loads. Force-based ATC 1996 and displacement-based ASCE 2013 procedures are examples of this approach. However, the influence of soil-structure-interaction is not clearly identifiable on these modifications.

There are two main approaches to include SSI effects explicitly in design, direct method and substructure method. Although theoretically possible, the direct method is not practical, because it models the entire structure and soil system in a single numerical model and performs the analysis in a single step. Since it avoids the use of a complex numerical model and long analysis time, substructure method is a better alternative for SSI analysis. The substructure method decomposes SSI problem into two distinct components, namely the kinematic and inertial interactions, and then combines the results to find the solution.

1.2. Summary and Scope

Aim of this research is to study practical procedures for performance-based seismic design of bridge structures subjected to soil-structure-interaction. This thesis consists of six chapters. Chapter 1 gives the motivation of the study, including the aim and objectives, and the outlines of the thesis. Chapter 2 presents a general view of SSI problems and how it is handled in seismic design guidelines. Most common static and dynamic approaches to solve SSI problems are presented. In chapter 3, geometric properties of two different bridge structures are given. Soil properties that are used in the analysis are presented, along with the correlations constructed from the field test data. Soil strata is defined at each meter from surface to bedrock. Ground motions; which are used in both strength-based and displacement-based analysis, are selected and scaled according to design criteria. Strength-based design of two bridges is introduced in this chapter. In chapter 4, structural system is introduced for both strength-based design and displacement-based analysis. Two different finite element models of the bridges are explained with the definitions of the structural elements. Finite element models are created for both linear and nonlinear analyses, in which

nonlinear behavior of structural elements and soil strata are explicitly defined. Nonlinearity of the soil strata is modelled as nonlinear *p-y*, *t-z* and *Q-z* springs. Site response analysis model that is constructed according to parameters given in Chapter 3, also given in this chapter. Input motion, which is established according to site response analysis, is applied on the structure via these springs. These models are used for both direct approach and substructure approach of SSI analysis. In chapter 5, analysis results are examined and compared. Response parameters compared include plastic rotations, and displacement and internal forces. Kinematic interactions and inertial interactions are investigated in the substructure method. Kinematic interaction shows how the motion of the foundation differs from the free-field motion due to varied stiffness, wave-scattering, etc. The inertial interaction describes the inertial forces developed in the structure by the foundation flexibility. Different models for kinematic interaction are developed, and the results for the substructure method are formed by combining the results of kinematic interaction and inertial interaction. Conclusions of the study are presented in Chapter 6.

2. LITERATURE REVIEW

During earthquakes, parts of incoming seismic waves are transmitted through the soil and foundation into the structure, and the rest are reflected back into the soil. In most applications using linear dynamic analysis, it is assumed that the structure is fixed-base (i.e., no waves are reflected back into the soil because soil is very stiff; (AASHTO, 2002)). When the soil is soft and flexible, it is not appropriate to model the foundation as fixed-base. When the structure is founded on a very stiff soil or rock, horizontal forces and moments at the base of the structure will not lead additional deformations in the soil surrounding the foundation (Kramer, 1996). Under the seismic excitation, foundation of the structure and the surrounding soil are interacted simultaneously that alter the ground motion. This interaction may be divided in to two phenomena called inertial interaction and kinematic interaction. Inertial interaction is the transmission of the inertial forces caused by the mass of the superstructure into the soil body causing further deformations in the soil. Kinematic interaction may be defined as the inability of the foundation due to its stiffness to follow the free field motions caused by earthquake ground motion.

One of the first introduction of soil-structure interaction effects into design guidelines was with ATC-3 (ATC, 1978). SSI is accounted for by reducing the base shear from the fixed-base solution. Later, this approach was included in the National Earthquake Hazard Reduction Program (NEHRP) seismic provisions. In Eurocode, there is no specific provisions and details on how to include SSI in design. According to Eurocode 8 (2004), soil-structure interaction shall be taken into account when;

i) For structures 2nd order effects play significant role,
ii) Structures with massive/deep foundations such as bridge piers,
iii) Slender tall structures
iv) Structures supported on very soft soils

ASCE 7-10, Minimum Design Loads for Buildings and Other Structures, provides Equivalent Lateral Force Procedure that is only valid for analysis with fixed-based condition with no foundation springs.

To include SSI effects, base shear (V) is modified as follows;

$$\tilde{V} = V - \Delta V \tag{2.1}$$

$$\Delta V = \left[C_s - \tilde{C}_s \left(\frac{0.05}{\tilde{\beta}}\right)^{0.4}\right] \bar{W} \leq 0.3V \tag{2.2}$$

The subscript ˜ denotes an SSI system.

C_s is the seismic response coefficient of the fixed base structure, $\tilde{\beta}$ is the fraction of critical damping for the structure-foundation system and $\bar{W}$ is the effective weight of the structure taken as 70% of the total seismic weight.

Effective period is established as;

$$\tilde{T} = T\sqrt{1 + \frac{\bar{k}}{K_y}\left(1 + \frac{K_y \bar{h}^2}{K_\theta}\right)} \tag{2.3}$$

T is the fundamental period of the structure and $\bar{k}$ is the stiffness of the fixed base structure; whereas, K_y is the lateral stiffness of the foundation and $\bar{h}$ is the effective height of the structure, which may be taken as 0.7 times the structural height.

$$\bar{k} = 4\pi^2 \left(\frac{\bar{W}}{gT^2}\right) \tag{2.4}$$

According to ASCE 7-10, effective damping $\tilde{\beta}$ of the structural system should not exceed 20% and should not be lower than 5% of the damping of fixed base system. According to ASCE 2010, SSI effects can be included in modal analysis, in a manner similar to equivalent lateral load analysis; however, it is applied only to the fundamental mode of vibration. The reduction (ΔV) is computed as in equivalent lateral load analysis.

Seismic response coefficient C_s is calculated as follows:

$$C_s = \frac{S_{DS}}{\frac{R}{I_e}} \tag{2.5}$$

I_e is the importance factor that may be taken equal to 1 for regular structures. R is the response modification factor that accounts for the ductility of the structure. S_{DS} is taken as design spectral response acceleration of the design response spectra at the fundamental period of the fixed base structure.

Besides ASCE 2010, most seismic provisions depend on non-linear static pushover methods such as Capacity Spectrum Method (ATC, 1996), Displacement Coefficient Method (BSSC,2000), Displacement Modification Method (FEMA 440, 2005.) and Linearization Method (FEMA 440, 2005). Demand and capacity are the two main elements of the performance-based design procedures. Earthquake ground motion is represented by the demand; whereas structures' ability to withstand seismic demand is named as the capacity. In order to establish the capacity curve, incremental pushover analysis is performed by a static lateral load pattern applied on the structure. Structural system is pushed until the target displacement is established. Base shear vs roof displacement is plotted to reflect the level of inelasticity in the structure.

One of the most common way to assess the seismic structural performance is Capacity Spectrum Method (ATC, 1996). To use this method, pushover curve (in terms of base shear and roof displacement) should be converted to capacity spectrum. With this approach, base shears and roof displacements of MDOF system is converted into spectral accelerations and spectral displacements of an equivalent SDOF system respectively. Seismic structural performance is established by comparing the capacity spectrum with the demand spectrum in Acceleration-Displacement Response Spectra (ADRS) format.

SSI can be adapted to the demand spectrum via reduction of demands in kinematic and inertial interactions according to ASCE (2013), and previously in FEMA 368 (2000), NEHRP Recommended Provisions for Seismic Regulations for New Buildings and Other Structures (2004) and FEMA 440 (2005).

Methodology presented in ASCE (2013) is mostly valid for buildings. Effects of kinematic interactions may be included by ratio of response spectra (RRS) factors, RRS_{bsa} for base slab averaging and RRS_e for embedment. RRS factors are multiplied by the spectral acceleration ordinates on the response spectrum. Base slab averaging is not permitted for structures located on soft clay sites, buildings with floor and roof diaphragms classified as flexible, and foundation components that are not laterally connected. Reductions of embedment is not allowed for structures located on firm rock sites, and foundation components that are not laterally connected. Total reduction cannot not be greater than 50% ($RRS = RRS_{bsa} \times RRS_e \geq 0.5$).

3. STRUCTURAL SYSTEM, SOIL PROPERTIES, GROUND MOTIONS AND DESIGN

Two bridges with different dynamic characteristics are considered for the evaluation and comparison of different SSI approaches. Both bridges have reinforced concrete piers resting above 16 piles with 1.0 m diameters. The superstructures of the bridges consist of cast-in-place post-tensioned C40/50 reinforced concrete hollow boxes. Pile caps, piers and cap beams are C35/45 reinforced concrete; whereas, the piles are C25/30 reinforced concrete. The decks of the both bridges are continuous and simply supported on the piers via steel reinforced elastomeric bearings. There are two elastomeric bearings on each pier. Elastomeric bearings can move in longitudinal direction but fixed in the transverse direction. Geometric properties of the bridges are given in Chapter 3.1.

3.1. Geometric Properties

Bridge-I that is used in the design consists of 3 spans and total length of 120.00 m; whereas, Bridge-II consists of 4 spans, which are 40.00 m long each. There are two lanes 3.00 m wide, two emergency shoulders 0.50 m wide, and two sidewalks 1.50 m wide on each side. The decks of both bridges are continuous and supported on the piers via steel reinforced elastomeric bearings. There are two elastomeric bearings on each pier. Elastomeric bearings can move in the longitudinal direction but fixed in the transverse direction. The pier heights for Bridge I are 28.00 m and 14.00 m, and the pier heights Bridge-II are all 14.00 m. The structural cross-sections are given in Figure 3.1 to 3.3 and in Table 3.1 and Table 3.2.

Table 3.1. Properties of the bridges.

Number of spans	3 / 4
Span lengths	40.00 m
Bridge length	120.00 m / 160.00 m
Bridge total width	10.00 m
Bridge skewness	-
Live load class	$H_{30} - S_{24}$
Lane width	7.00 m (3.50x2)
Number of lanes	2 lanes
Live load reduction factor	1.00
Left pavement width	2.00 m
Right pavement width	1.00 m
Deck height	2.00 m

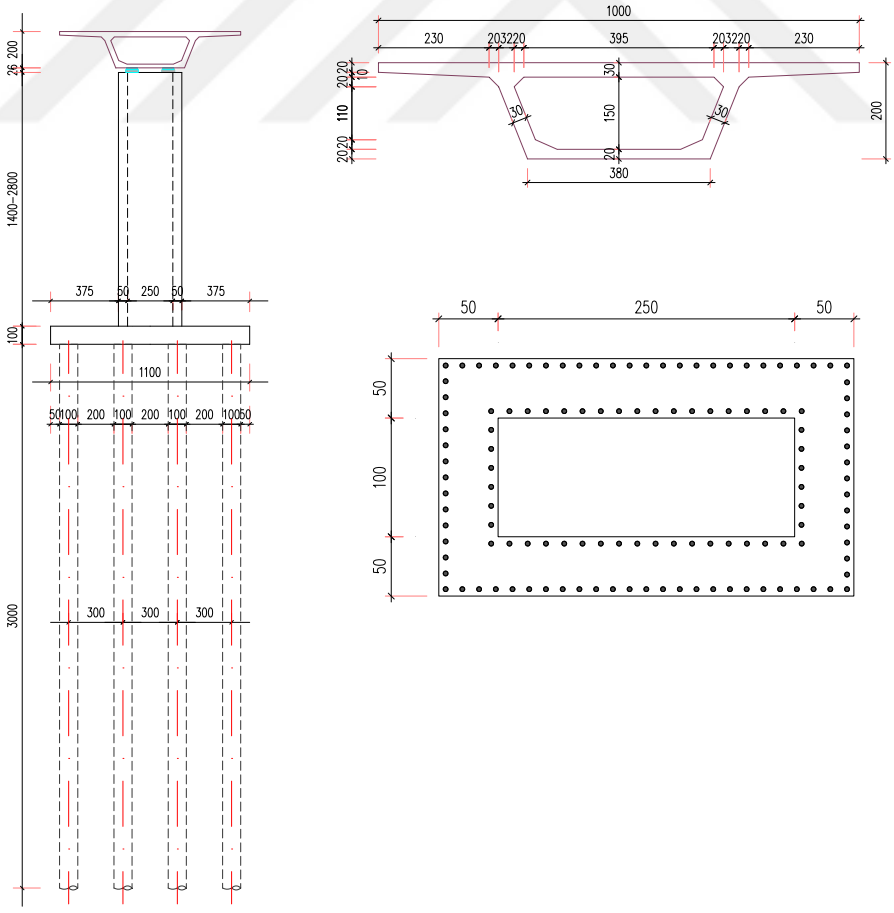

Figure 3.1. Section drawings of the pier and the superstructures.

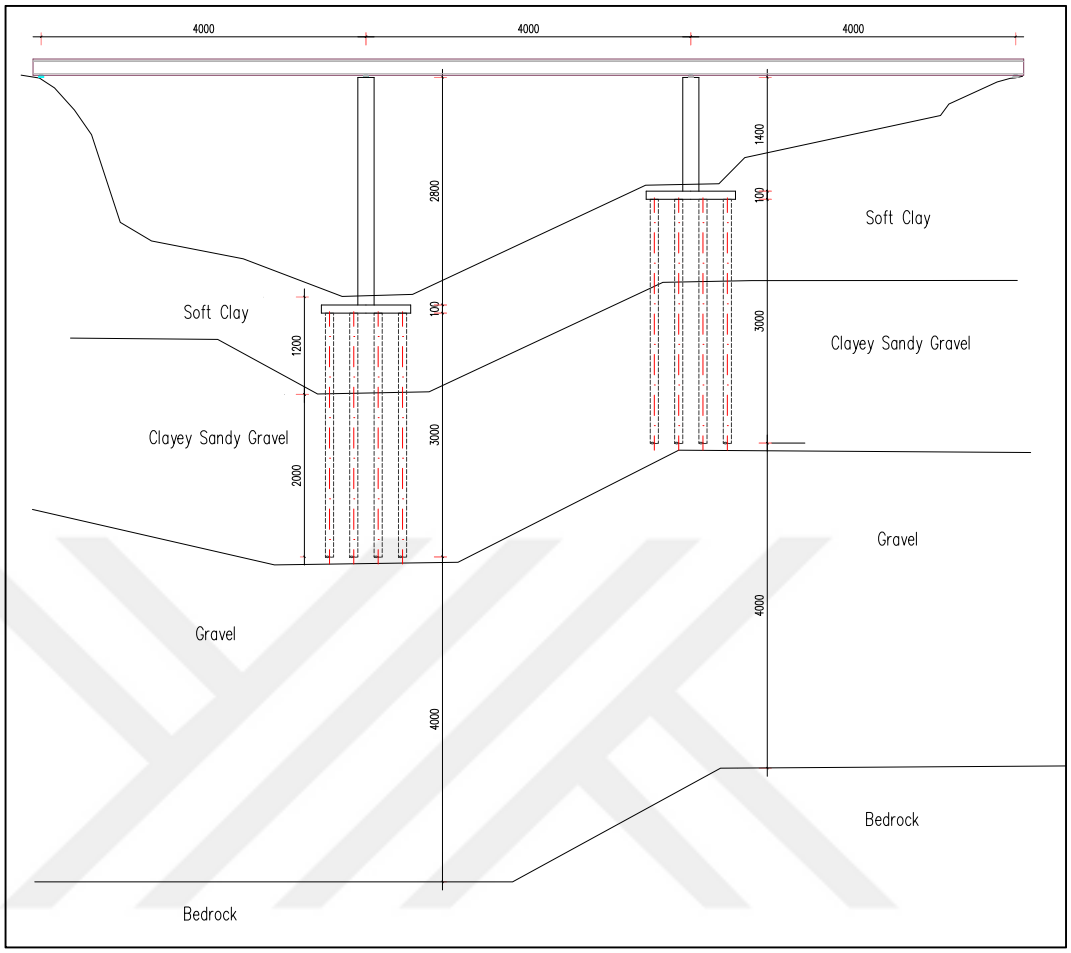

Figure 3.2. Bridge-I and the soil profile.

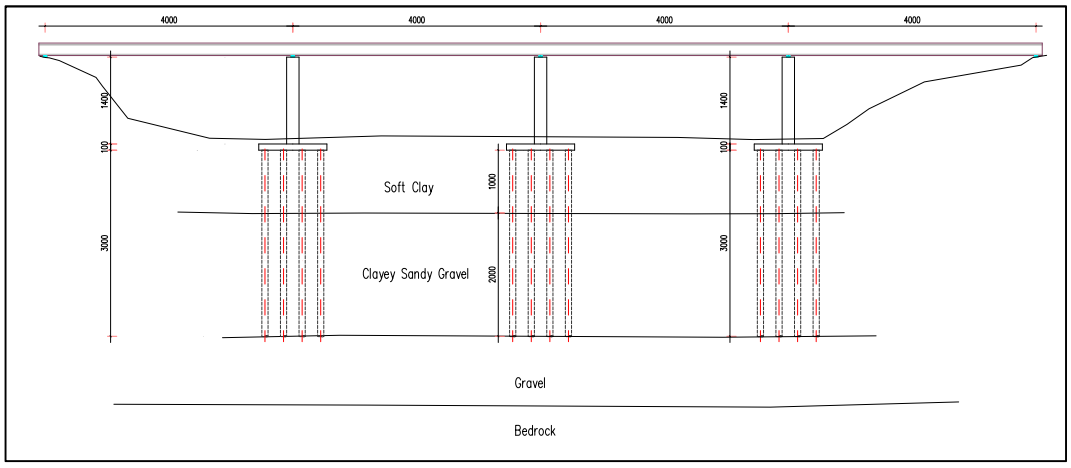

Figure 3.3. Bridge-II and the soil profile.

Table 3.2. Section properties of the superstructures.

Cross section area:	4.67 m²
Moment of inertia about 3 axis:	2.3836 m4
Moment of inertia about 2 axis:	26.7717 m4
Torsional constant:	5.3051 m4

3.2. Soil Properties

Defining the soil properties and modeling the soil behavior are important, when SSI is included in the analysis. Soil properties used in the analyses are given in the Table 3.3 and shown in Figure 3.4. Soil unit weight (ɣ), stiffness of the soil layers (k), ε_{50} and undrained shear strength (c_u) of clay layer are interpreted from the shear wave velocity (V_s) and SPT$(N)_{60}$ values identified from the borehole analysis. First 12 m from the surface comprise of soft clay layer. Clayey sandy gravel layers start from 12 m to 27 m below the surface. As the depth increases, strength of the gravel layers increases. Beyond 27 m, gravel layer continues until the bedrock is reached at 70 m.

Table 3.3. Soil properties.

S*	ϕ	c_u	ε_{50}	ɣ (kN/m³)	SPT$(N)_{60}$	V_s (m/s)	k (KN/m³)	Soil Type
0	0	35	0.02	18	3	120	4	Soft clay
12	30			19	10	320	6.6	Clayey sandy gravel
14	30			19	10	320	13.2	Clayey sandy gravel
16	30			19	15	320	26.4	Clayey sandy gravel
18	32			19	16	320	39.6	Clayey sandy gravel
20	32			19	14	320	52.8	Clayey sandy gravel
22	32			19	20	340	66	Clayey sandy gravel
24	34			19	32	340	79.2	Clayey sandy gravel
26	34			19	38	340	92.4	Clayey sandy gravel
27	33			19	36	340	99	Clayey sandy gravel
33	38			20	R	360	99	Gravel
40	38			20	R	360	99	Gravel
50	38			20	R	380	99	Gravel
60	40			20	R	400	99	Gravel
70	40			23	R	760	99	Bedrock
*Distance from ground to beginning of each layer								

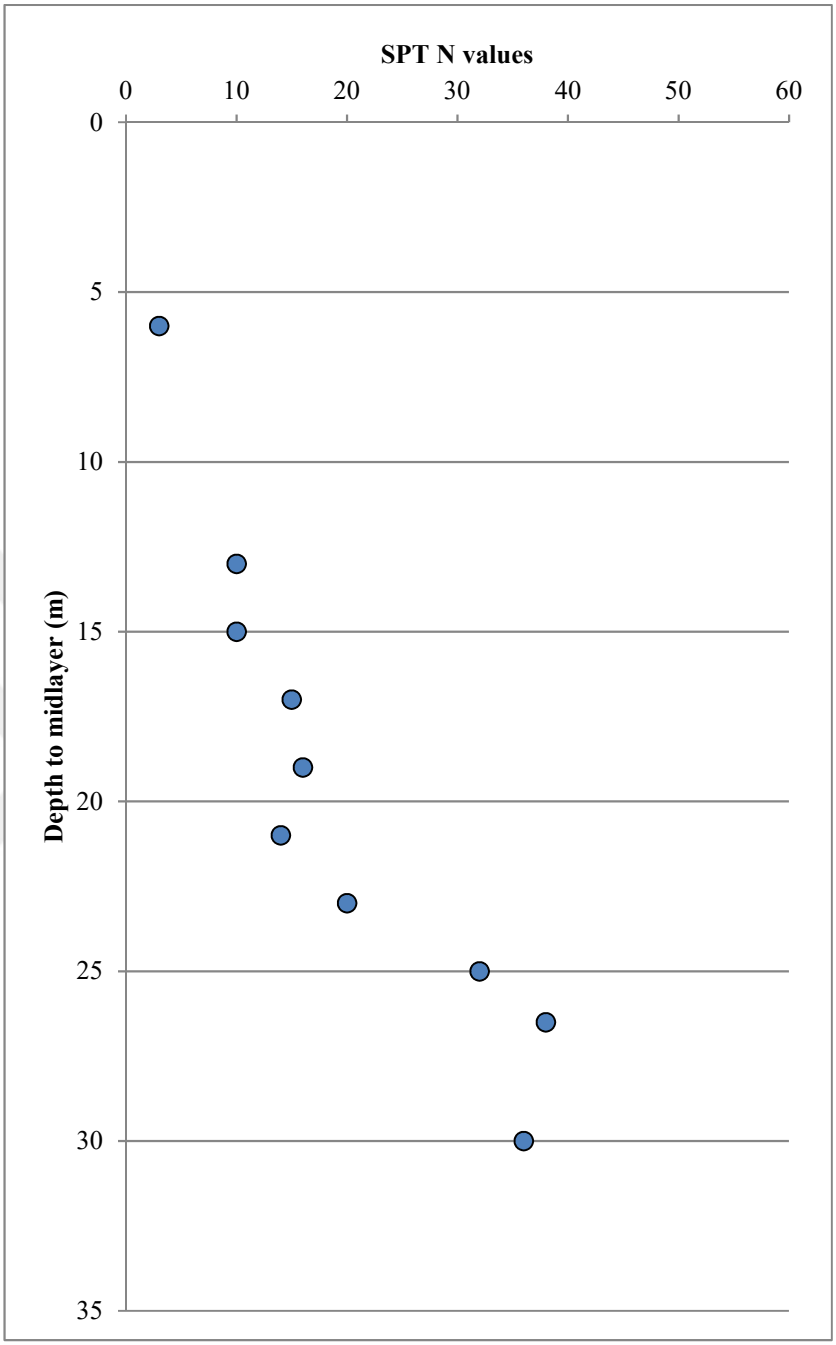

Figure 3.4. SPT N - depth graph.

3.3. Ground Motion Selection and Scaling

To investigate various approaches used to incorporate SSI on structural response, we need acceleration time histories. There are three commonly used approaches to select acceleration time histories for the analysis:

-Design response spectrum compatible artificial records.
-Simulated records from seismological models.
-Accelerograms recorded in real earthquakes

In this study, real earthquake records are used. The records selected should match the seismicity and the site characteristics of the location, and the hazard level selected for the structure. In the study, 19 records are used to study the response in the transverse direction of the bridge. The response in the longitudinal direction is not considered. The list of earthquakes considered are given in Table 3.4, and the time histories selected for the analysis are shown in Figure 3.5 through 3.24.

Table 3.4. Earthquakes selected for the analysis.

Record No	Earthquake	Time	Magnitude	PGA (g)
68_090	San Fernando	02/09/71	6.61	0.210
125_000	Friuli	05/06/76	6.50	0.351
169_352	Imperial Valley	10/15/79	6.53	0.351
174_11230	Imperial Valley	10/15/79	6.53	0.380
721_000	Superstition Hills	11/24/87	6.54	0.358
725_270	Superstition Hills	11/24/87	6.54	0.446
752_000	Superstition Hills	11/24/87	6.54	0.529
767_000	Loma Prieta	10/18/89	6.93	0.555
829_360	Cape Mendocino	04/25/92	7.01	0.549
900_270	Landers	06/28/92	7.28	0.245
953_279	Northridge	1/17/94	6.69	0.516
960_270	Northridge	1/17/94	6.69	0.482
1111_000	Kobe	01/16/95	6.90	0.509
1116_000	Kobe	01/16/95	6.90	0.243
1148_000	Kocaeli	08/17/99	7.51	0.219
1158_270	Kocaeli	08/17/99	7.51	0.358
1244_101n	Chi-Chi	09/20/99	7.62	0.440
1602_090	Duzce	11/12/99	7.62	0.822
1787_090	Hector Mine	10/16/99	7.13	0.337

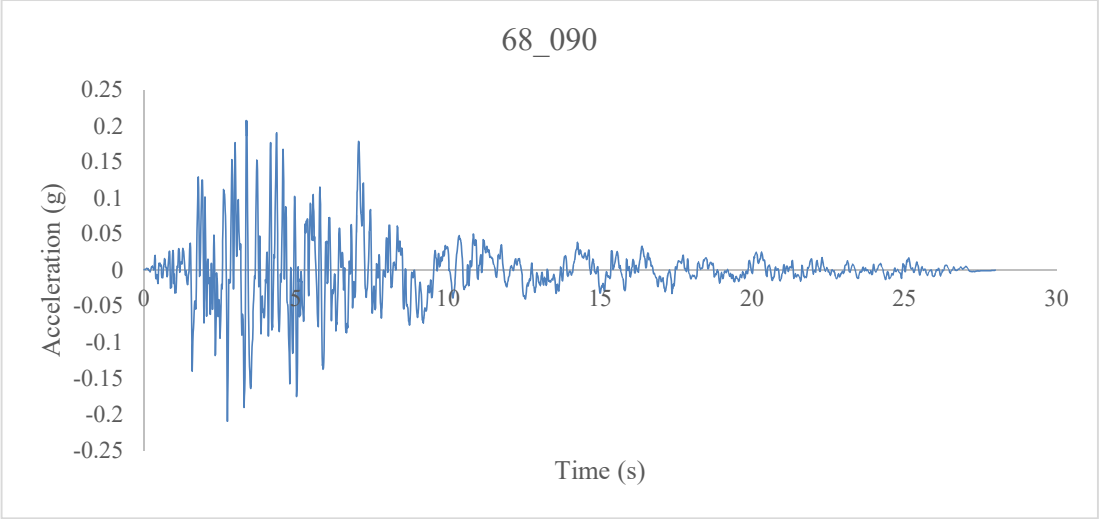

Figure 3.5. San Fernando 02/09/71 14:00, La Hollywood Stor Lot, 090 (USGS station 135).

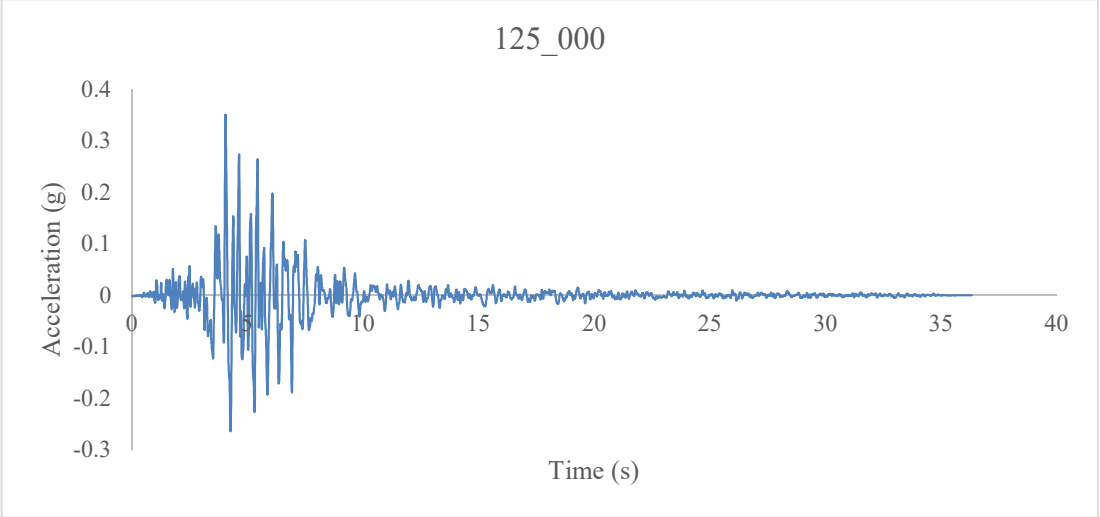

Figure 3.6. Friuli, Italy 05/06/76 2000, Tolmezzo.

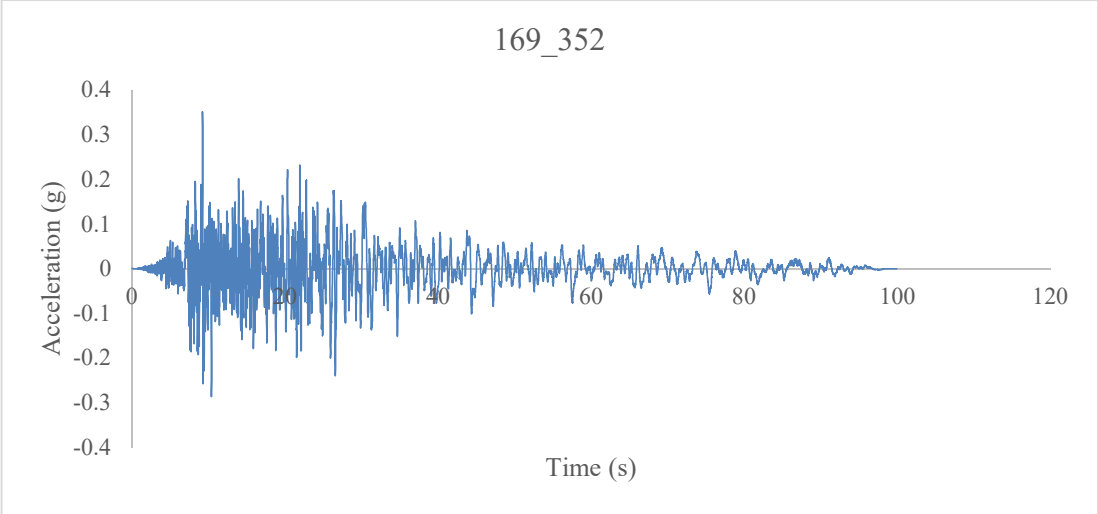

Figure 3.7. Imperial Valley 10/15/79 2316, Delta, 262 (UNAM/UCSD station 6605).

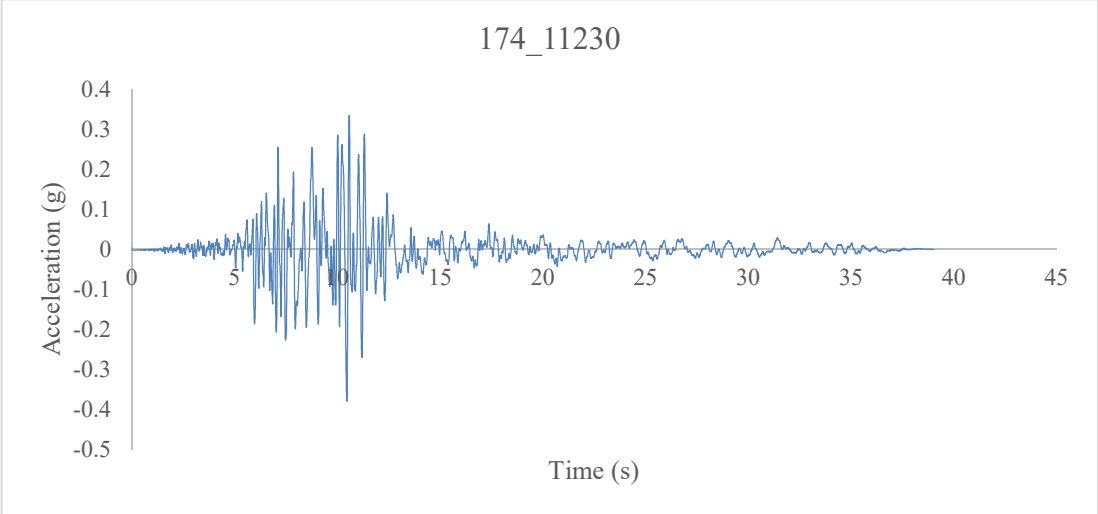

Figure 3.8. Imperial Valley 10/15/79 2316, El Centro Array #11, 140 (USGS station 5058).

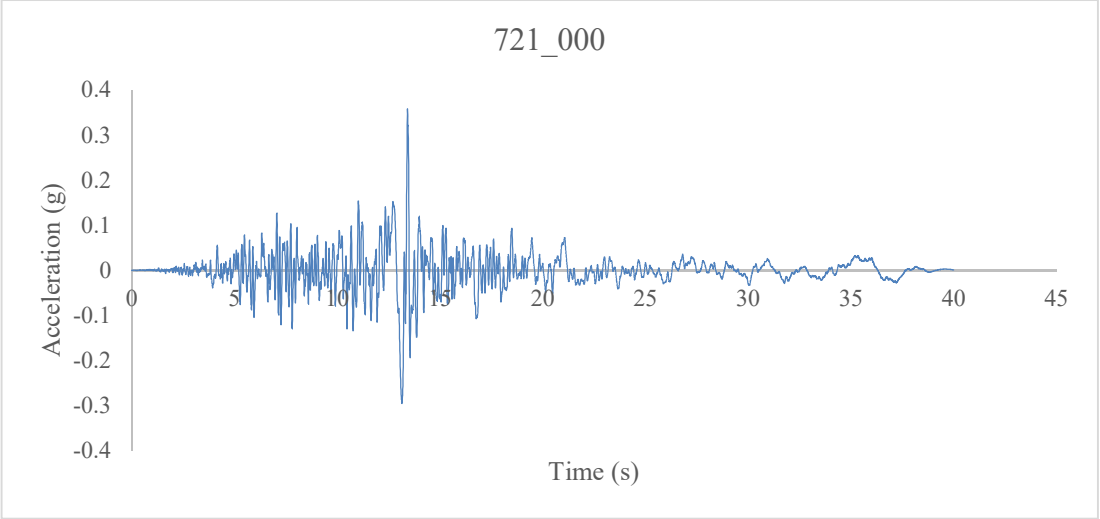

Figure 3.9. Superstition Hills 11/24/87 13:16, El Centro Imp Co Center.

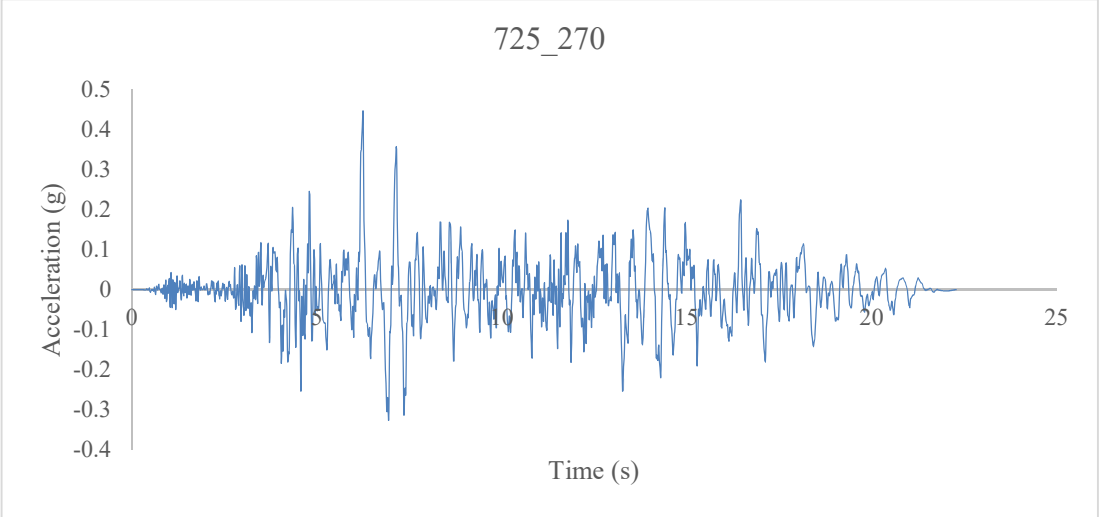

Figure 3.10. Superstition Hills 11/24/87 13:16, POE, 270 (USGS station temp).

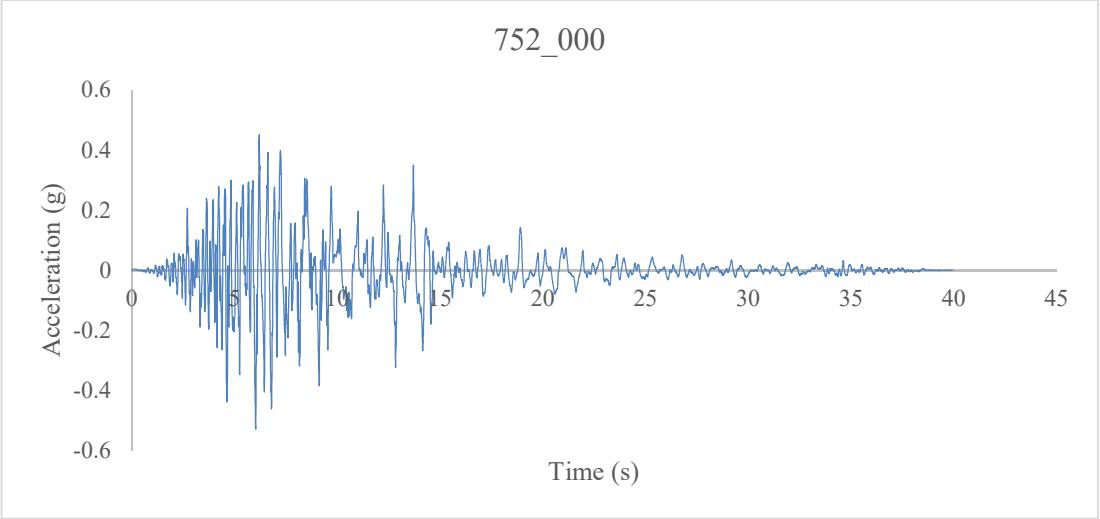

Figure 3.11. Superstition Hills 11/24/87 13:16, POE, 270 (USGS station temp).

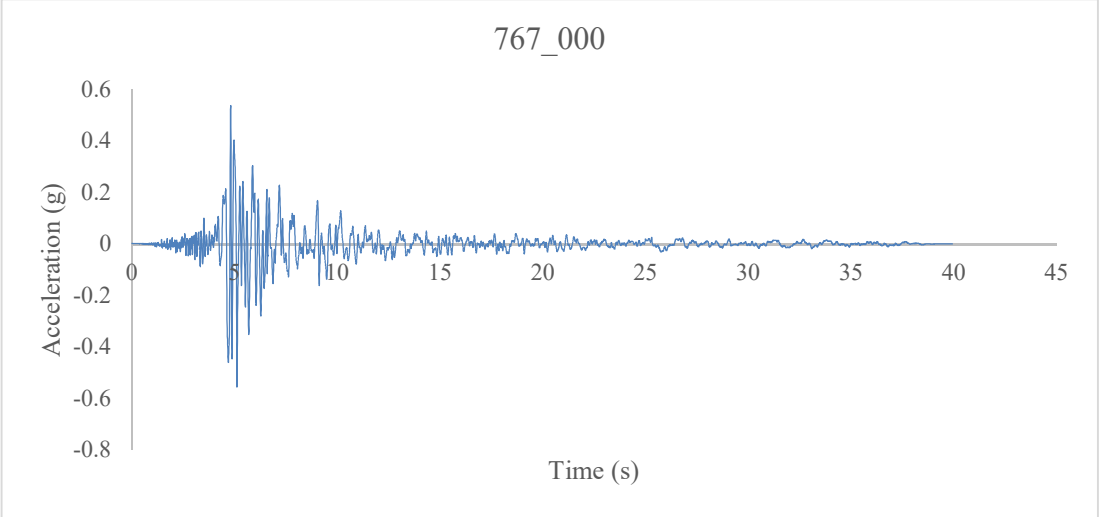

Figure 3.12. Loma Prieta 10/18/89 00:05, Gilroy Array #3, 000 (CDMG station 47381).

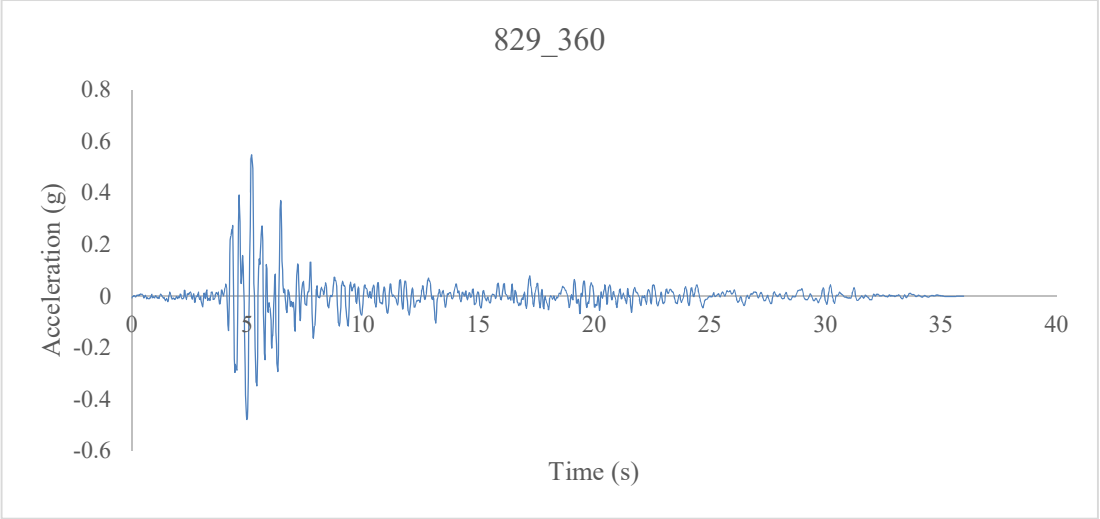

Figure 3.13. Cape Mendocino 04/25/92 1806, Rio Dell overpass FF, 270 (CDMG station 89324).

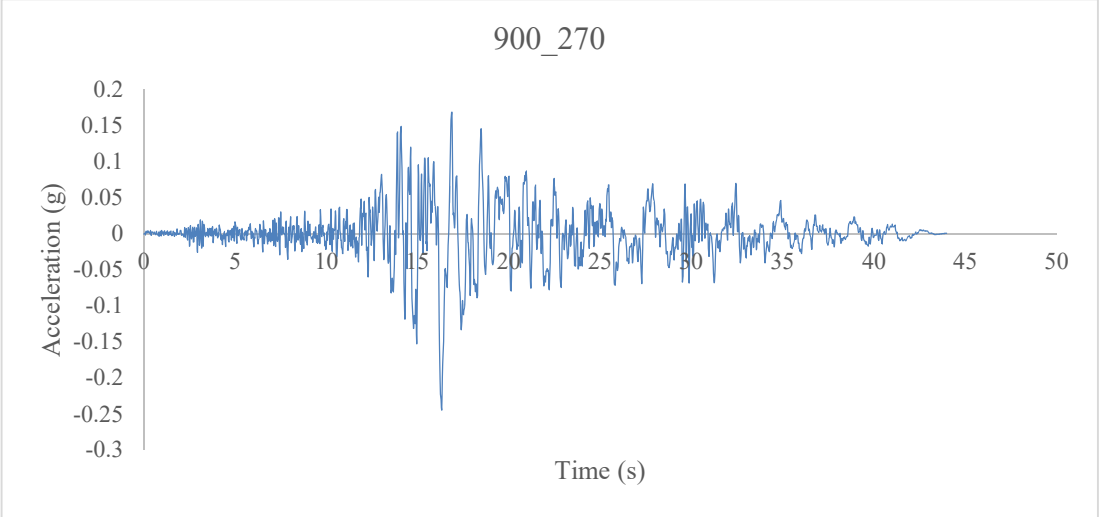

Figure 3.14. Landers 06/28/92 1158, Yermo fire station, 270 (CDMG station 22074).

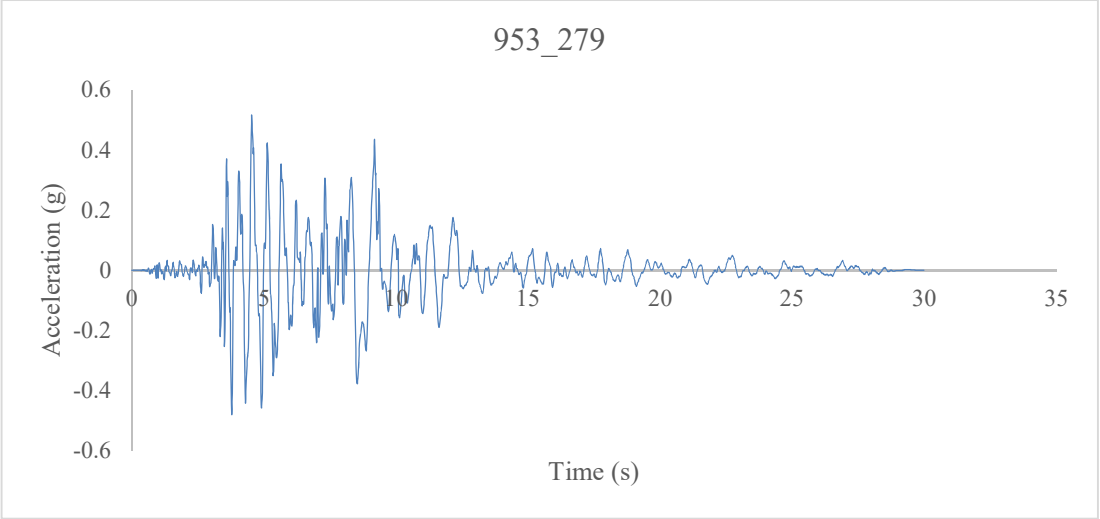

Figure 3.15. Northridge EQ 1/17/94, 12:31, Beverly Hills - 14145 Mulh, 009 (USC station 90013).

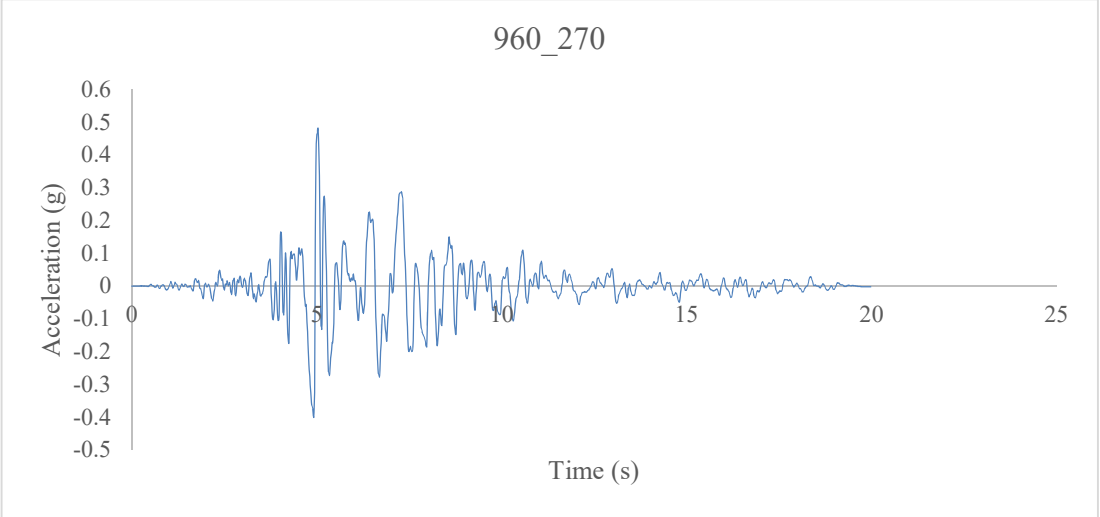

Figure 3.16. Northridge EQ 1/17/94, 12:31, Canyon Country - W Lost Canyon, 000 (USC station 9).

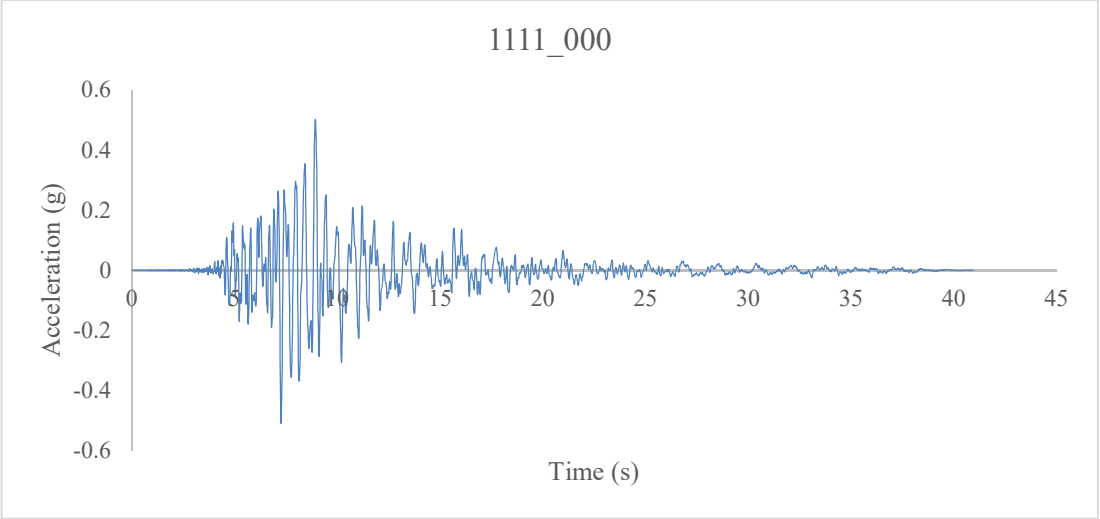

Figure 3.17. Kobe 01/16/95 2046, Nishi-Akashi, 000 (CUE).

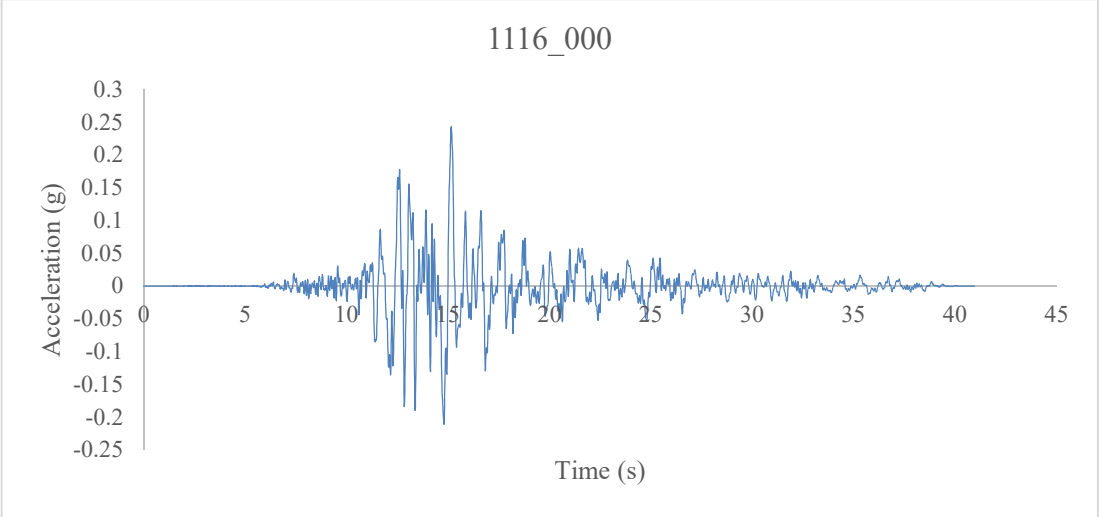

Figure 3.18. Kobe 01/16/95 2046, Shin-Osaka, 000 (CUE).

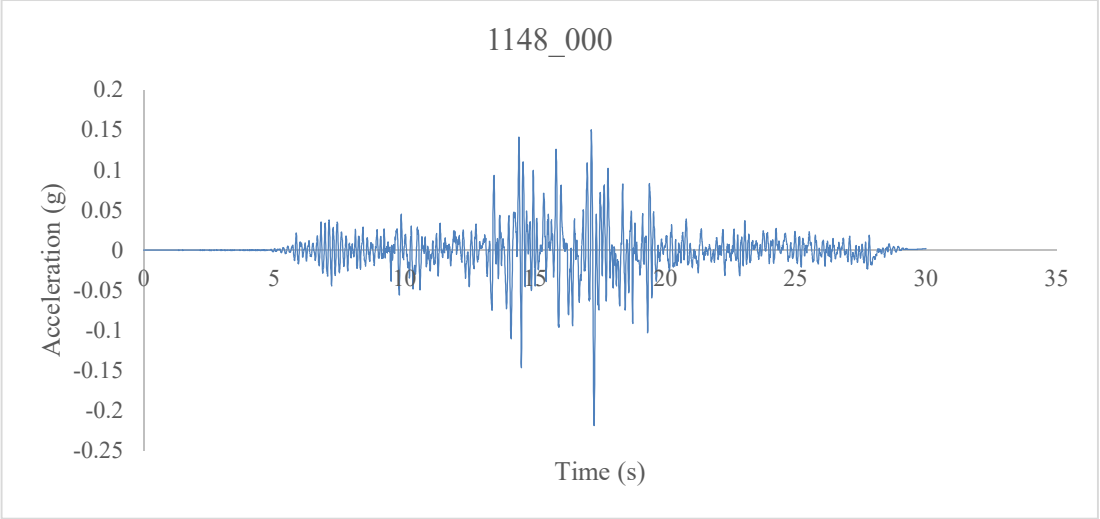

Figure 3.19. Kocaeli 08/17/99, Arcelik, 000 (KOERI).

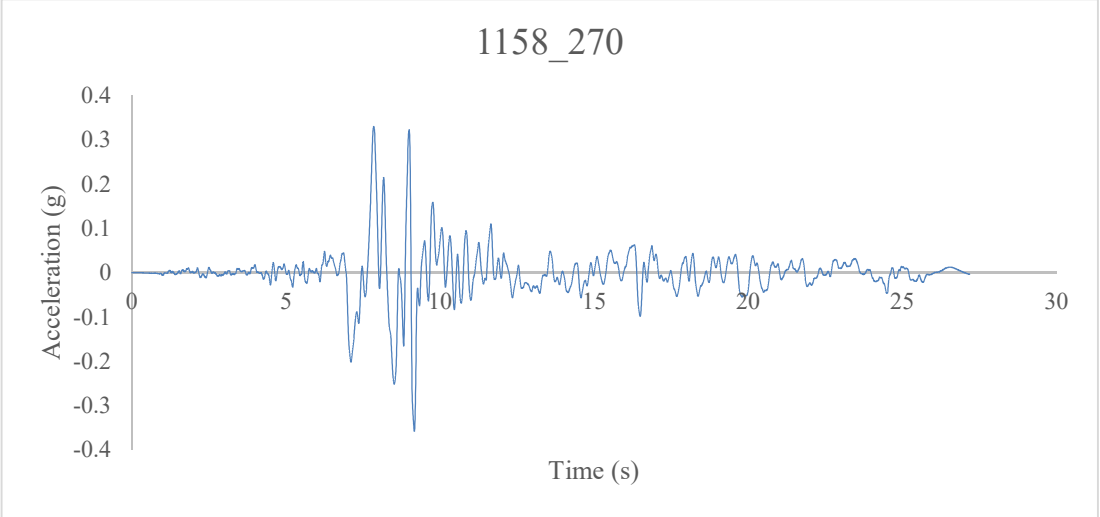

Figure 3.20. Kocaeli 08/17/99, Duzce, 180 (ERD).

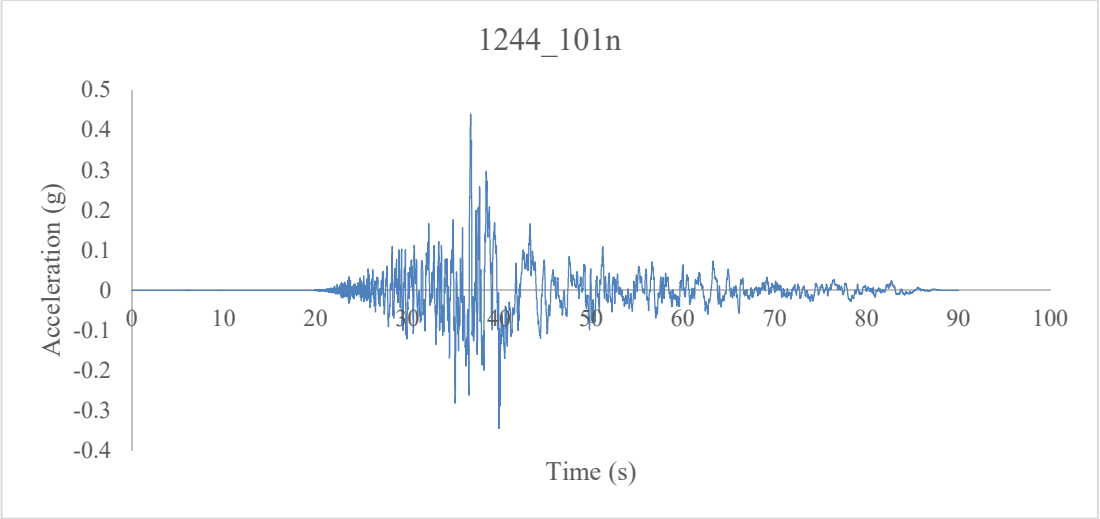

Figure 3.21. Chi-Chi 09/20/99, CHY101, E.

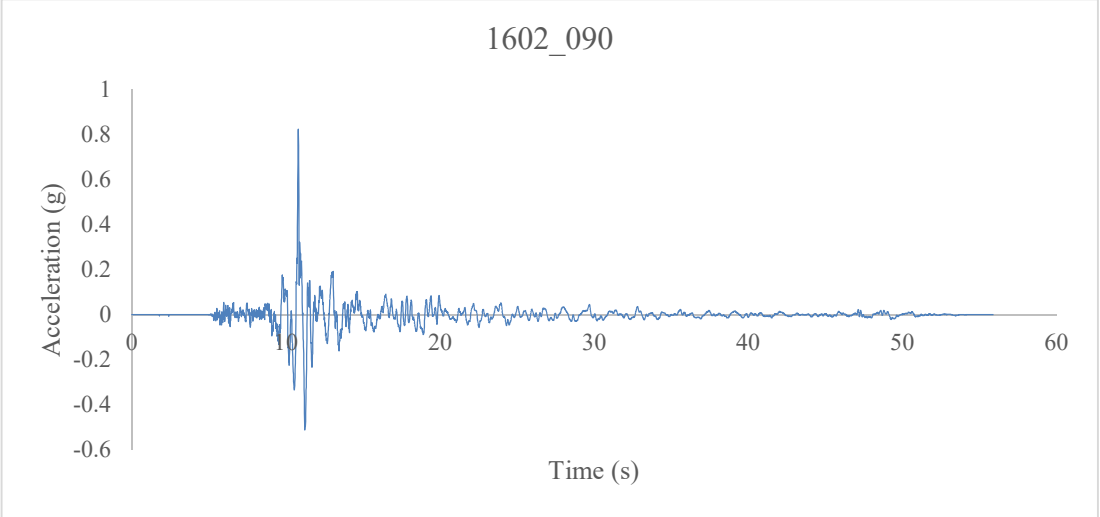

Figure 3.22. Duzce 11/12/99, Bolu, 000 (ERD).

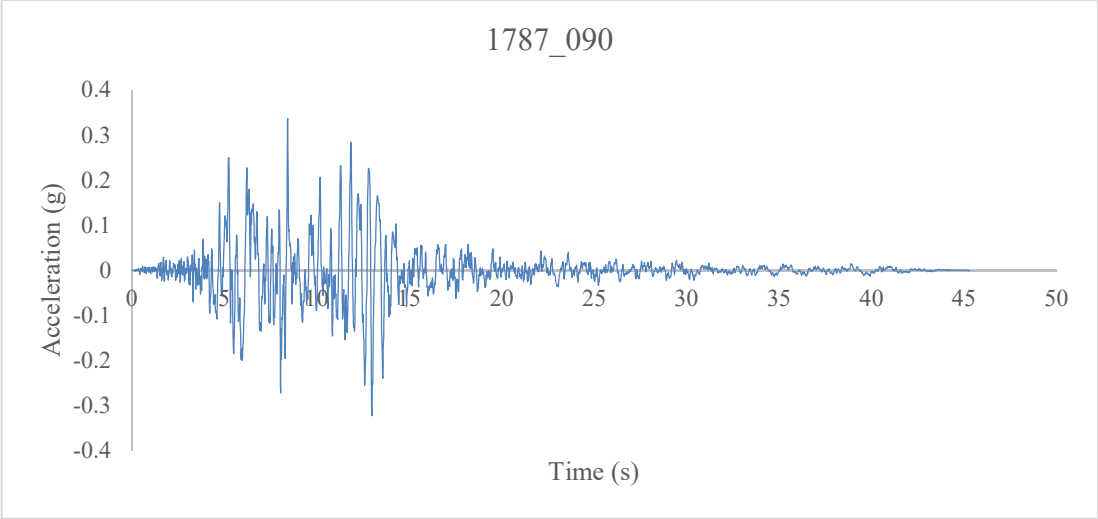

Figure 3.23. Hector Mine 10/16/99 02:47, HEC, 000.

For scaling ground motions, a target spectrum for soil class C, shown in Figure 3.24, is created according to AASHTO Guide Specifications for LRFD Seismic Bridge Design Article 3.10.2.1. The target spectrum has the acceleration values of 1.5 g and 0.53 g at periods 0.2 sec (S_s) and 1.0 sec (S_1), respectively, and the peak acceleration (PGA) value 0.60 g. Target spectrum is used solely to scale the ground motion data selected for the study.

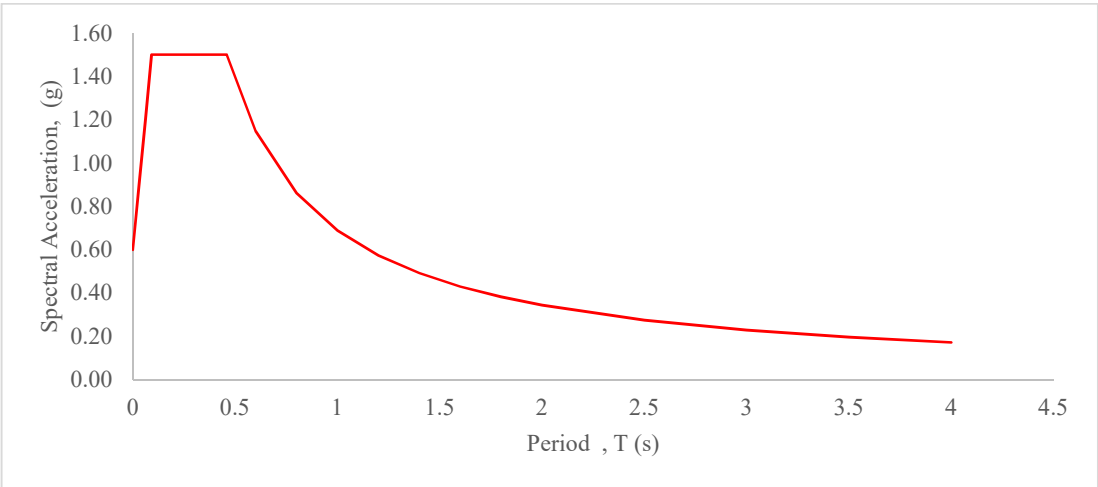

Figure 3.24. Target spectrum.

The comparison of the response spectra of unscaled accelerograms with target spectrum are plotted in Figure 3.25.

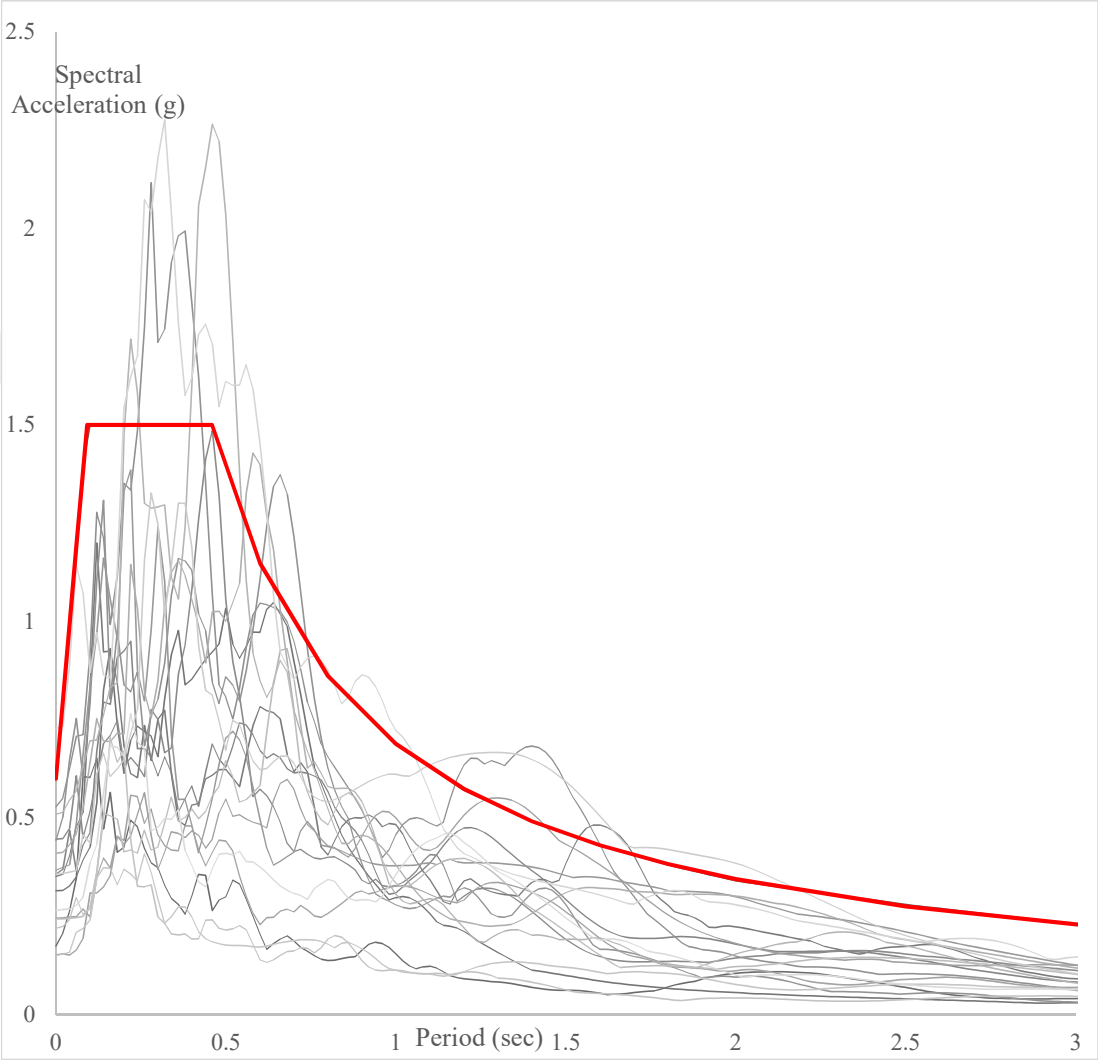

Figure 3.25. %5 Damped response spectrum of raw data with target spectrum.

Accelerograms are scaled to match the target spectrum by using the wavelets algorithm proposed by Abrahamson [1992] and Hancock et al. [2006]. The comparison after the scaling is shown in Figure 3.26.

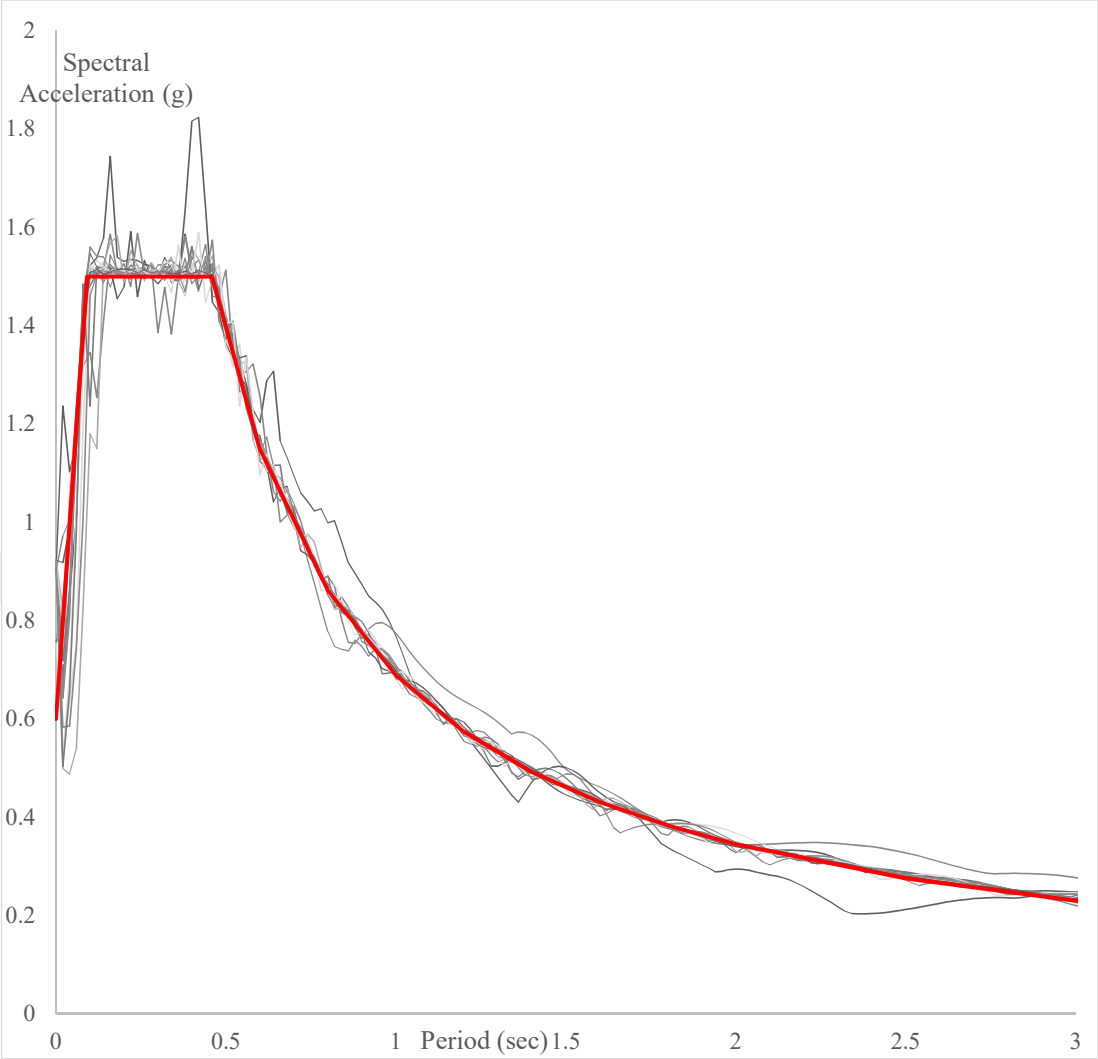

Figure 3.26. %5 Damped response spectrum of matched data with target spectrum.

3.4. Design of Bridges

For the strength-based design of the bridge, AASHTO LRFD Bridge Design Specifications (2012) is used. The modelling details of the bridges are given in Chapter 0. Response spectrum analysis is performed for linear seismic design. The piers are assumed to deform inelastically when seismic forces exceed their design level. Design levels are calculated by dividing the elastically computed forces by the appropriate response modification factors. The response modification factor is assumed to be 3.0 for both directions, according to AASHTO LRFD Bridge Design Specifications Table 3.10.7.1-1 (2012).

3.4.1. Loads Considered for Design

Self-weight of the structure is calculated with respect to weight of the structural elements and fill, and the other loads on the deck of the bridge.

Asphalt loading: 10 m x 0.05 m x 23 kN/m³ = 11.5 kN/m
Guardrail and handrail loading: 2 x 1.5 kN/m = 3 kN/m
Pavement loading: (2+1) m x 0.20 m x 25 kN/m³ = 15 kN/m

H30-S24 vehicular loading is considered for the design. One axis of the truck axle loading is given in Figure 3.27. Half of the live loads are added to the mass of the system.

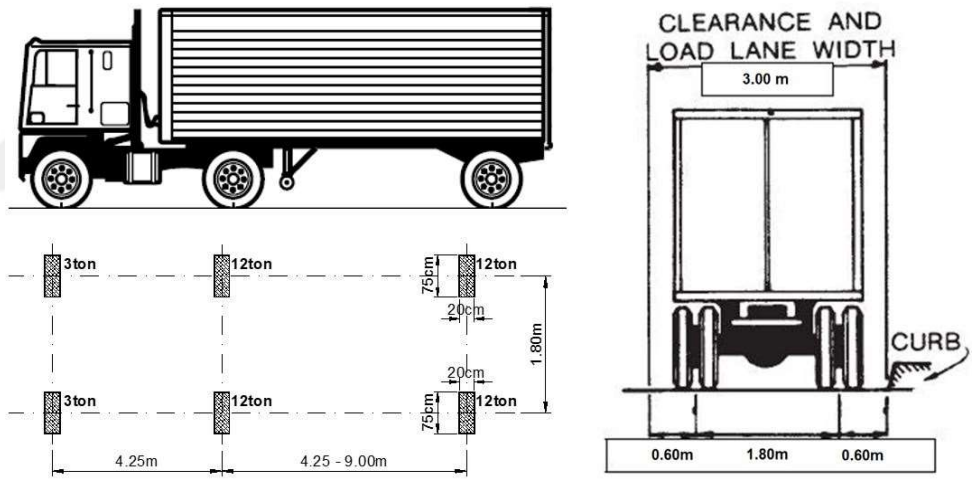

Figure 3.27. H30-S24 truck live load.

Live load impact factor (*Ø*) for 40m span is;

$$Ø = 1+15 / (L+37) = 1.19 \quad (3.1)$$

5 kN/m² pedestrian live load is considered on the foot walk.

3.4.2. Response Spectrum analysis

Response spectrum analysis is used to determine elastic seismic demand of the bridge elements. Maximum modal responses of different modes are calculated and combined by using the SRSS method. Since the response spectrum analysis is based on the linear behavior, the results are used only for the preliminary design of the structure.

According to local seismicity and soil conditions many codes around the world, suggest different design response spectrum calculation methods. However, these methods provide a general solution including the site conditions only with a rough distinction. In order to make a better evaluation, response spectrum including local site effects is defined with the results of site response analysis. Details of the site response analyses are given in Chapter 4.1.2. The response spectrum, created from the acceleration-time history data obtained at the ground level of the site response analysis, accounting site effects is given in Figure 3.28.

Response Spectrum analysis is made according to this spectrum in both orthogonal directions. %30 effect of one direction is added to other orthogonal direction in the combinations. Half of the live load is added as mass to the dead load in the response spectrum analysis.

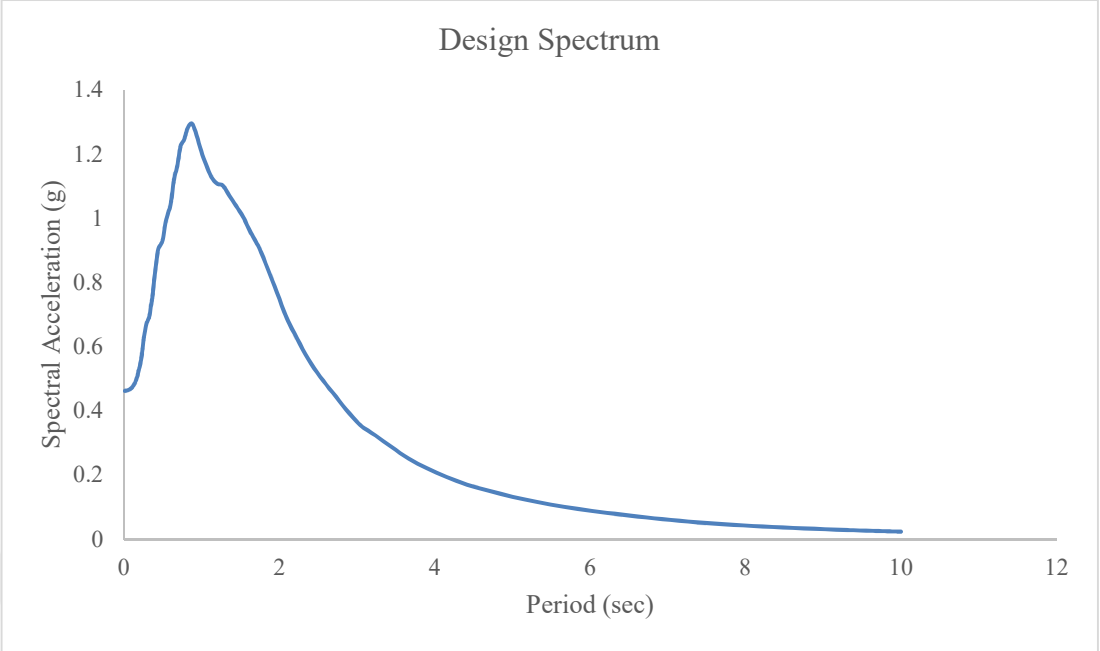

Figure 3.28. Design spectrum.

3.4.3. Capacity Estimation

Estimation of strength and deformability of the structural elements is necessary for comparing the seismic demands and evaluate the structure's ability to withstand these demands. Nonlinear deformation characteristic of the structure depends on the nonlinear material behavior that given in Section 4.1. Structural elements, which are probable to exhibit nonlinear behavior, are idealized mathematically to represent nonlinear moment-curvature relations. Ratio of the rotation at a specific section of the element divided by the yield rotation is the mathematical description of the term ductility. Ductility is an important concept while evaluating the structural capacity under seismic excitation due to ability to withstand earthquake forces with displacement instead of strength.

Moment curvature analysis is a widely used method to estimate flexural strength of a section. There are several software programs available for moment curvature analysis. CSiCol (CSI, 2019), and Section Designer utility of SAP2000 (CSI, 2019) are widely used for this purpose. In this study, SAP2000 Section Designer is used for designing pier sections. Cross-section of the pier can be seen in the Figure 3.29. Concrete and structural steel

properties of the piers with 28.00 m and 14.00 m height are defined in the software and rebar ratio is taken as 1.69% and 2.24% respectively.

For piers, strain at unconfined compressive strength is $2x10^{-3}$ and ultimate unconfined strain capacity is $5x10^{-3}$. Transverse reinforcement ratio does not involve in the capacity calculations, as the confinement is not included in the moment curvature analysis. Thus, there is only one cross-section is analyzed for each pier, since longitudinal reinforcement does not change along the pier height. Moment-curvature diagrams may be seen in between Figure 3.30 to Figure 3.33, whereas, analyzed pier section is given in Figure 3.29. Moment-curvature diagrams are used in strength-based design of the bridges while inertial loads are exerted to the foundation system. Moment transferred to the foundation system from the pier is limited to the plastic moment values given in Figure 3.30 to Figure 3.33.

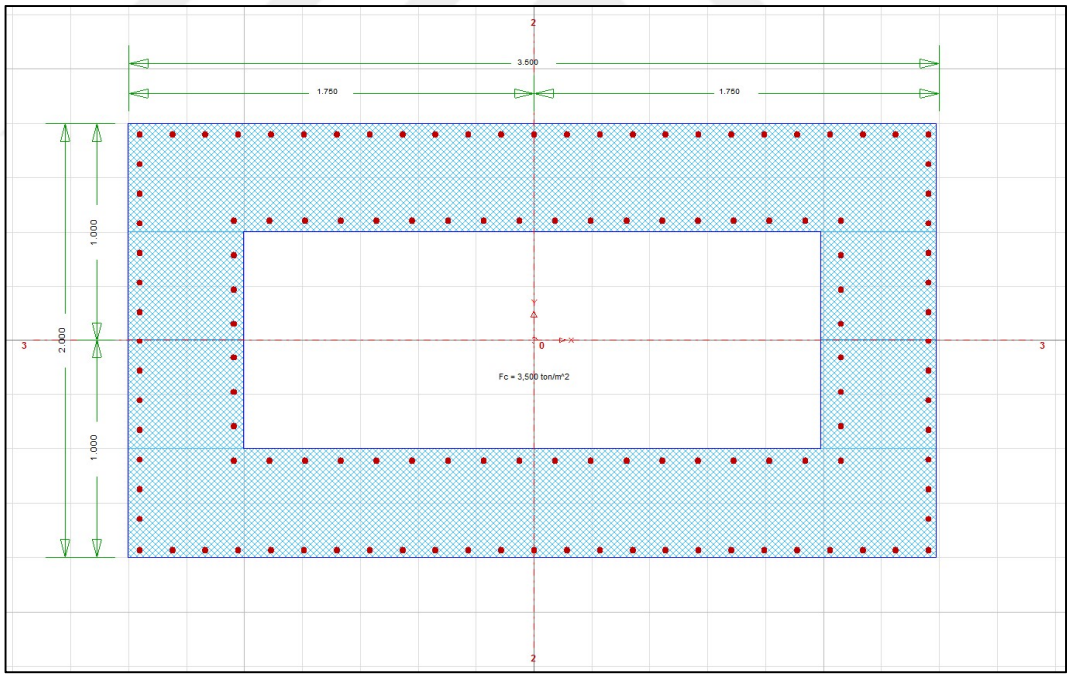

Figure 3.29. Cross-section of the pier.

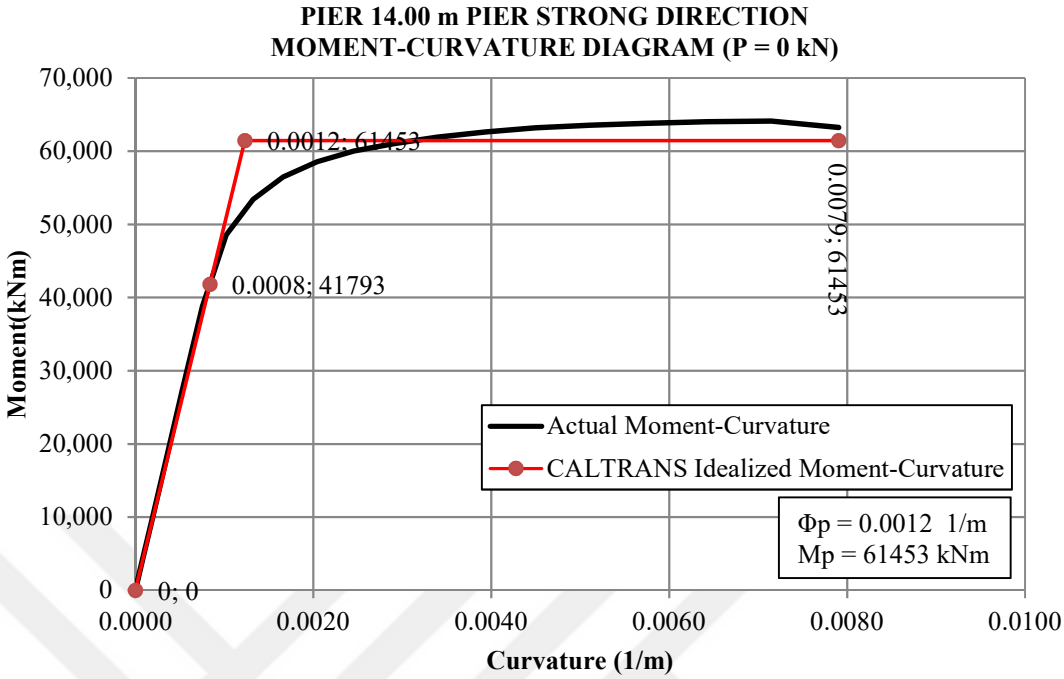

Figure 3.30. Pier 14.00 m pier strong direction moment-curvature diagram.

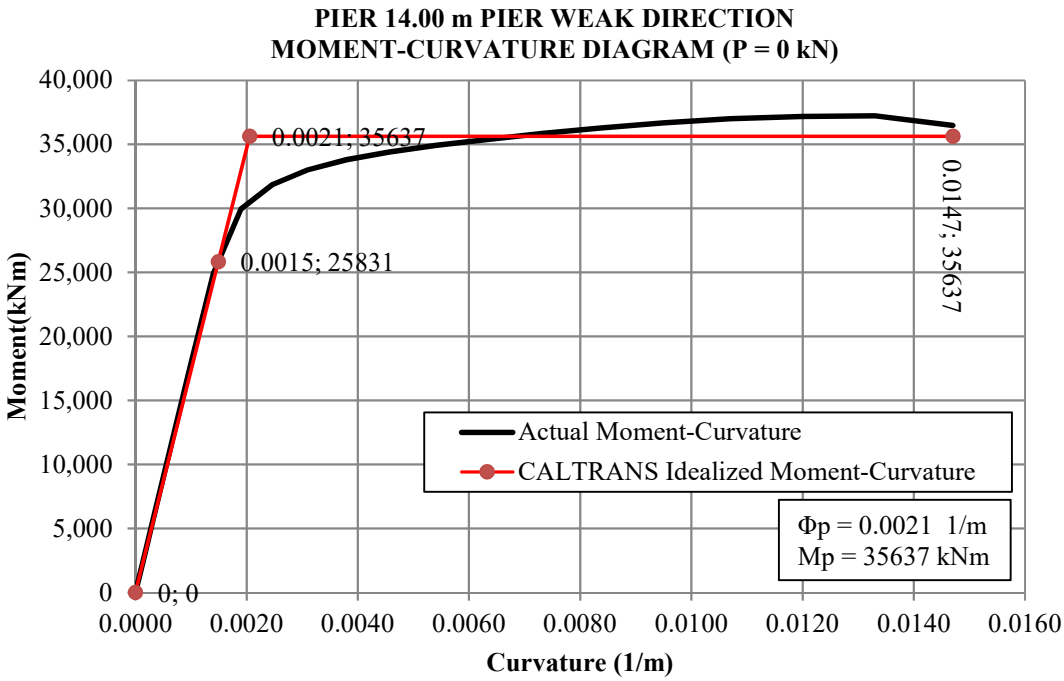

Figure 3.31. Pier 14.00 m pier weak direction moment-curvature diagram.

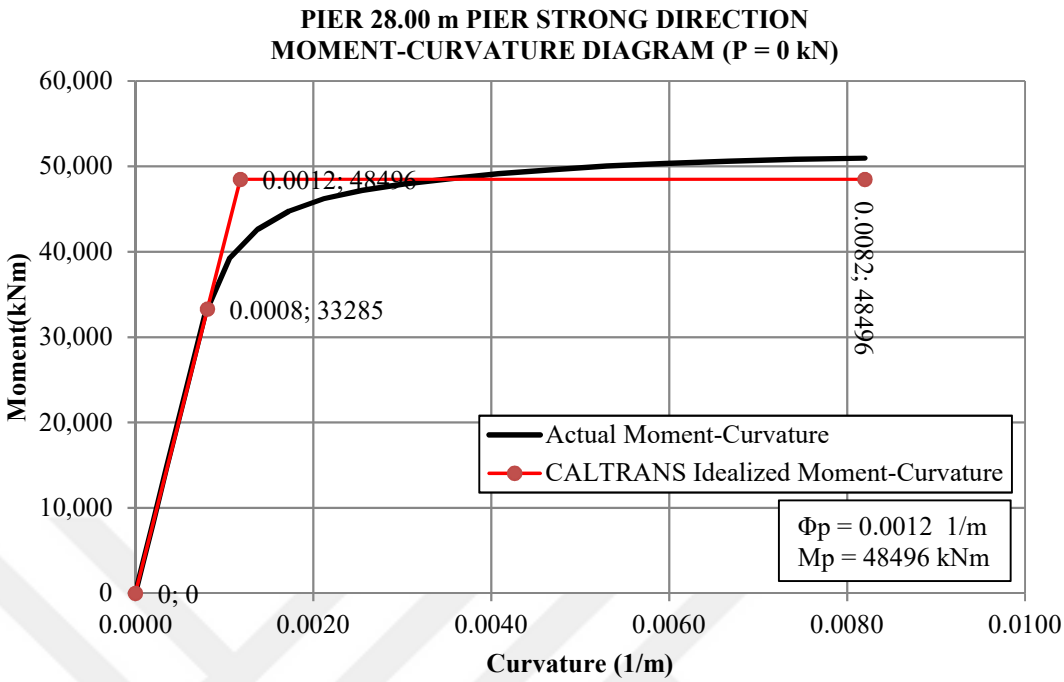

Figure 3.32. Pier 28.00 m pier strong direction moment-curvature diagram.

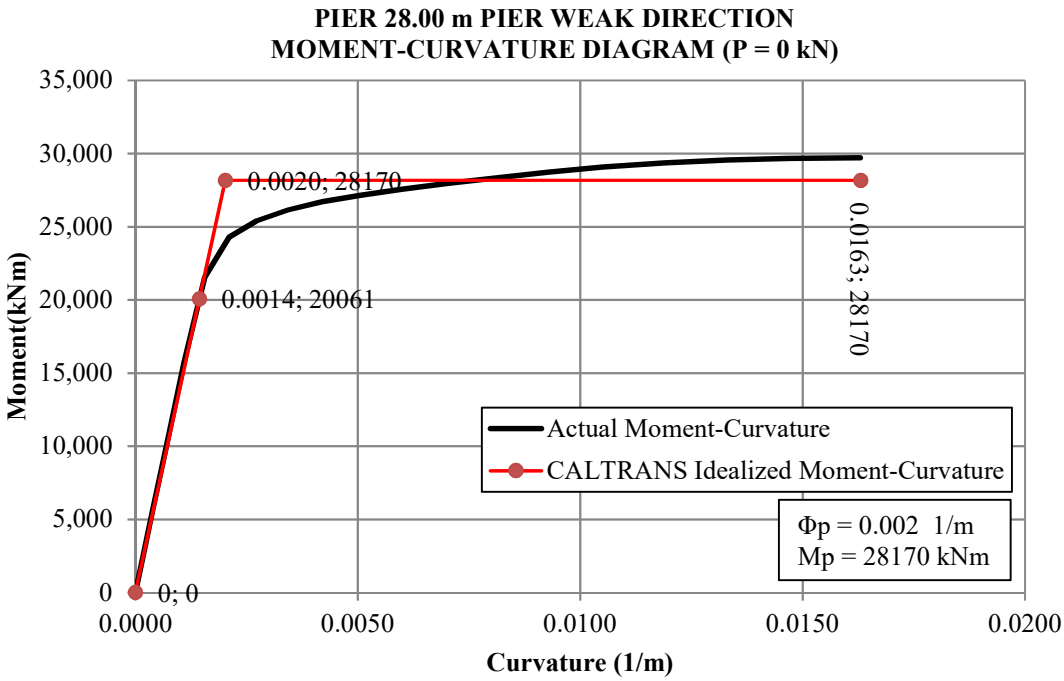

Figure 3.33. Pier 28.00 m pier weak direction moment-curvature diagram.

4. COMPERATIVE STUDY OF NONLINEAR TIME HISTORY AND SUBSTRUCTURE SSI ANALYSIS

Main objective in this study is to compare the results of Nonlinear Time History (NTH) analysis with Substructure SSI analysis method. Analyses methods vary from basic linear approaches to complex non-linear analyses. In this study, a modal analysis is established to obtain the fundamental periods of the structure; a linear response spectrum analysis is conducted for preliminary design purposes. With these methods, linear demand of the structure is obtained, and fundamental periods are acquired. For inelastic displacements, NTH analysis methods are used.

4.1. Modelling

4.1.1. Models for Structural Analysis

As stated in the chapter 3.1, bridges are consisted of deck, cap beams, piers, pile-caps and piles as structural elements. Analytical models used for these elements are explained below.

4.1.1.1. Modeling of Deck. The decks that carry high gravity loads should remain elastic during earthquakes to transfer the loads to the pile-caps via piers. Deck is modeled as beam elements that acquire the properties of the deck section. Total mass of the deck is assumed at the center of gravity and mass moment of inertia is taken according to that point. Cross-section of the box girder is shown in Figure 3.1. C40/50 Mander (Mander, 1988) unconfined concrete model is used for the section in the analysis.

4.1.1.2. Modeling of Elastomeric Bearings. There are 2 elastomeric bearings on each pier and abutments. Elastomeric bearings allow movement in the longitudinal direction of the bridge. The movement in the transverse direction is restricted by shear keys. Elastomeric bearings are modeled as linear springs, which can move in longitudinal direction, but fixed in the transverse direction. Properties of the elastomeric bearings used for stiffness calculations are:

W = Bearing width = 600 mm

L = Bearing length = 500 mm

H = Bearing thickness = 114 mm

h_{ri} = Elastomeric layer thickness = 82 mm

G = Shear modulus of elastomer = 1430 kN/m²

K_h = Lateral stiffness of the elastomer

$$K_h = \frac{W \times L \times G}{h_{ri}} = \frac{0.6 \times 0.5 \times 1430}{0.082} = 5231.7\ kN/m \quad (4.1)$$

Axial and rotational stiffness of the bearings are assumed to be infinitely rigid.

4.1.1.3. Modeling of Piers. Piers are modeled as beam elements based on the properties given in Table 4.1 and Table 4.2. Pier and the pile-cap connections are allowed to go through substantial plastic deformations. As shown in Figure 4.1, the pier is connected to the geometric center of the elastomeric bearings with fictitious members. Elastomeric bearings are also connected to the geometric center of the box girder via fictitious members. Fictitious members are massless and infinitely rigid beam elements. Geometric center of the box girder is connected to the level of elastomeric bearings with fictitious members, while elastomeric bearings are linked to the pier with the same members to consider eccentricity of the loadings excited.

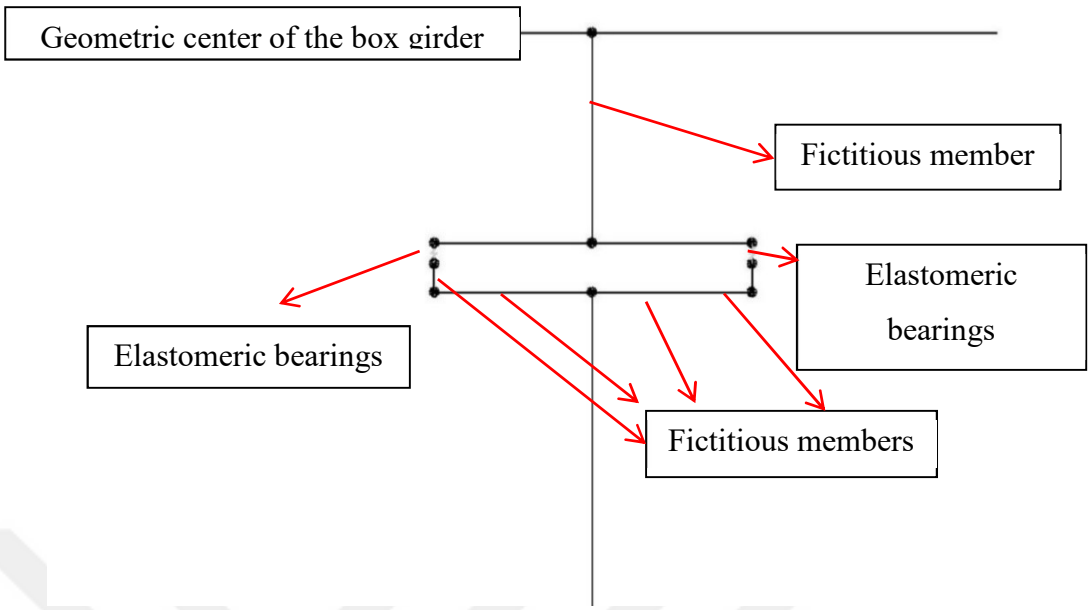

Figure 4.1. Modelling of superstructure – pier connection.

Table 4.1. Effective flexural stiffness of 14.00 m pier section.

Properties	**Abbr.**	**Value**	**Unit**
Axial load	N	10800	kN
Plastic moment capacity of pier or pile calculated using axial forces due to vertical loads.	M_p	72458	kNm
Yield curvature	ϕ_y	0.00121	m/rad
Effective Flexural Stiffness (M_p / ϕ_y)	$(EI)_e$	59882645	kNm
Moment of Inertia around the axis	I	5.7109	m^4
Modulus of Elasticity	E	34000000	kN/m^3
Flexural Stiffness	EI	194170600	kNm
Ratio ($(EI)_e$/EI)		0.31	

Table 4.2. Effective flexural stiffness of 28.00 m pier section.

Properties	**Abbr.**	**Value**	**Unit**
Axial load	N	13825	kN
Plastic moment capacity of pier or pile calculated using axial forces due to vertical loads.	M_p	63824	kNm
Yield curvature	ϕ_y	0.001181	m/rad
Effective Flexural Stiffness (M_p / ϕ_y)	$(EI)_e$	54042337	kNm
Moment of Inertia around the axis	I	5.7109	m^4
Modulus of Elasticity	E	34000000	kN/m^3
Flexural Stiffness	EI	194170600	kNm
Ratio ($(EI)_e$/EI)		0.28	

Pier structural model and assigned P-M-M hinge locations may be seen in the Figure 4.2. P-M-M hinge details are given in Section 4.1.1.7. In the nonlinear analysis effective flexural stiffness of the piers are considered as in Table 4.1 and Table 4.2.

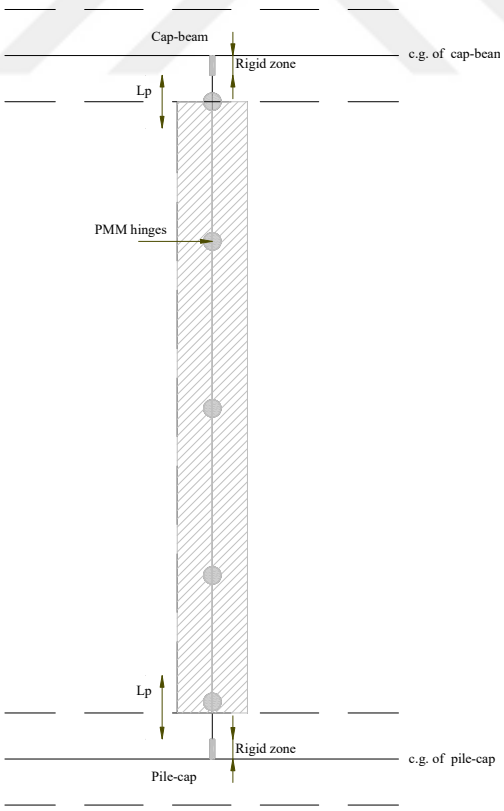

Figure 4.2. Pier structural model.

4.1.1.4. Modeling of Pile-caps. Pile caps are modeled as moment carrying shell elements. Pile caps should stay elastic during the earthquake. In the model, pile cap thickness is 1 m.

4.1.1.5. Modeling of Piles. Piles are modeled as beam elements that match the properties of the pile cross-section. Pile and the pile-cap connections are allowed to experience substantial plastic deformations.

Simple dynamic linear Winkler methods (Winkler, 1867) are frequently used for seismic analysis of piles due to ease of use. Although Winkler methods might be sufficient for static analysis, use of non-linear *p-y* curves would become necessary in seismic cases where the soil deformations undergo into the plastic zone.

Piles that are used in the model have 1 m diameter and 3 m center-to-center distance in the pile group. Beam elements are divided into 1 m pieces through the pile length. On each node, *p-y* and *t-z* link elements are assigned. More details are given in Appendix A.

First P-M hinge is located just below the pile-cap boundary. Rest of the expected P-M hinges locations with equal spacings of 1 meter throughout the pile length are given in Figure 4.3. In the nonlinear analysis, effective flexural stiffness of the piers and the related parameters considered are given in Table 4.3. Pile structural model and assigned P-M hinge locations may be seen in Figure 4.3.

Table 4.3. Effective flexural stiffness of pile section.

Properties	**Abbr.**	**Value**	**Unit**
Axial load	N	2550	kN
Plastic moment capacity of pier or pile calculated using axial forces due to vertical loads.	M_p	2048	kNm
Yield curvature	ϕ_y	0.004383	m/rad
Effective Flexural Stiffness (M_p / ϕ_y)	$(EI)_e$	467259.87	kNm
Moment of Inertia around the axis	I	0.0485	m^4
Modulus of Elasticity	E	31000000	kN/m^3
Flexural Stiffness	EI	1503500	kNm
Ratio ($(EI)_e$/EI)		0.31	

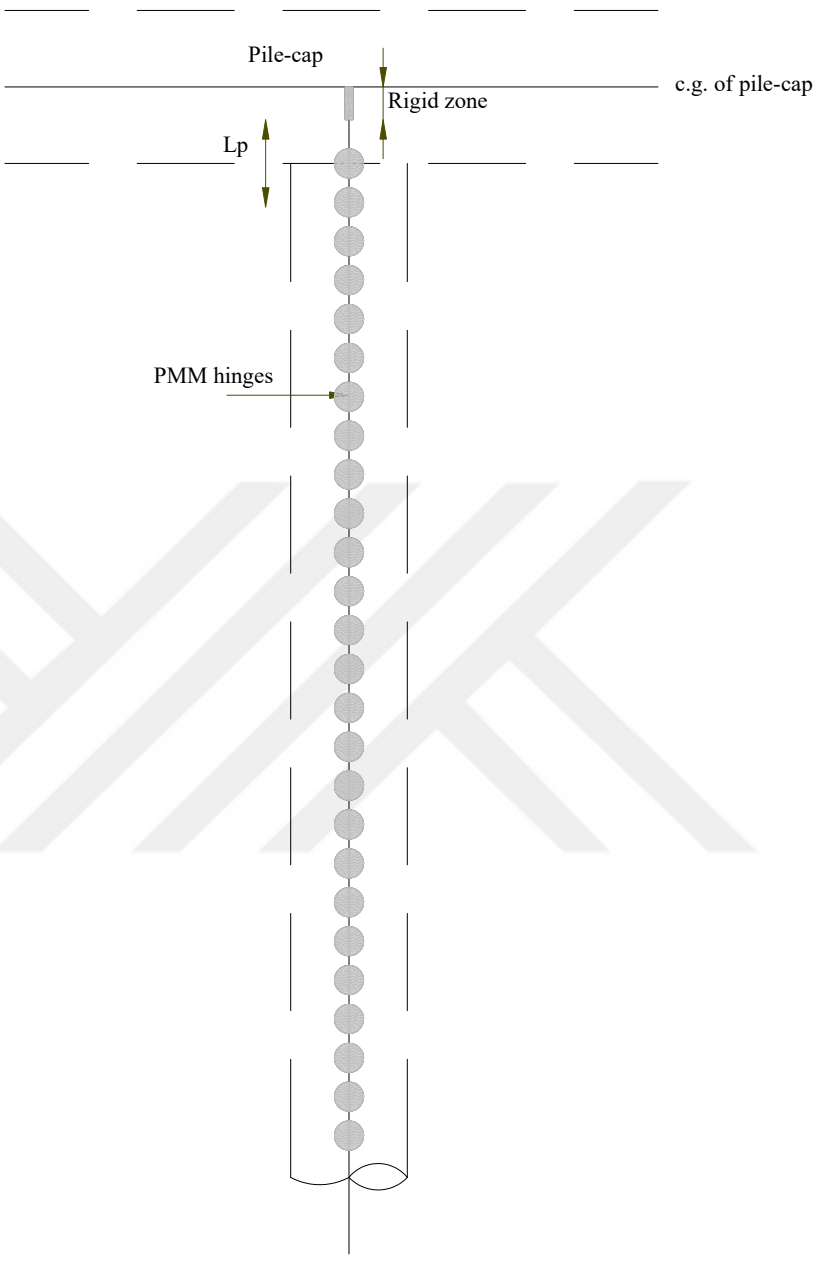

Figure 4.3. Pile system analysis model.

4.1.1.6. Material Properties. The Mander model (Mander, 1988) is used for unconfined concrete. The characteristic strength of the concrete is taken as 35 MPa for piers and 25 MPa for piles, as shown in the Figure 4.4 and Figure 4.5. Design strength of the concrete is taken as 23.3 MPa for piers and 16.7 MPa for piles. For both members, the tensile strength of the concrete is taken as zero. Strength classes for concrete is given in Table 4.4.

Table 4.4. Strength classes for concrete.

	Unit Weight (kN/m³)	Modulus of Elasticity (MPa)	Specified Concrete Compressive Strength (MPa)	Poisson Ratio	Coefficient of Thermal Expansion
C25/30	25.00	31000	25	0.2	1.00E-05
C35/45	25.00	34000	35	0.2	1.00E-05

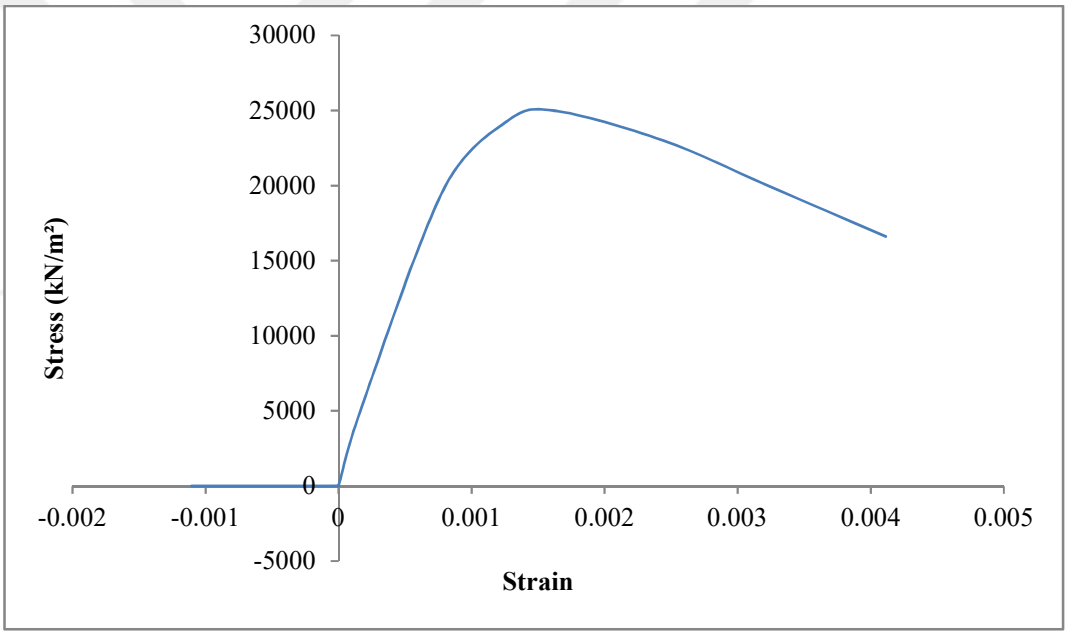

Figure 4.4. Mander unconfined concrete model for piles, f_{ck}=25 MPa.

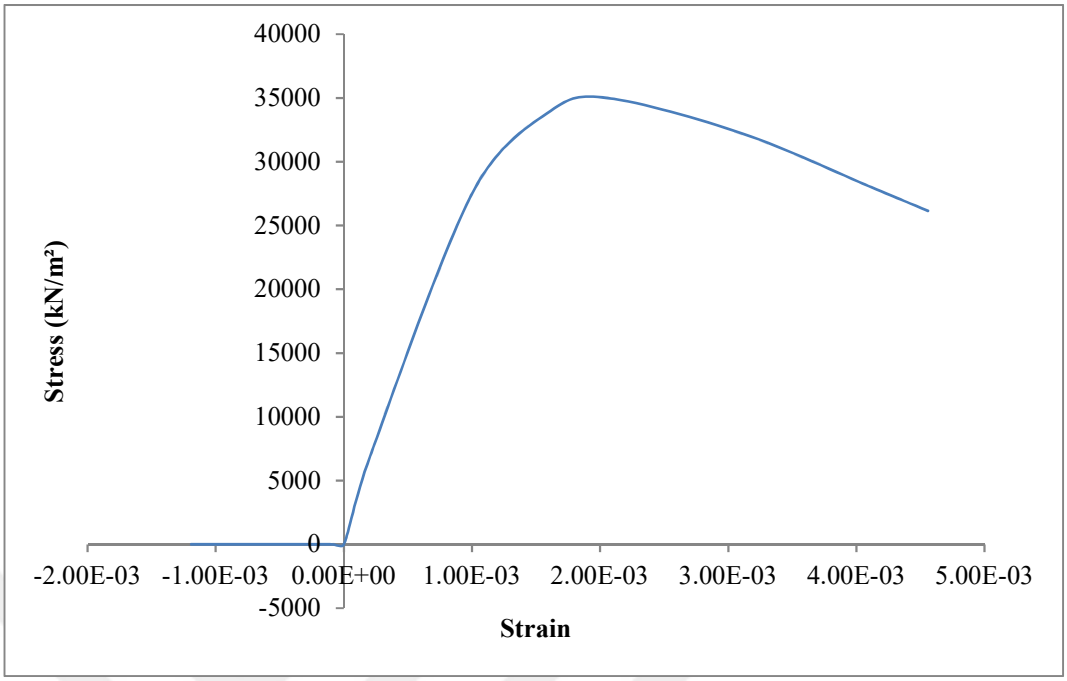

Figure 4.5. Mander unconfined concrete model for piers, f_{ck}=35 MPa.

For reinforcing steel, it is assumed that the stress-strain curves are identical for both tension and compression cases. Stress-strain relationship used in the model is expressed as an elasto-plastic curve, as shown in Figure 4.6. Mechanical properties of reinforcing steel are given in Table 4.5.

Table 4.5. Mechanical properties of reinforcing steel.

	Unit Weight (kN/m³)	Modulus of Elasticity (MPa)	Yield Strength (MPa)	Ultimate Strength (MPa)	Coefficient of Thermal Expansion
S420	78.50	200000	420	520	1.17E-05

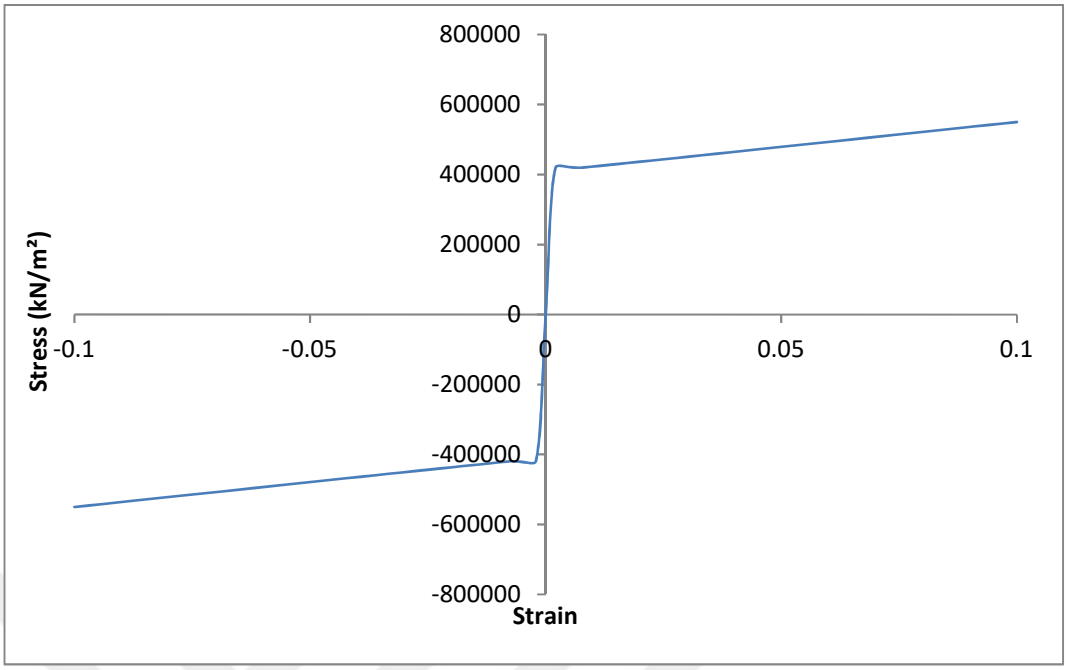

Figure 4.6. Reinforcing steel S420 stress-strain curve, f_{yk}=420Mpa.

4.1.1.7. Reinforced Concrete Hinge Properties. For the nonlinear behavior, it is assumed that nonlinear deformations occur in the plastic-hinge zones. The length of the plastic deformation region, which is known as the Plastic Hinge Length for concrete piers, is calculated via the following equation, taken from Section 3.2.4.1 of Technical Standards for Ports, Harbor Facilities, Railroads, and Airports in Turkey (2008);

$$L_p = 0.08\,H + 0.022\,f_{yk}\,d_b \geq 0.044\,f_{yk}\,d_b \tag{4.2}$$

H : Height of the pier

d_b : Diameter of the longitudinal reinforcement

f_{yk} : Characteristic yield strength of reinforcement

and for piles;

$L_p = 0.5\,h$ (h: height of the section)

For 28.00 m Pier:

$$L_p = 0.08 * 28 + 0.022 * 420 * 0.022 \geq 0.044 * 420 * 0.022$$
$$= 2.44\ m$$

For 14.00 m Pier:

$$L_p = 0.08 * 14 + 0.022 * 420 * 0.022 \geq 0.044 * 420 * 0.022$$
$$= 1.32\ m$$

Moment-curvature relationship can be defined as described in Section 3.4.3, as well as the ability to identify and inspect yield surfaces with a sufficient number of points and to obtain plastic shape changes in this way. P-M-M type plastic hinges are used for piers and piles. P-M-M interaction surfaces are obtained via build-in section designer of software SAP2000 for both pier and pile sections.

These diagrams (P-M-M) are designated in the software as hinges defined by the yield surfaces as seen in Figure 4.7 to Figure 4.10. In this way, nonlinear behavior can be transferred to the model as close to reality as possible.

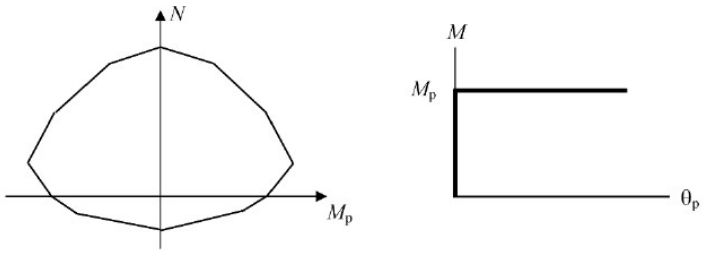

Figure 4.7. 2D yield surface and elasto-plastic moment-plastic hinge relationship.

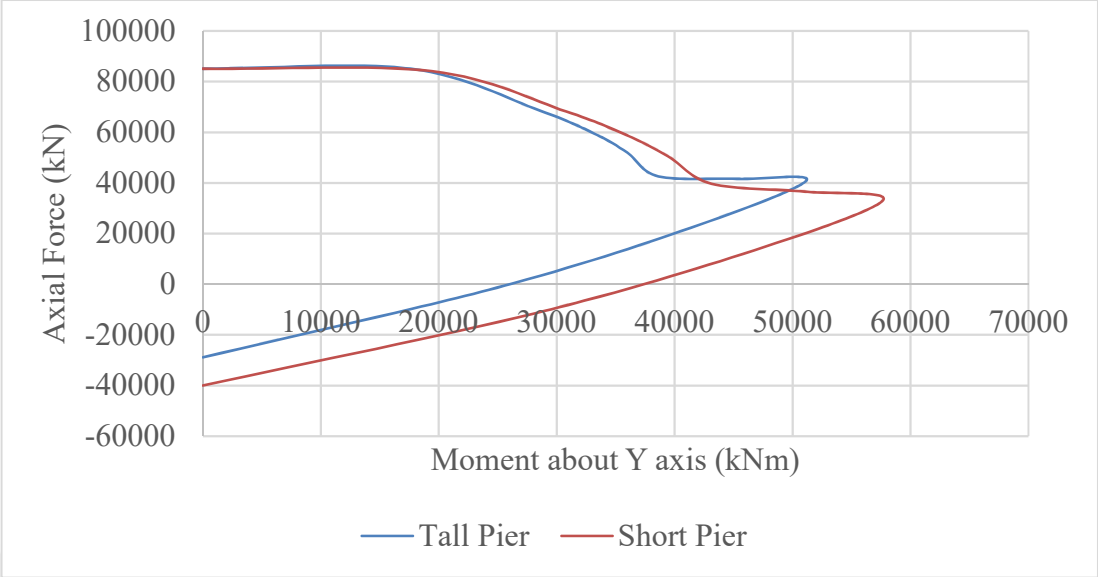

Figure 4.8. Typical P-M interaction diagram for piers.

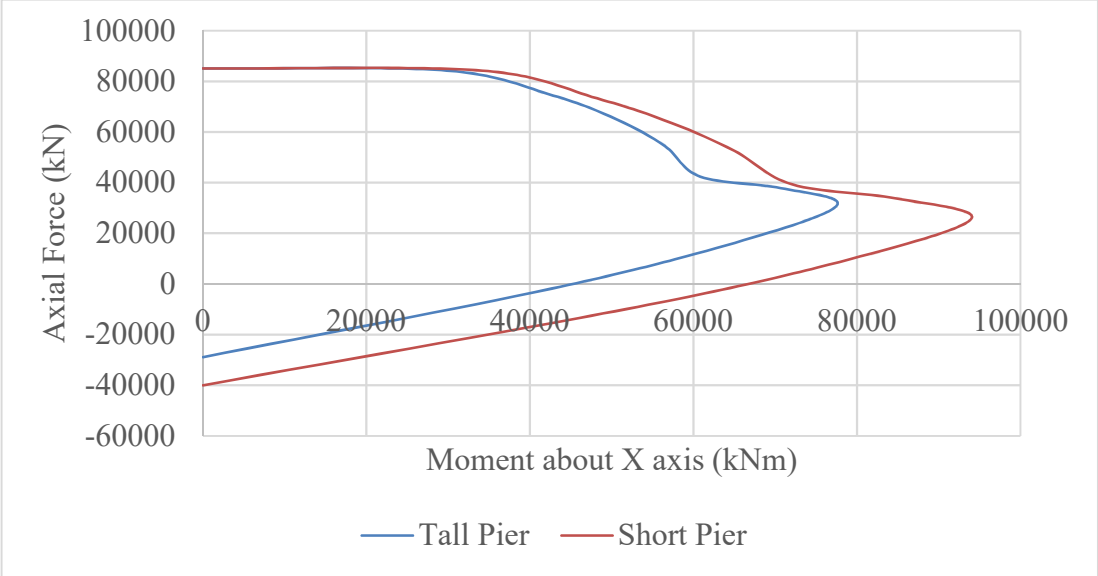

Figure 4.9. Typical P-M interaction diagram for piers.

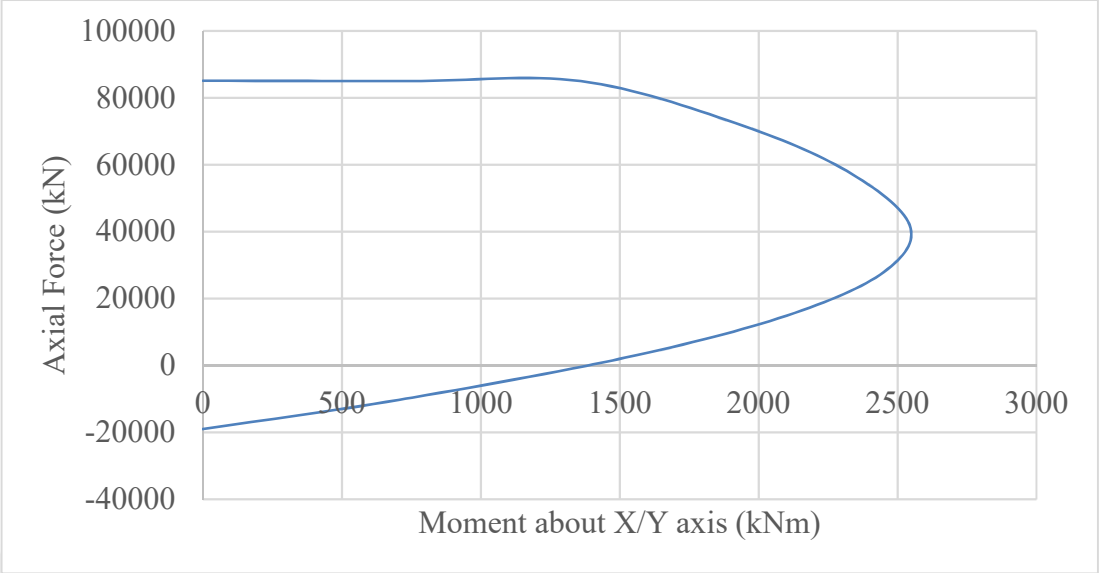

Figure 4.10. Typical P-M interaction diagram for piles.

4.1.1.8. Modeling of Soil. Piles groups carry both axial and lateral loads. Behavior of the piles depends on the stiffness of both soil and the axial capacity of the pile. Complicated nonlinear behavior of soil under seismic excitation with nonlinear structural system needs modelling of the soil and the structure together by using Finite Element Method or Finite Difference Method. However, computational difficulties of these methods lead into search of simpler models capturing behavior of vibrating soil-foundation system for common engineering practices. Deformation or frequency dependent coupled/uncoupled springs are most common to be used to model the soil compliance. In this chapter, nonlinear deformation dependent spring models that are used in the study are revealed.

- Determination of *p-y* Springs.

There are 16 piles at each bridge pier with 3 m distance from center to center, as shown in Figure 4.11. Reduction factors for piles in group action are calculated according to Appendix A.8 and can be seen in Figure 4.12. In Figure 4.12, calculations are performed while loading is acting in the transverse direction of the bridge.

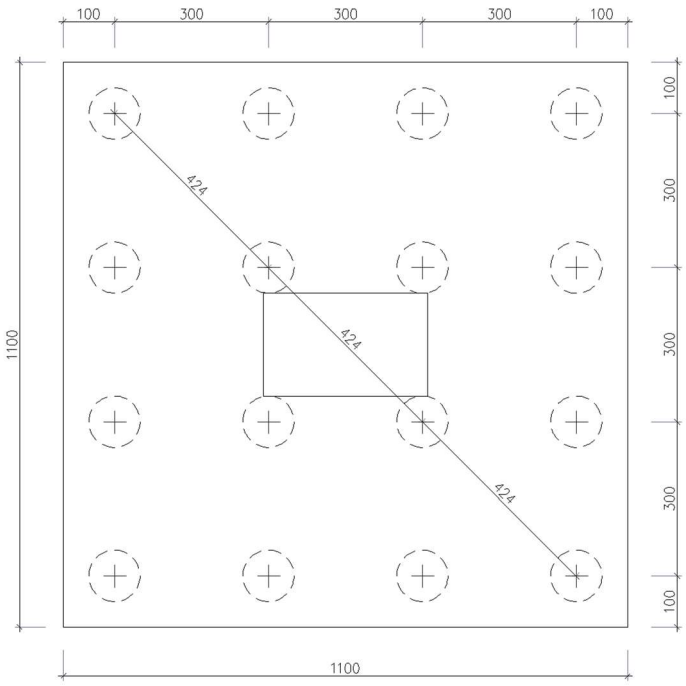

Figure 4.11. Pier foundation geometry.

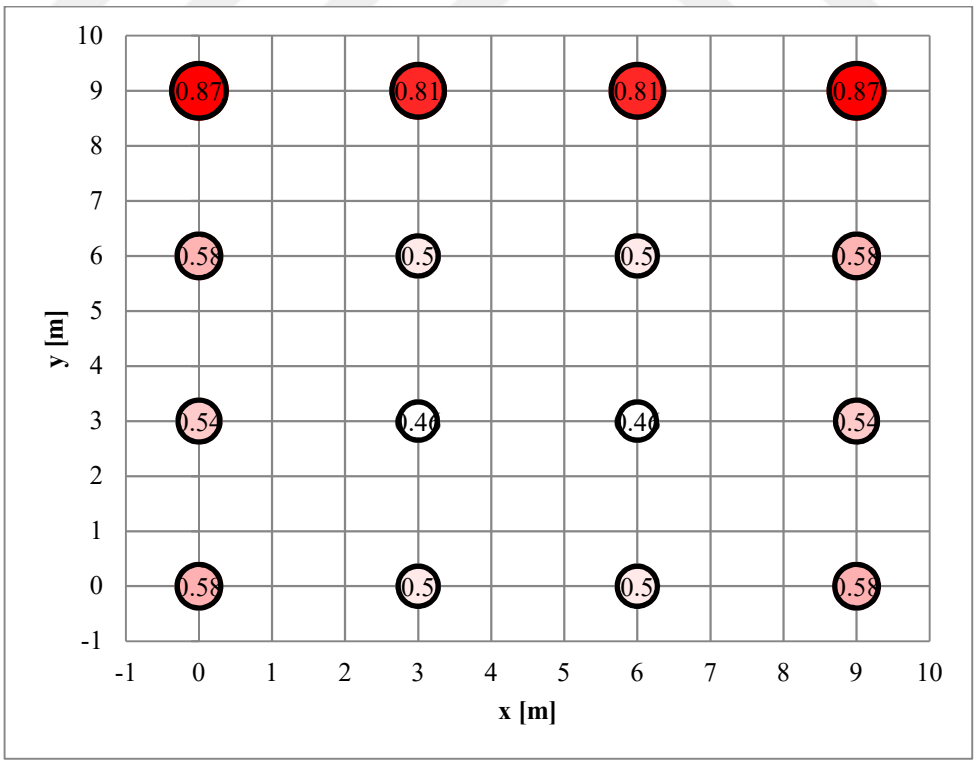

Figure 4.12. Pile layout and α factors for the *p-y* springs.

The *p-y* springs for each soil layer, with parameters given in the Table 3.3, are calculated according to Appendix A.1 and A.3. First 12 m from the ground surface is soft layer and the rest is clayey sandy gravel. Pile cap is buried 1 m from the ground surface and the thickness of the pile cap is 1 m. Thus, the pile top is at 2 m depth from the surface. Piles are divided into 30 equivalent lengths (1 m each) and the *p-y* curves are determined at the center point of each layer. As illustrated in the Figure 4.13, the *p-y* curves for soft clay layer under cyclic loading get stiffer as the depth increases. After the critical depth is overpassed, *p-y* curve remains constant for greater depths for soft clay layer. For this study, critical depth, z_r is 5.92 m after $y = 15y_{50}$, where y is the soil deflection and y_{50} is the soil deflection at one-half the ultimate soil resistance, according to Appendix A.3.

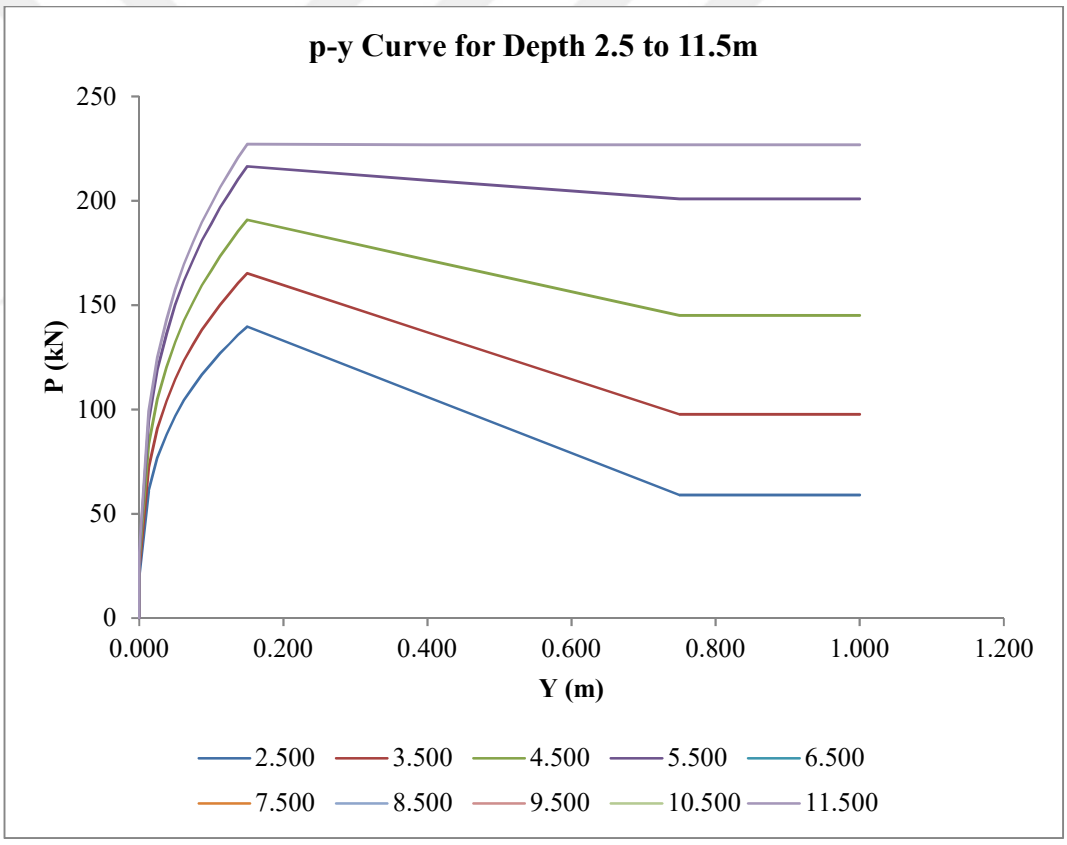

Figure 4.13. The *p-y* curves for soft clay layers 2.5 to 11.5 m depth from surface.

As shown in Figure 4.14, the *p-y* curves for sand layer under cyclic loading get stiffer as the depth increases.

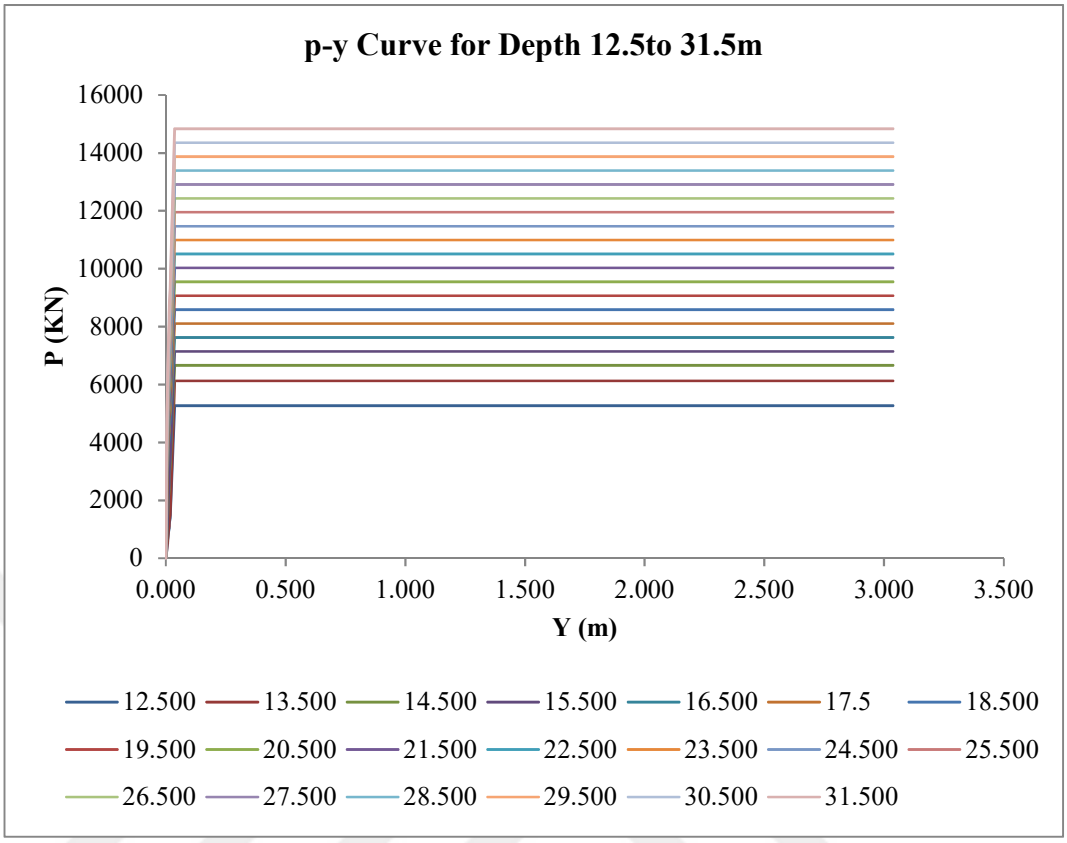

Figure 4.14. The *p-y* curves for sand layers 12.5 to 31.5 m depth from surface.

- Determination of Non-Linear *t-z* and *Q-z* Springs.

Pile foundations are constructed to carry both axial and lateral loads. These loads might be static or cyclic. Axial loads are carried by both end-bearing capacity of the piles and the skin friction. Axial tip deflection and mobilized end-bearing resistance are represented by *Q-z* curves, whereas the relation between pile deflection and mobilized shear force is defined by *t-z* curves. Following sections give more detail about these curves.

Axial Load Transfer (t-z) Springs.

American Petroleum Institute (API 2A, 2000) recommended *t-z* springs are given in Table 4.6 and Table 4.7.

Table 4.6. Recommended *t-z* curves for clays (API 2A, 2000).

z/D	***t/t*$_{max}$**
0.0016	0.30
0.0031	0.50
0.0057	0.75
0.0080	0.90
0.0100	1.00
0.0200	0.70 - 0.90
∞	0.70 - 0.90

Table 4.7. Recommended *t-z* curves for sands (API 2A, 2000).

***z* (mm)**	***t/t*$_{max}$**
0.000	0.00
0.100	1.00
∞	1.00

Where;

z : Local pile deflection (mm)

D : Diameter of pile (mm)

t : Mobilized soil pile adhesion (kPa)

t_{max} : Maximum soil-pile adhesion or unit skin friction capacity (kPa)

$$0.70 < t_{res}/t_{max} < 0.90$$

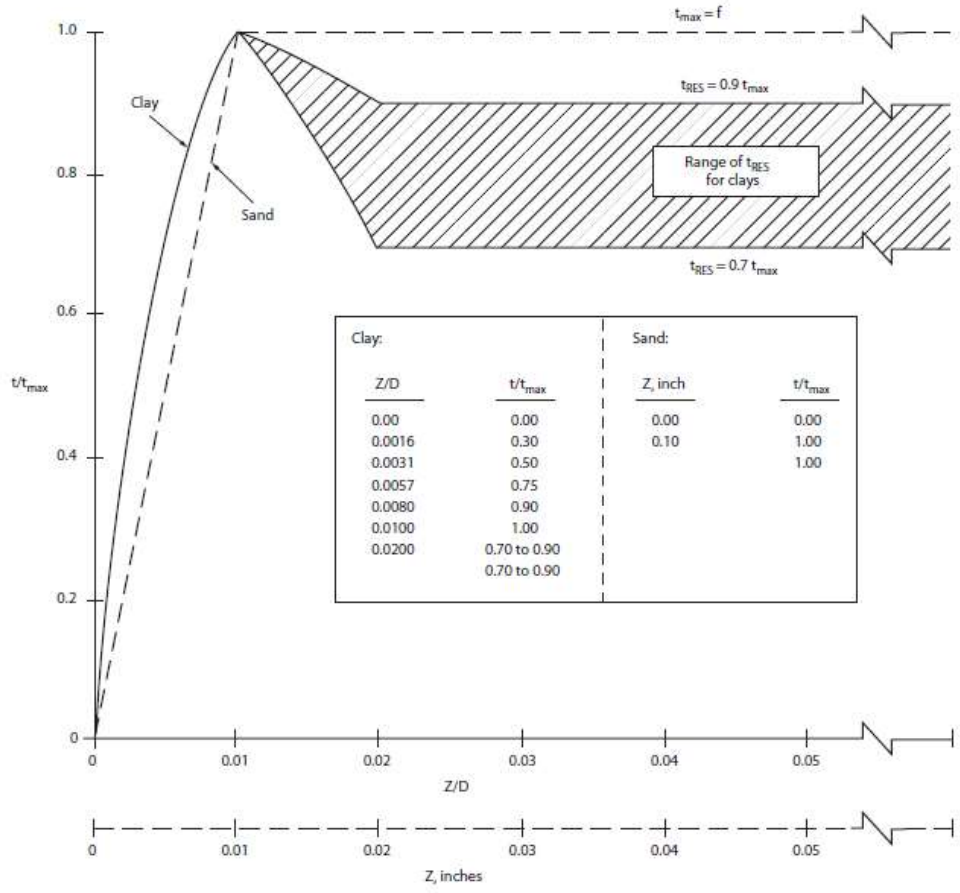

Figure 4.15. Typical *t-z* curves (API 2A, 2000).

t/t_{max} vs Z/D graph is given in the Figure 4.15. t_{max} value should be calculated according to American Petroleum Institute Section 6.4 (API 2A, 2000). Unit friction capacity differs according to the soil type.

For cohesive soils the formulation is:

$$f = \alpha\, c_u \tag{4.3}$$

α = a dimensionless factor

c_u = undrained shear strength of the soil

Each *t-z* curve is calculated on the center point of each layer. In the same section formulation of the factor α is given as;

$$\alpha = 0.5\ \Psi^{-0.5} \quad for\ \Psi \leq 1.0 \qquad (4.4)$$
$$\alpha = 0.5\ \Psi^{-0.25}\ for\ \Psi > 1.0$$

with $\alpha \leq 1.0$,

Where,

$$\Psi = c_u / p'_o \qquad (4.5)$$

p'_o = Effective overburden pressure (kPa)

For cohesionless soil,

$$f = \beta\, p'_o \qquad (4.6)$$

β = Dimensionless shaft friction factor

D = Diameter of pile (mm)

Undrained shear strength "c_u" is taken as 35 kPa according to Table 3.3.

Table 4.8. Design parameter table for cohesionless siliceous soil.

Relative Density	**Soil Description**	**Shaft Friction Factor β**	**Limiting Shaft Friction Values (kPa)**	**End Bearing Factor N_q**	**Limiting Unit End Bearing Values (MPa)**
Very loose Loose Loose Medium Dense Dense	Sand Sand Sand-Silt Silt Silt	Not Applicable	Not Applicable	Not Applicable	Not Applicable
Medium Dense	Sand-Silt	0.29	67	12	3
Medium Dense Dense	Sand Sand-Silt	0.37	81	20	5
Dense Very Dense	Sand Sand-Silt	0.46	96	40	10
Very Dense	Sand	0.56	115	50	12

Shaft friction factor "β" is taken as 0.37 according to Table 4.8.

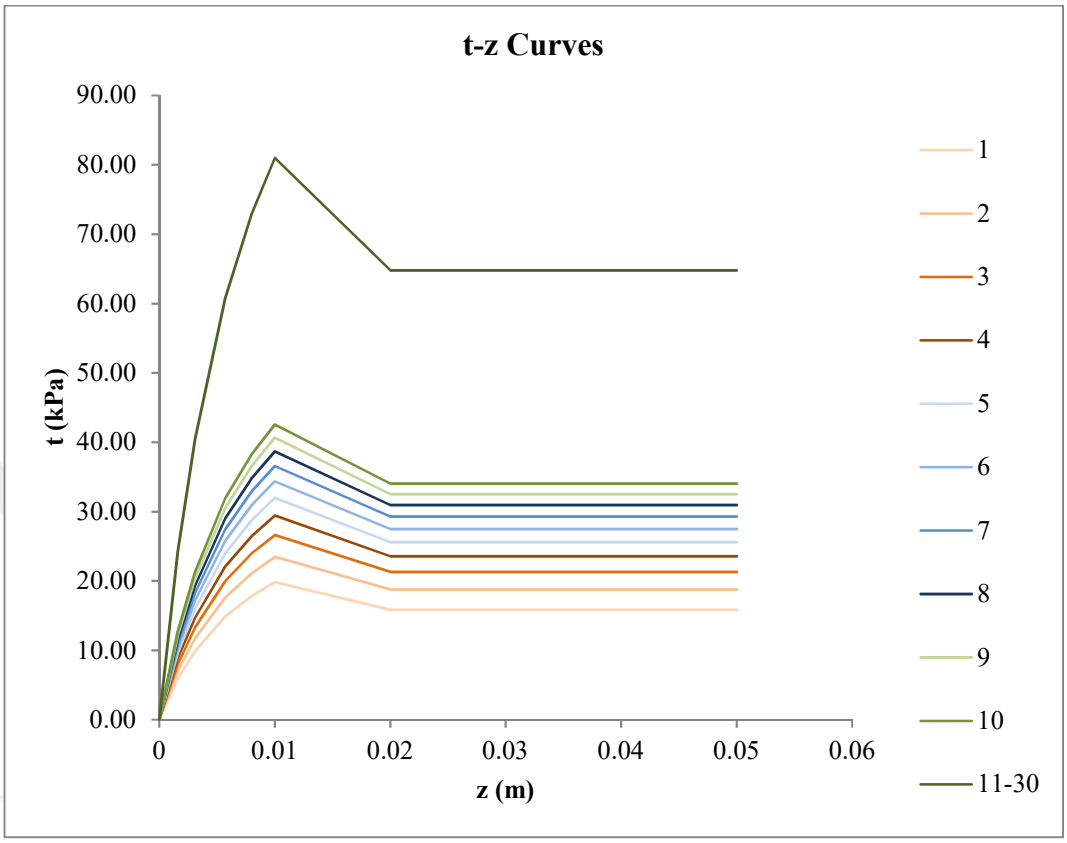

Figure 4.16. *t-z* curves for each soil layer.

As can be seen in the Figure 4.16, in cohesive soils, as the depth increases the soil pile adhesion increases. For cohesionless soil, *t-z* relation is independent of the parameter depth.

Tip Load Displacement (Q-z) Springs.

The end bearing capacity curves (*Q-z*) are determined as outlined in American Petroleum Institute (API 2A, 2000). It is stated that 10% of pile dimeter axial movement is necessary to mobilize the full end bearing resistance.

Table 4.9. *Q-z* curves for clays and sands (API 2A, 2000).

z/D	***Q/Q$_p$***
0.002	0.25
0.013	0.50
0.042	0.75
0.073	0.90
0.100	1.00

Where,

z = Axial tip deflection, (mm),

D = Diameter of pile, (mm),

Q = Mobilized end bearing capacity, (kN).

Q_p = Total end bearing, (kN),

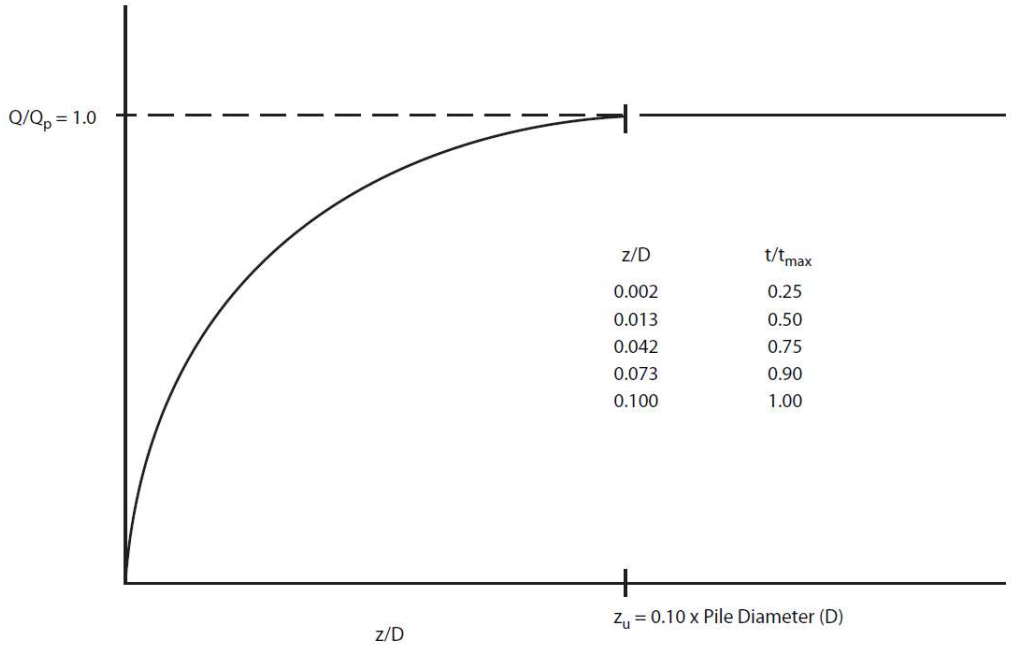

Figure 4.17. Typical *Q-z* curve.

For piles end bearing in cohesionless soil, the unit end bearing q can be computed via eq. 4.7 (API 2A, 2000);

$$q = N_q \, p'_o \tag{4.7}$$

Where,

N_q = dimensionless bearing capacity factor,

p'_o = effective overburden pressure at the studied depth

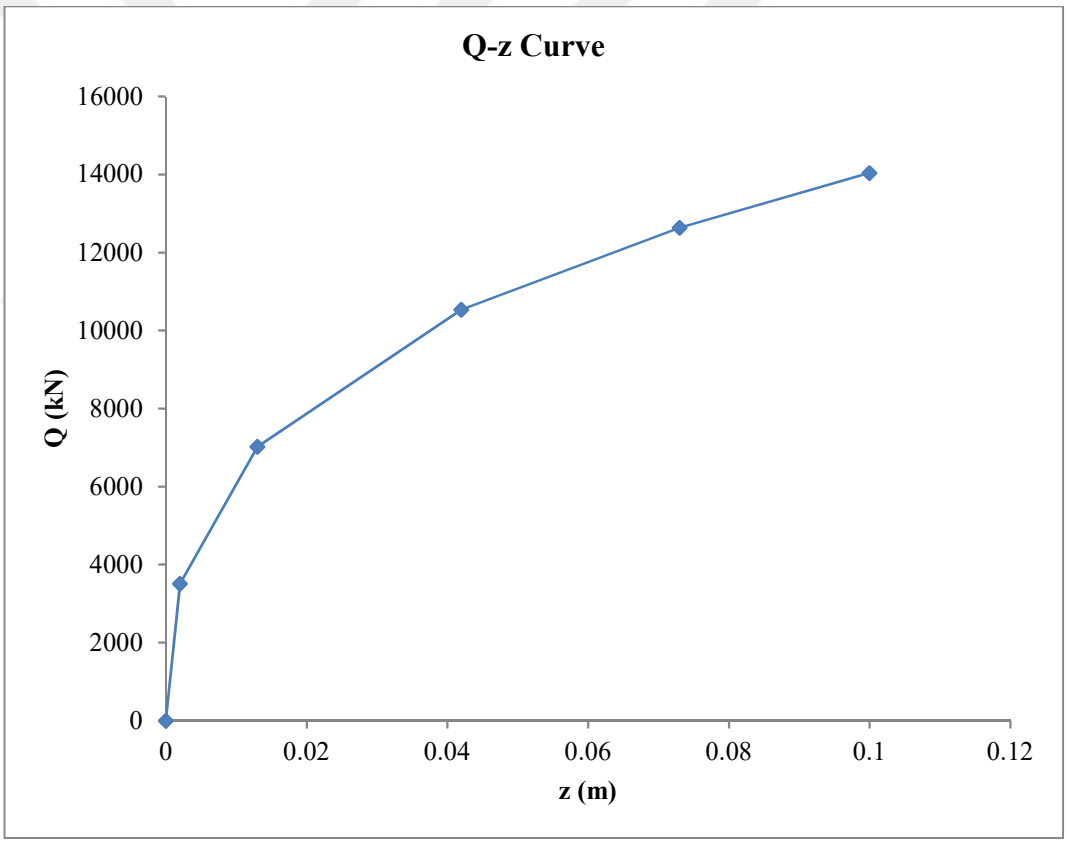

Figure 4.18. Pile tip load-displacement (Q-z) curve for the bottom soil layer.

Pile tip load-displacement (Q-z) curve is given in Figure 4.18.

4.1.2. Site Response Analysis Model

Site response analysis is conducted by calculating the response spectra via frequency-domain solution of the dynamic response equations of a SDOF system subjected to base accelerations. Fourier Amplitude Spectrum (FAS) of ground accelerations gives the frequency content of excitation at frequencies.

$$f_i = \frac{i}{\Delta t * n} \tag{4.8}$$

f_i is the i-th frequency and n is the number of points in Fourier Transform

The transfer function for the relative displacement with respect to bedrock of a SDOF system under base excitation is

$$H(f) = \frac{1}{(2\pi f_n)^2} \cdot \frac{1}{\left[1 - \left(\frac{f}{f_n}\right)^2 + 2i\xi_n\left(\frac{f}{f_n}\right)\right]} \tag{4.9}$$

$\boldsymbol{\xi}_n =$ damping

$f_n =$ natural frequency of the oscillator

Site response obtained via the frequency-domain formulation gives the Fourier spectrum of ground motion on the surface. Time histories of surface accelerations are calculated by taking the inverse Fourier transform of Fourier spectrum.

For site response analysis, software “Deepsoil” is used. Equivalent linear analysis in frequency domain is performed for given soil layer properties. Soil layer properties used in the software can be seen in Table 3.3. Elastic half-space assumption is made when outcrop record is used. Frequency independent damping is used. Scaled ground records given in Section 3.3 are used for the dynamic response analysis.

Deepsoil software gives relative displacements of each layer with respect to one in below, starting from bedrock. By summing the relative displacements cumulatively starting

from the bottom at each time step, total displacements are determined. In order to minimize the calculation time, a Matlab code is developed for this purpose.

Deepsoil PGA vs depth, maximum shear strain (%) vs depth, and stress ratio vs depth graphs are given below for each record from Figure 4.19 to Figure 4.37. As seen in these figures, shear strain ratio increases dramatically while passing through from denser granular material to soft clay layers.

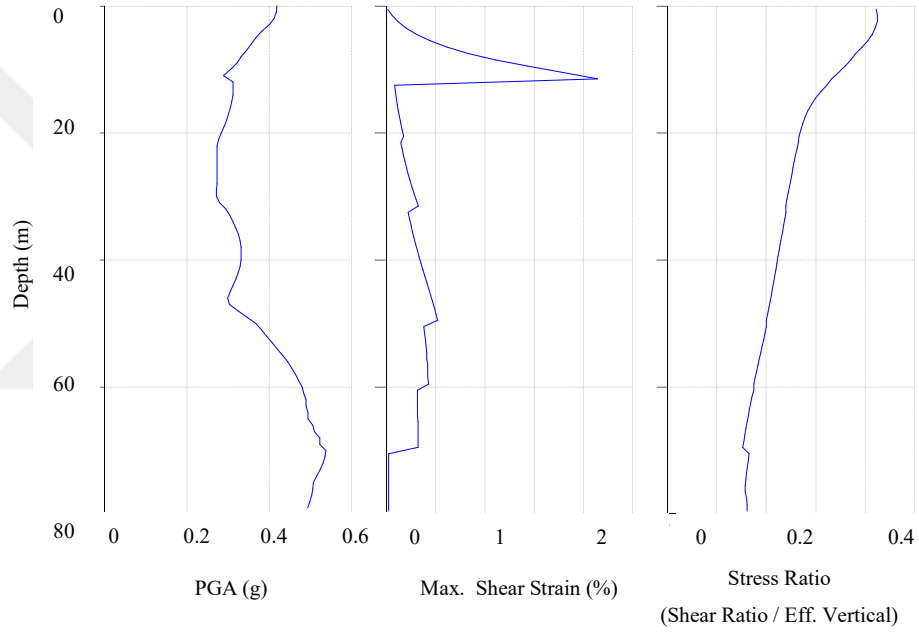

Figure 4.19. Record 68_090 site response analysis summary diagrams.

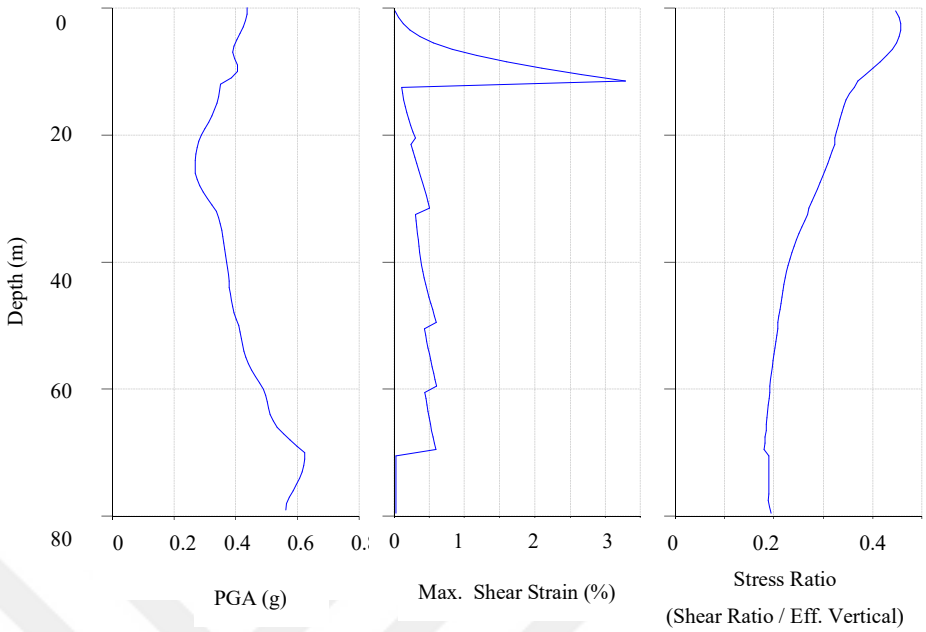

Figure 4.20. Record 125_000 site response analysis summary diagrams.

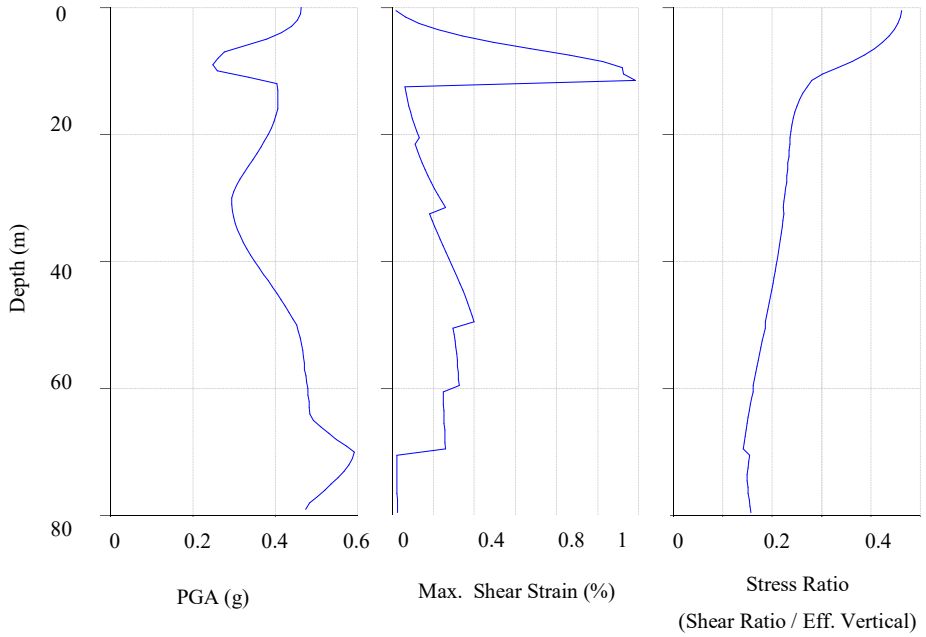

Figure 4.21. Record 169_352 site response analysis summary diagrams.

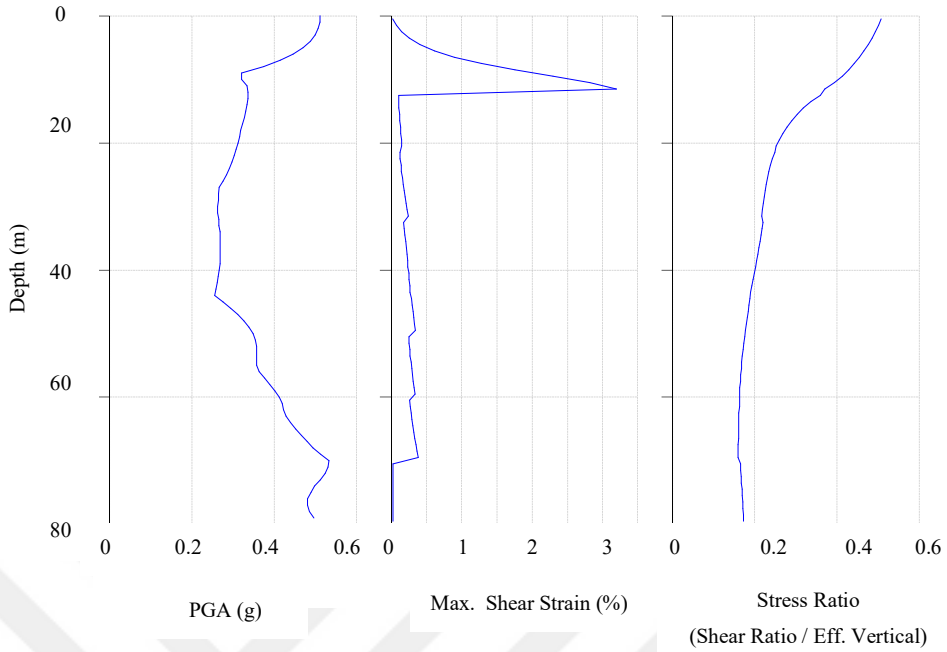

Figure 4.22. Record 174_11230 site response analysis summary diagrams.

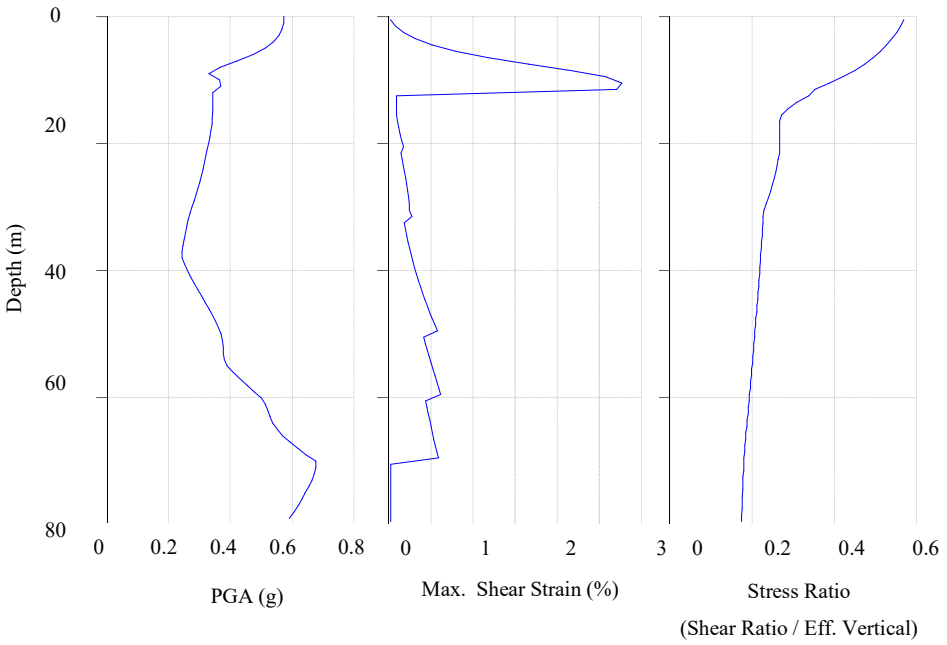

Figure 4.23. Record 721_000 site response analysis summary diagrams.

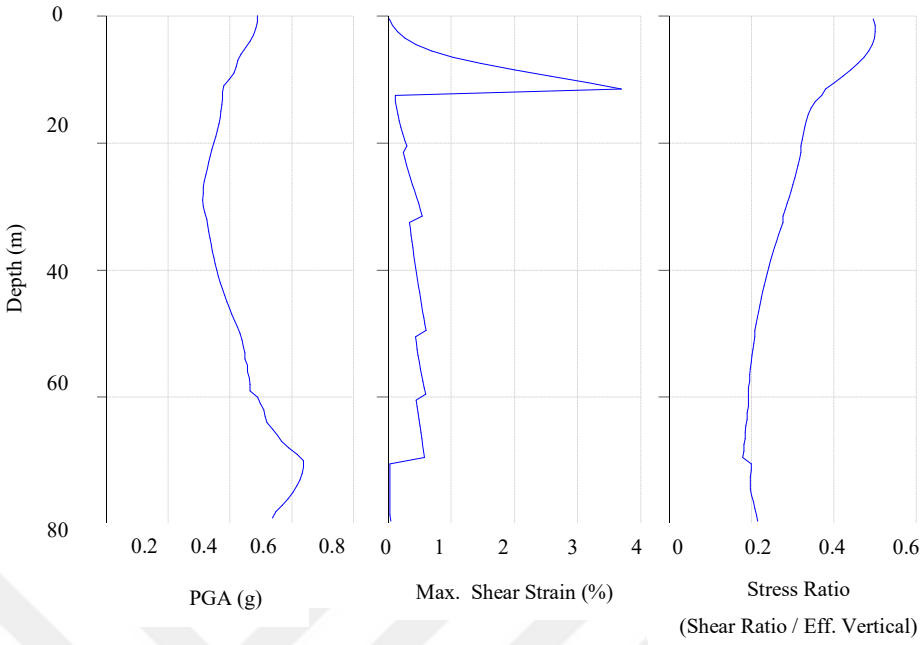

Figure 4.24. Record 725_270 site response analysis summary diagrams.

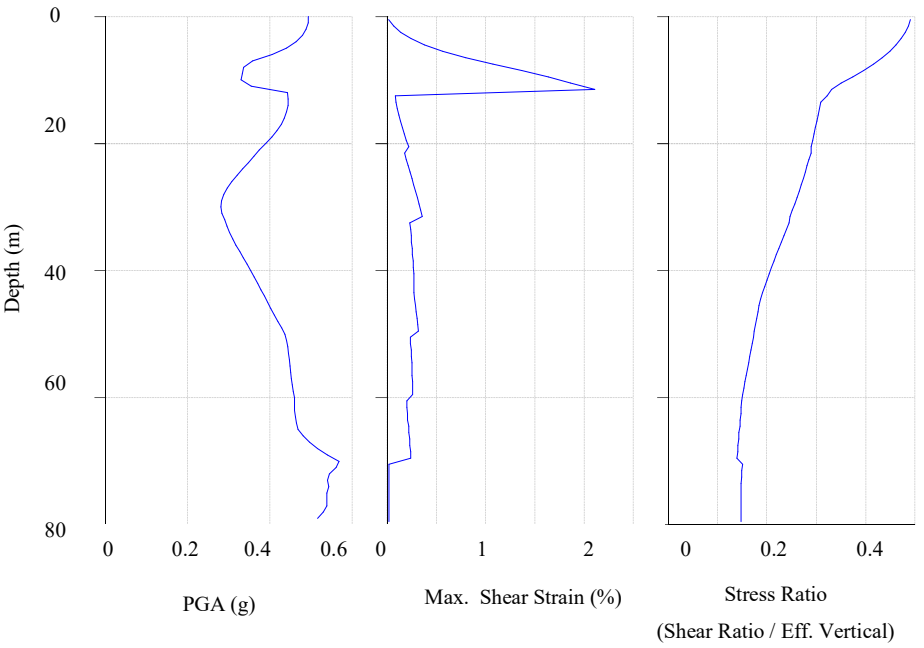

Figure 4.25. Record 752_000 site response analysis summary diagrams.

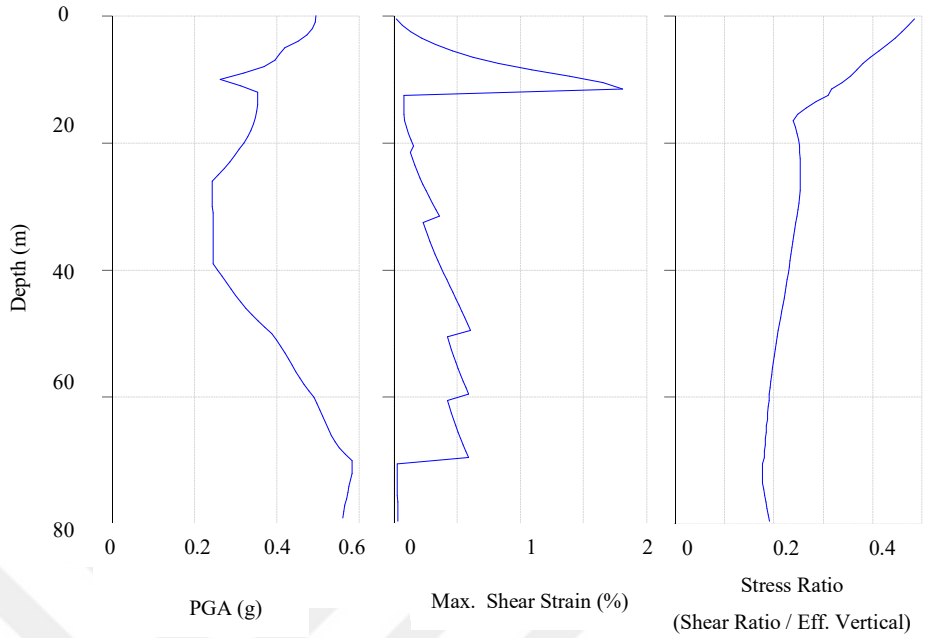

Figure 4.26. Record 767_000 site response analysis summary diagrams.

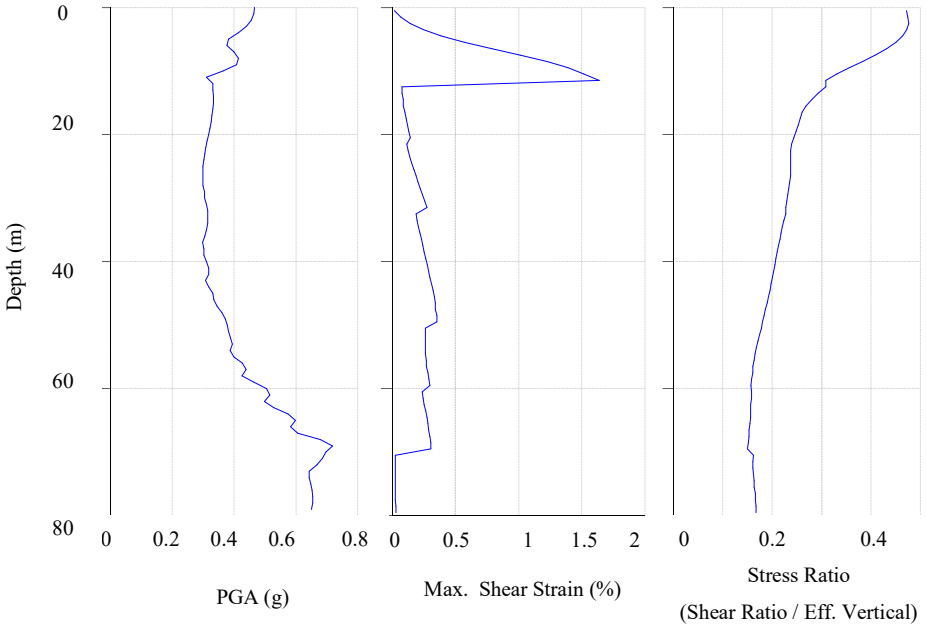

Figure 4.27. Record 829_360 site response analysis summary diagrams.

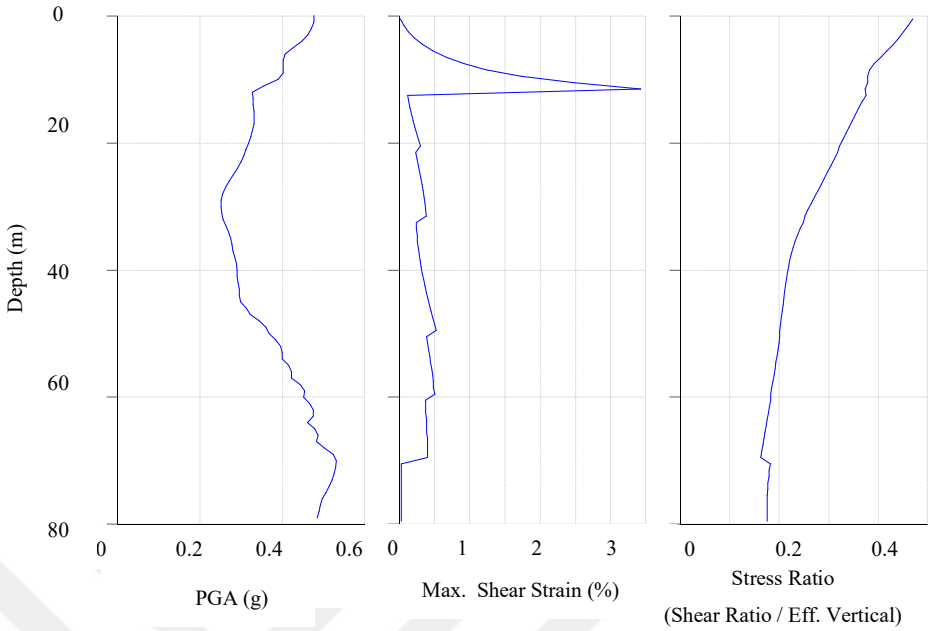

Figure 4.28. Record 900_270 site response analysis summary diagrams.

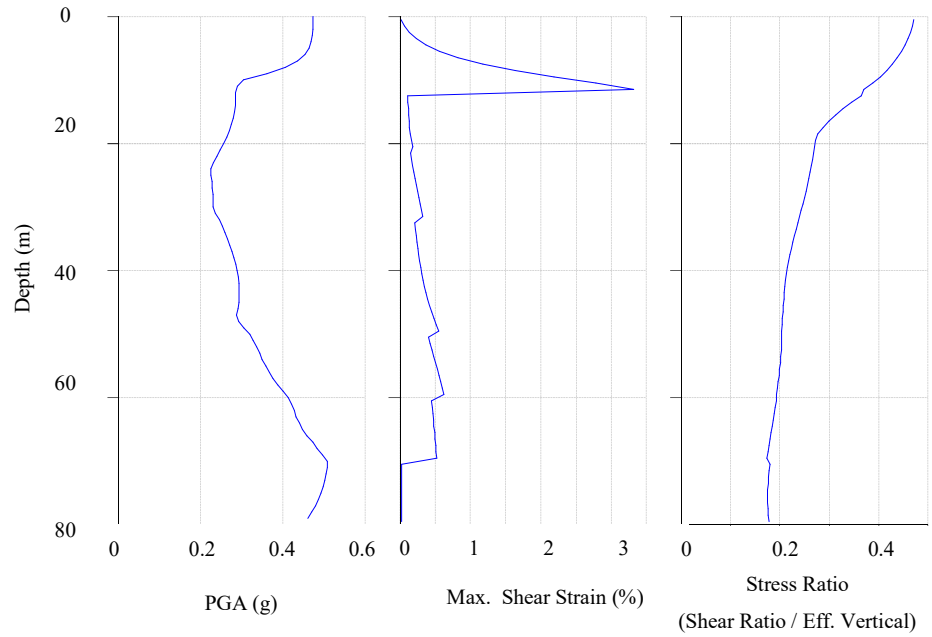

Figure 4.29. Record 953_279 site response analysis summary diagrams.

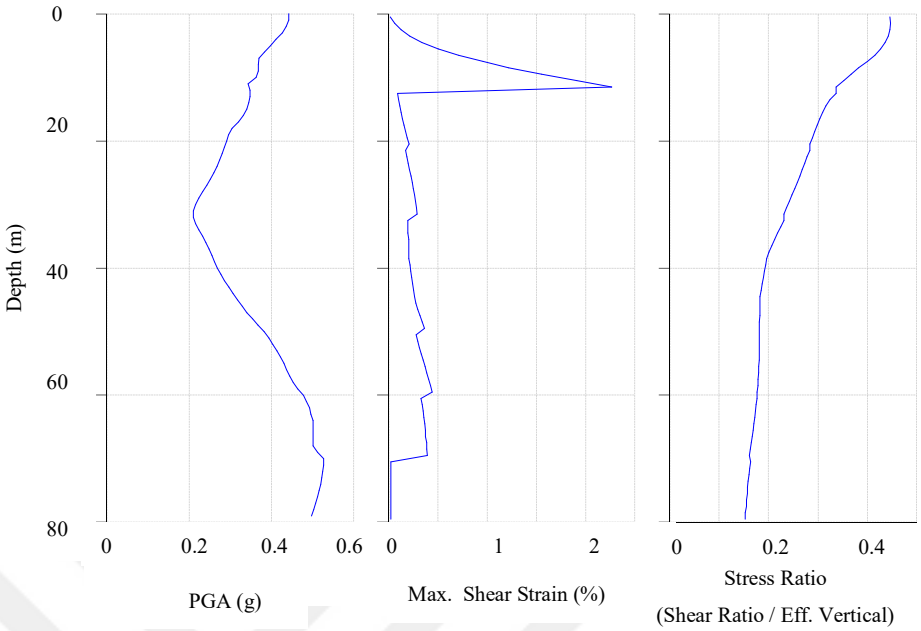

Figure 4.30. Record 960_270 site response analysis summary diagrams.

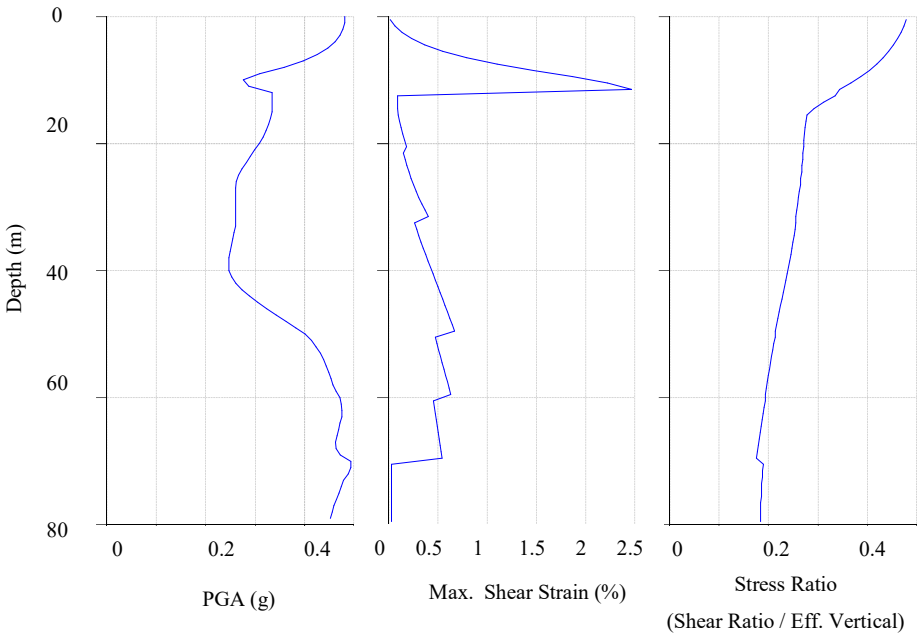

Figure 4.31. Record 1111_000 site response analysis summary diagrams.

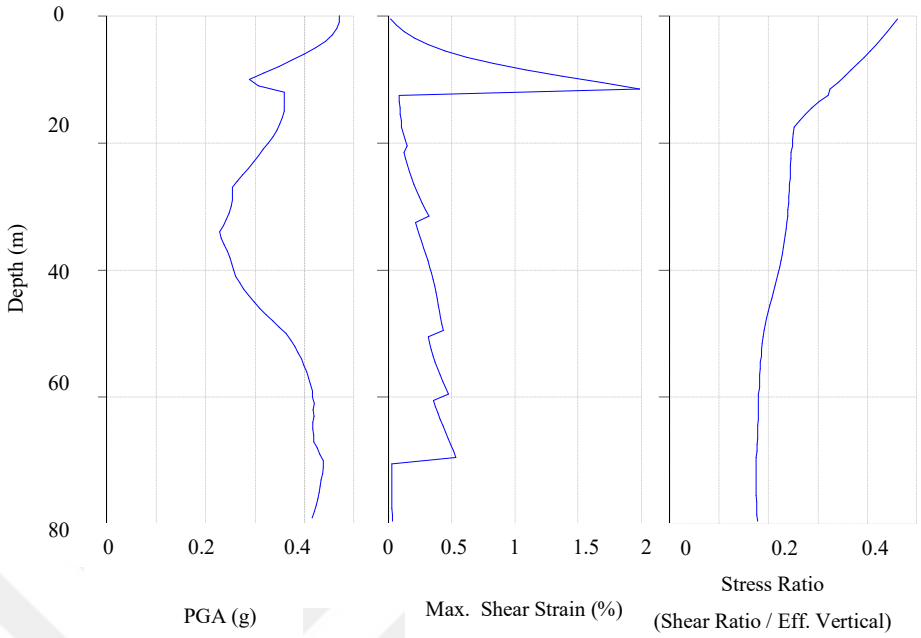

Figure 4.32. Record 1116_000 site response analysis summary diagrams.

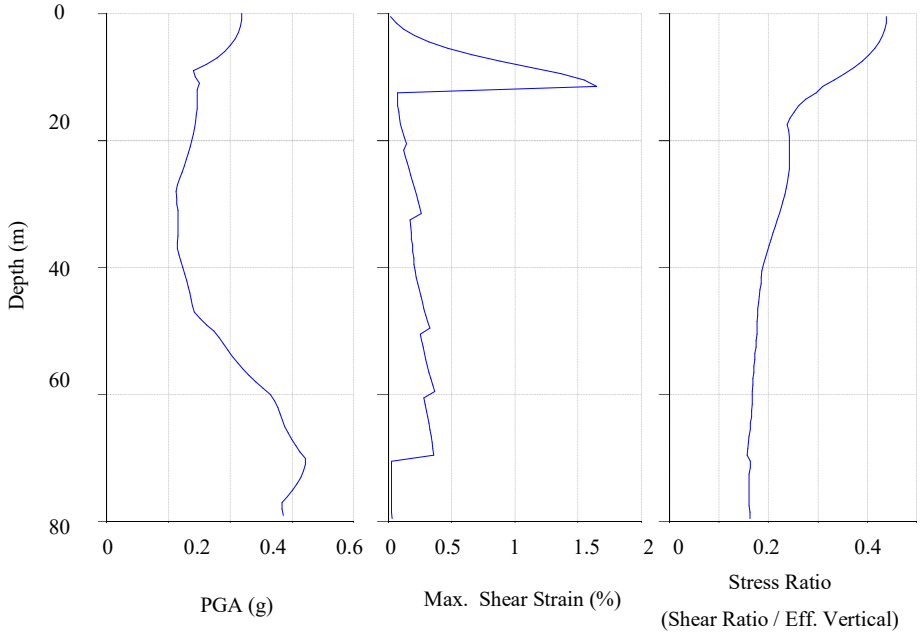

Figure 4.33. Record 1148_000 site response analysis summary diagrams.

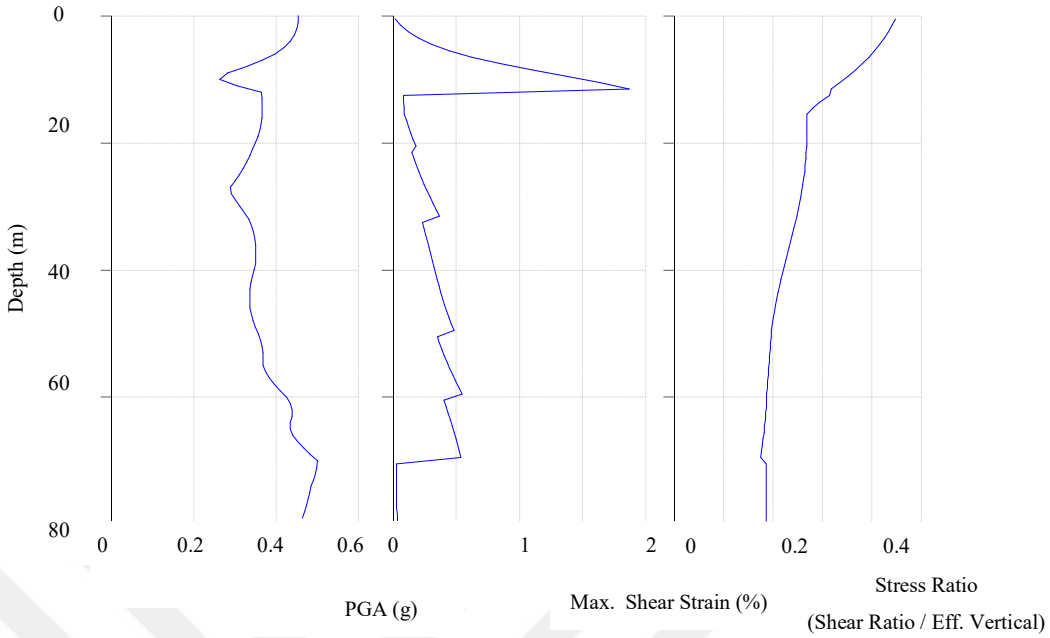

Figure 4.34. Record 1158_270 site response analysis summary diagrams.

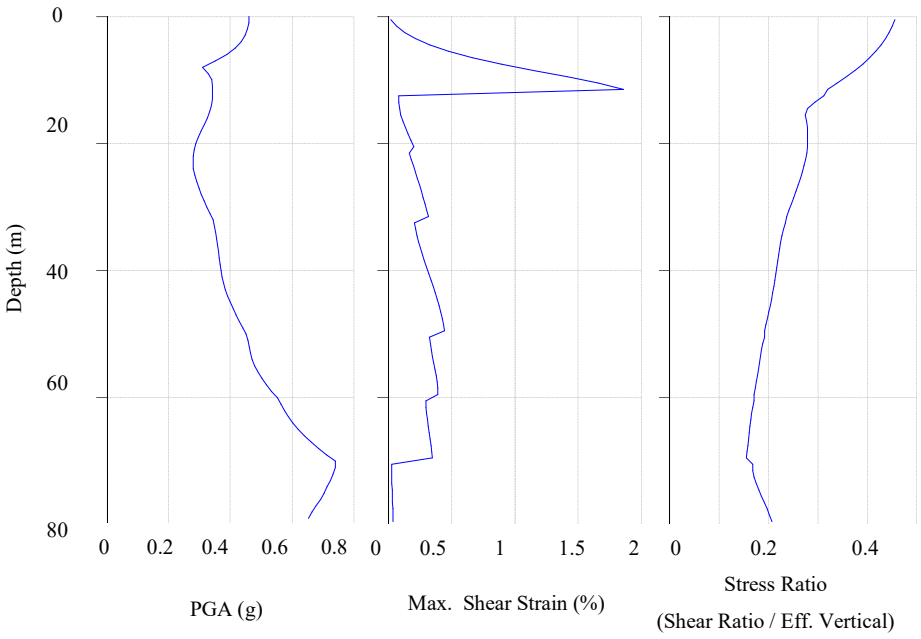

Figure 4.35. Record 1244_101n site response analysis summary diagrams.

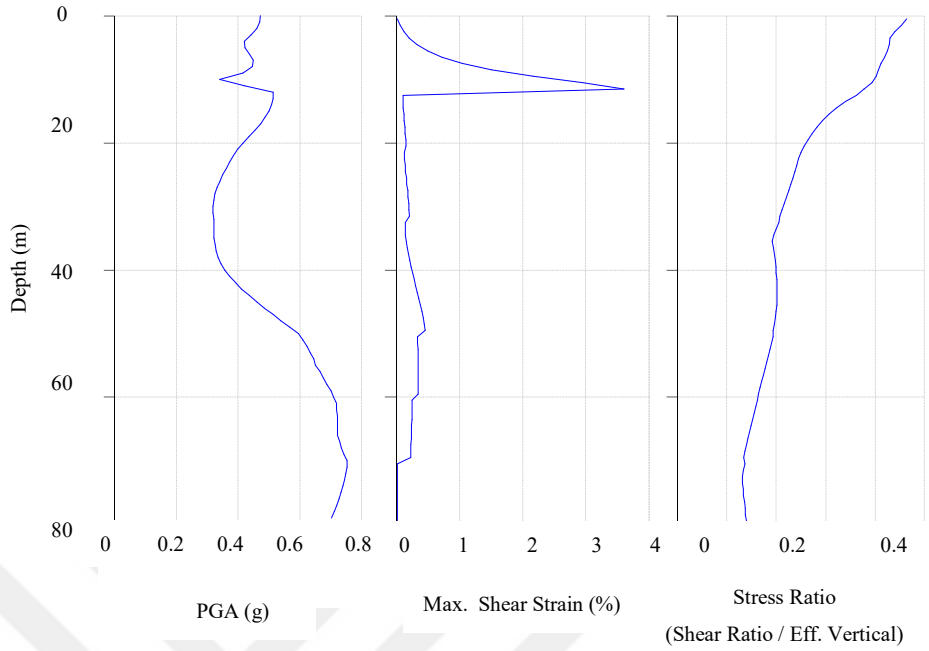

Figure 4.36. Record 1602_090 site response analysis summary diagrams.

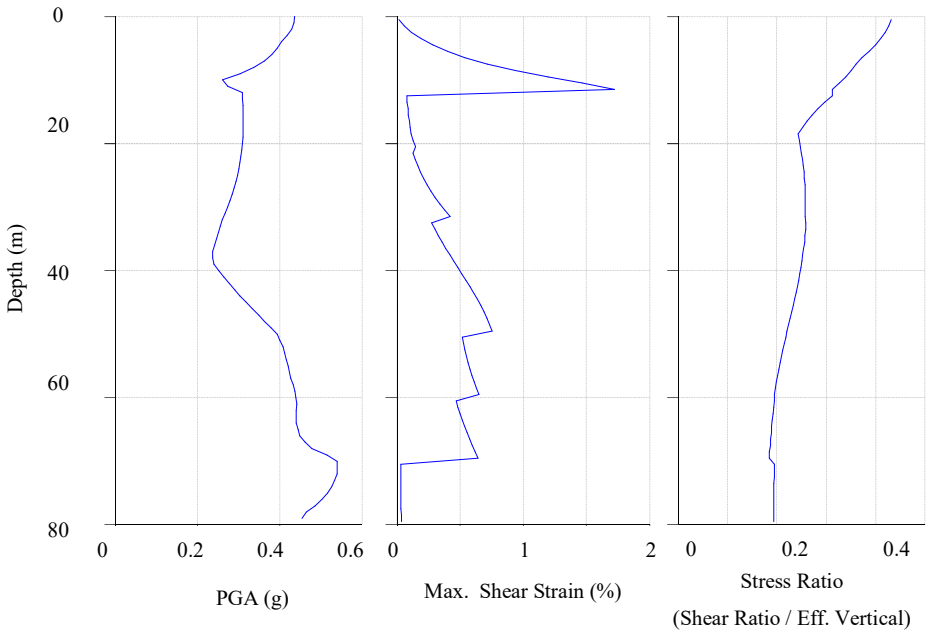

Figure 4.37. Record 1787_090 site response analysis summary diagrams.

4.2. Direct Method

In the direct method of soil-structure interaction analysis, both soil and structure are considered together under seismic effects. Seismic waves originating from the source propagate through soil media and reach to the structure's foundation. Waves are partially reflected by the foundation back to the soil environment, and partially transmitted to the superstructure causing vibrations.

Soil-structure analysis used in the study include the followings:

I) Pile-soil interaction is accounted for by non-linear *p-y, t-z, Q-z* curves as given in Section 4.1.1.
II) Site response analysis is performed for the given geotechnical data. Lateral displacement time histories are calculated for each layer for given earthquakes.
III) Lateral total displacements are calculated by combining layer displacements and applied to the piles via non-linear *p-y* curves. Dynamic load-displacement analysis is performed with a model including both sub and superstructure with nonlinear properties.

4.2.1. Application of Soil Displacement to Structural System

Link elements with the properties of *p-y* curves calculated according to Appendix A assigned to each node on the pile element while one end of the *p-y* link elements attached to the pile node and the other end fixed. Total displacements obtained in the site response analysis in Section 4.1.2, are used as ground motion records to apply to each link elements along the soil profile for each horizontal direction. Total displacements for each horizontal ground motion record directions are implemented to each compression-only *p-y* link elements for each time instant simultaneously. Including nonlinear models of the structure, nonlinear soil-pile-structure system analysis is performed in the time domain under displacement loading specified at each node of piles.

Equation of motion of superstructure, pile and soil mutual system is given below.

$$\begin{bmatrix} M_{ss} & 0 & 0 \\ 0 & M_{bb} & 0 \\ 0 & 0 & M_{pp} \end{bmatrix} \begin{Bmatrix} \Delta\ddot{u}_s^t \\ \Delta\ddot{u}_b^t \\ \Delta\ddot{u}_p^t \end{Bmatrix} + \begin{bmatrix} C_{ss} & C_{sb} & 0 \\ C_{bs} & (C_{bb}^s + C_{bb}^p) & C_{bp} \\ 0 & C_{pb} & (C_{pp} + C_{pp}^g) \end{bmatrix} \begin{Bmatrix} \Delta\dot{u}_s^t \\ \Delta\dot{u}_b^t \\ \Delta\dot{u}_p^t \end{Bmatrix}$$
$$+ \begin{bmatrix} K_{ss} & K_{sb} & 0 \\ K_{bs} & (K_{bb}^s + K_{bb}^p) & K_{bp} \\ 0 & K_{pb} & (K_{pp} + K_{pp}^g) \end{bmatrix} \begin{Bmatrix} \Delta u_s^t \\ \Delta u_b^t \\ \Delta u_p^t \end{Bmatrix} = - \begin{Bmatrix} 0 \\ 0 \\ K_{pg}\Delta u_g^t \end{Bmatrix} \quad (4.10)$$

s = superstructure

b = base

p = pile

g = free field

M_{ij} = Mass submatrix

C_{ij} = Damping submatrix

K_{ij} = Stiffness submatrix

u^t_g = Free field ground record data

K^g_{pp} and K_{pg} submatrices represent p-y curves

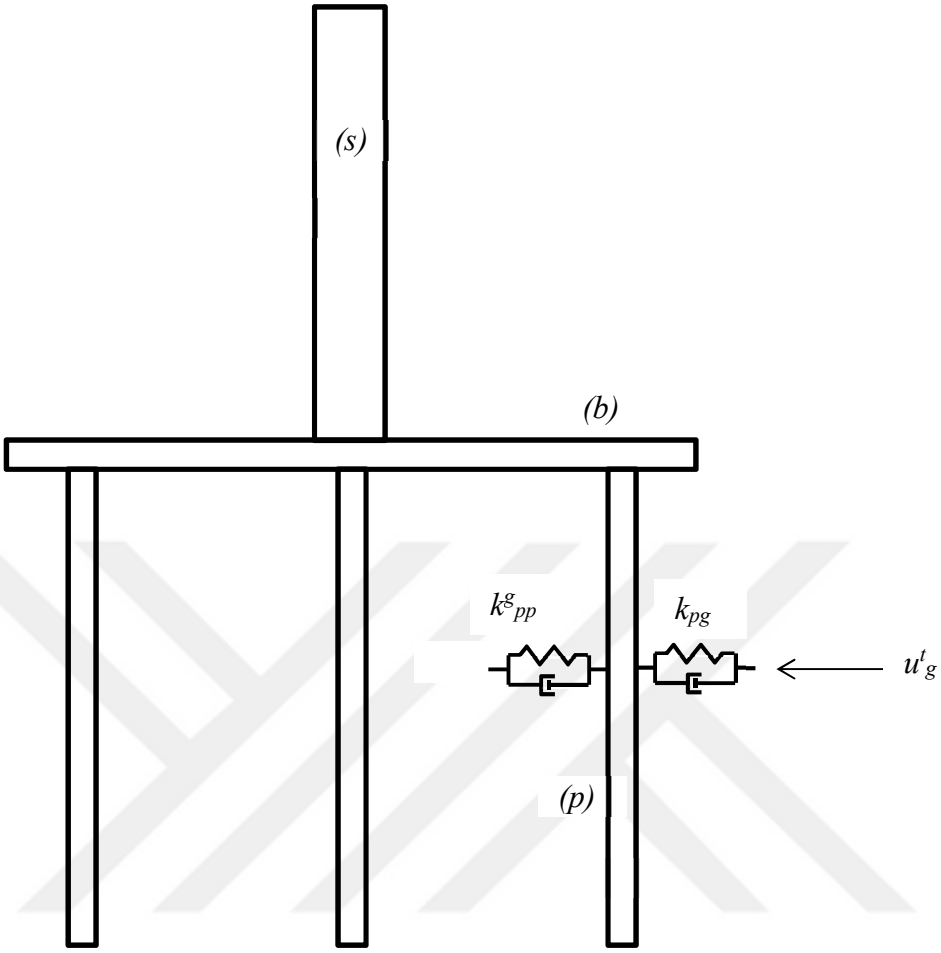

Figure 4.38. Superstructure – pile – soil mutual system schematic figure.

Rayleigh Damping is used for the nonlinear displacement time history analysis cases, which the damping matrix is calculated as a linear combination of the stiffness matrix and mass matrix scaled by period of the structure for the calculation of the damping value. The damping matrix C is formed as follows:

$$C = \eta M + \delta K \tag{4.11}$$

Where;

M is mass matrix

K is stiffness matrix

η is the mass-proportional damping coefficient

δ is the stiffness-proportional damping coefficient

Relationships between the modal equations and orthogonality conditions allow this equation to be rewritten as (Wilson, 2004):

$$\xi_n = \frac{1}{2w_n}\eta + \frac{w_n}{2}\delta \tag{4.12}$$

Where,

ξ_n is the critical damping ratio

w_n is the natural frequency

By writing Eq. 4.12 for two selected modal damping values, eta and delta coefficients are solved. Due to softening of structural elements after yielding, reasonably lower frequencies/higher periods should be used.

4.3. Substructure Method

In the substructure method, structure is evaluated in two stages, called as kinematic interaction and inertial interaction. Kinematic interaction shows the nonlinear response of piles under cyclic loading. Inertial interaction is important for the nonlinear response of the superstructure. Responses of these two interaction analyses are combined by using their absolute values.

4.3.1. Kinematic interaction

For the kinematic interaction, the model developed in Section 4.2 is used. Lateral displacement profiles are calculated with the help of lateral displacement response time histories. These displacement profiles are established as follows;

1- Maximum envelope lateral relative displacements of the soil profile with respect to bedrock for all time instants.
2- Total lateral displacements of the soil profile including bedrock displacements in the instant of maximum surface displacement.
3- Relative lateral displacements of the soil profile with respect to bedrock at the instant of maximum surface displacement.

4- Total lateral displacements of the soil profile including bedrock displacements at the instant of maximum drift along the pile length.
5- Relative lateral displacements of the soil profile with respect to bedrock at the instant of maximum drift along the pile length.

Displacement profiles are implemented to the piles via non-linear *p-y* curves and can be seen as follows:

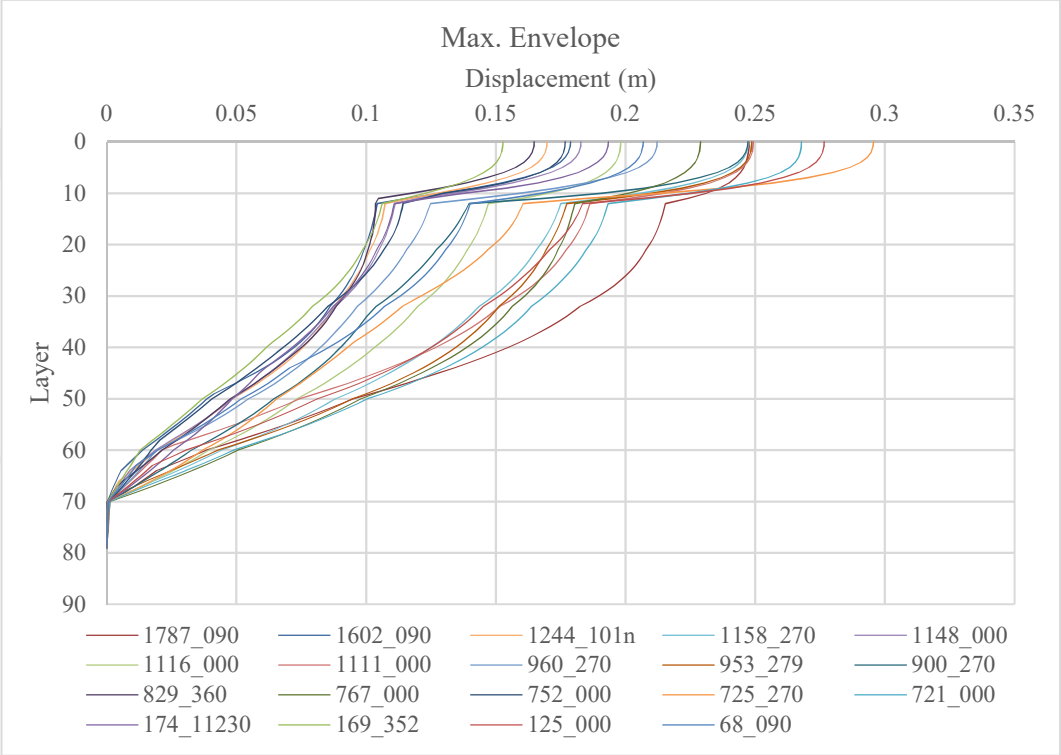

Figure 4.39. Max. envelope lateral soil displacements relative to bedrock.

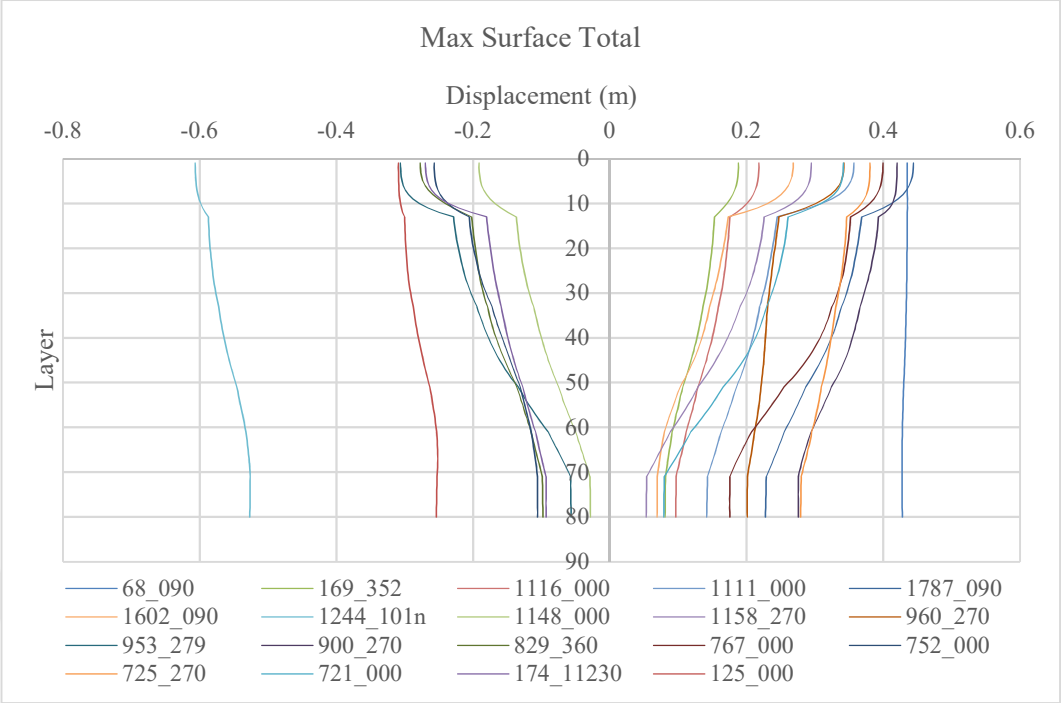

Figure 4.40. Total lateral displacements of the soil profile at the instant of maximum surface displacement.

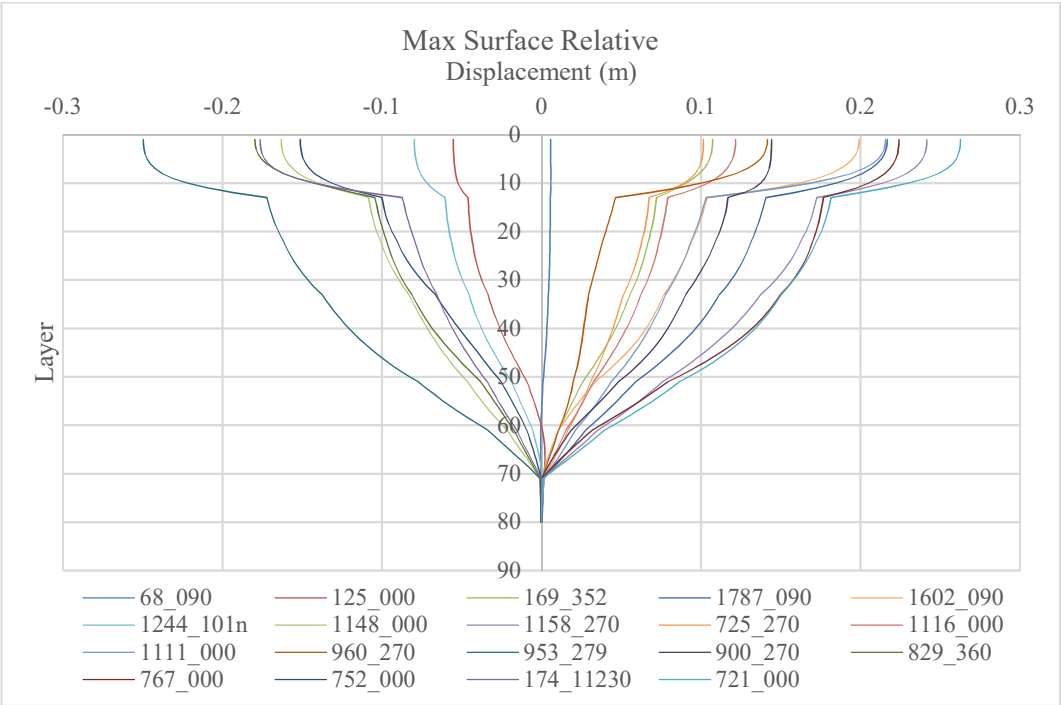

Figure 4.41. Relative lateral displacements of the soil profile with respect to bedrock at the instant of maximum surface displacement.

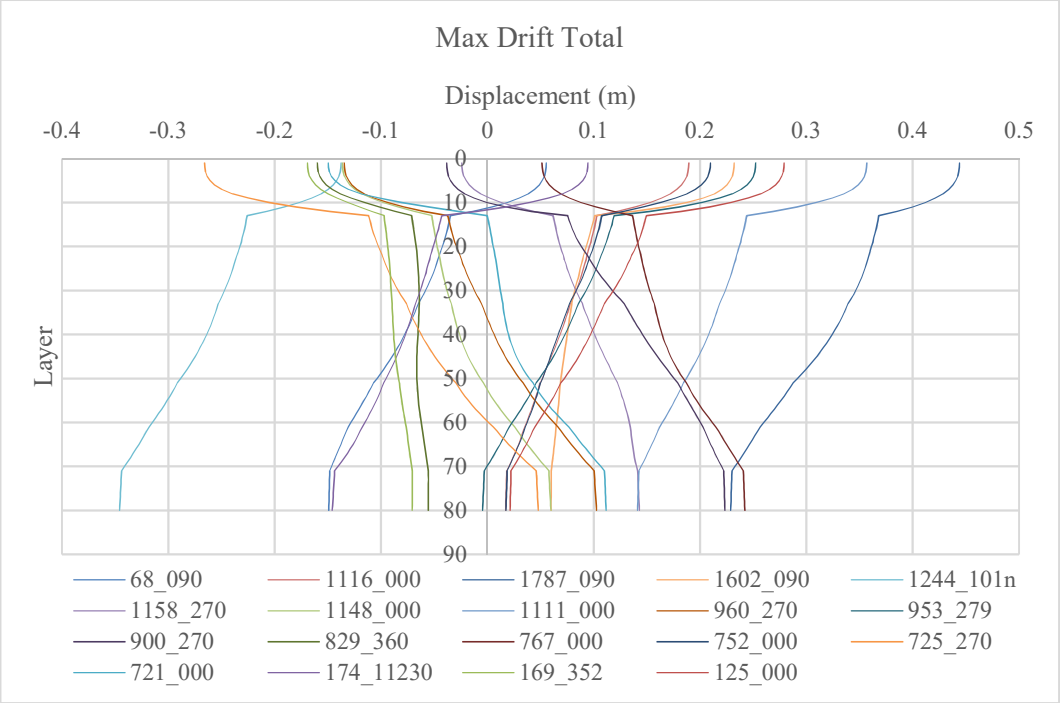

Figure 4.42. Total lateral displacements of the soil at the instant of maximum drift along the pile length.

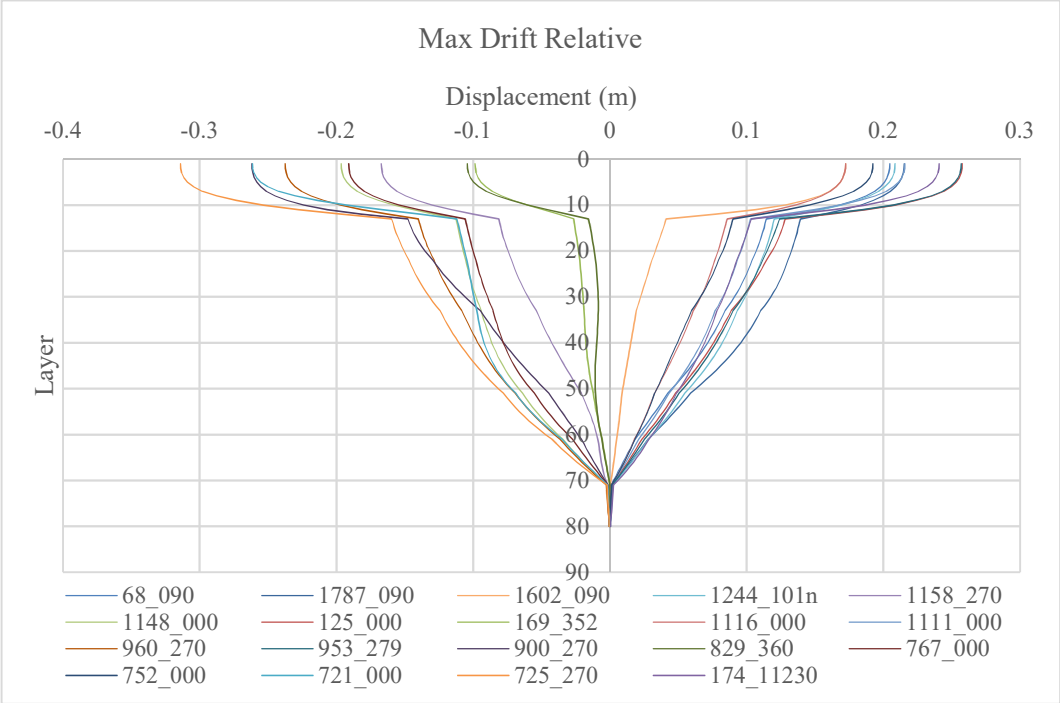

Figure 4.43. Relative lateral displacements of the soil with respect to bedrock at the instant of maximum drift along the pile length.

4.3.2. Inertial Interaction

Inertial Interaction analysis is conducted via Incremental Equivalent Earthquake Load Method. The purpose of the Incremental Equivalent Earthquake Load Method is to perform a nonlinear push-over analysis under the influence of equivalent seismic loads, stepped up monotonically up to the yield limit, in proportion to the dominant vibration mode. At each step of the push-over analysis following the vertical load analysis, the displacements, plastic deformations, internal force increments, and their cumulative values in the pile-foundation system are calculated and the maximum values corresponding to the seismic demand in the last step are calculated.

During the incremental push-over analysis, it can be assumed that the equivalent seismic load distribution remains constant, independent of the plastic hinge formations in the pile-foundation system. In this case, the load distribution is defined as proportional to the value obtained by multiplying the dominant modal amplitude calculated for the linear elastic behavior and the related mass at the initial step of the analysis.

With the constant load distribution push-over analysis, the push-over curve (top displacement versus base shear) is obtained. By applying coordinate transformation to the push-over curve, the modal capacity diagram (i.e., modal displacement versus modal acceleration) can be obtained. Modal capacity diagram represents the structure's ability to resist the seismic demand. Seismic Demand Spectrum is established with the design spectrum that was given in the Section 3.4.2.

Modal capacity diagram is established as follows:

1. Modal acceleration $a_1^{(i)}$ is calculated for the i'th pushover step (dominant mode).

$$a_1^{(i)} = \frac{V_{x,1}^{(i)}}{M_{x,1}} \tag{4.13}$$

$M_{x,1}$ indicates the effective modal mass

2. Modal displacement $d_1^{(i)}$ is calculated for i'th pushover step (dominant mode)

$$d_1^{(i)} = \frac{u_{xT,1}^{(i)}}{\phi_{xT,1}\Gamma_{x,1}} \tag{4.14}$$

$\Gamma_{x,1}$ indicates modal participating factor of the first mode.

Maximum modal displacement is calculated according to modal capacity diagram, which evaluated with the elastic design spectrum that is given in the Section 3.4.2. According to the definition, maximum modal displacement $d_1^{(p)}$ is equal to the nonlinear spectral displacement $Sd_{i,1}$.

$$d_1^{(p)} = Sd_{i,1} \tag{4.15}$$

Nonlinear spectral displacement is calculated as;

$$Sd_{i,1} = C_R\, S_{de,1} \tag{4.16}$$

$$C_{R,1} = \frac{\mu(R_{y,1}, T_1)}{R_{y,1}} \tag{4.17}$$

S_{de} is the corresponding period's elastic spectral displacement; whereas C_R is the spectral displacement ratio, and R_y is the yield strength reduction factor. $\mu(R_{y,1},T_1)$ indicates the ductility demand according to natural period and yield strength of the structure.

$$R_y = \frac{S_{ae,1}}{a_{y,1}} \tag{4.18}$$

$S_{ae,1}$ is the elastic spectral pseudo-acceleration demand of the corresponding mode and $a_{y,1}$ is the yield strength of the equivalent SDOF system.

$$\mu(R_{y,1},T_1) = R_y \text{ for } T_1 > T_B \tag{4.19}$$
$$\mu(R_{y,1},T_1) = 1 + (R_y - 1)(T_B/T_1) \text{ for } T_1 \leq T_B$$

$$C_R = 1 \text{ for } T_1 > T_B \tag{4.20}$$

$$C_R = \frac{1+(R_y-1)\frac{T_B}{T_1}}{R_y} \geq 1 \text{ for } T_1 \leq T_B$$

Seismic demand $u^{(p)}_{xT,1}$ is calculated as

$$u^{(p)}{}_{xT,1} = \phi_{xT,1}\Gamma_{x,1}{d_1}^p \tag{4.21}$$

In the inertial interaction model, the same mathematical model, generated for the kinematic interaction, is used, but piles are modelled without mass. In the model, the initial rigidities of soil springs are used.

Table 4.10. Bridge I & II seismic demand.

Input	Bridge I Demand (m)	Bridge II Demand (m)
th_68_090	0.418	0.439
th_125_000	0.421	0.503
th_169_352	0.232	0.429
th_174_11230	0.394	0.476
th_721_000	0.390	0.388
th_725_270	0.405	0.117
th_752_000	0.317	0.478
th_767_000	0.435	0.413
th_829_360	0.200	0.468
th_900_270	0.445	0.474
th_953_279	0.259	0.424
th_960_270	0.107	0.053
th_1111_000	0.319	0.411
th_1116_000	0.271	0.436
th_1148_000	0.245	0.277
th_1158_270	0.354	0.436
th_1244_101n	0.762	0.450
th_1602_090	0.239	0.446
th_1787_090	0.500	0.379
Mean Demand	0.353	0.394

5. ANALYSIS RESULTS

5.1. Direct Method Analysis Results

The displacement time histories from the analyses are given in the following figures. 14.00 m high piers and the outer row of piles are chosen for the comparisons. As expected, for most of the records, plastic hinges are formed at the pile-cap level, or the soil transition interface, where the sudden stiffness changes occur. Bridge I displacement-time history results are given in Figure 5.1 to Figure 5.5; whereas bridge II results are given in Figure 5.6 to Figure 5.10.

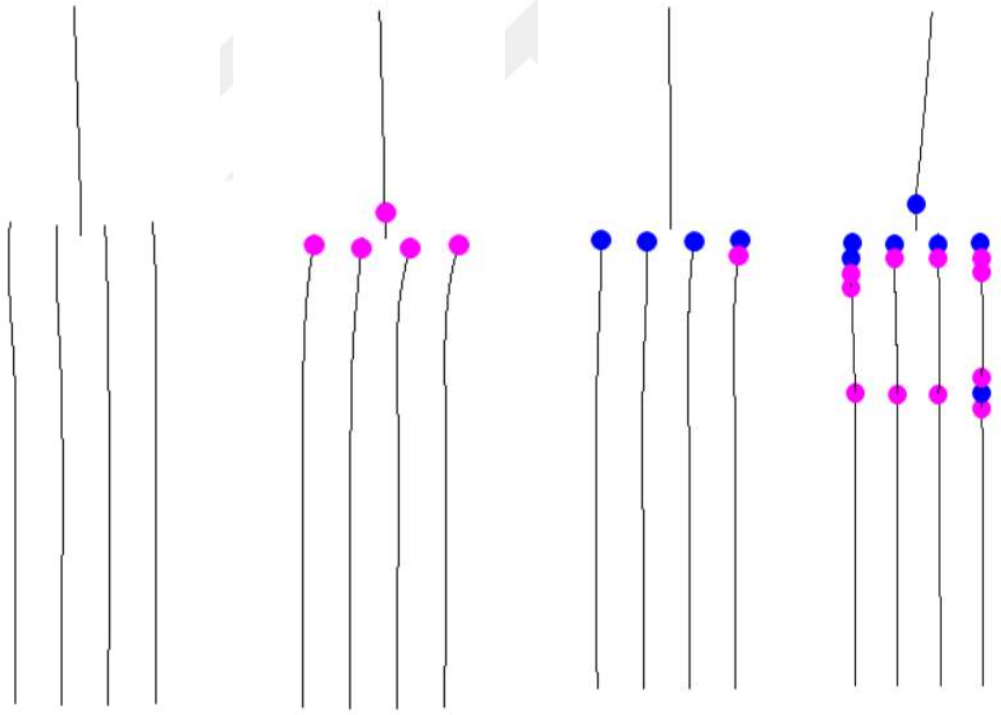

Figure 5.1. Bridge I record 68_090 / 174_11230 / 767_000 / 829_360 plastic hinge formation.

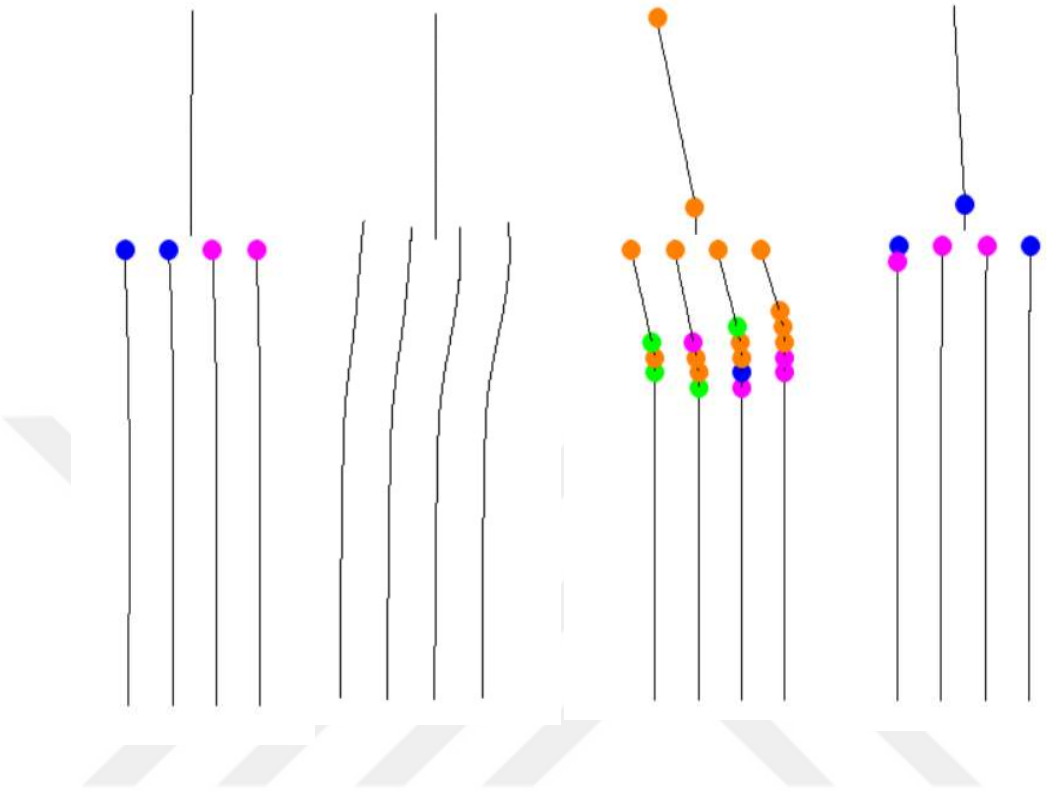

Figure 5.2. Bridge I record 960_270 / 1148_000 / 1244_101n / 1602_090 plastic hinge formation.

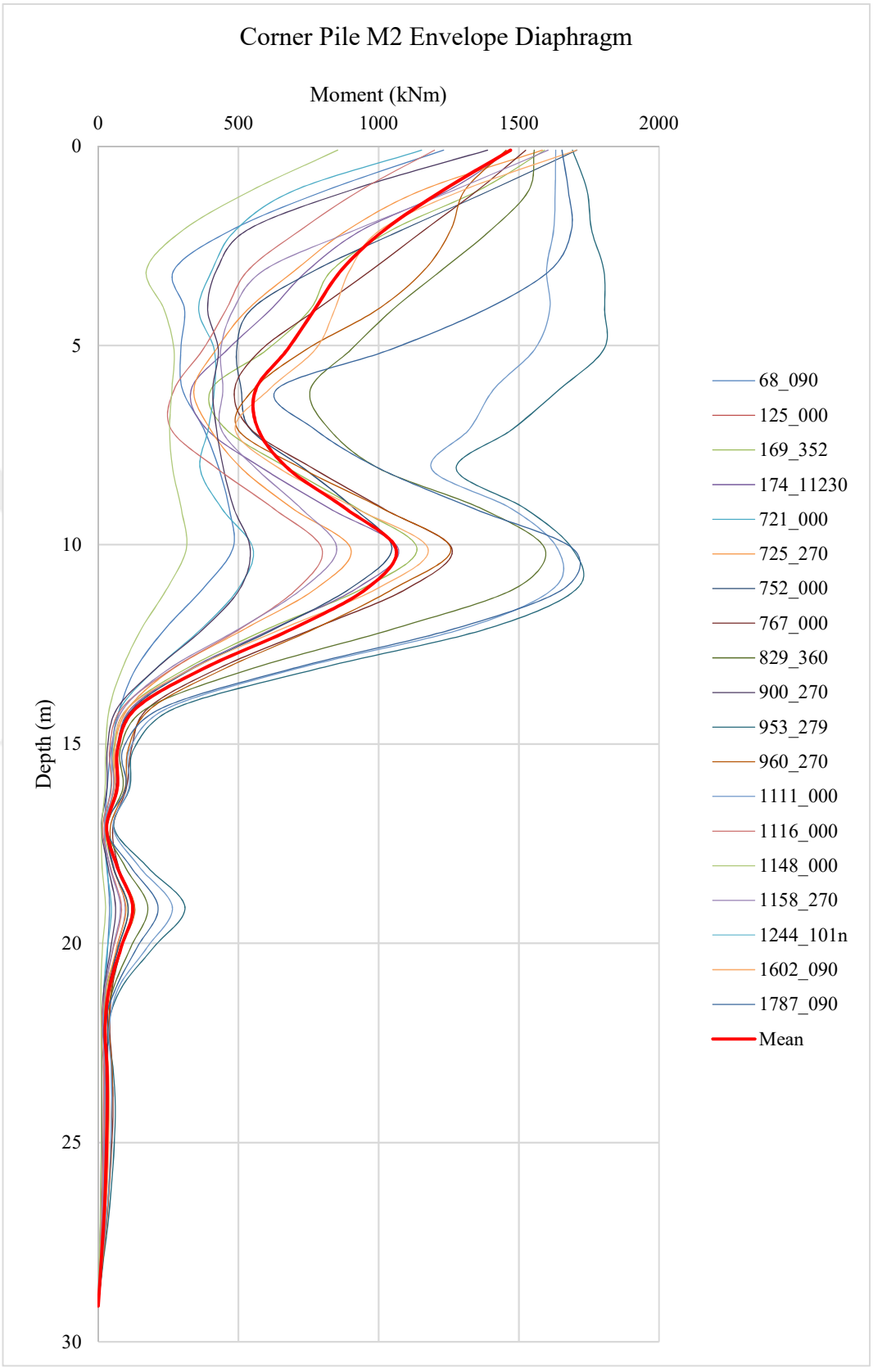

Figure 5.3. Bridge I displacement time history envelope moment diagram.

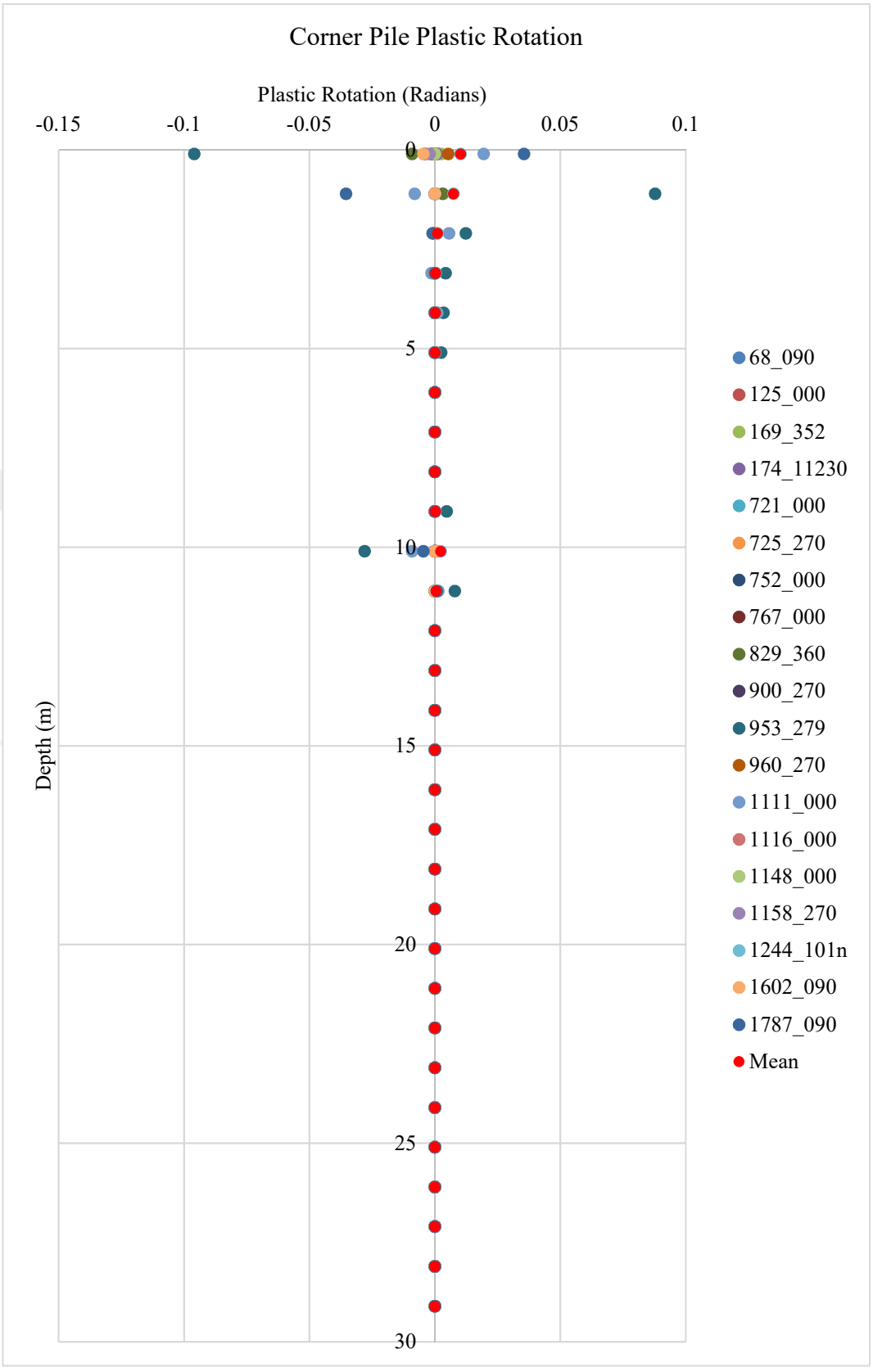

Figure 5.4. Bridge I displacement time history plastic hinge rotation.

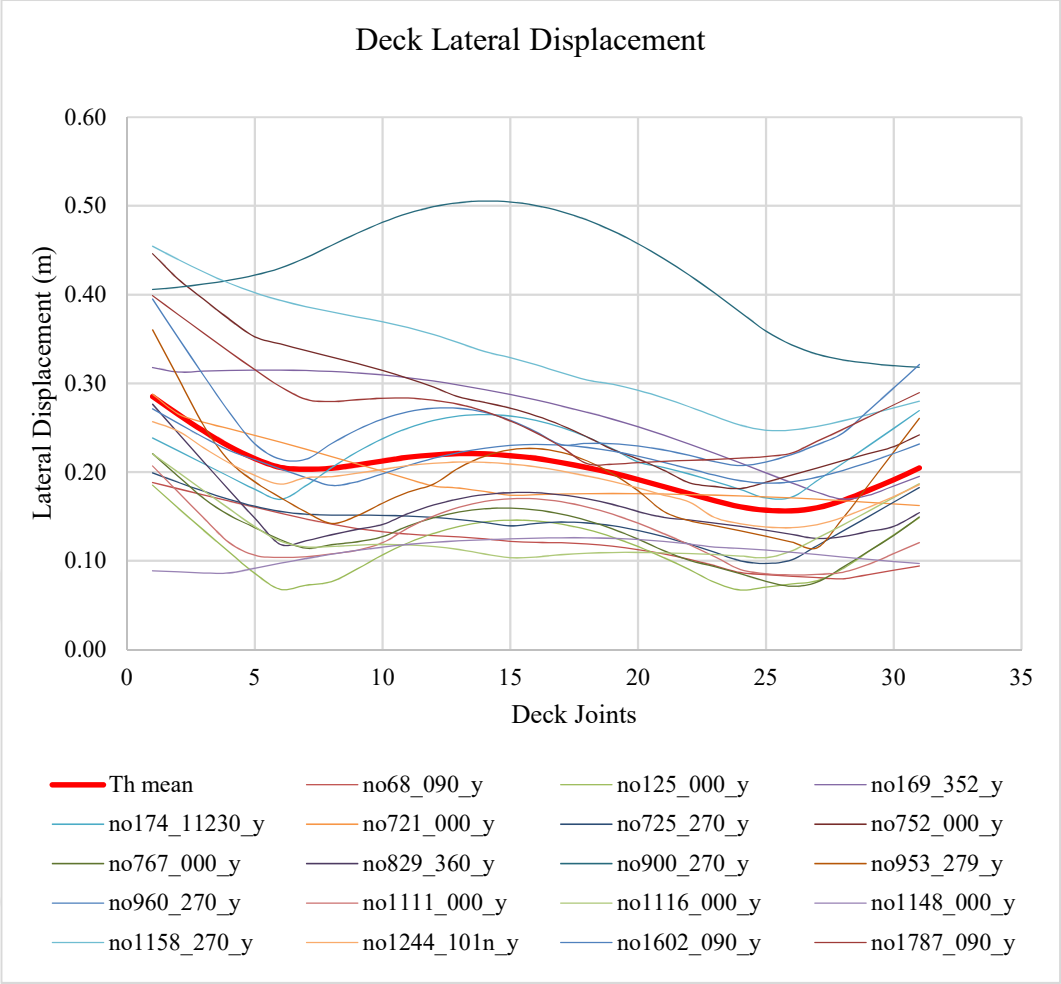

Figure 5.5. Bridge I displacement time history deck lateral displacement.

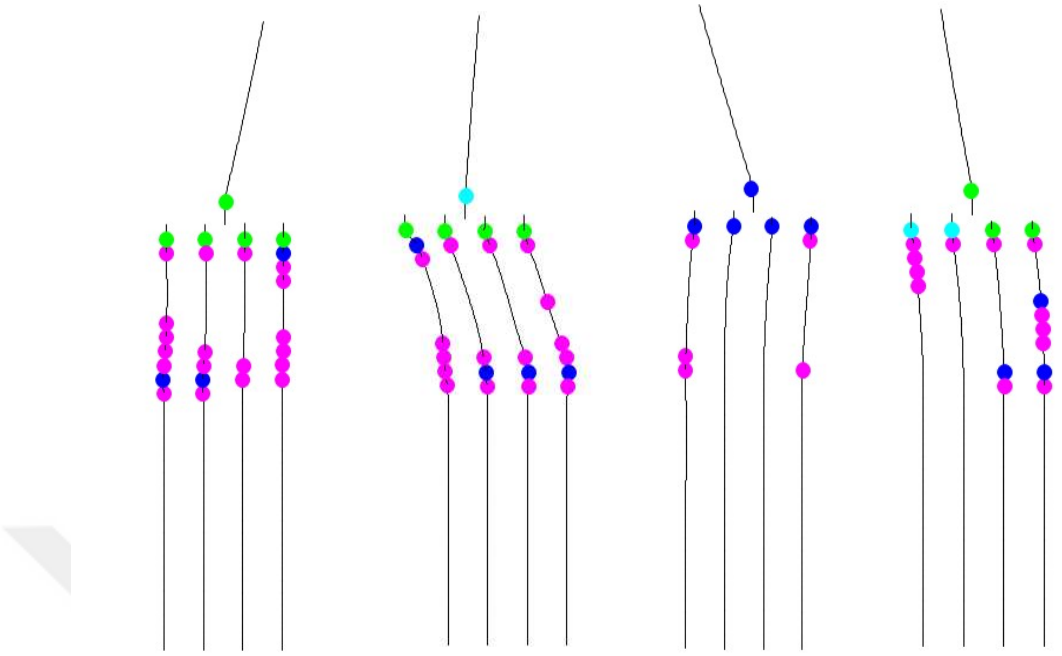

Figure 5.6. Bridge II record 68_090 / 174_11230 / 767_000 / 829_360 plastic hinge formation.

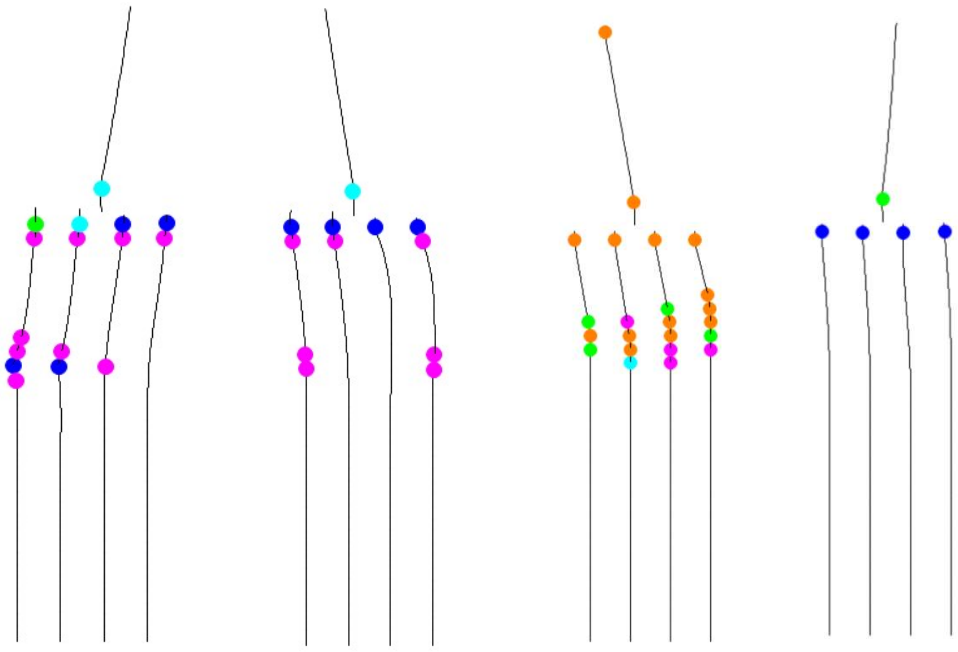

Figure 5.7. Bridge II record 960_270 / 1148_000 / 1244_101n / 1602_090 plastic hinge formation.

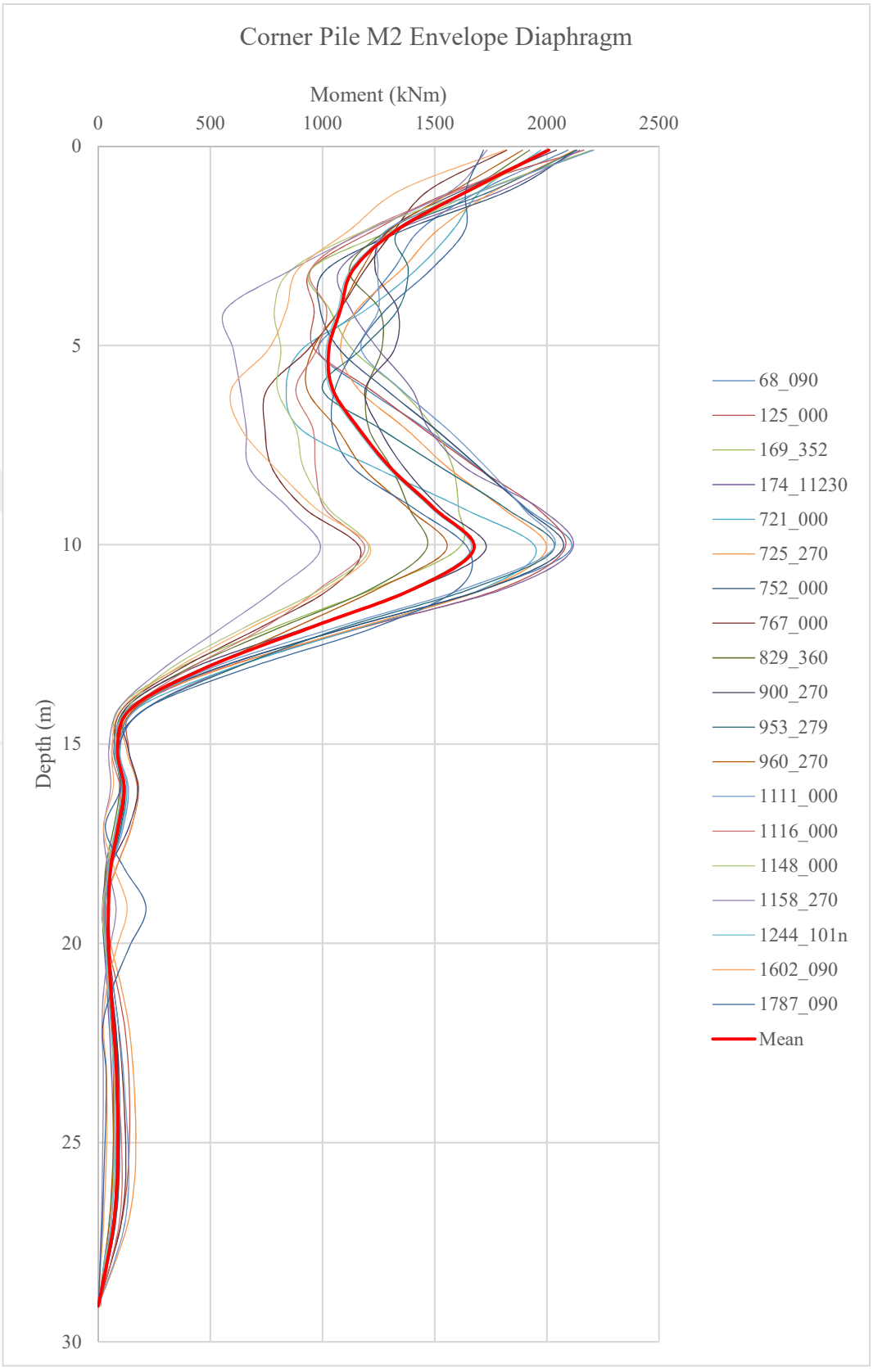

Figure 5.8. Bridge II displacement time history envelope moment diagram.

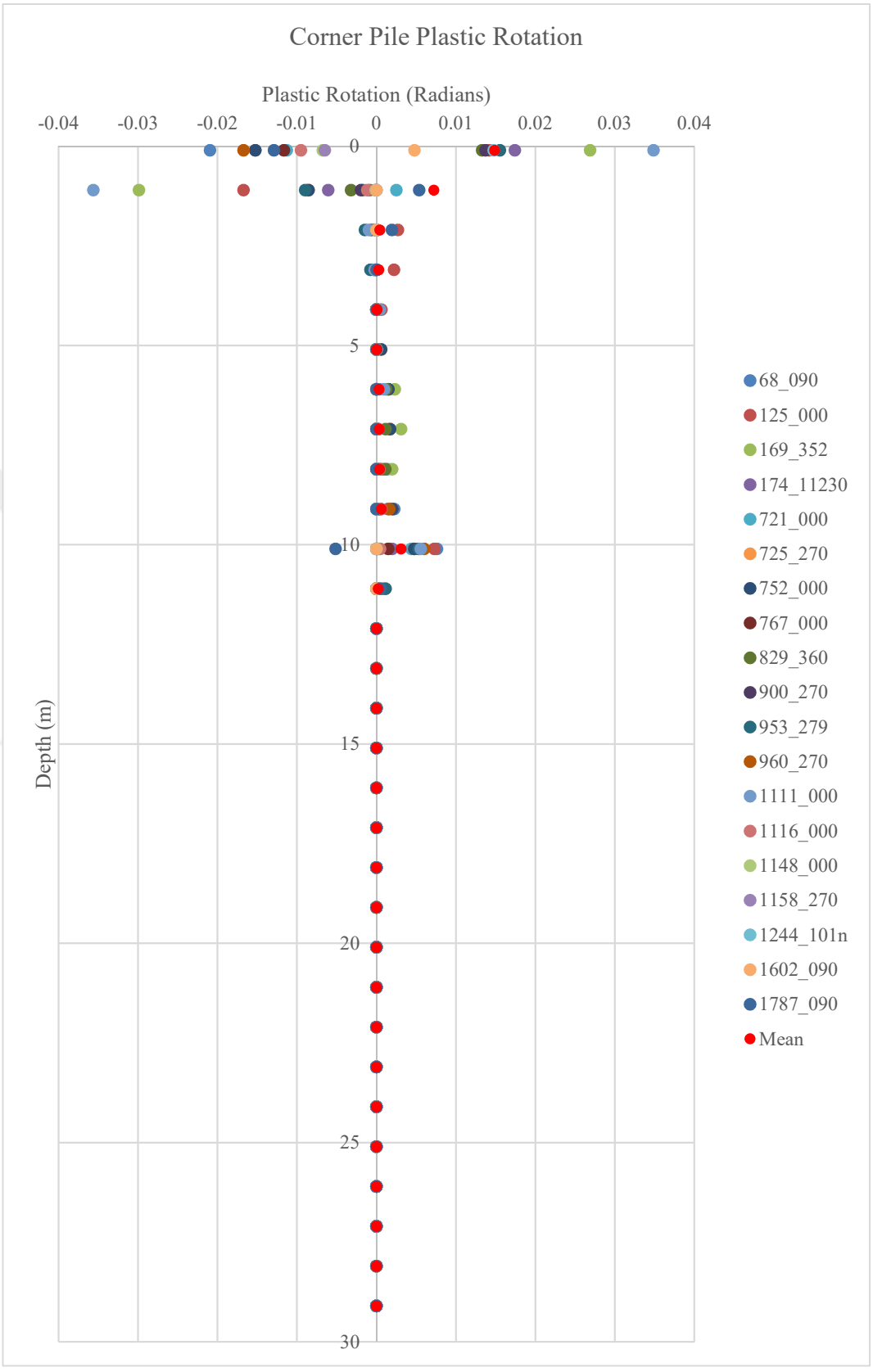

Figure 5.9. Bridge II displacement time history plastic hinge rotation.

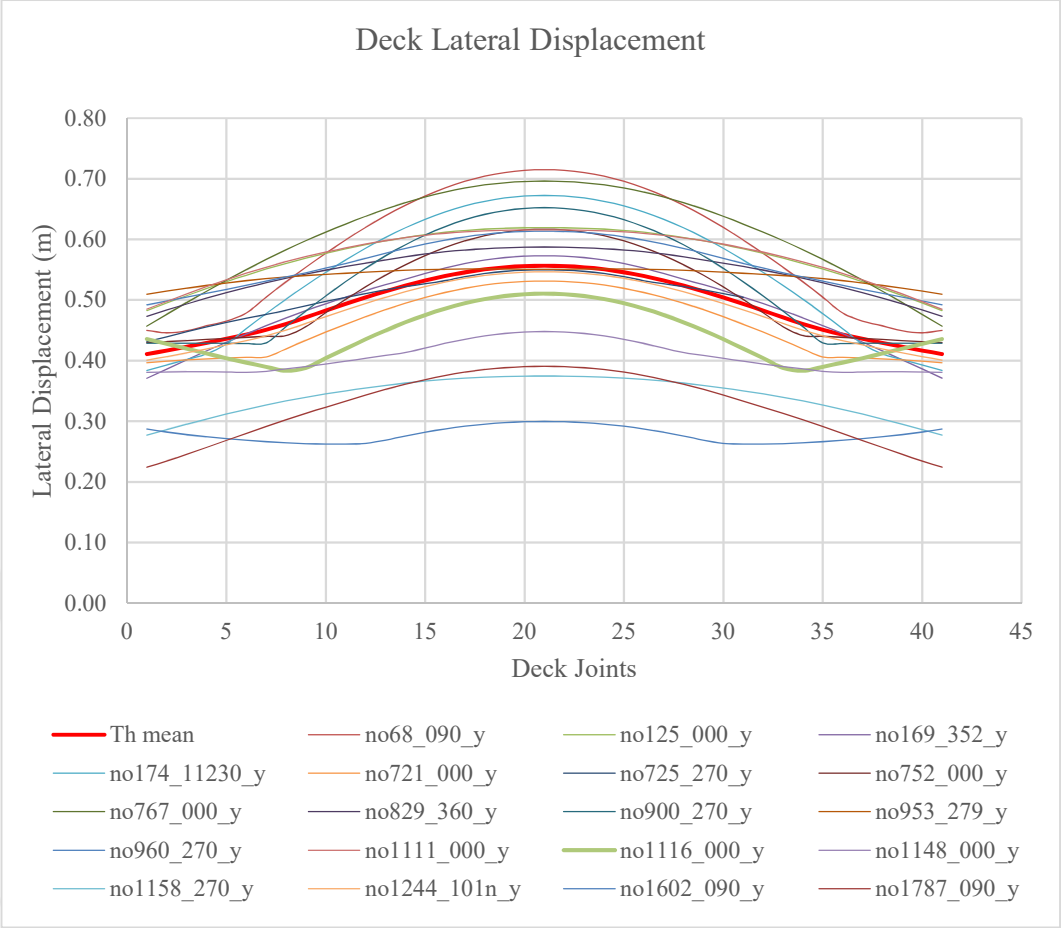

Figure 5.10. Bridge II displacement time history deck lateral displacement.

5.2. Substructure Method Analysis Results

5.2.1. Kinematic Interaction Analysis Results

Kinematic analysis results for Bridge I can be seen in Figure 5.11 to Figure 5.17, and in Figure 5.18 to Figure 5.24 for Bridge II. For both bridges analyzed, largest moments occur where the soil stiffness changes sharply, and at the pile cap level, as expected. Analyses are conducted for both the total and the relative (with respect to bedrock) lateral displacements of the soil profile. The maximum drift along the pile length gives the highest moment results and the higher rotations as in the Figure 5.12 and Figure 5.19. It is seen that lateral displacement of the soil profile, at the instant of maximum surface displacement, causes the biggest displacement at the deck level. Moment diagrams given for both bridges are absolute mean values of 19 seismic records.

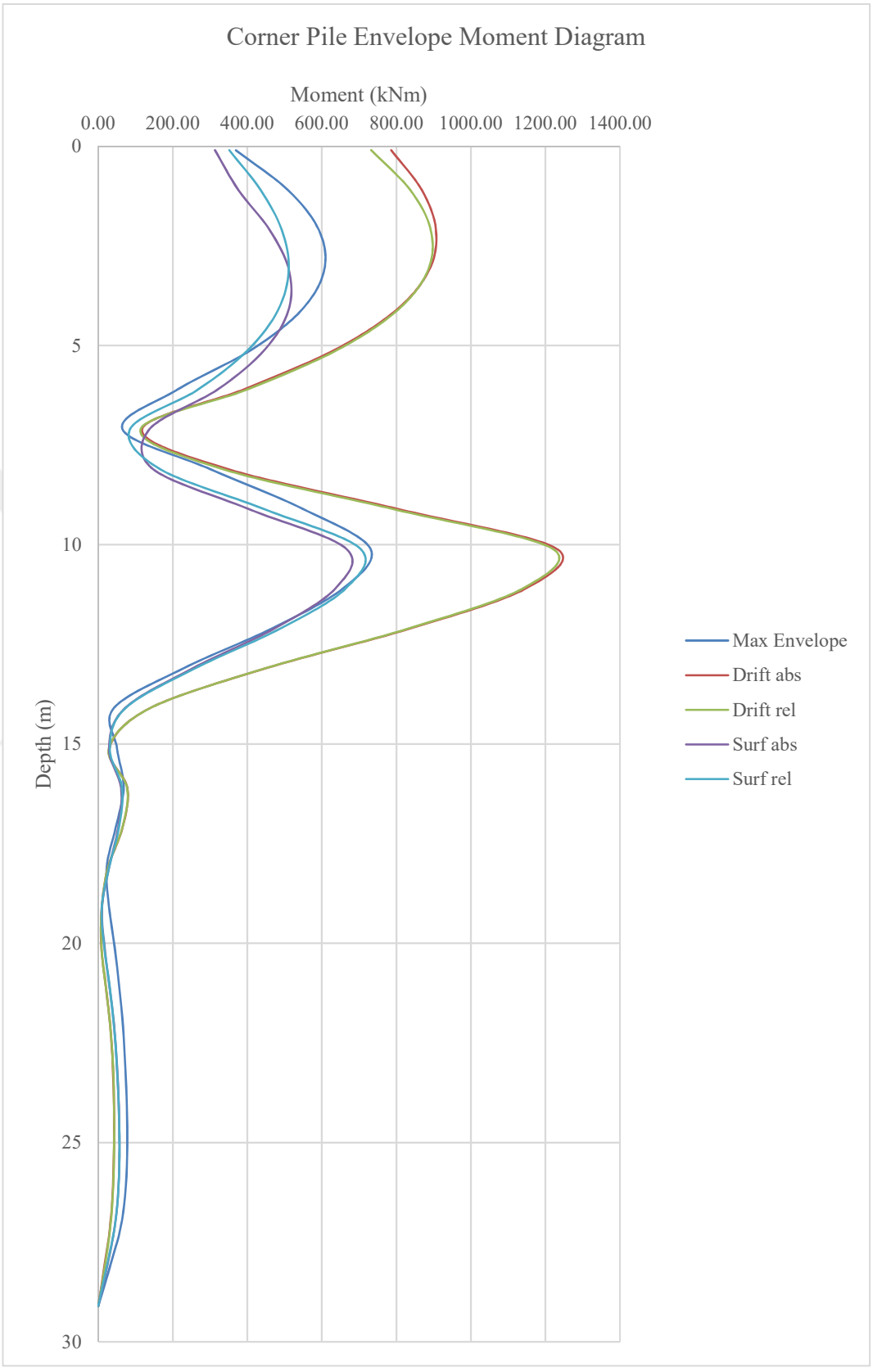

Figure 5.11. Bridge-I kinematic interaction envelope moment diagram.

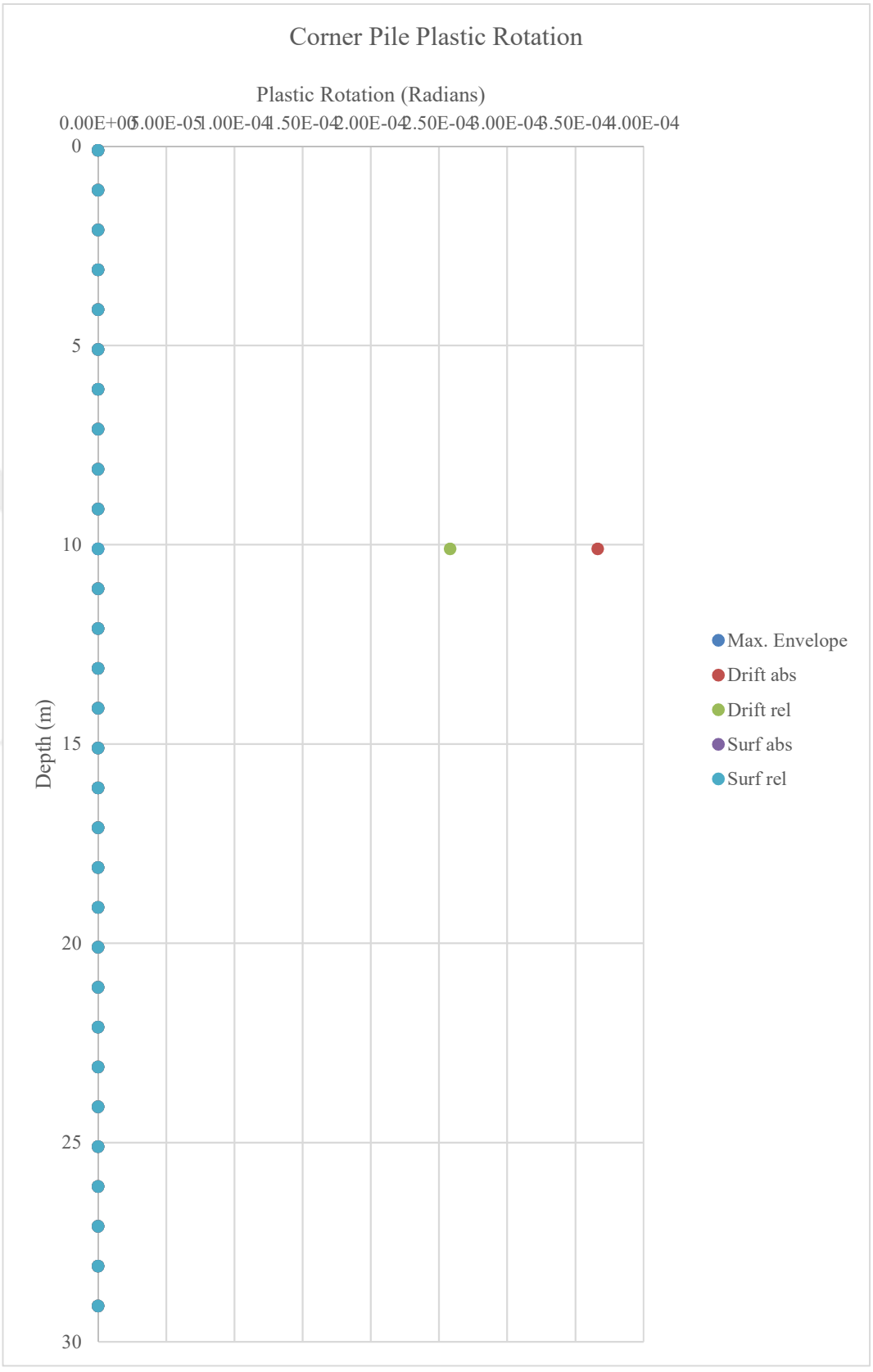

Figure 5.12. Bridge-I kinematic interaction plastic hinge rotation.

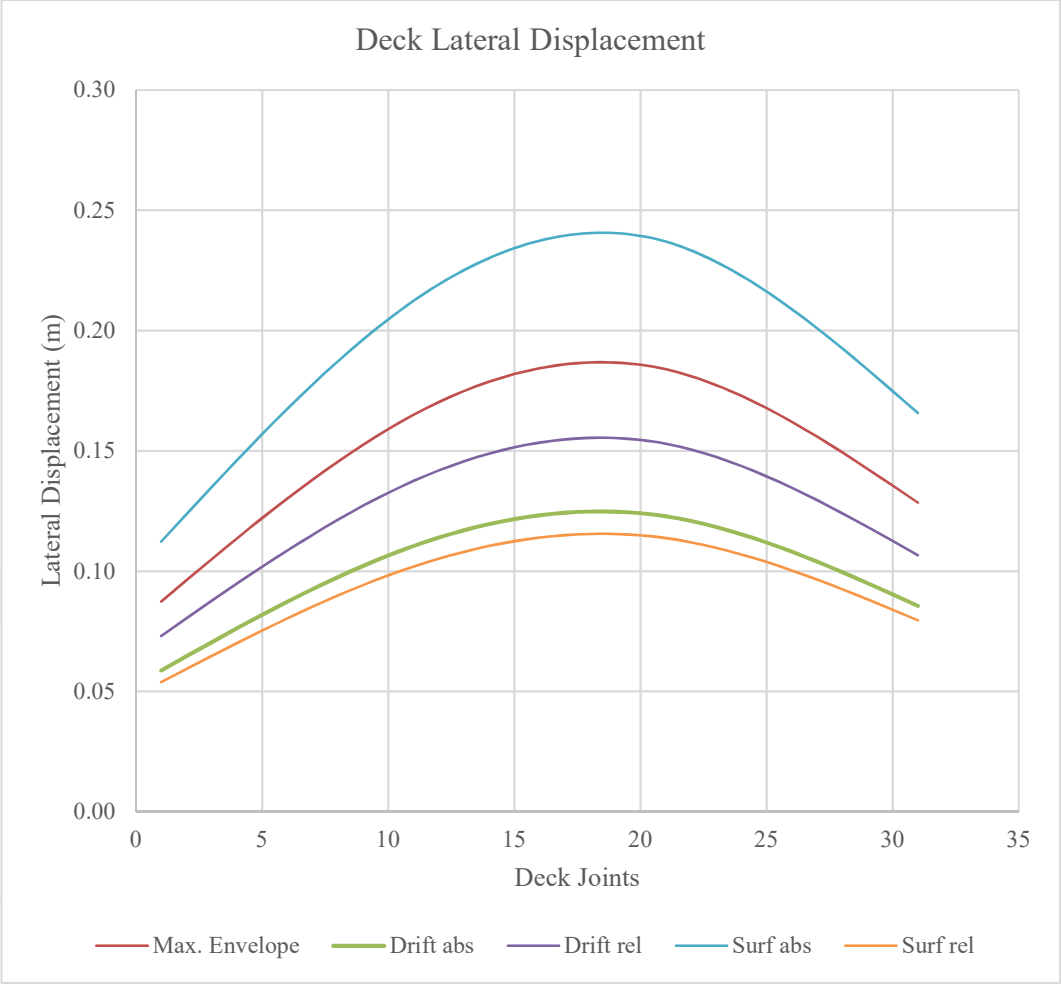

Figure 5.13. Bridge-I kinematic interaction deck lateral displacement.

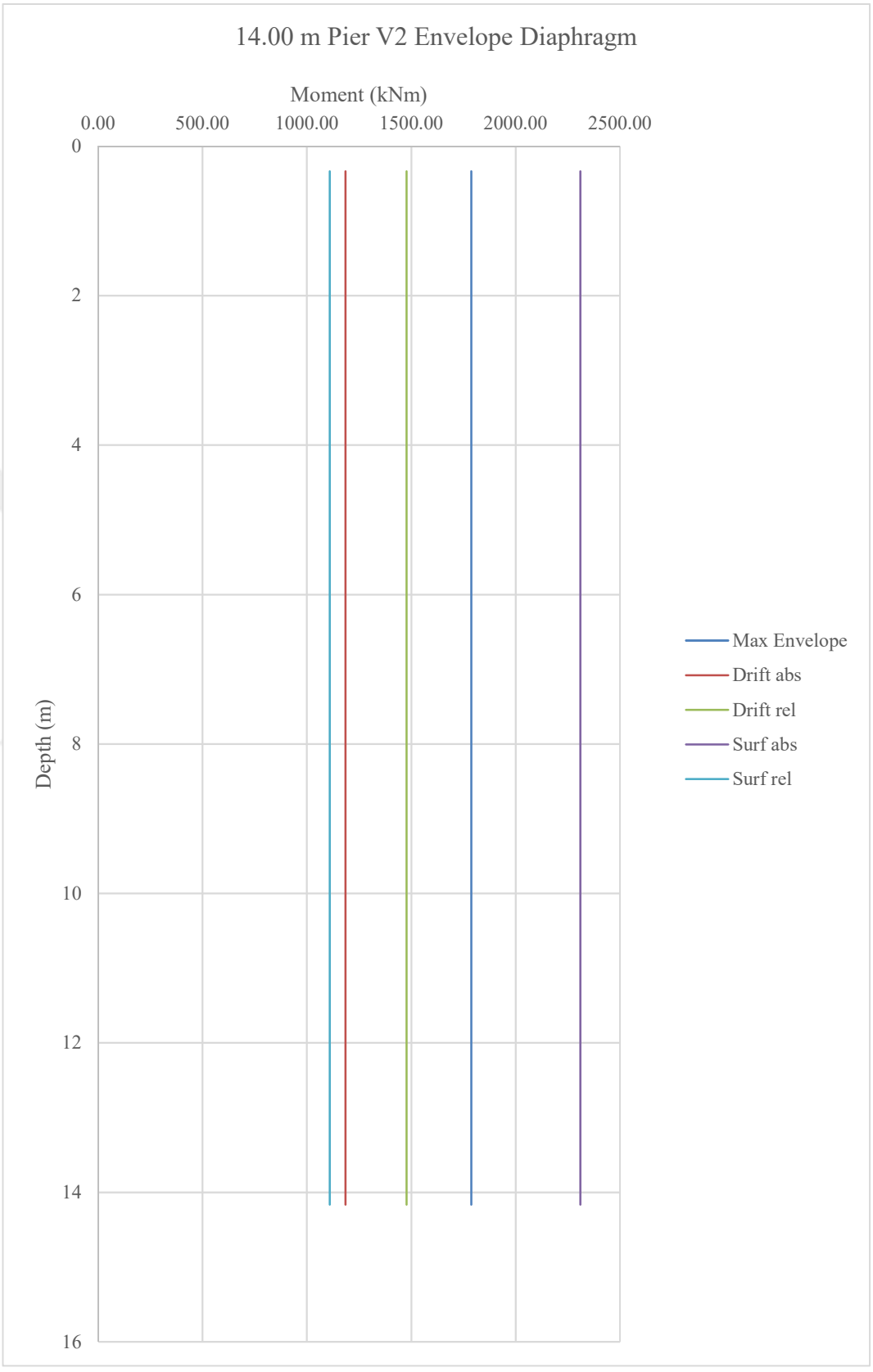

Figure 5.14. Bridge-I 14.00 m pier envelope shear force diagram.

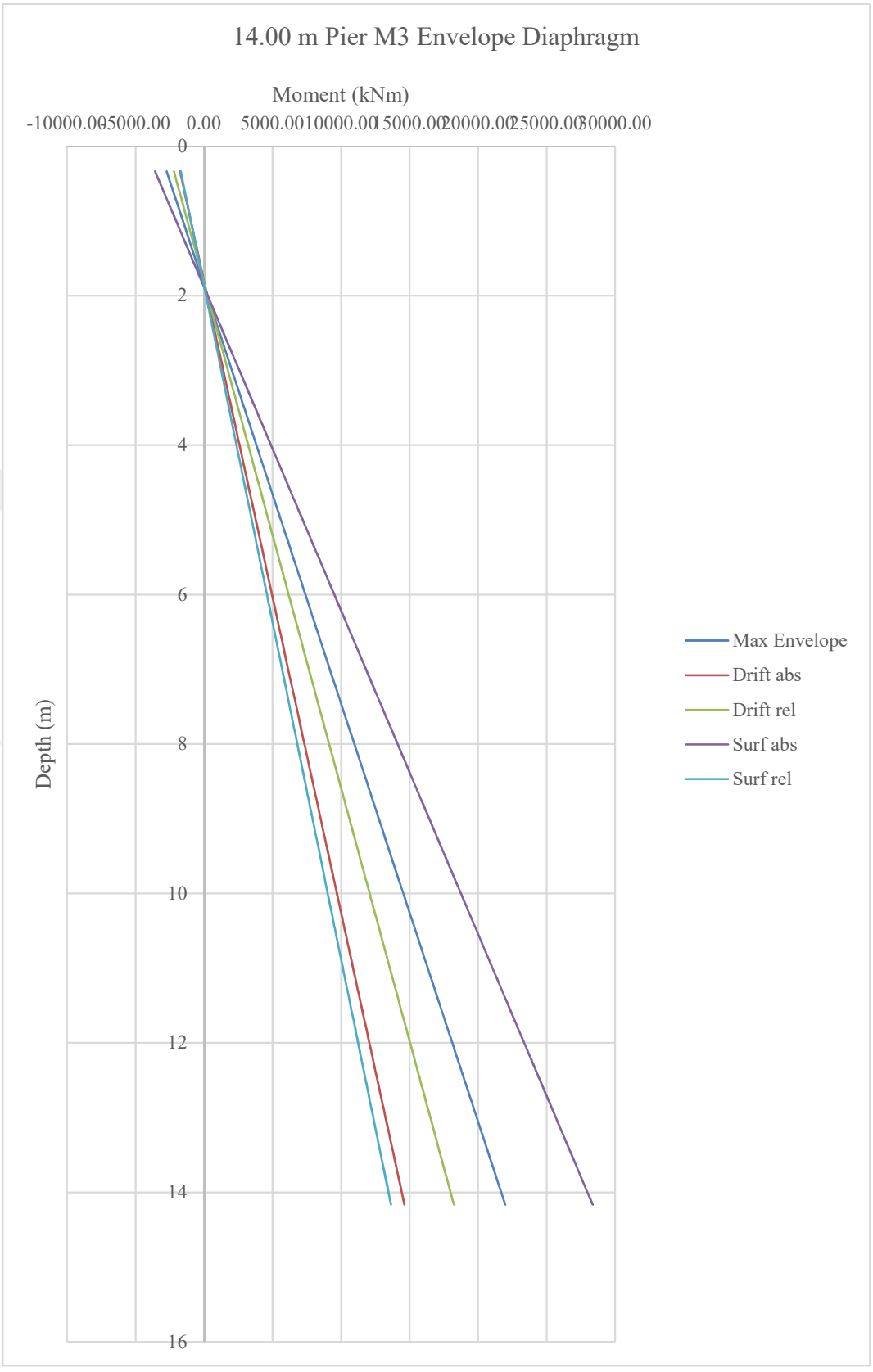

Figure 5.15. Bridge-I 14.00 m pier envelope moment diagram.

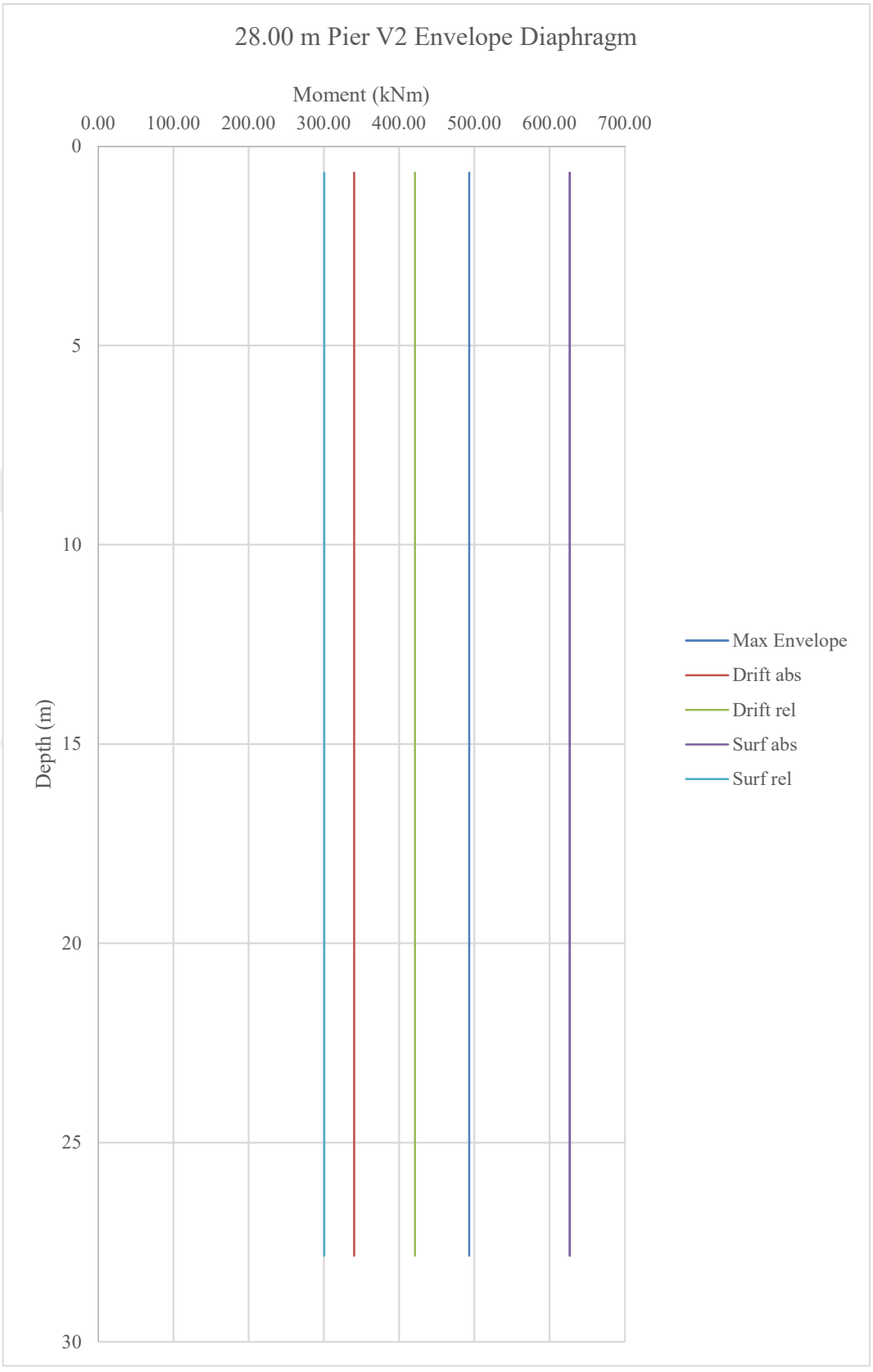

Figure 5.16. Bridge-I 28.00 m pier envelope shear force diagram.

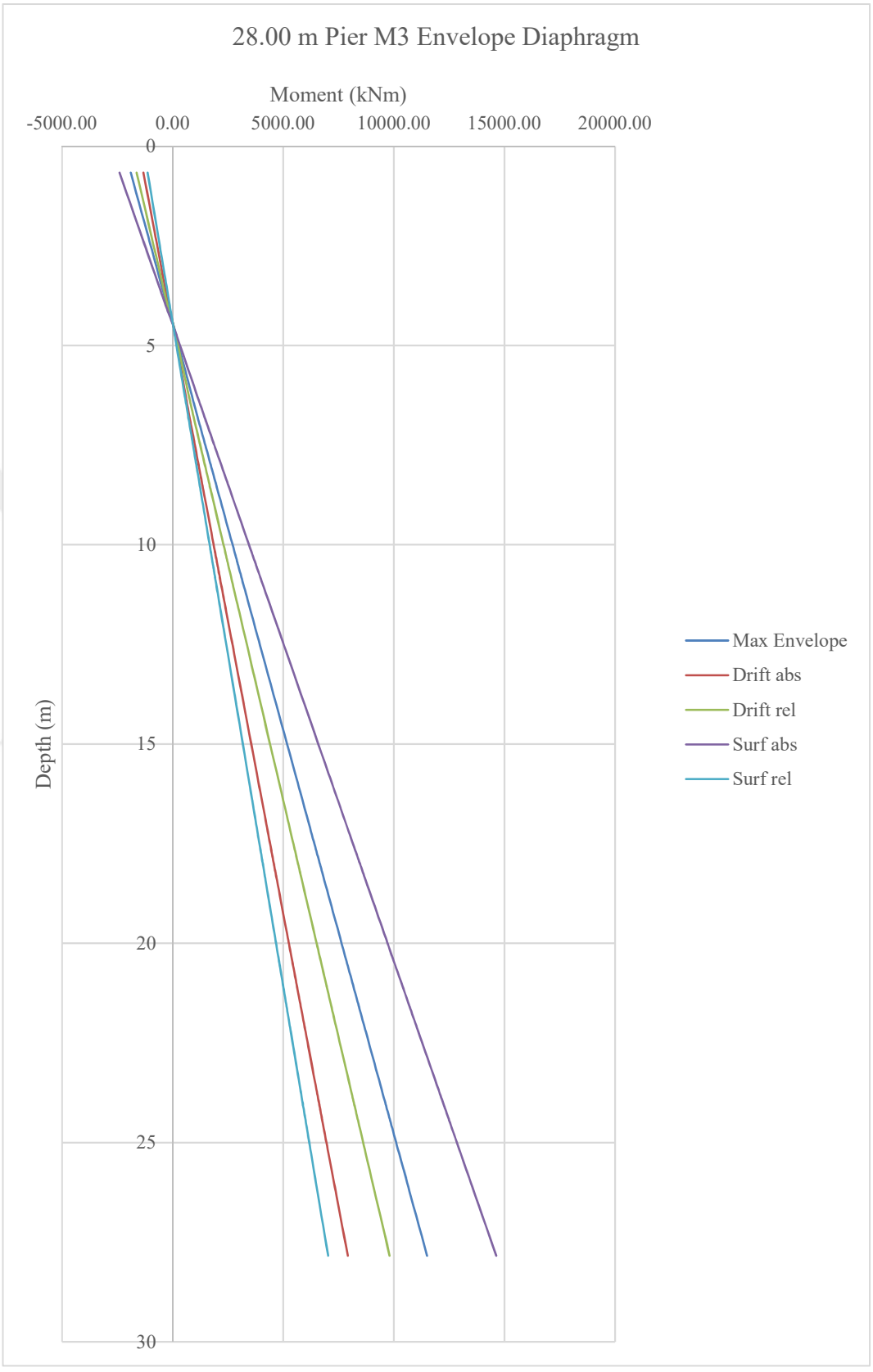

Figure 5.17. Bridge-I 28.00 m pier envelope moment diagram.

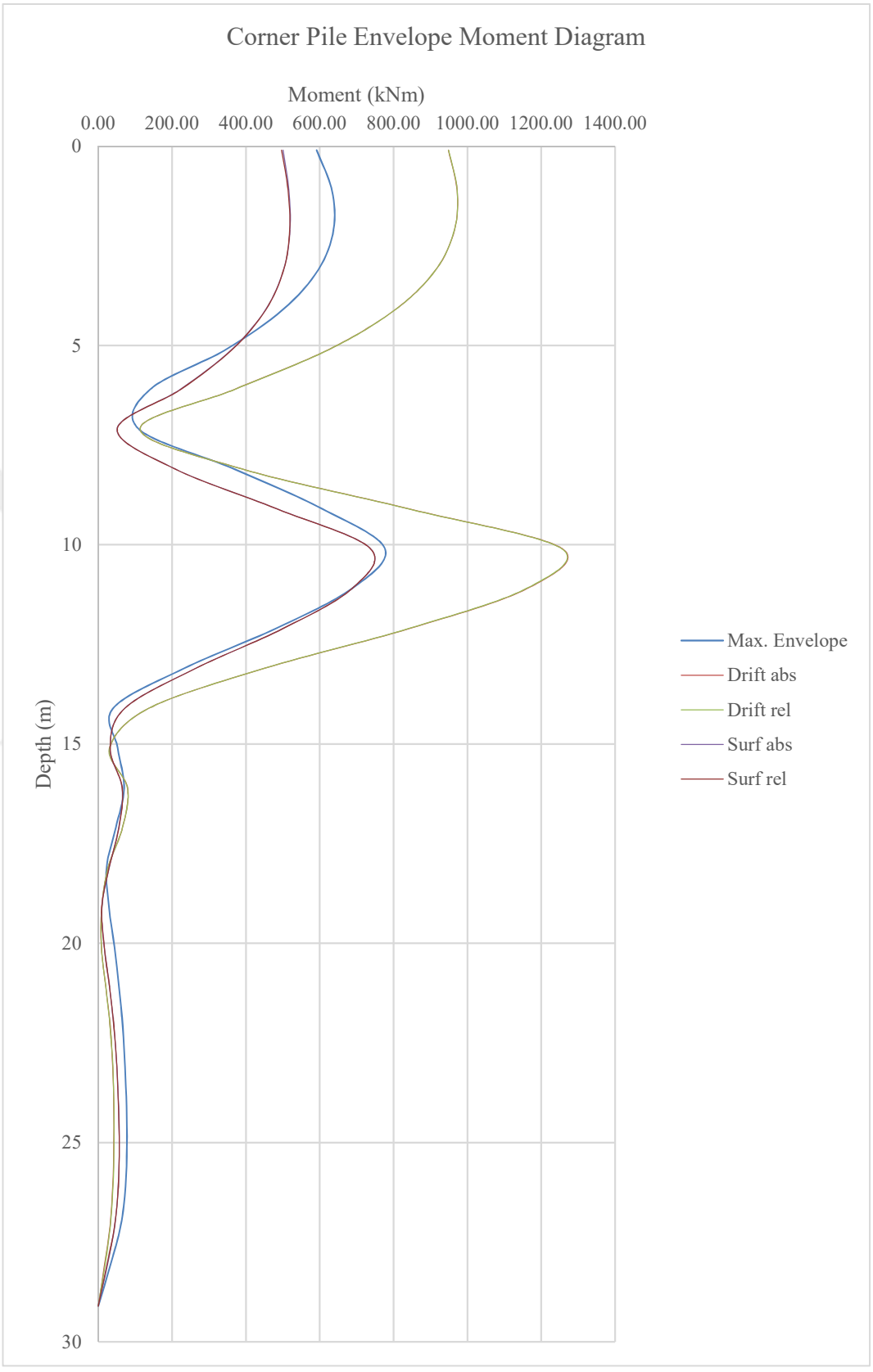

Figure 5.18. Bridge II kinematic interaction envelope moment diagram

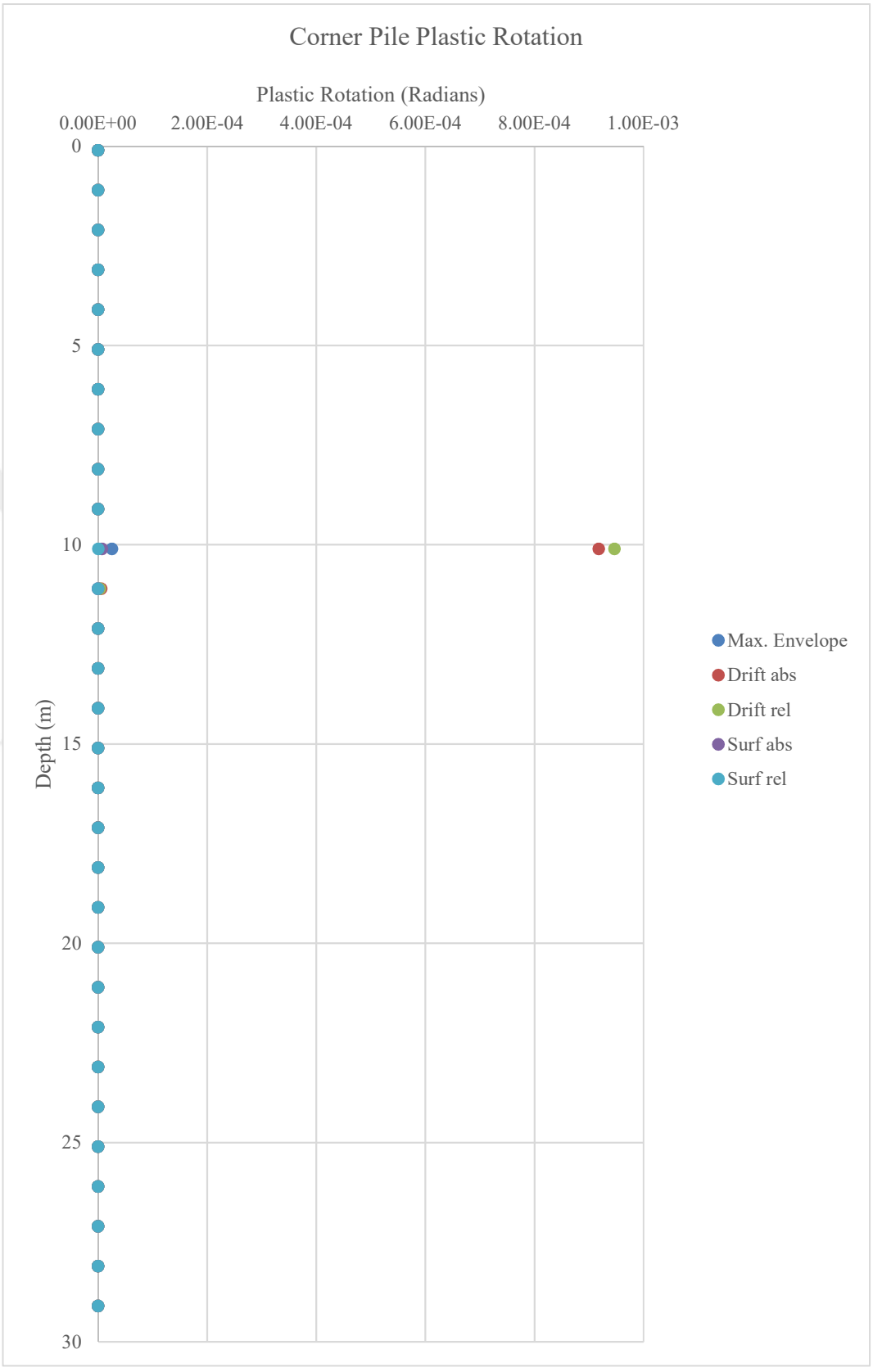

Figure 5.19. Bridge II kinematic interaction plastic hinge rotation.

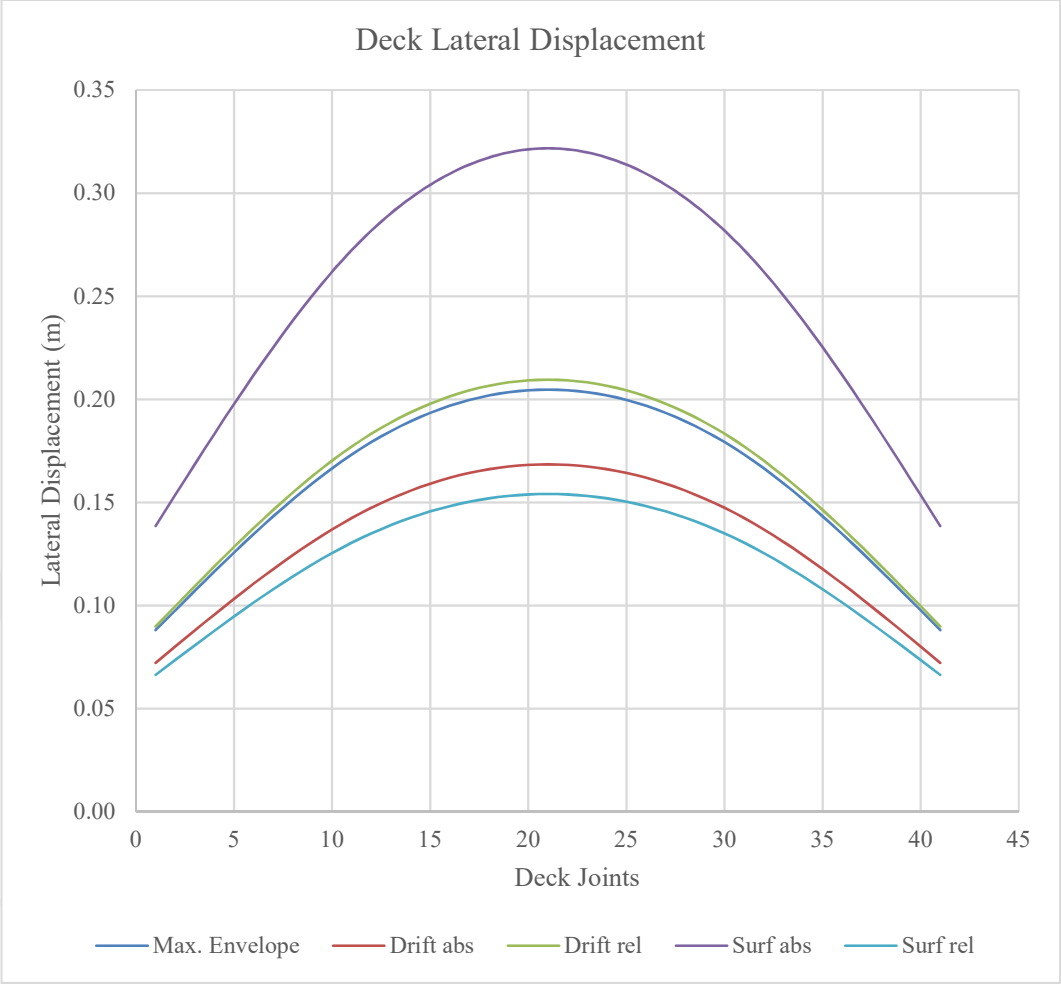

Figure 5.20. Bridge II kinematic interaction deck lateral displacement.

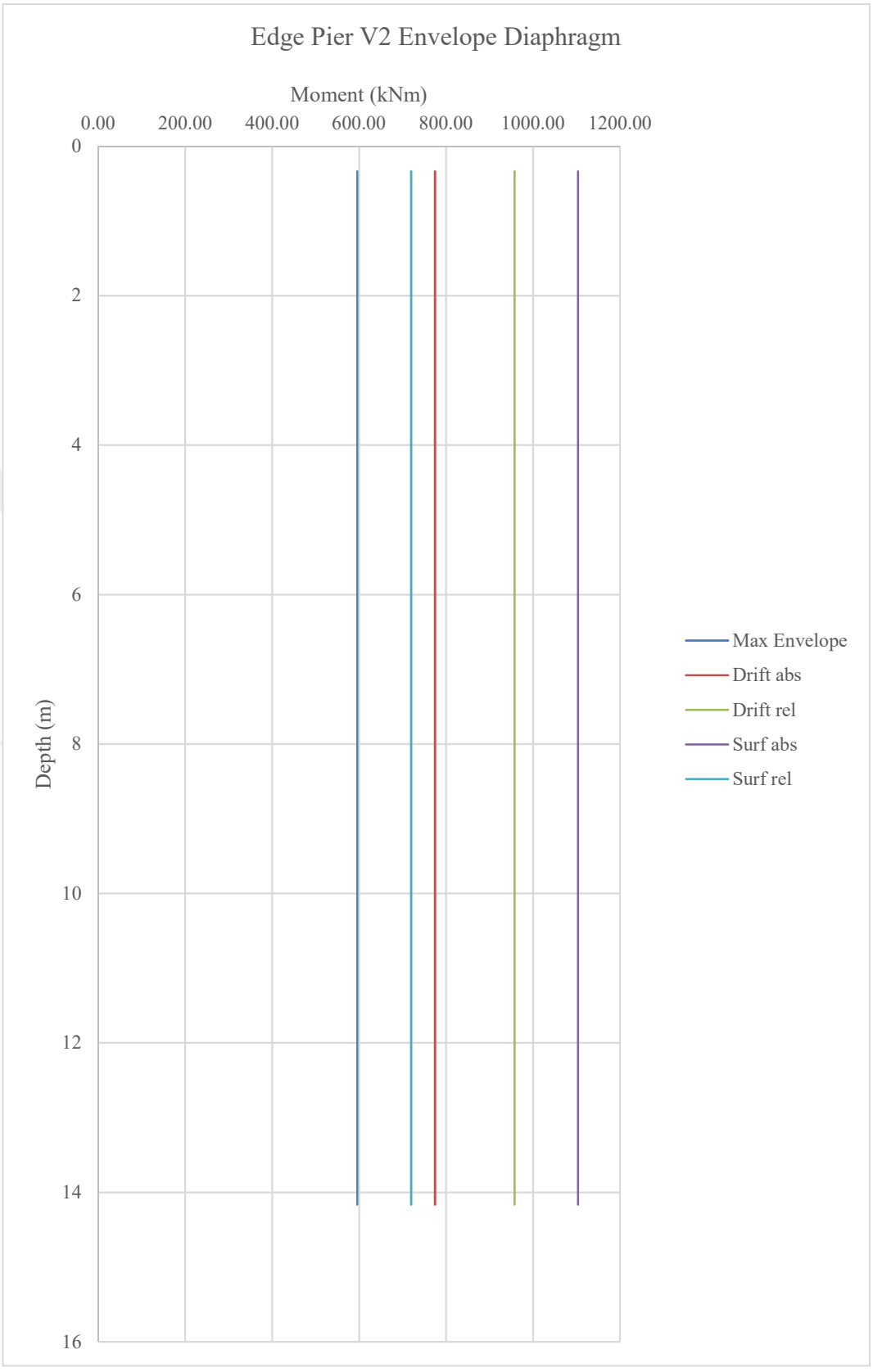

Figure 5.21. Bridge-II edge pier envelope shear force diagram.

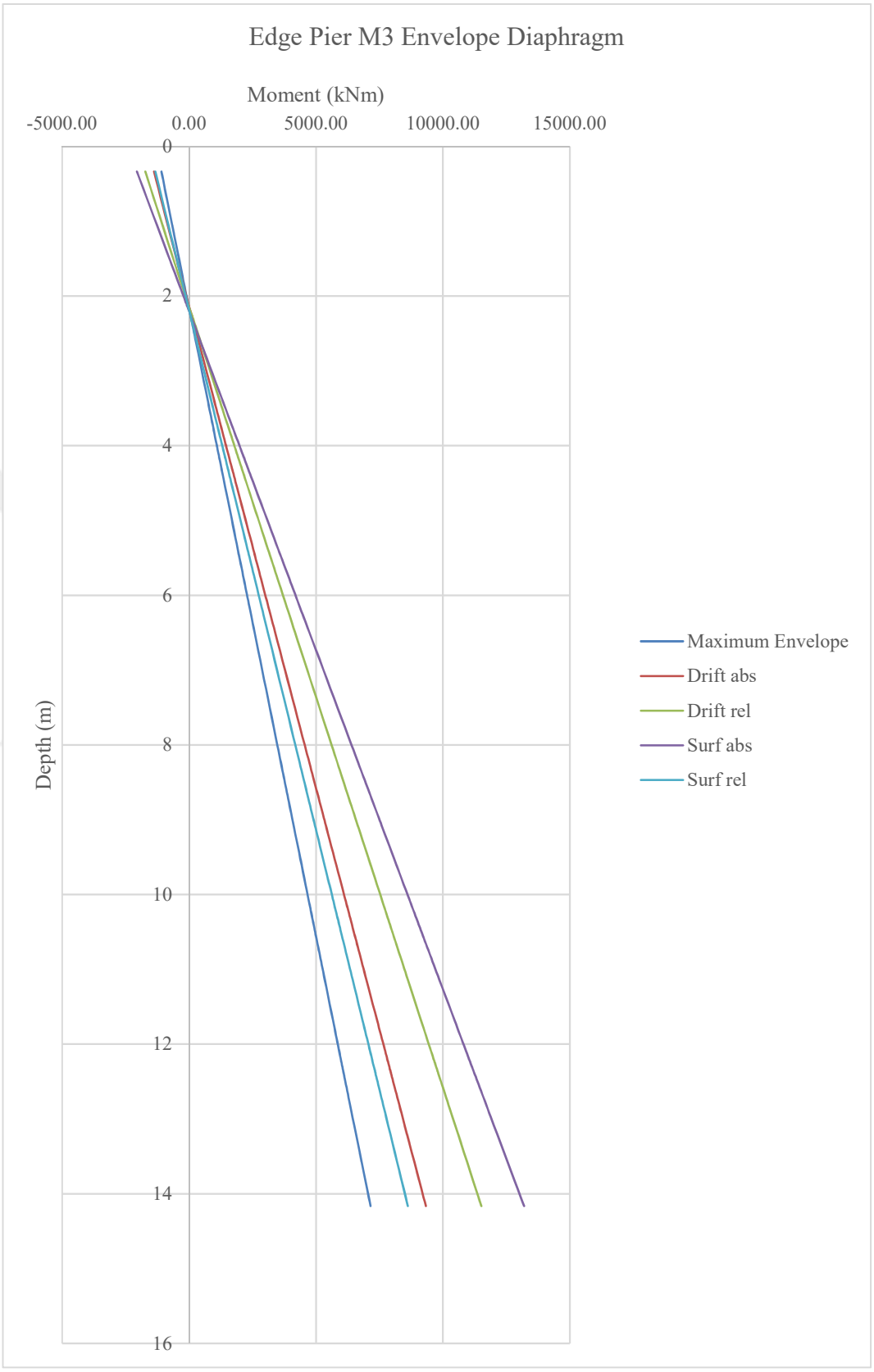

Figure 5.22. Bridge-II edge pier envelope moment diagram.

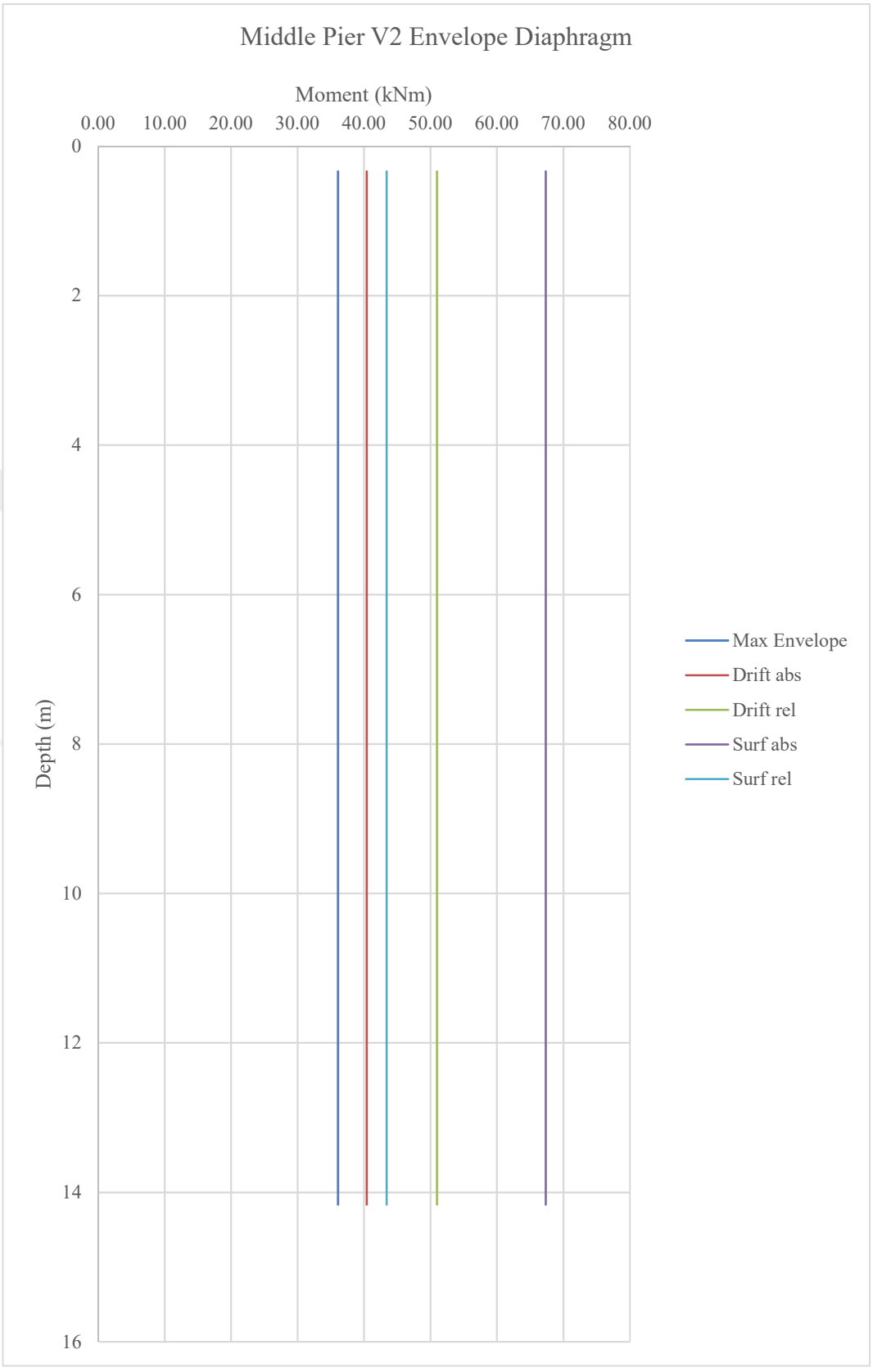

Figure 5.23. Bridge-II middle pier envelope shear force diagram.

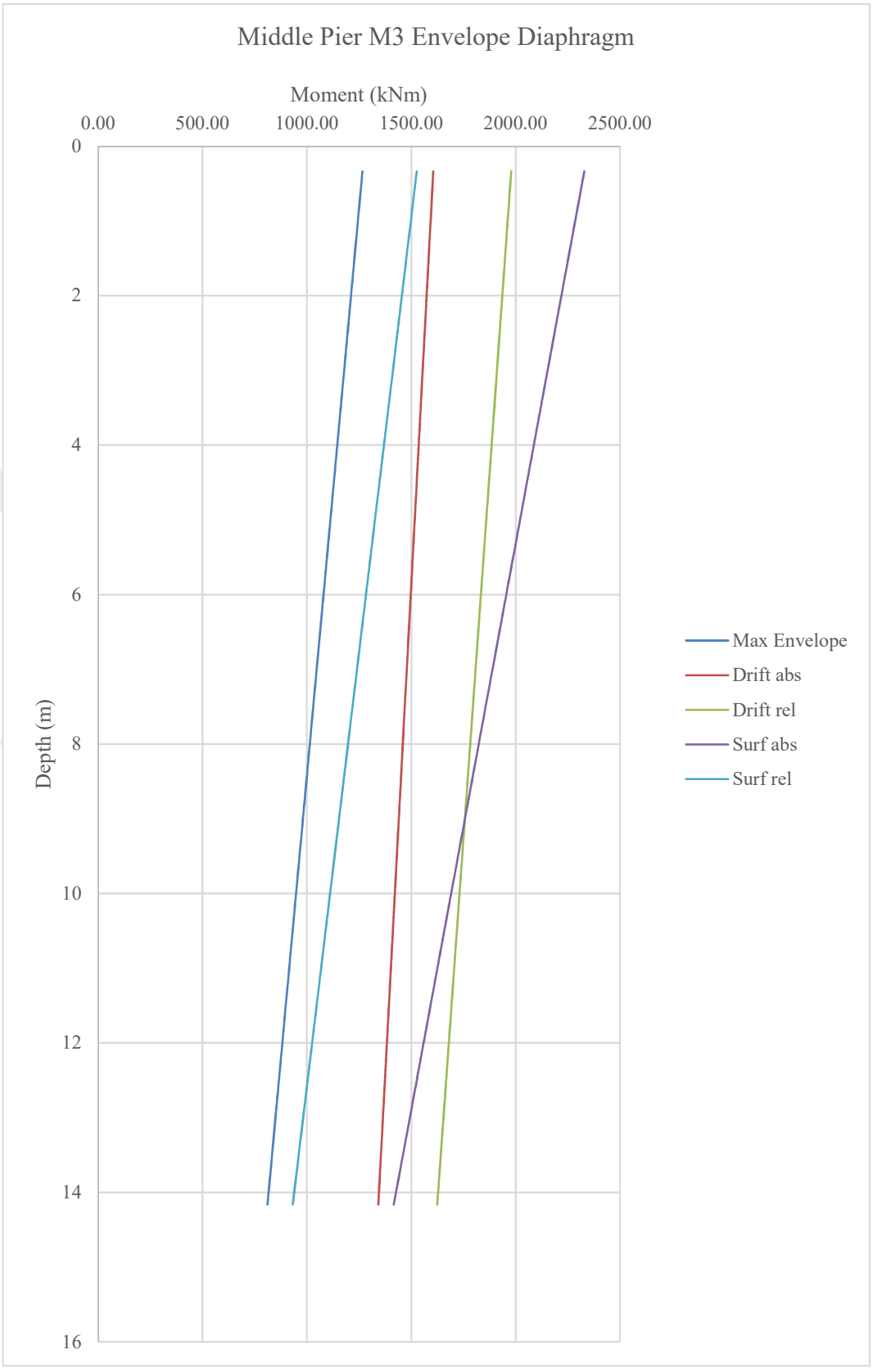

Figure 5.24. Bridge-II middle pier envelope moment diagram.

5.2.2. Inertial Interaction Analysis Results

For the both bridges analyzed, no plastic hinge formation is encountered along the piles. Under kinematic interaction, maximum pile moment occurs around 10m, where the soil stiffness changes sharply. Under inertial interaction it is on the surface level, as expected. For piers, maximum internal forces are encountered at the bottom of the piers, where the pier is connected to the pile-cap. Results are given in Figure 5.25 to Figure 5.38.

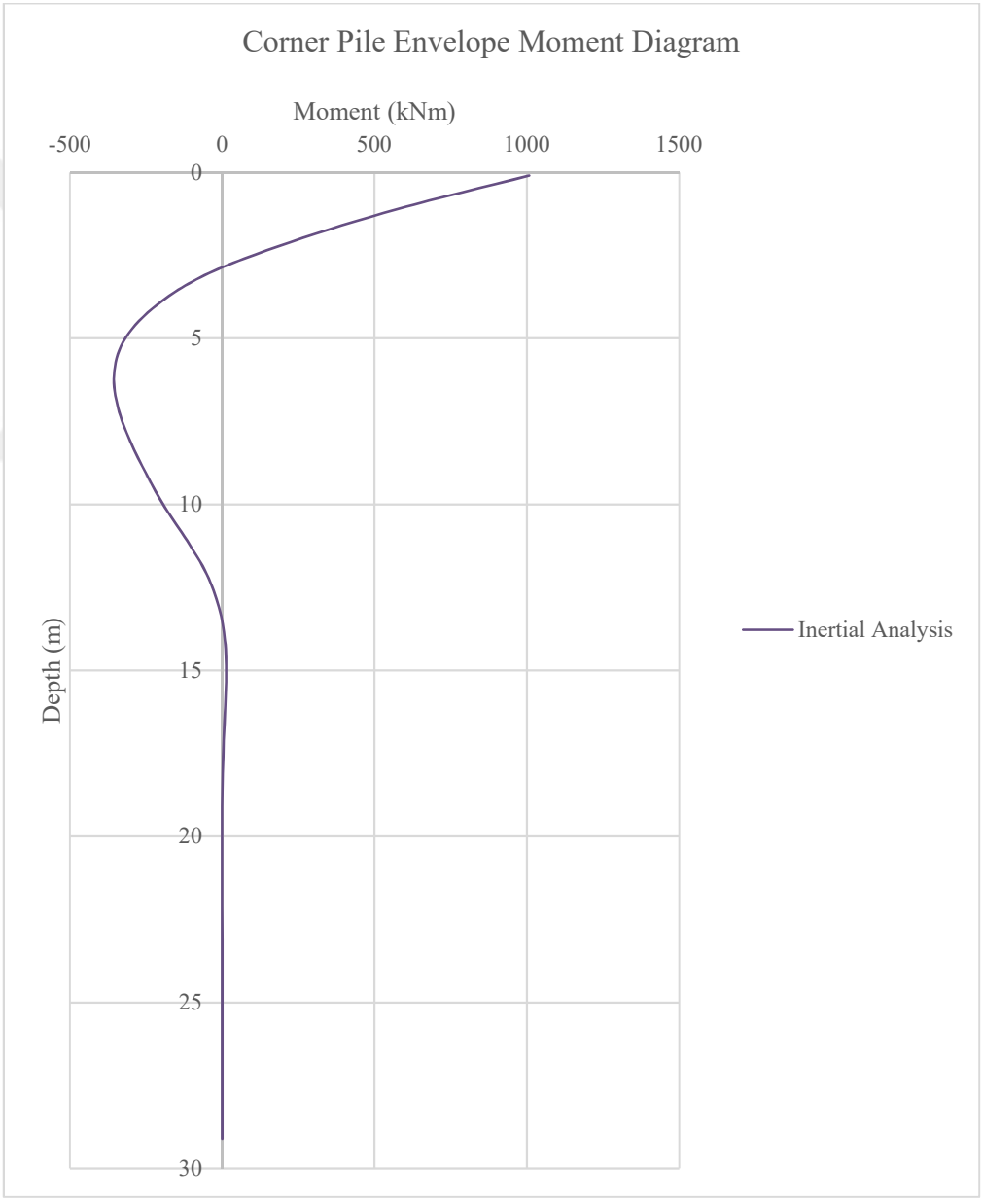

Figure 5.25. Bridge-I inertial interaction pile envelope moment diagram.

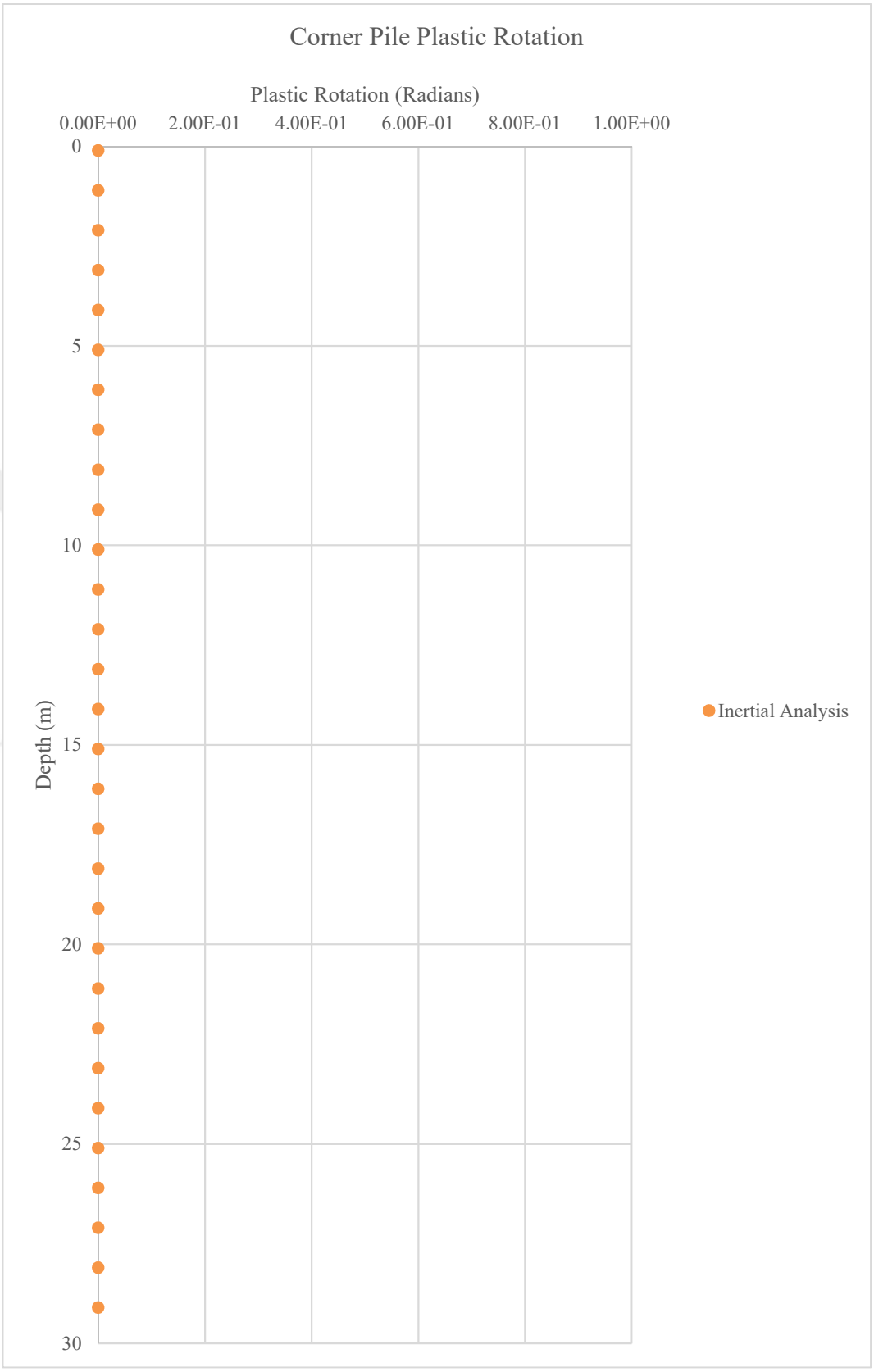

Figure 5.26. Bridge-I inertial interaction plastic hinge rotation.

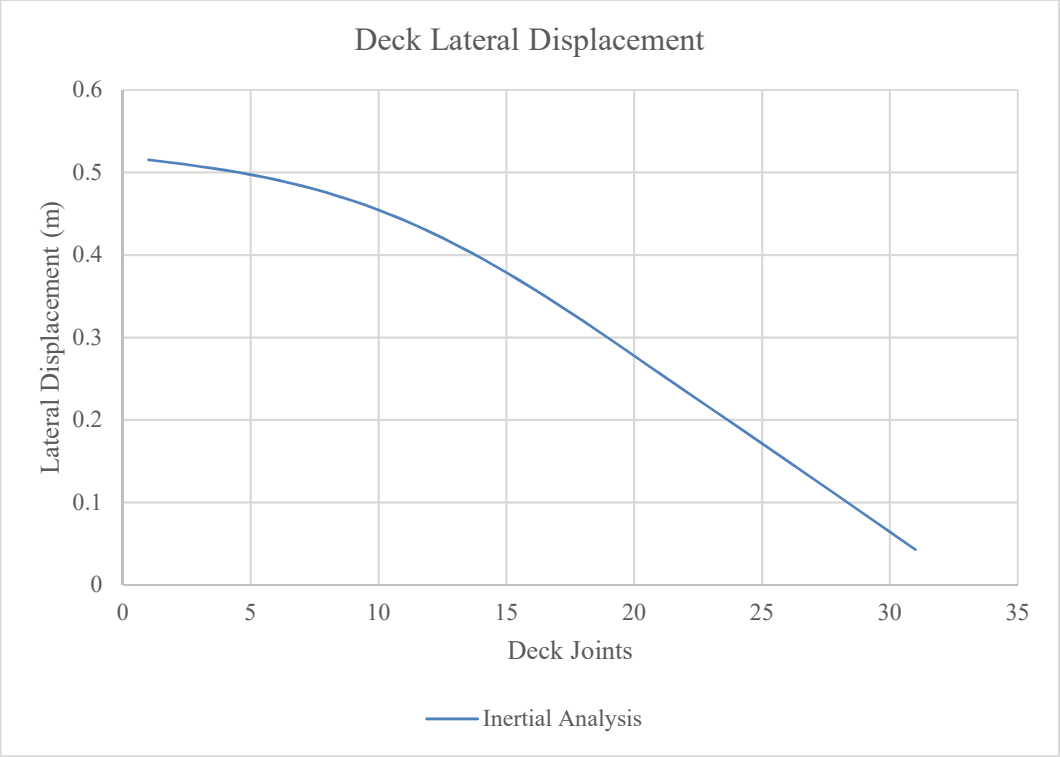

Figure 5.27. Bridge-I inertial interaction deck lateral displacement.

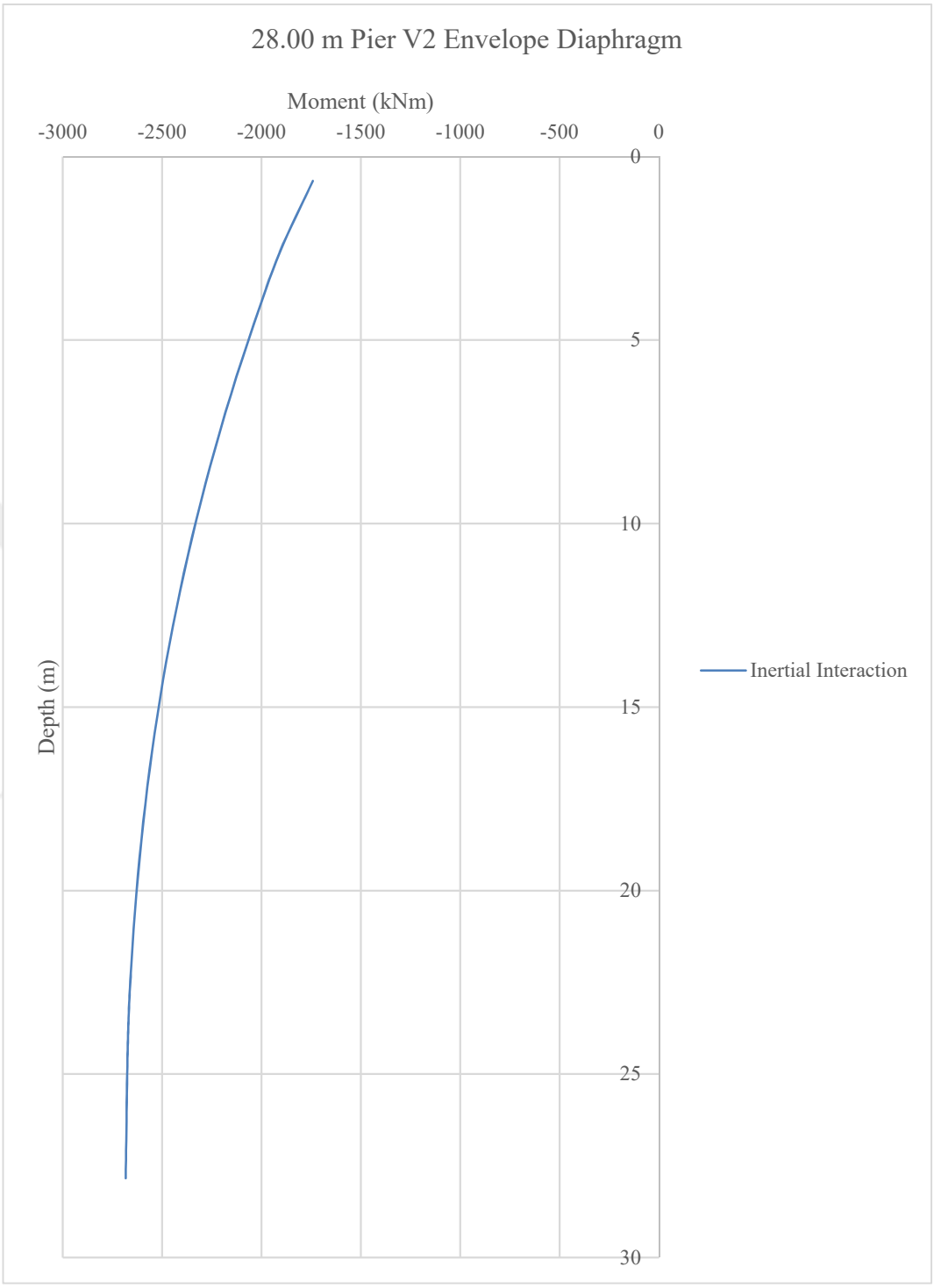

Figure 5.28. Bridge-I inertial interaction 28.00m pier envelope shear force diagram.

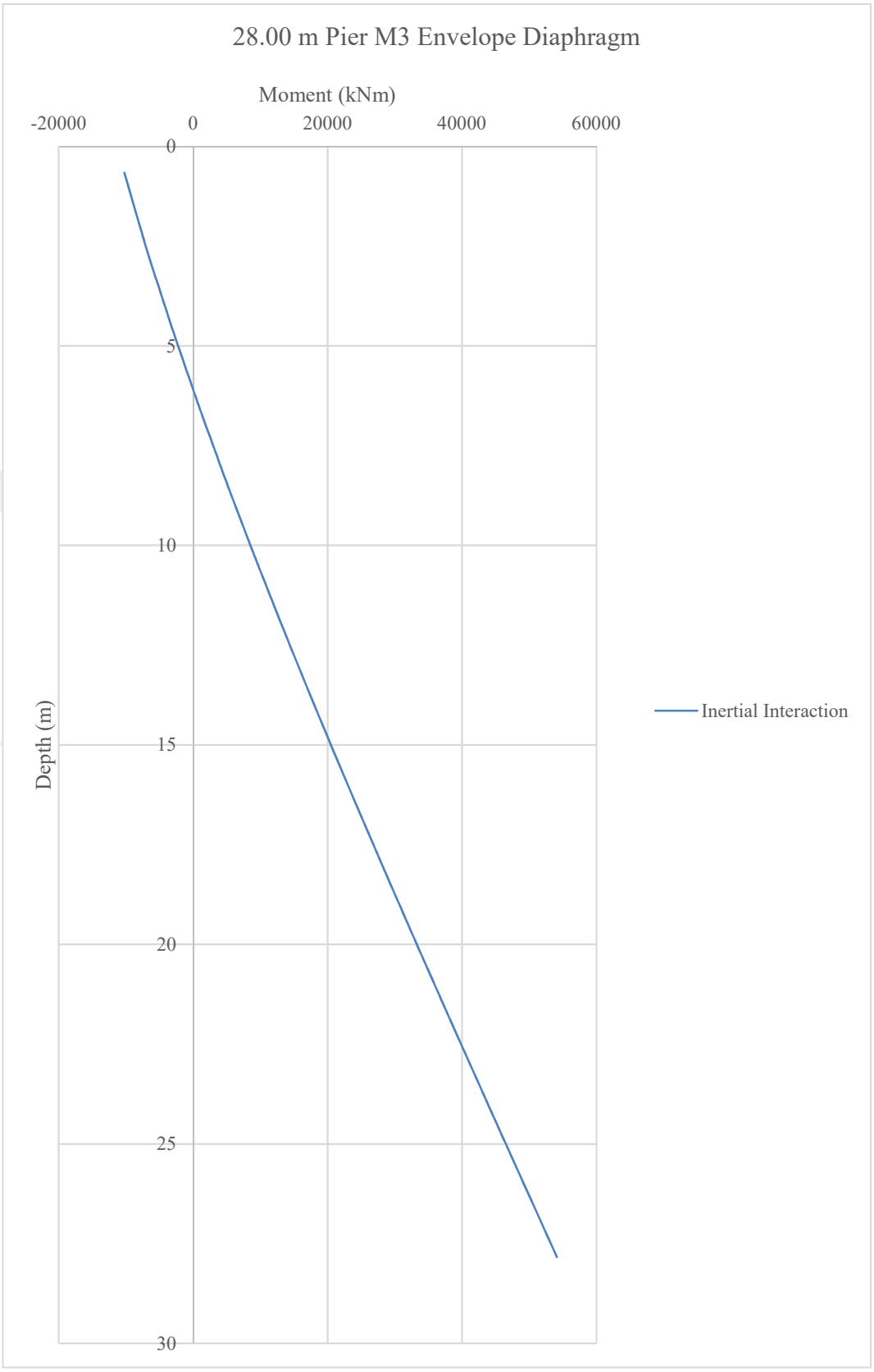

Figure 5.29. Bridge-I inertial interaction 28.00m pier envelope moment diagram.

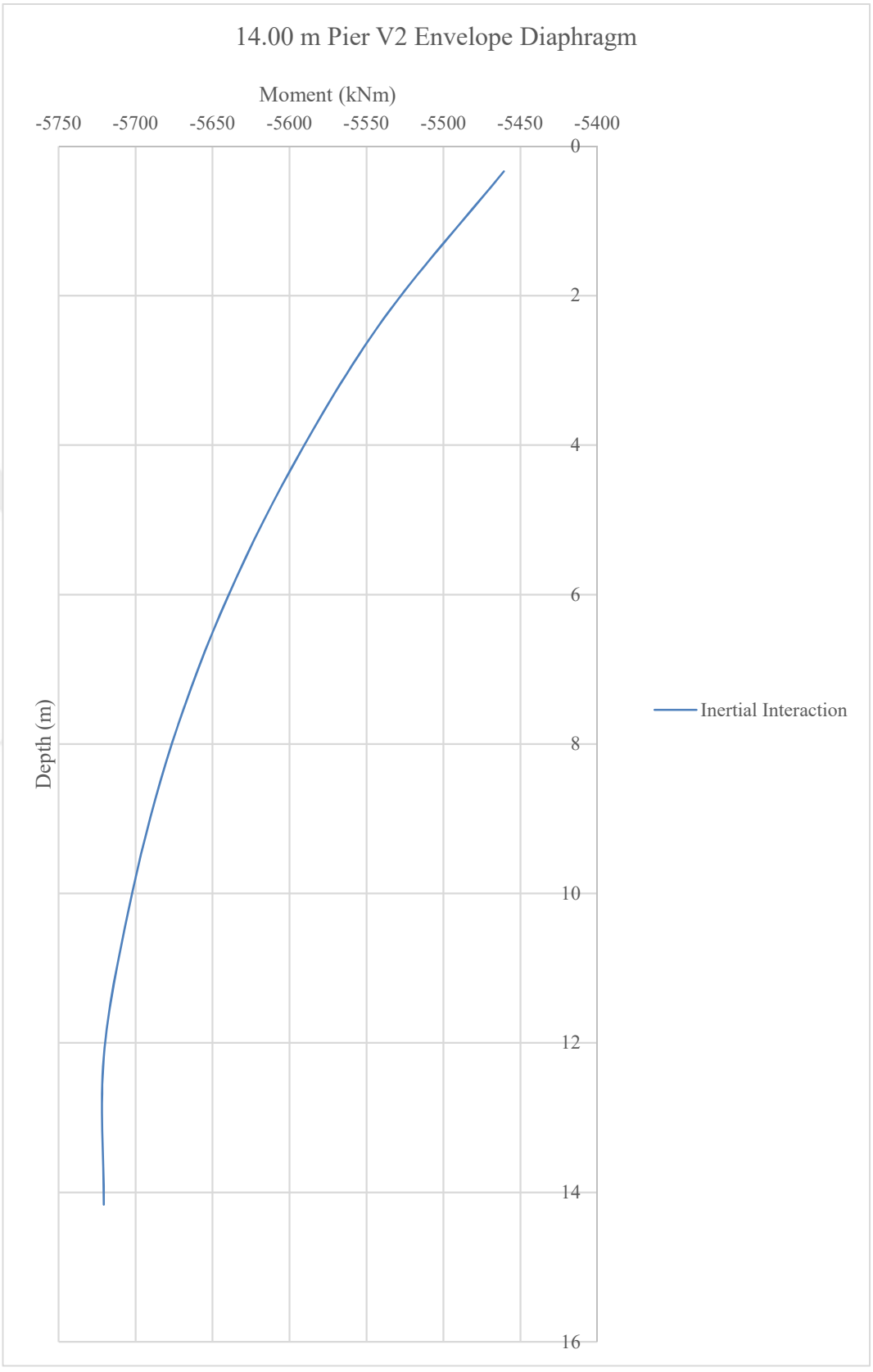

Figure 5.30. Bridge-I inertial interaction 14.00m pier envelope shear force diagram.

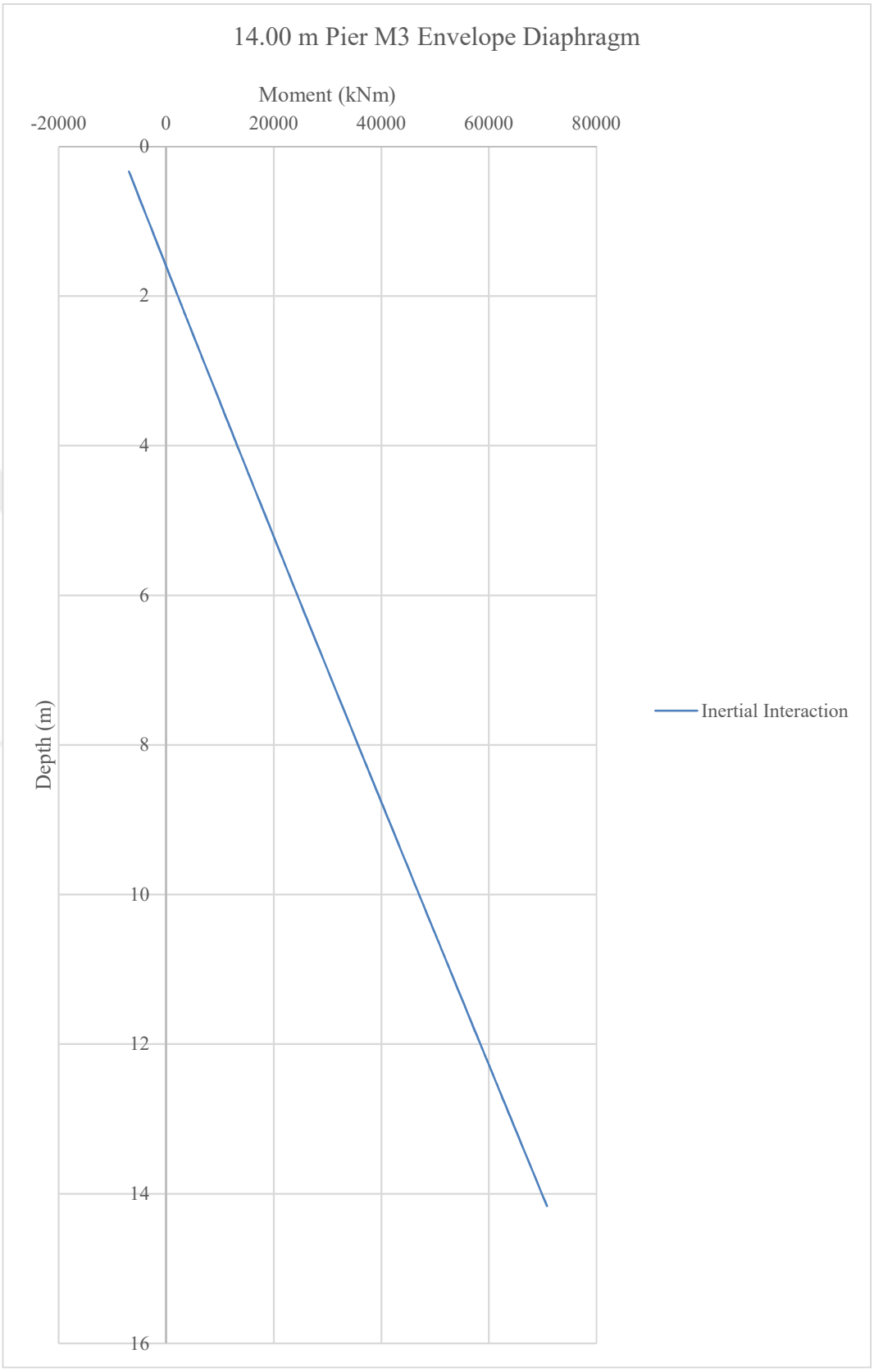

Figure 5.31. Bridge-I inertial interaction 14.00m pier envelope moment diagram.

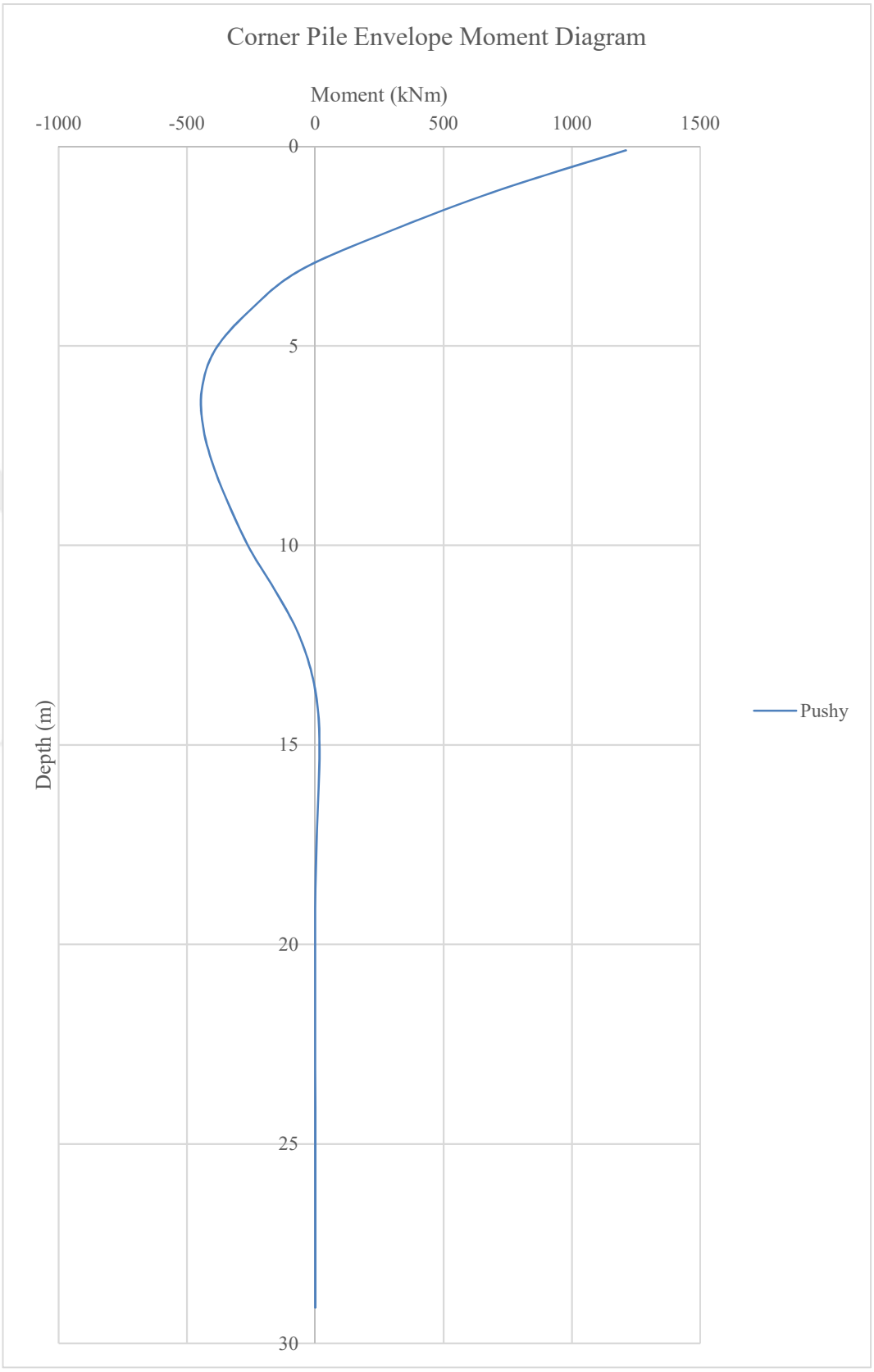

Figure 5.32. Bridge II inertial interaction pile envelope moment diagram.

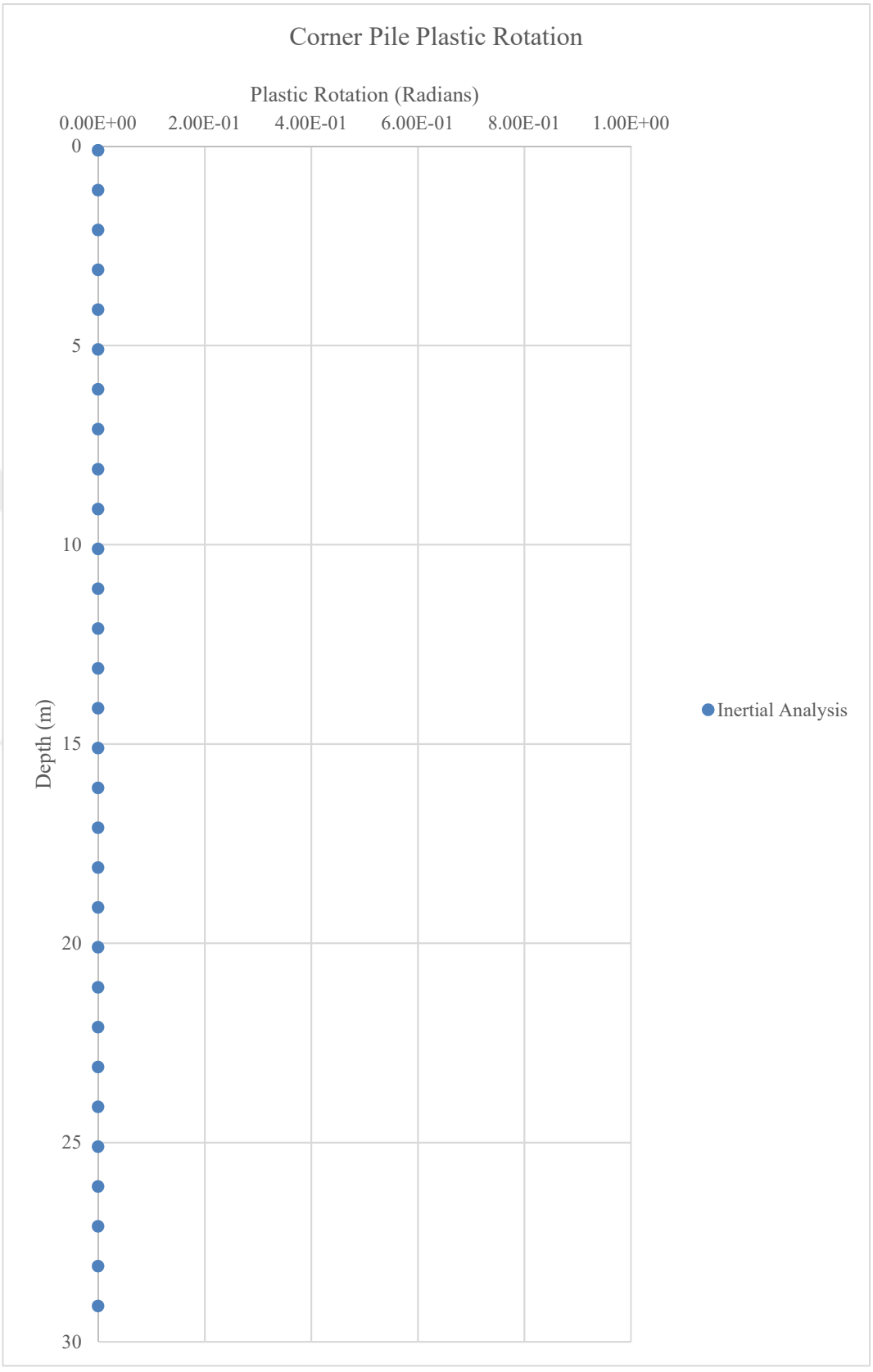

Figure 5.33. Bridge II inertial interaction plastic hinge rotation.

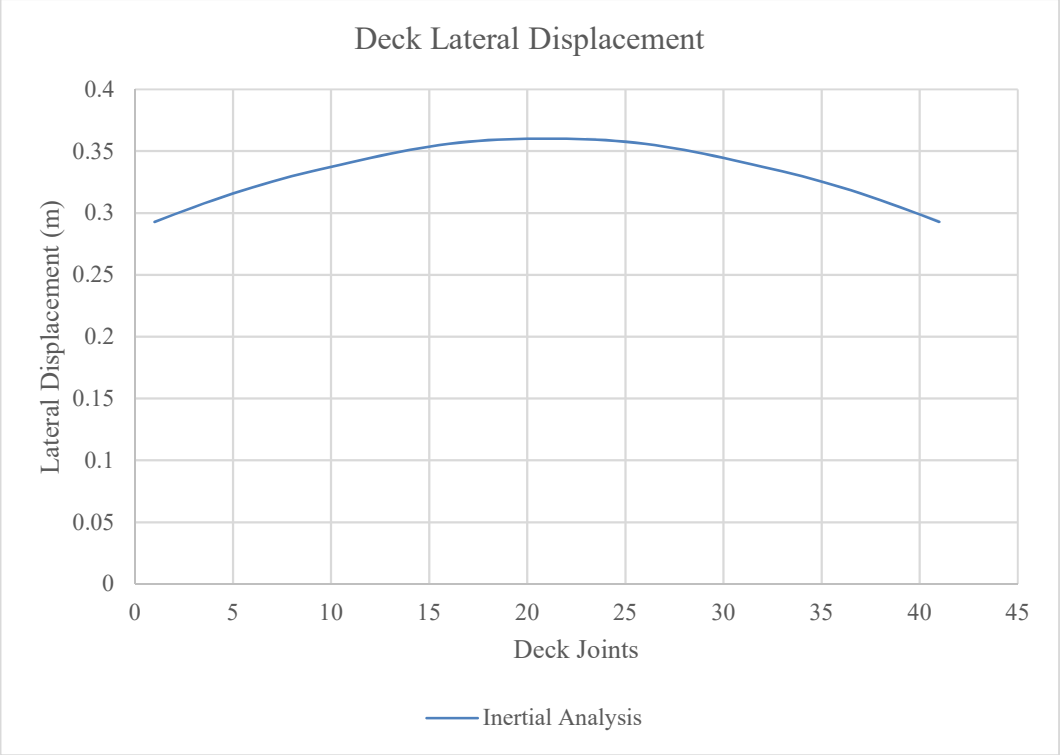

Figure 5.34. Bridge II inertial interaction deck lateral displacement.

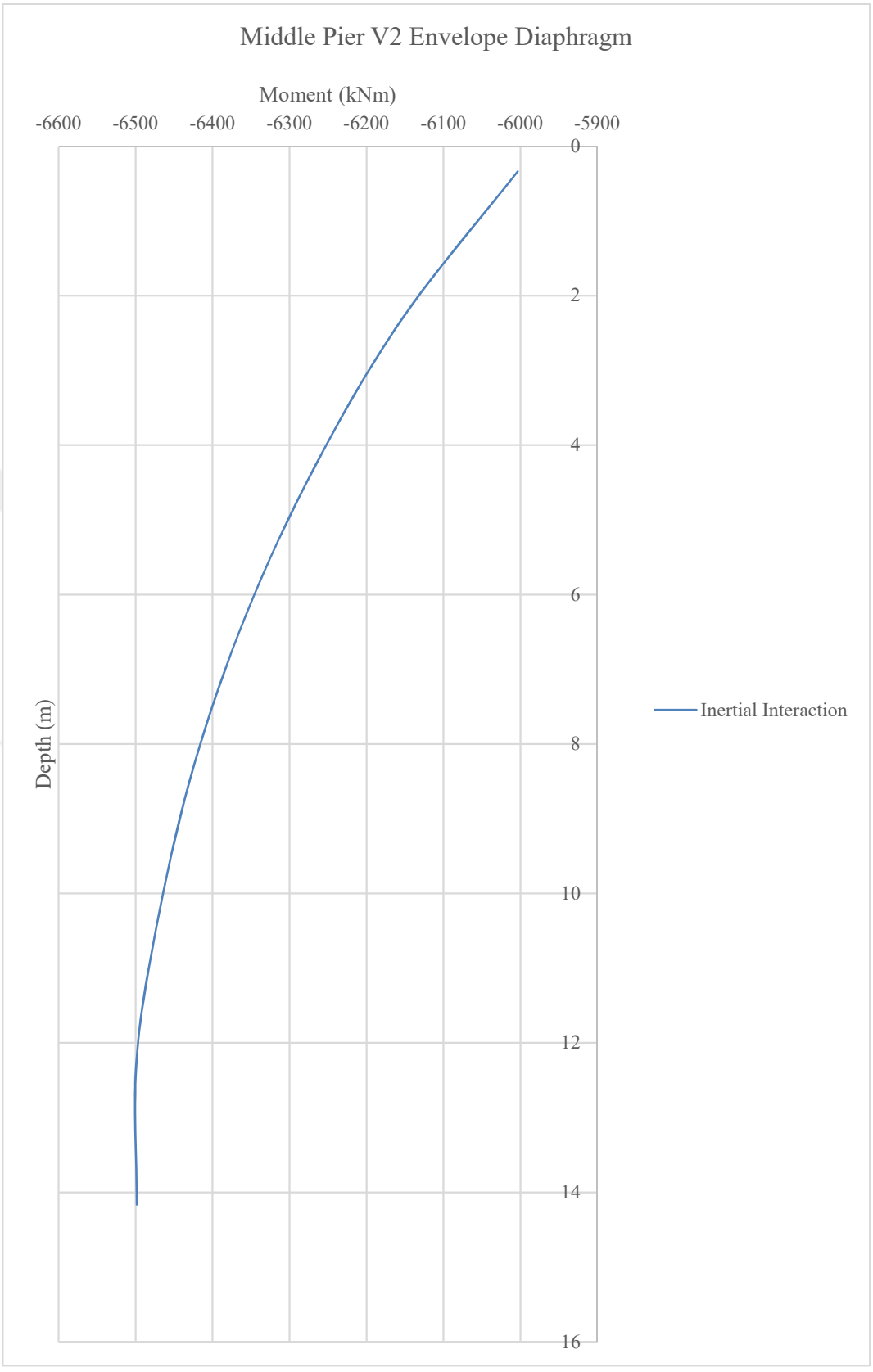

Figure 5.35. Bridge-II inertial interaction middle pier envelope shear force diagram.

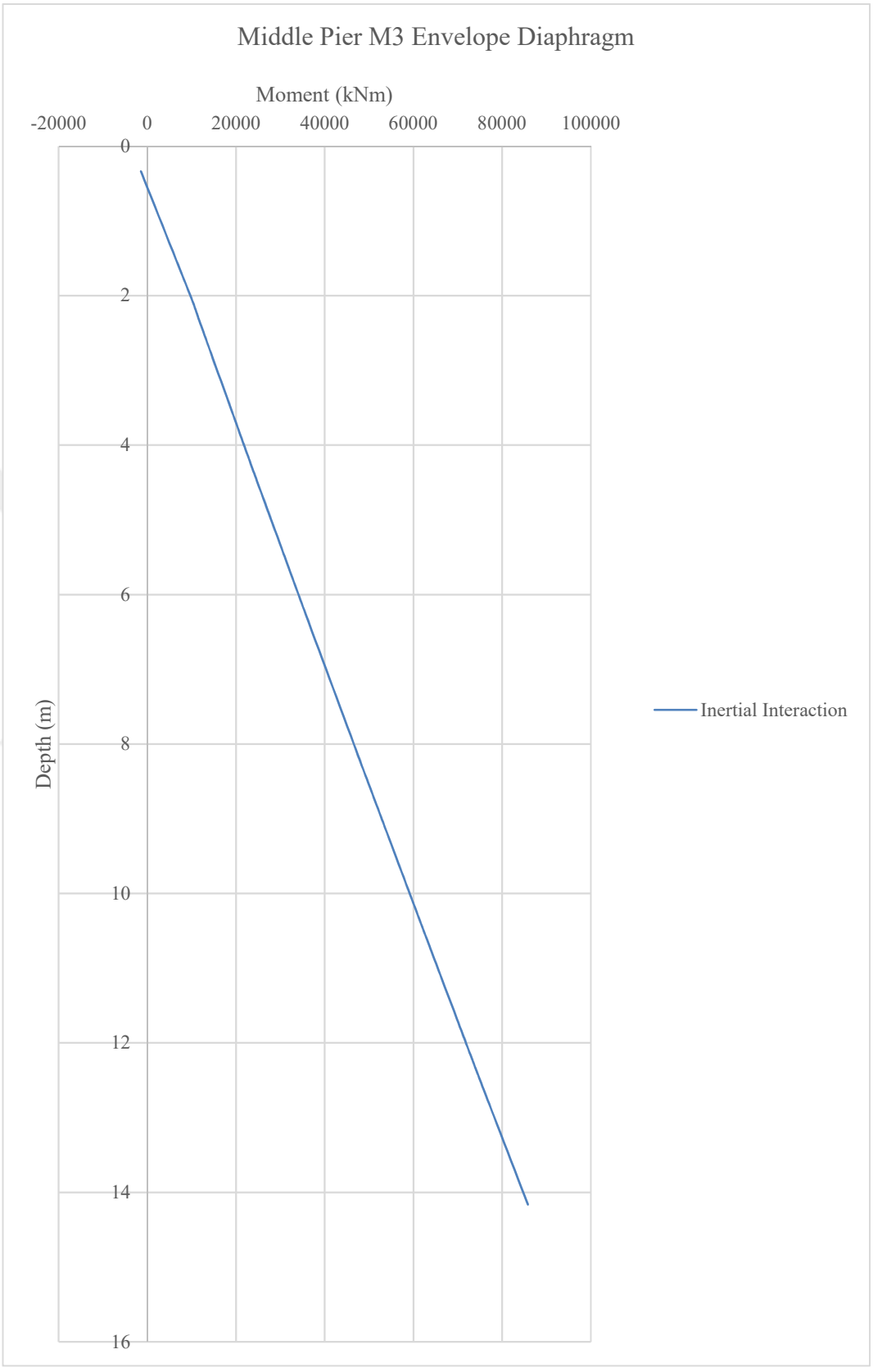

Figure 5.36. Bridge-II inertial interaction middle pier envelope moment diagram.

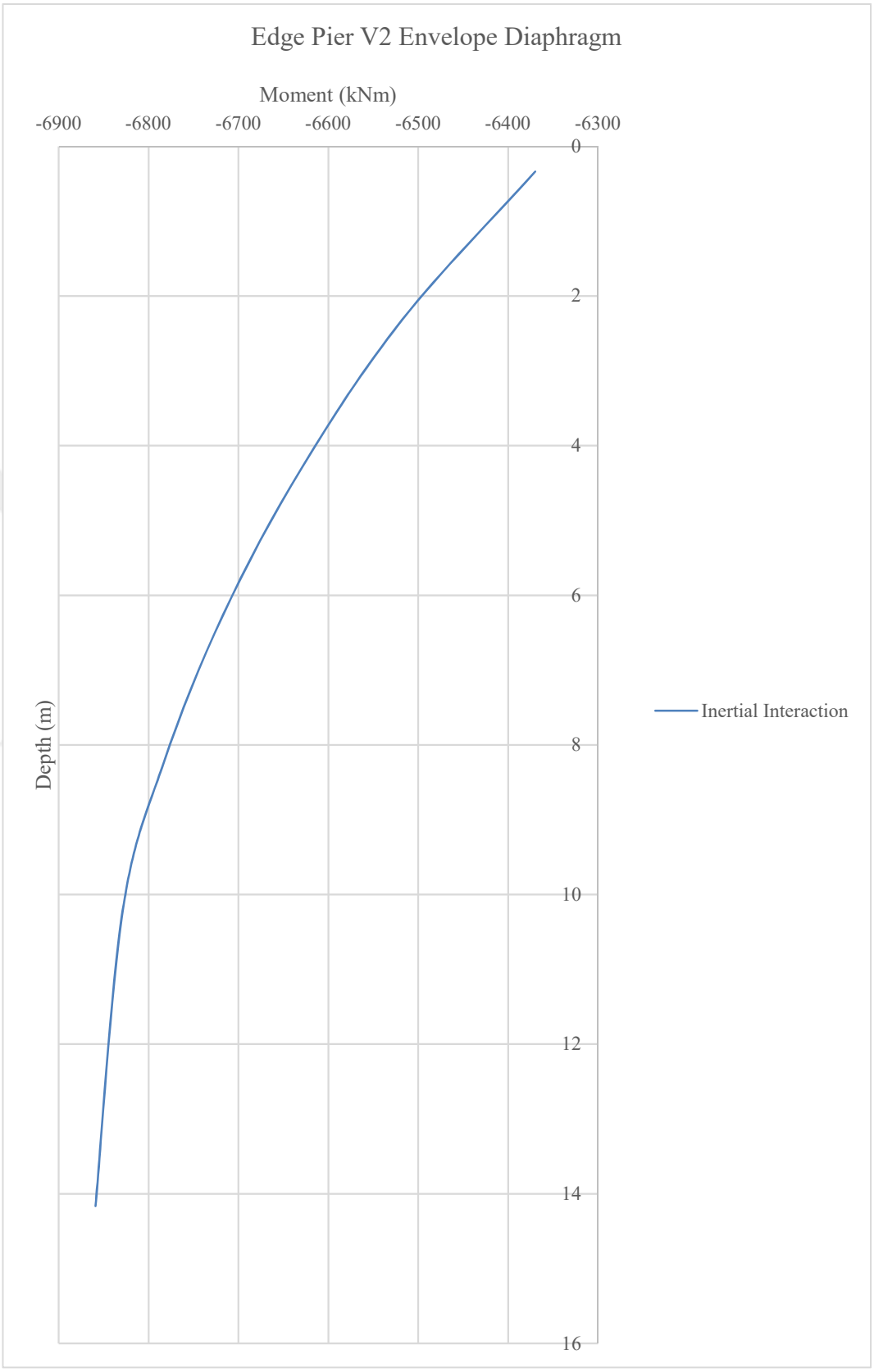

Figure 5.37. Bridge-II inertial interaction edge pier envelope shear force diagram.

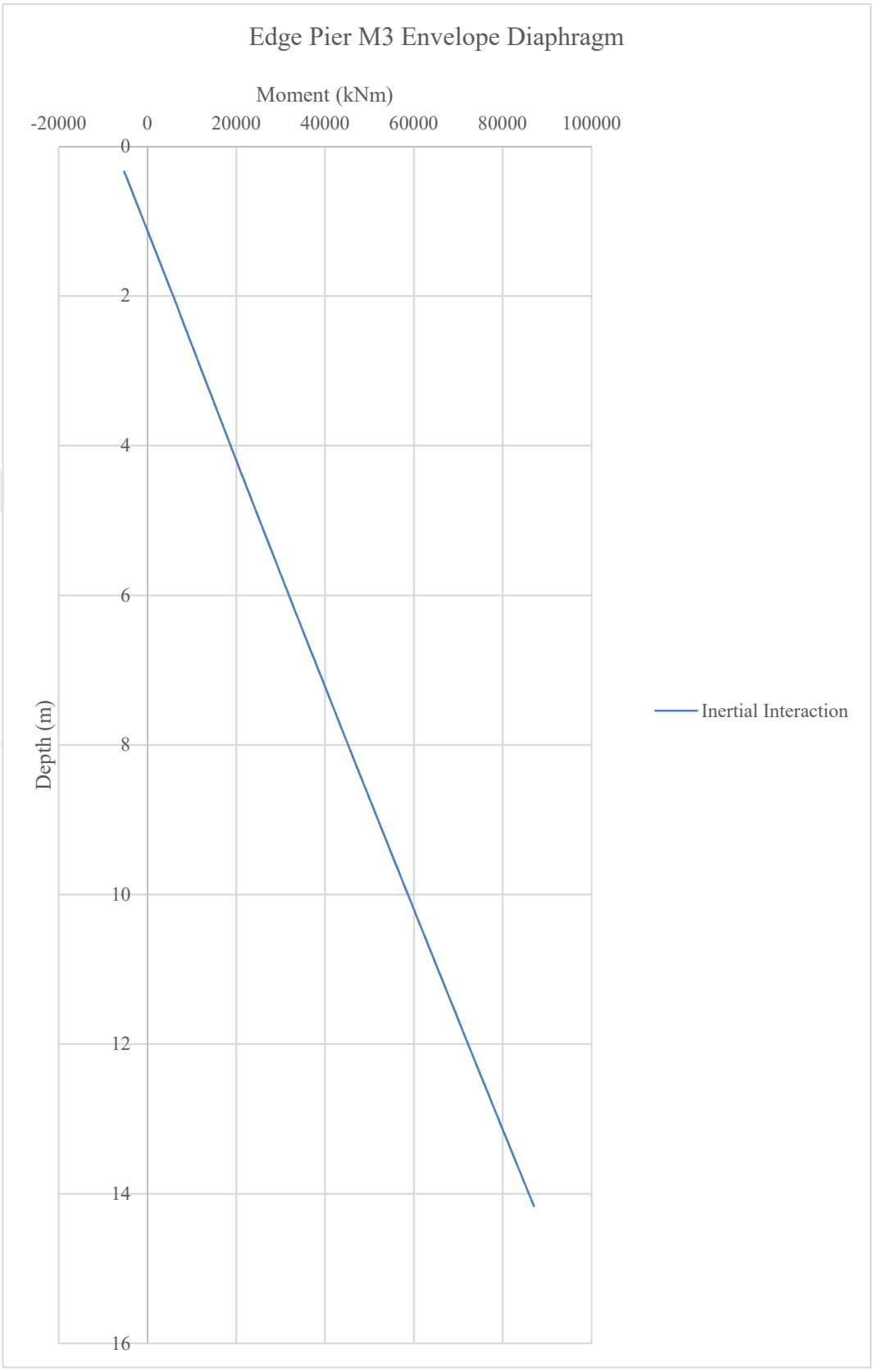

Figure 5.38. Bridge-II inertial interaction edge pier envelope moment diagram.

6. CONCLUSIONS

Results are examined in four distinct categories. Corner pile moment diagrams, corner pile plastic hinge rotations, pier shear force and moment diagrams, and deck displacements are compared from linear and nonlinear analyses. Nonlinear static analysis is composed of kinematic analysis of pile system and inertial analysis of superstructure system. Kinematic and inertial analysis results are combined according to two different methods. First, by adding the results directly, and next by adding the results after multiplying one of them with 0.5. Results for both linear and nonlinear analyses are given simultaneously in Figure 6.1 to Figure 6.14.

Both nonlinear analyses show that bridges undergo plastic rotations at load carrying structural elements. Moreover, internal forces of all structural elements are underestimated by linear analysis, when compared to nonlinear analysis. It can be concluded that nonlinear analysis, including soil-structure-interaction, is crucial for bridge structures founded on soft soil layers.

When the direct method and the substructure method of soil-structure interaction analyses are compared, in terms of internal forces and displacements, simplified static analysis gives somewhat similar results for internal forces throughout the piles and piers, but plastic hinge formations are clearly underestimated unlike the dynamic analysis. For deck displacements, simplified method is a better indicator for regular bridges with equal pier heights. The study shows that it is important to establish seismic demands by kinematic interaction analysis by considering different approaches for structural behavior, as mentioned in Section 4.3.1. Except the rotations developed throughout the pile length, it is possible to use simplified soil-structure interaction method, instead of dynamic analysis, for determining the pile internal forces for regular bridges.

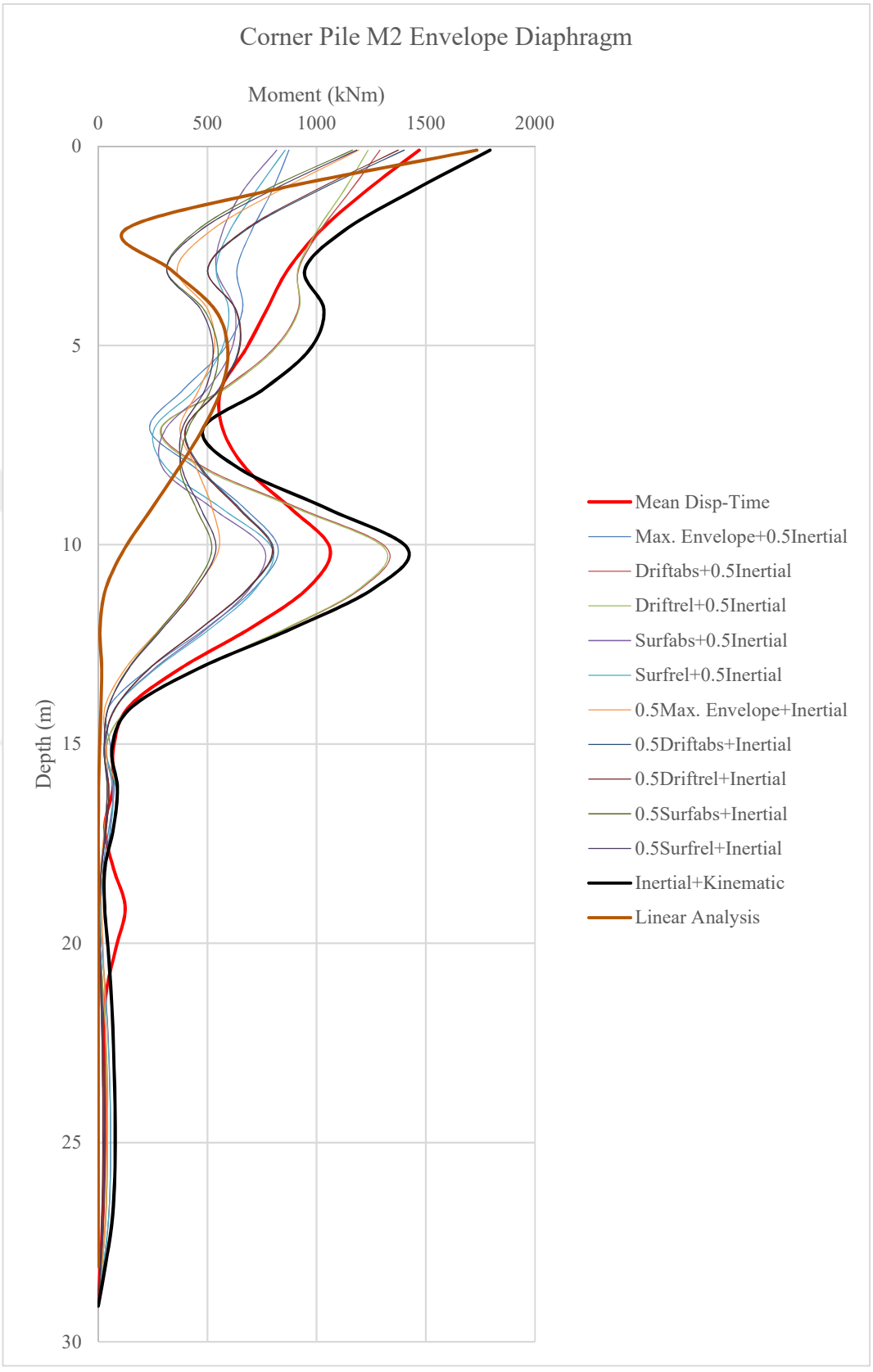

Figure 6.1. Bridge-I pile envelope moment diagram comparison.

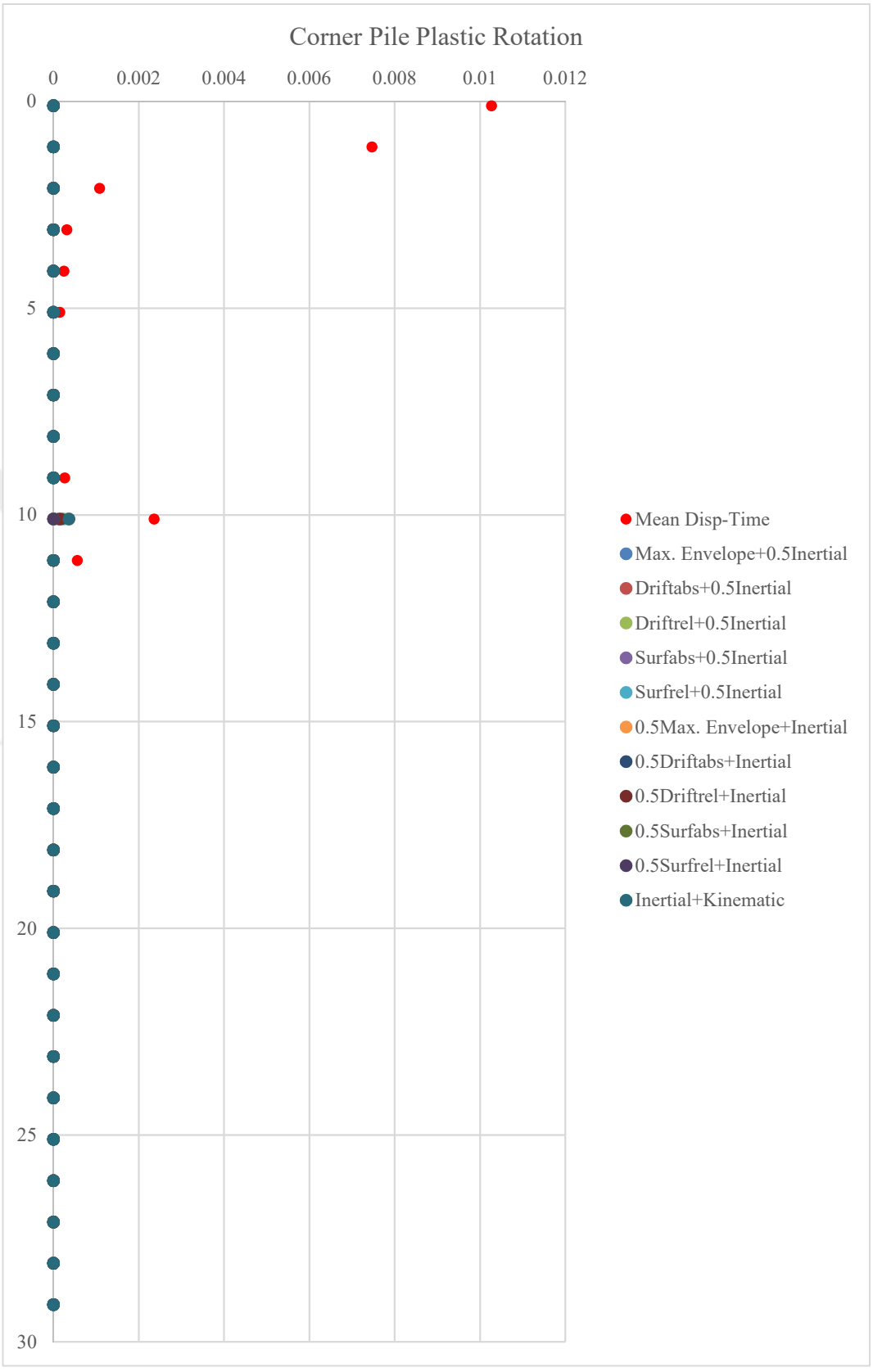

Figure 6.2. Bridge-I corner pile plastic rotation comparison.

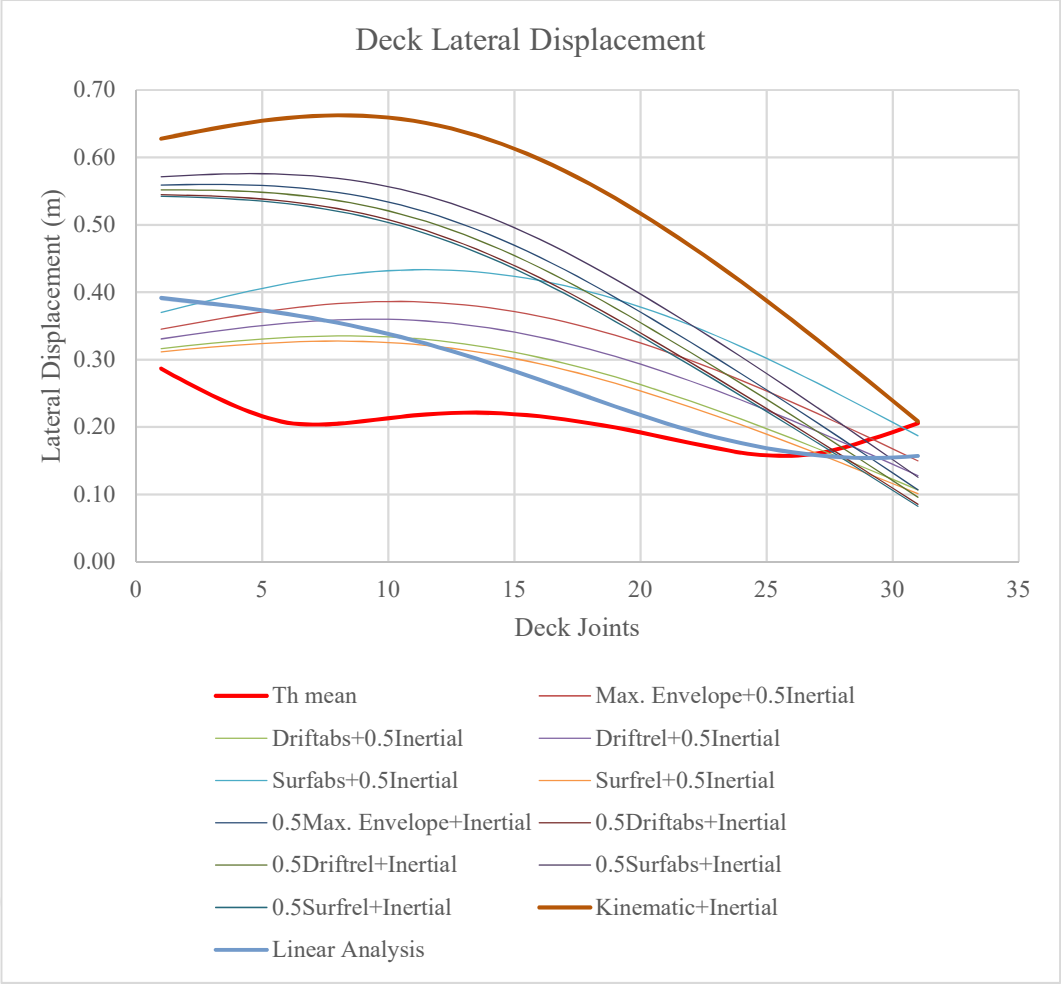

Figure 6.3. Bridge-I deck lateral displacement comparison.

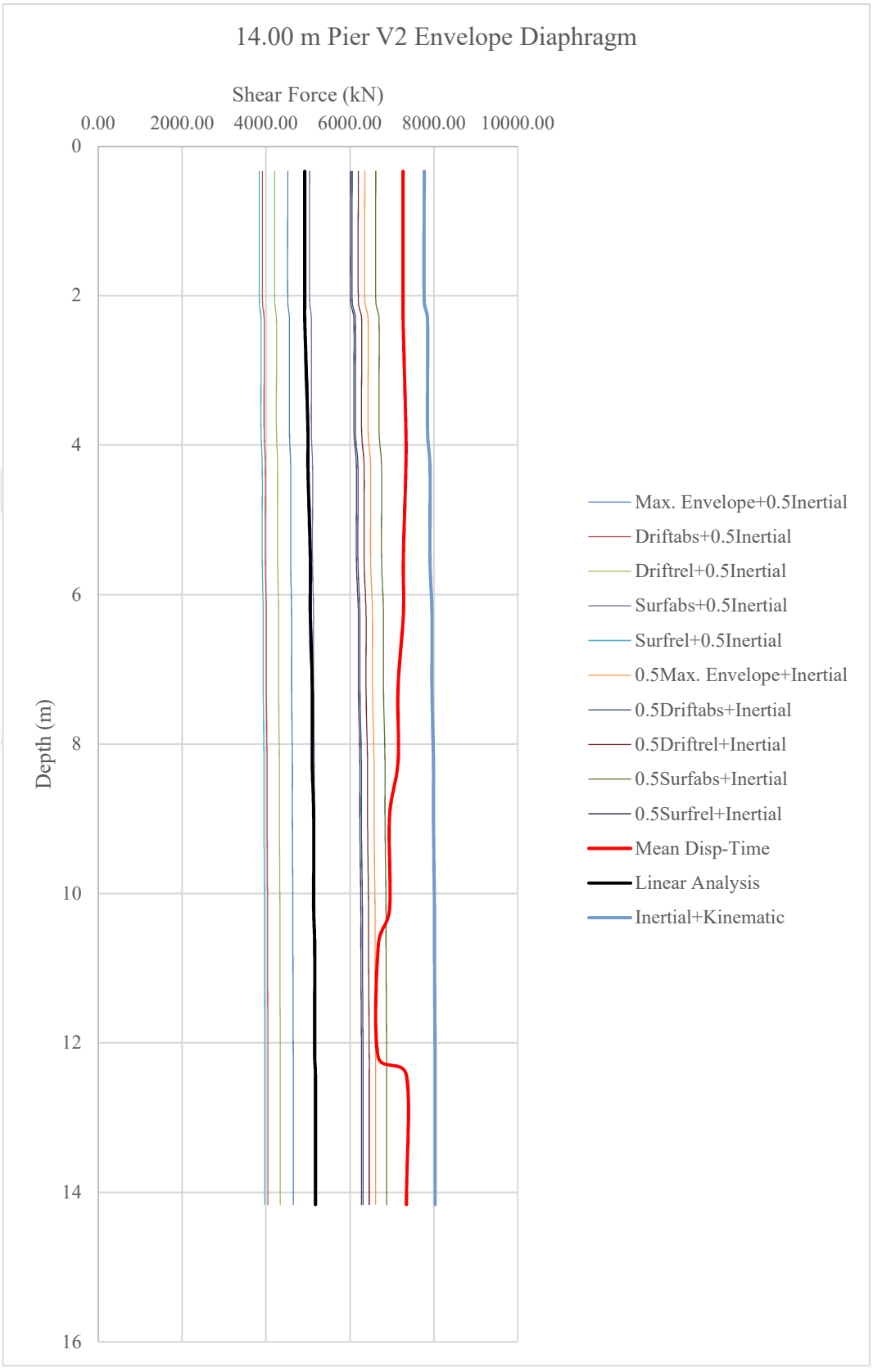

Figure 6.4. Bridge-I 14.00 m pier envelope shear force diagram comparison.

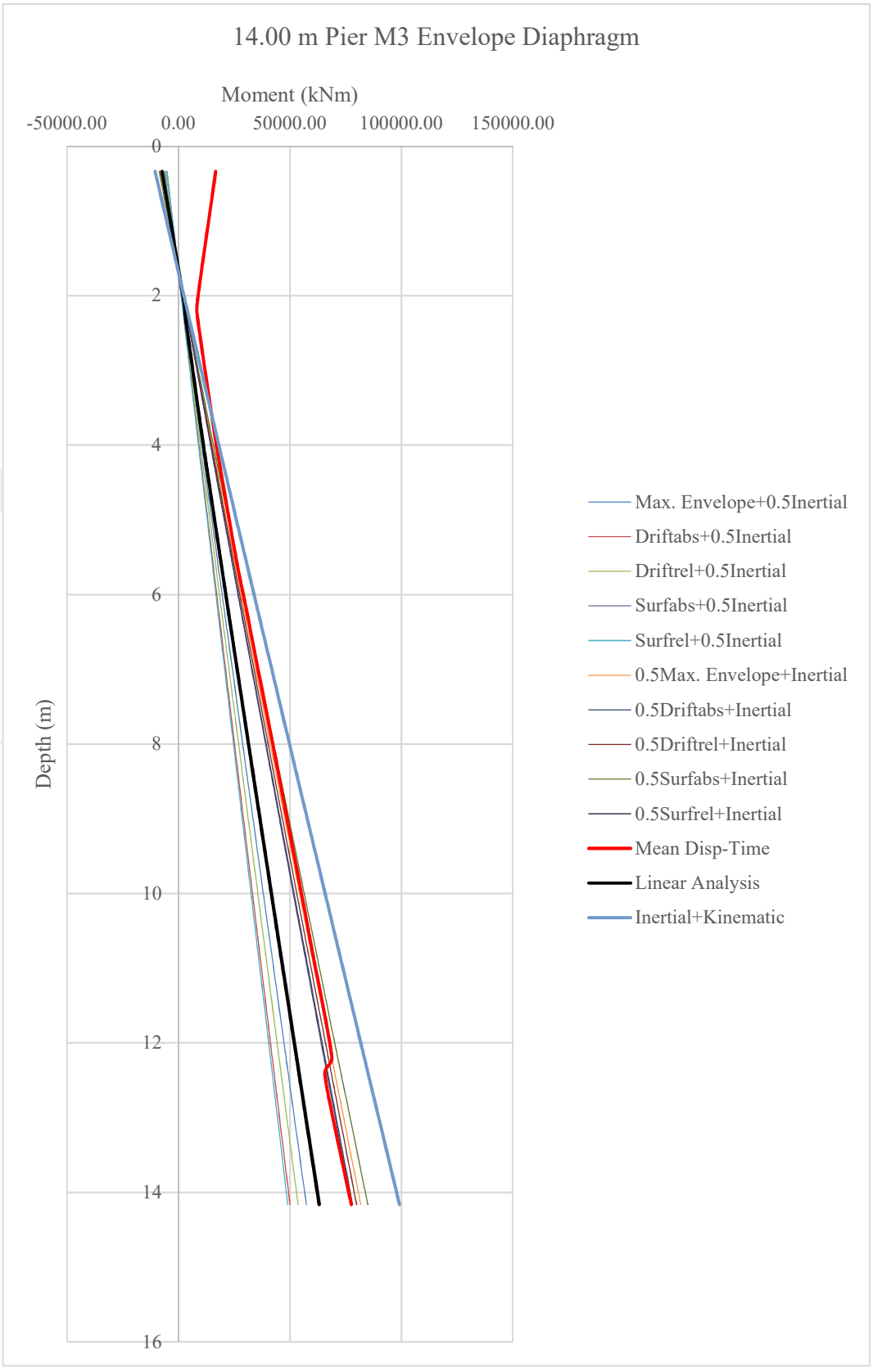

Figure 6.5. Bridge-I 14.00 m pier envelope moment diagram comparison.

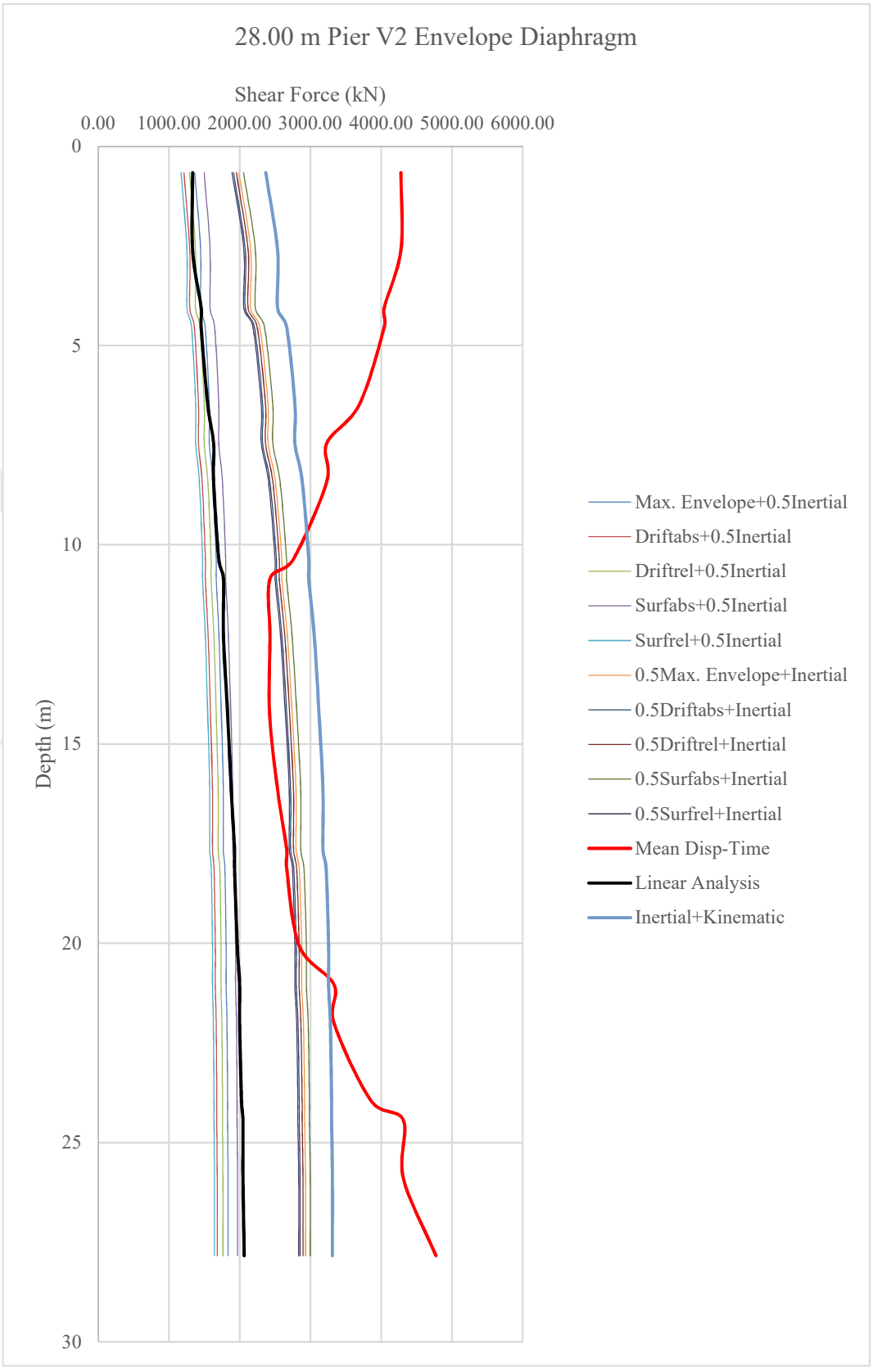

Figure 6.6. Bridge-I 28.00 m pier envelope shear force diagram comparison.

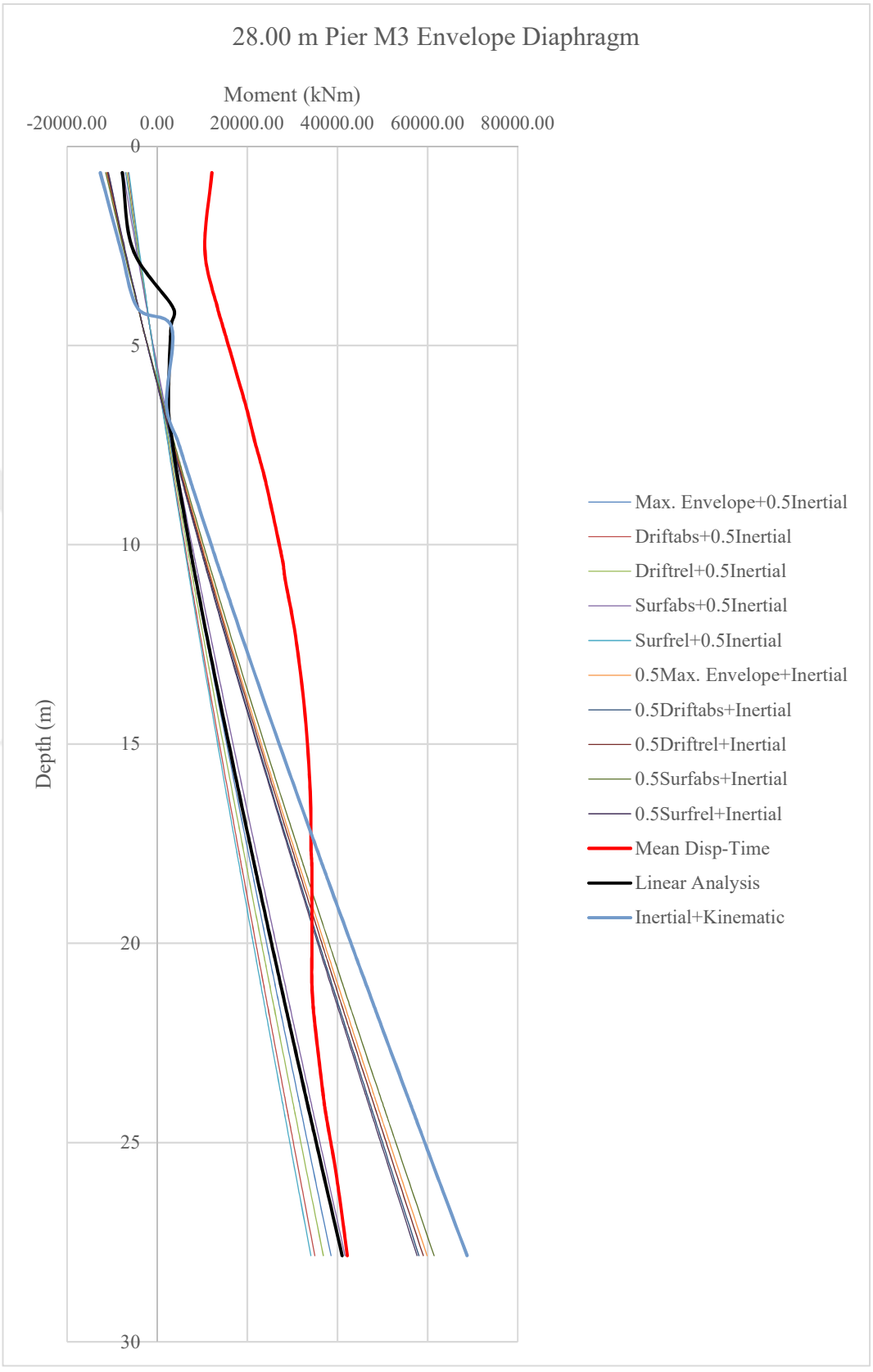

Figure 6.7. Bridge-I 28.00 m pier envelope moment diagram comparison.

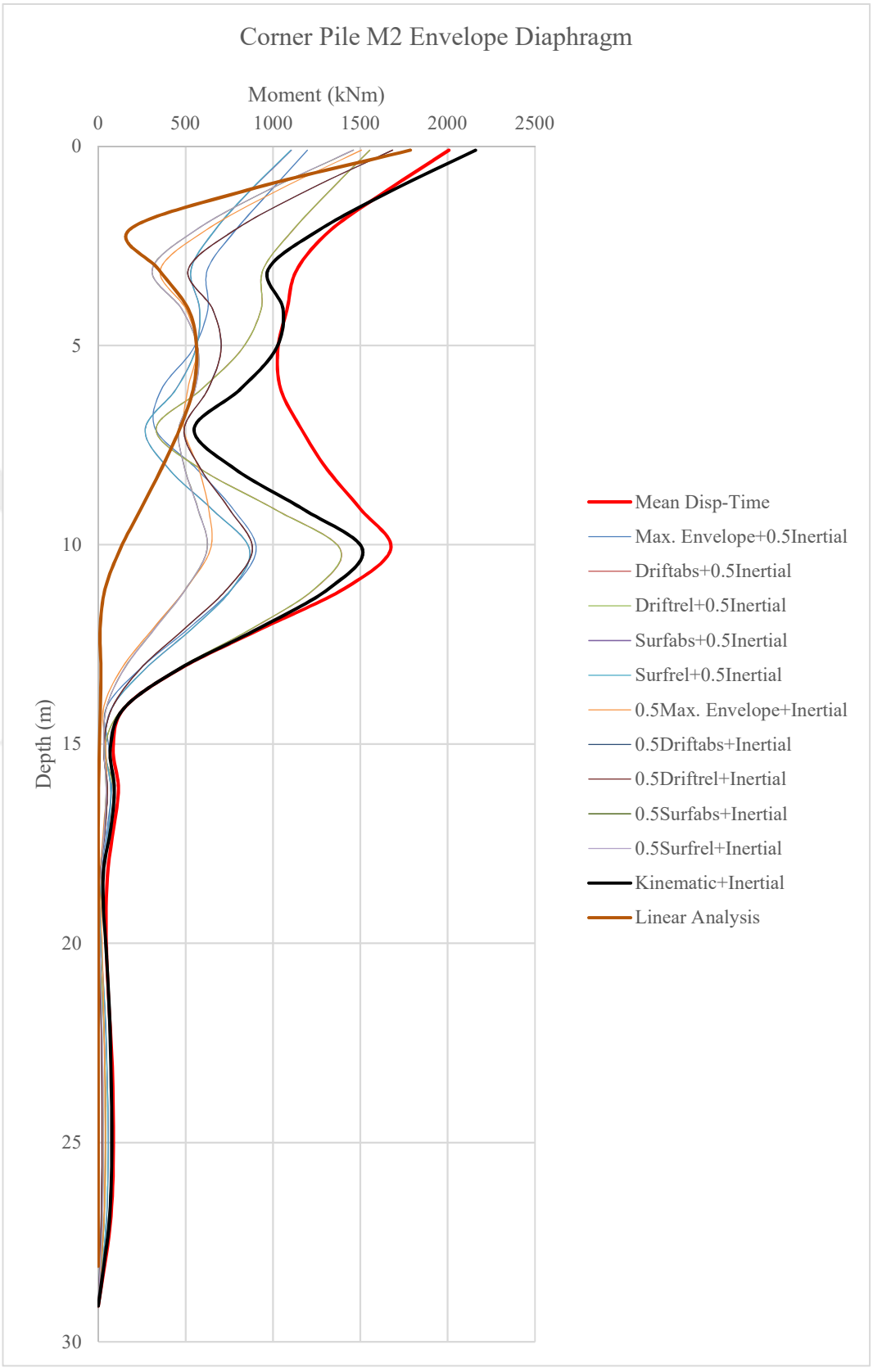

Figure 6.8. Bridge-II corner pile envelope moment diagram comparison.

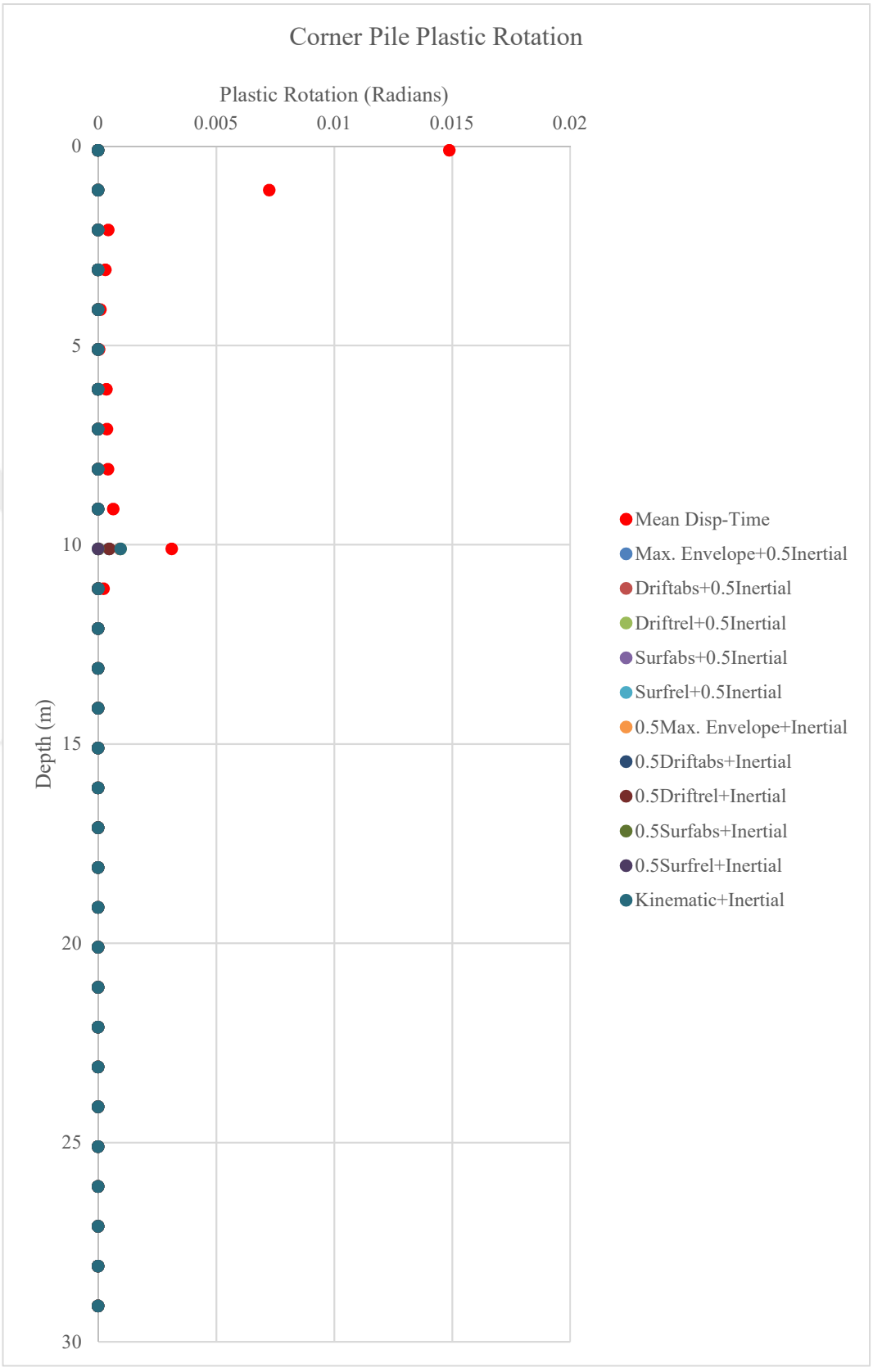

Figure 6.9. Bridge-II corner pile plastic rotation comparison.

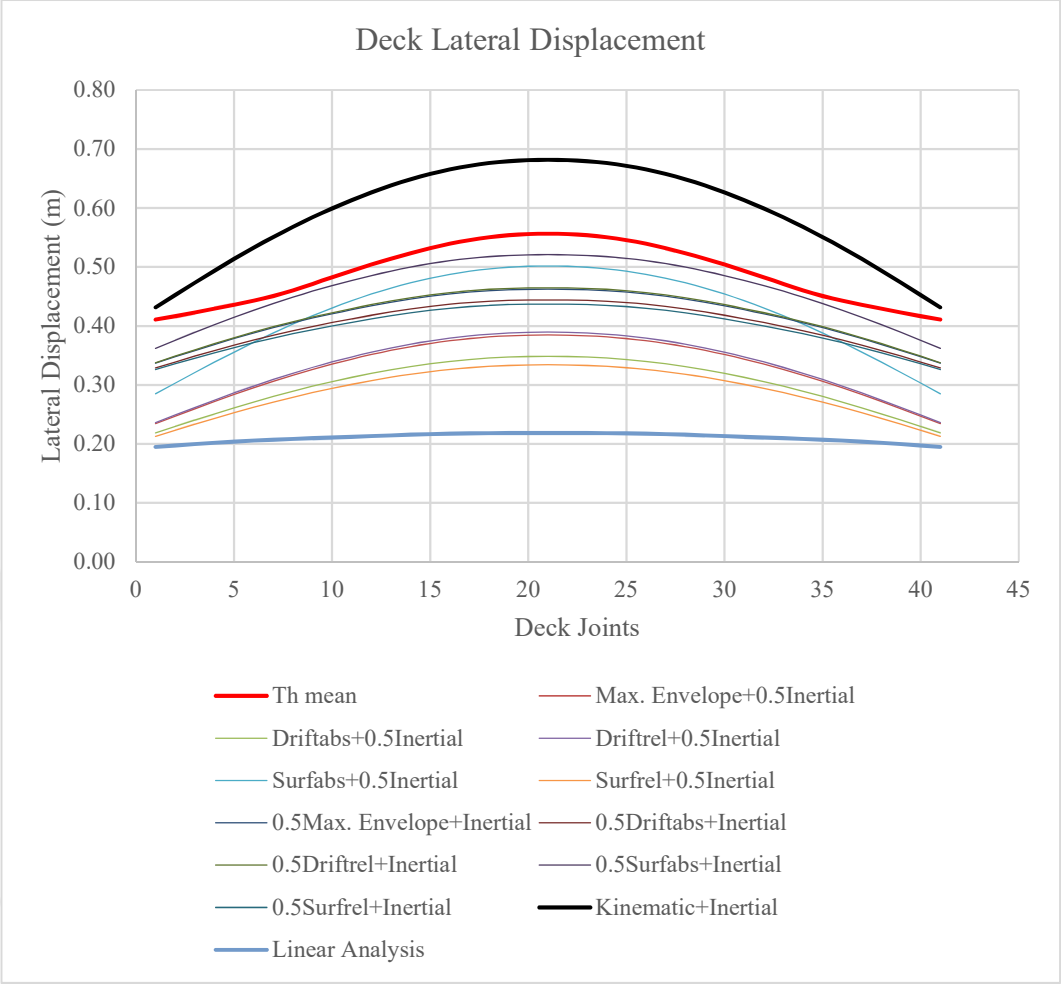

Figure 6.10. Bridge-II deck lateral displacement comparison.

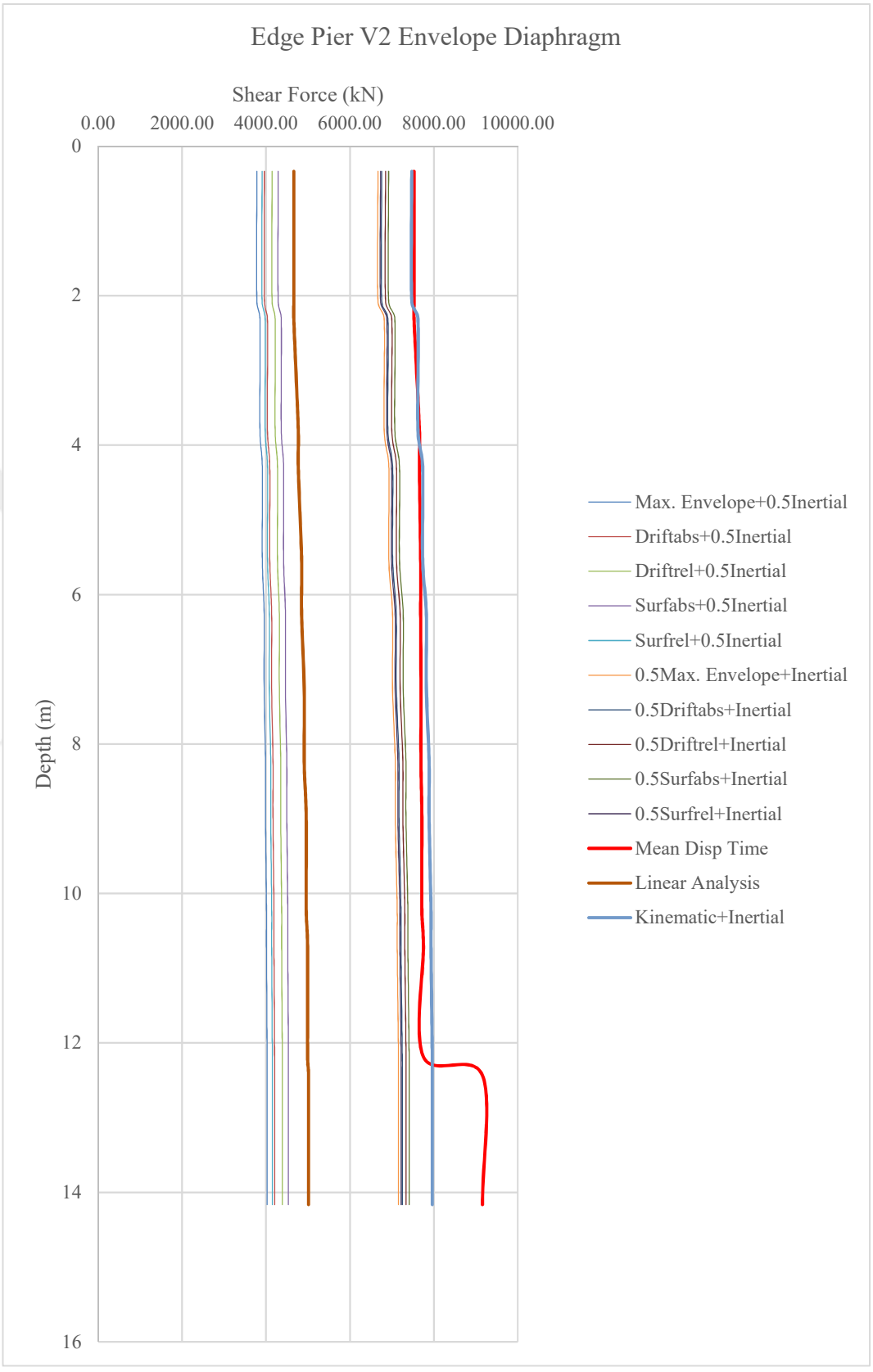

Figure 6.11. Bridge-II edge pier envelope shear force diagram comparison.

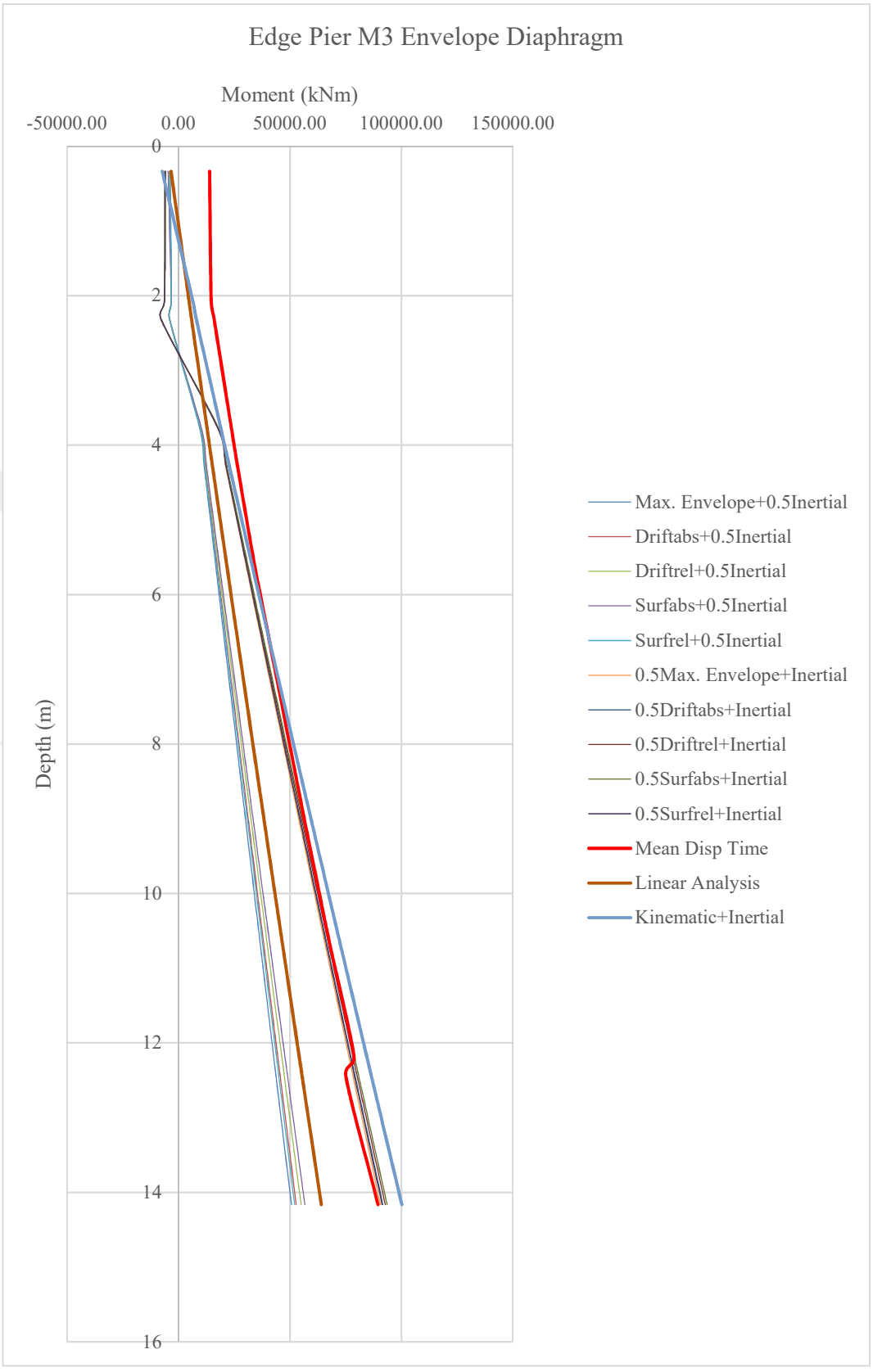

Figure 6.12. Bridge-II edge pier envelope moment diagram comparison.

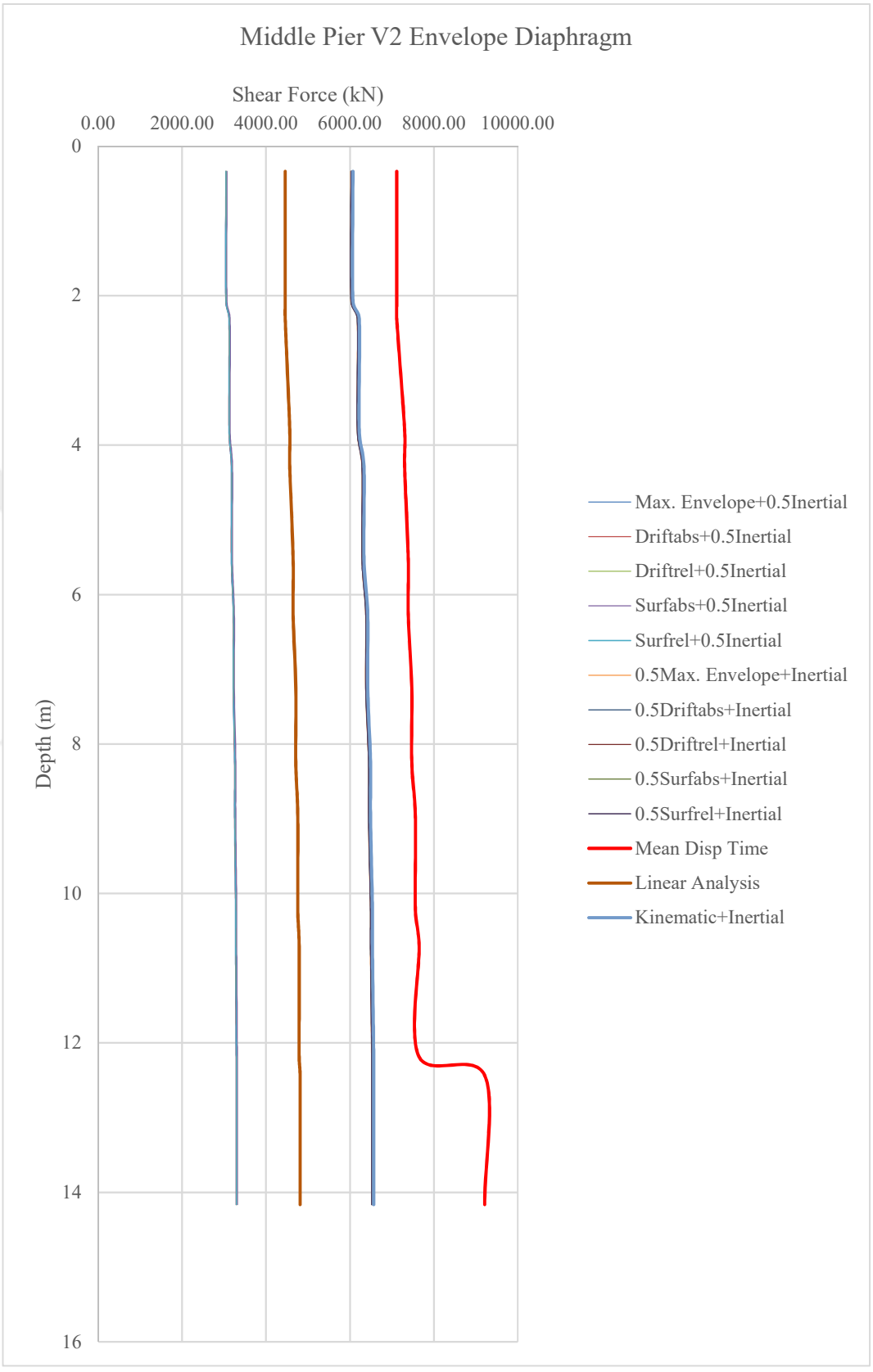

Figure 6.13. Bridge-II middle pier envelope shear force diagram comparison.

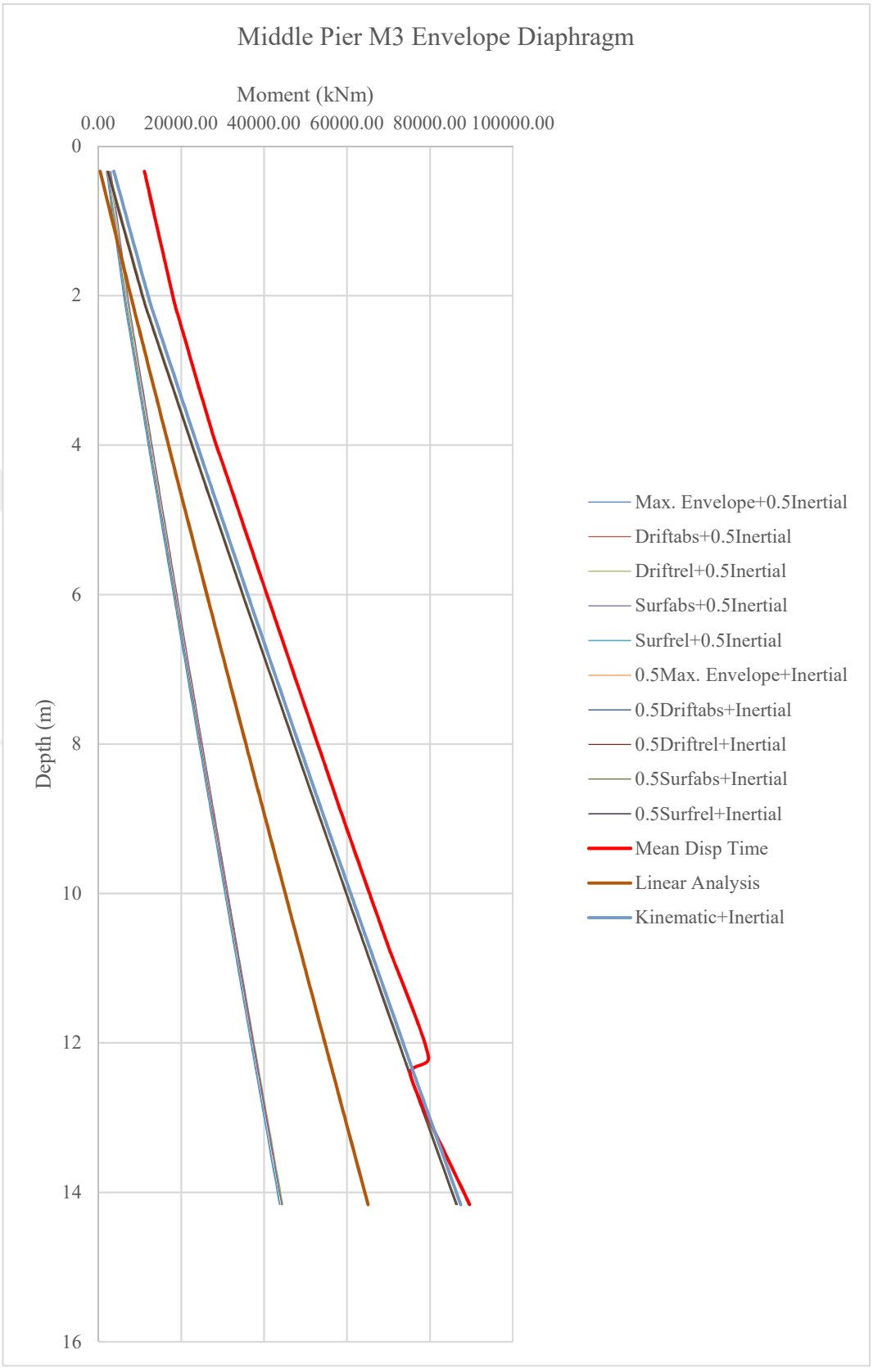

Figure 6.14. Bridge-II middle pier envelope moment diagram comparison.

REFERENCES

AASHTO, “Standard Specifications for Highway Bridges”, 17th Edition, *American Association of State Highway Transportation Officials*, Washington D.C., 2002.

AASHTO, “LRFD Bridge Design Specifications”, *American Association of State Highway Transportation Officials*, Washington D.C., 2012.

Abrahamson, N.A., 1992, “Non-stationary Spectral Matching”, *Seismological Research Letters* 63,30, 1992.

API, “Recommended practice for planning, designing and constructing fixed offshore platforms-Working stress design”, 21th Edition, *American Petroleum Institute*, Washington D.C., 1994.

ASCE, “Minimum Design Loads for Buildings and Other Structures”, *American Society of Civil Engineers*, Virginia, 2010.

ASCE, “Seismic Evaluation and Retrofit of Existing Buildings”, *American Society of Civil Engineers*, Virginia, 2013.

ATC-3, “Tentative Provisions for the Development of Seismic Regulations for Buildings”, *Applied Technology Council*, Redwood City, California, 1978.

ATC-40, “Seismic Evaluation and Retrofit of Concrete Buildings”, *Applied Technology Council*, Redwood City, California, 1996.

BSSC, “NEHRP Prestandard and Commentary for the Seismic Rehabilitation of Buildings”, *Federal Emergency Management Agency (FEMA 356)*, Washington D.C., 2000.

CEN, “Design of Structures for Earthquake Resistance”, *EC8, EN 1998-5:2004 Comité Européen de Normalisation*, Brussels, 2004.

CSI, “CSiCOL Reinforced Concrete Column Design Software”, Computers and Structures Inc., Berkeley, California, 2019.

CSI, “SAP2000 Integrated Software for Structural Analysis and Design”, Computers and Structures Inc., Berkeley, California, 2019.

FEMA, “NEHRP Recommended Provisions for Seismic Regulations for New Buildings and Other Structures”, *Federal Emergency Management Agency (FEMA 368)*, Washington D.C., 2000.

FEMA, “Improvement of Nonlinear Static Seismic Analysis Procedures”, *Federal Emergency Management Agency (FEMA 440)*, Washington D.C., 2005.

Hancock, J., Watson-Lamprey, J., Abrahamson, N.A., Bommer, J.J., Markatis, A., McCoy, E., and Mendis, R., “An Improved Method of Matching Response Spectra of Recorded Earthquake Ground Motion Using Wavelets”, *Journal of Earthquake Engineering 10*, 67–89, 2006.

Kramer, S.L., “Geotechnical Earthquake Engineering”, New Jersey, Prentice Hall, 1996.

Mander, J.B., Priestly, M.J.N., Park, R., “Theoretical Stress-Strain Model for Confined Concrete.”, *Journal of Structural Engineering 8*, pp. 1804-1826, 1988.

MathWorks, “MATLAB- The Language of Technical Computing”, *The Math works*, Natick, USA, 2013.

Matlock, H., “Correlations for Design of Laterally Loaded Piles in Soft Clay”, *Proceedings, 2nd Annual Offshore Technology Conference*, Houston, TX, pp. 577-594, 1970.

Reese, L.C., Van Impe, W.F., “Single Piles and Pile Groups Under Lateral Loading”, London, Taylor & Francis Group, 2001.

Reese, L.C., Isenhower W.M., Wang S.T., “Analysis and Design of Shallow and Deep Foundations”, John Wiley & Sons, Hoboken, NJ, 2006.

Standards, Turkey, “Technical Standards for Ports, Harbor Facilities, Railroads, and Airports in Turkey”, DLHA, Turkey, 2007.

Wilson, E.L., “Static and Dynamic Analysis of Structures”, 4th Edition, Berkeley, 2004.

Winkler, E., “Die Lehre von der Elastizität und Festigkeit”, Prag, 1867.

APPENDIX A: DETERMINATION OF NON-LINEAR *p-y* CURVES

Lateral soil resistance and deflection relations are examined according to guide of American Petroleum Institute (API 2A, 2000) and Reese and Van Impe (2001). Detailed calculation guides are given under the related sections.

A.1 *p-y* Springs for Sand Under Static and Cyclic Loading

According to American Petroleum Institute (API 2A,2000), *p-y* relation for sand assumed as non-linear.

p-y relation is expressed as below for sand layers in static and cyclic loading cases.

$$p = A \times p_u \times tanh[\frac{k \times H}{A \times p_u} \times y]$$

Where,

A : = 0.9 for cyclic loading

= $(3.0 - 0.8 \times H/D) \geq 0.9$ for static loading

p_u : Ultimate bearing capacity at depth H (kN/m)

k : Initial modulus of subgrade reaction (kN/m^3)

y : Lateral deflection (m)

H : Depth (m)

As examining the sand layer, ultimate lateral bearing capacity changes through depth.

By calculating the ultimate lateral bearing capacity, smaller of p_u from below should be used.

$$p_{us} = (C_1 \times H + C_2 \times D)\, x\, \gamma \times H$$

$$p_{ud} = C_3 \times D\, x\, \gamma \times H$$

Where:

p_u : Ultimate resistance (kN/m) (s: shallow, d: deep)

γ : Effective soil weight (kN/m^3)

H : Depth (m)

φ' : Angle of internal friction of sand (deg)

C_1, C_2, C_3 : Coefficients

D : Average pile diameter (m)

C1, C2 and *C3* coefficients can be seen in Figure A.1.

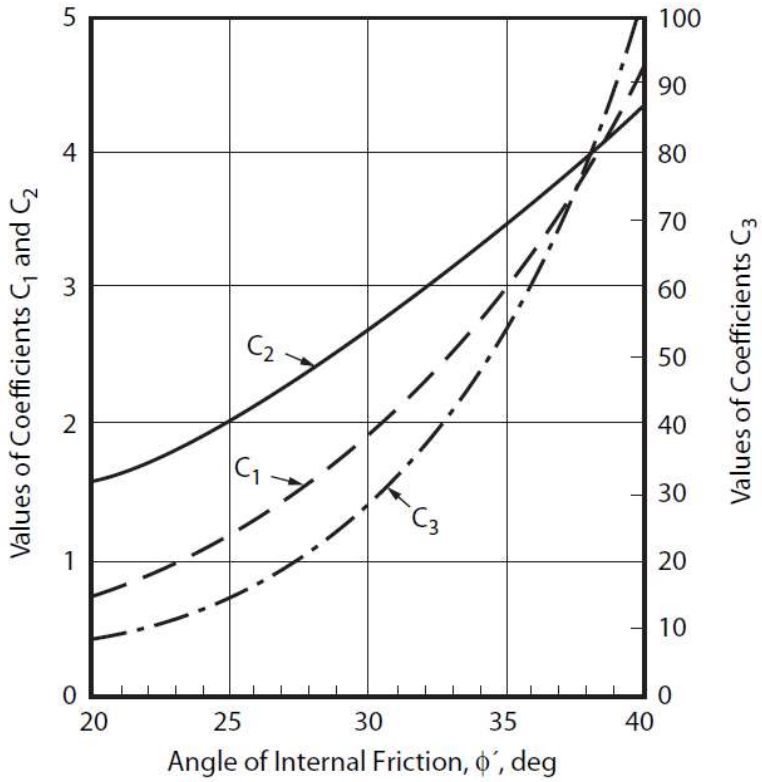

Figure A.1. *C1, C2, C3* coefficients according to angle of internal friction (API 2A,2000).

A.2 *p-y* Springs for Soft Clay Under Static Loading

According to Reese & Van Impe (2001), *p-y* relations for soft clay in case of static loading can be given as follows;

1. Undrained shear strength c_u and submerged unit weight are obtained. ε_{50} should be obtained according to Table A.1.

2. By calculating the ultimate soil resistance, smaller of p_{ult} from below should be used.

$$p_{ult} = \left[3 + \frac{\gamma'}{c_u}z + \frac{J}{b}z\right]c_u b$$

$$p_{ult} = 9c_u b$$

Where,
γ' = average effective unit weight from ground surface to *p-y* curve
z = depth from the ground surface to *p-y* curve
c_u = shear strength at depth z
b = width of pile

According to Matlock (1970), $J = 0.5$ for soft clay and $J = 0.25$ for a medium clay

3. Compute the deflection y_{50}, at one-half the ultimate soil resistance from the following equation:

$$y_{50} = 2.5\varepsilon_{50}\, b$$

4. Points describing the *p-y* curve are now computed from the following relationship.

$$\frac{p}{p_{ult}} = 0.5\left(\frac{y}{y_{50}}\right)^{1/3}$$

p is constant after $y = 8y_{50}$

Table A.1. ε_{50} for normally consolidated clays (Reese and Van Impe, 2001).

Consistency of clay	c_a **(kPa)**	ε_{50}
Soft	<48	0.02
Medium	48-96	0.01
Stiff	96-192	0.005

A.3 *p-y* Springs for Soft Clay Under Cyclic Loading

1. In case of cyclic loading, *p-y* curve is obtained same as static case for the part, when *p* less than $0.72p_u$.

2. Calculations below should be done to acquire the transition depth z_r.

$$p_{ult} = \left[3 + \frac{\gamma'}{c_u}z + \frac{J}{b}z\right]c_u b$$

$$p_{ult} = 9c_u b$$

$$z_r = \frac{6c_u b}{(\gamma' b + Jc_u)})$$

3. $z \geq z_r$, then $p = 0.72p_{ult}$ for y > $3y_{50}$.

4. $z \geq z_r$, then p decreases from the $0.72p_{ult}$ at $y = 3y_{50}$ to the at $y = 15y_{50}$.

$$p = 0.72p_{ult}(\frac{z}{z_r})$$

p remains same after $y = 15y_{50}$.

p-y springs for soft clay in the presence of free water can be seen in Figure A.2.

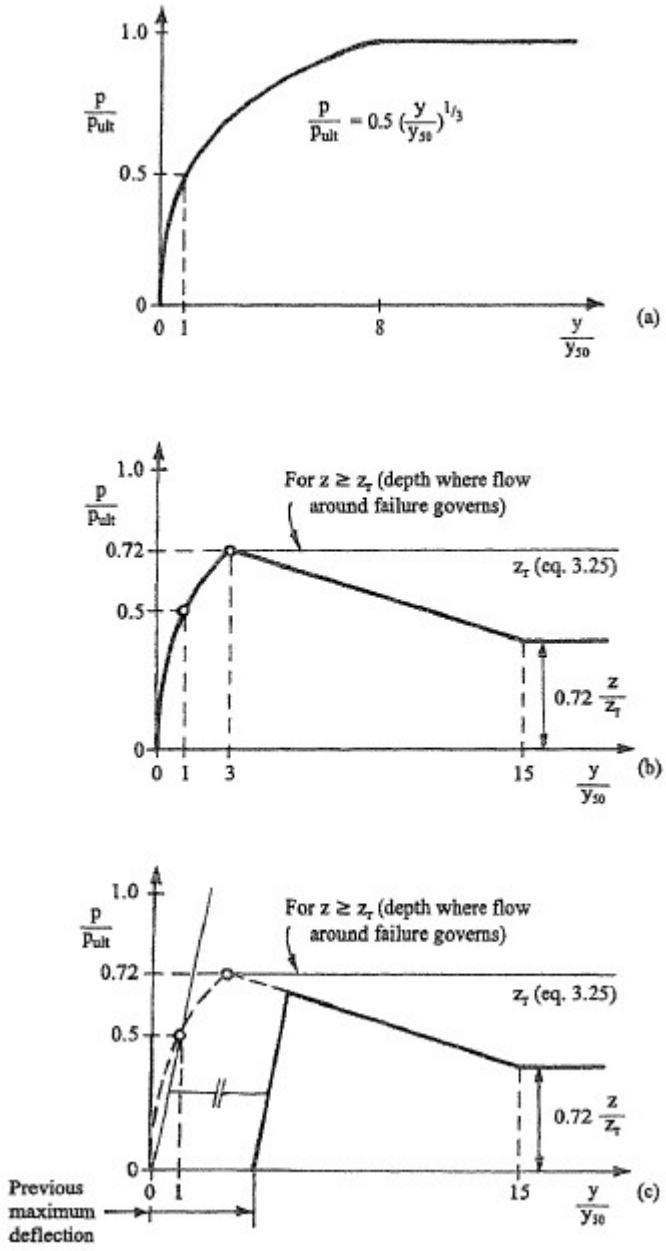

Figure A.2. *p-y* springs for soft clay in the presence of free water, (a) static; (b) cyclic; (c) after cyclic loading (Matlock, 1970).

A.4 *p-y* Springs for Stiff Clay with free water Under Static Loading

According to Reese & Van Impe (2001), *p-y* relations for stiff clay in the presence of free water for static loading given as follows;

1. Undrained shear strength c_u, submerged soil unit weight γ' and pile diameter b are obtained.

2. Average undrained shear strength c_a is calculated for given depth values.

3. By calculating the ultimate soil resistance, smaller of p from below should be used.

$$P_{ct} = 2c_a b + \gamma' bz + 2.83 c_a z$$
$$p_{cd} = 11 c_u b$$

4. Initial straight part of the p-y curve is established by the equation below,

$$p = (k_s z)\, y$$

k_s should be chosen from the Table A.2.

5. $y_{50} = \varepsilon_{50}\, b$ equation is solved. ε_{50} should be chosen from the Table A.3.

6. First parabolic part of the p-y curve is obtained via equation below and p_c should be taken as minimum of p_{ct} and p_{cd}.

$$p = 0.5 p_c (y/y_{50})^{0.5}$$

7. Second parabolic portion of the curve is calculated via equation below;

$$p = 0.5 p_c \left(\frac{y}{y_{50}}\right)^{0.5} - 0.055 p_c \left(\frac{y - A_s y_{50}}{A_s y_{50}}\right)^{1.25}$$

Part of the curve; where, $y = A_s y_{50}$ to $y = 6A_s y_{50}$.is determined with this equation.

8. Next straight-line portion of the curve is calculated via equation below;

$$p = 0.5p_c(6A_s)^{0.5} - 0.411p_c - \frac{0.0625}{y_{50}}p_c(y - 6A_s y_{50})$$

Part of the curve; where, $y = 6A_s y_{50}$ to $y = 18A_s y_{50}$.is determined with this equation.

9. Final straight-line portion of the *p-y* curve is determined as;

$$p = 0.5p_c(6A_s)^{0.5} - 0.411p_c - 0.75p_cA_s$$

or,

$$p = p_c(1.225(A_s)^{0.5} - 0.75A_s - 0.411)$$

Table A.2. K_{py} for overconsolidated clays (Reese and Van Impe, 2001).

Item	**Average Undrained Shear Strength (kPa)**		
	50-100	**100-200**	**300-400**
k_{pys} (static) MN/m³	135	270	540
k_{pyc} (cyclic) MN/m³	55	110	540

Table A.3. ε_{50} for overconsolidated clays (Reese and Van Impe, 2001).

Item	**Average Undrained Shear Strength (kPa)**		
	50-100	**100-200**	**300-400**
ε_{50}	0.007	0.005	0.004

p-y springs for static loading in stiff clay in the presence of free water are given in Figure A.4.

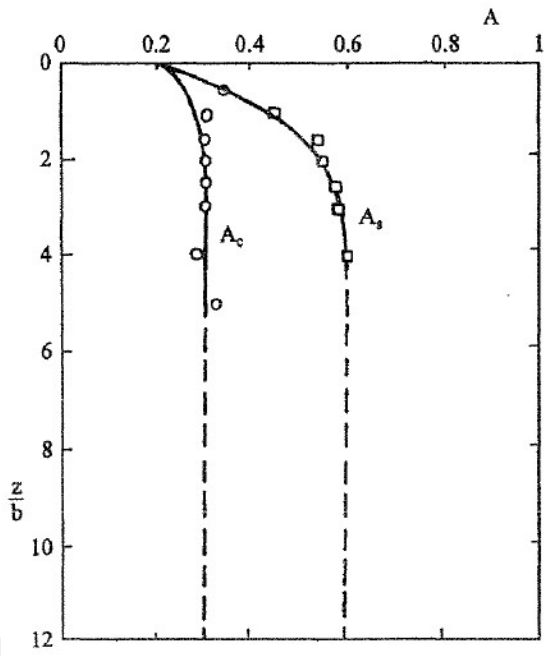

Figure A.3. A_c and A_s (Reese and Van Impe, 2001).

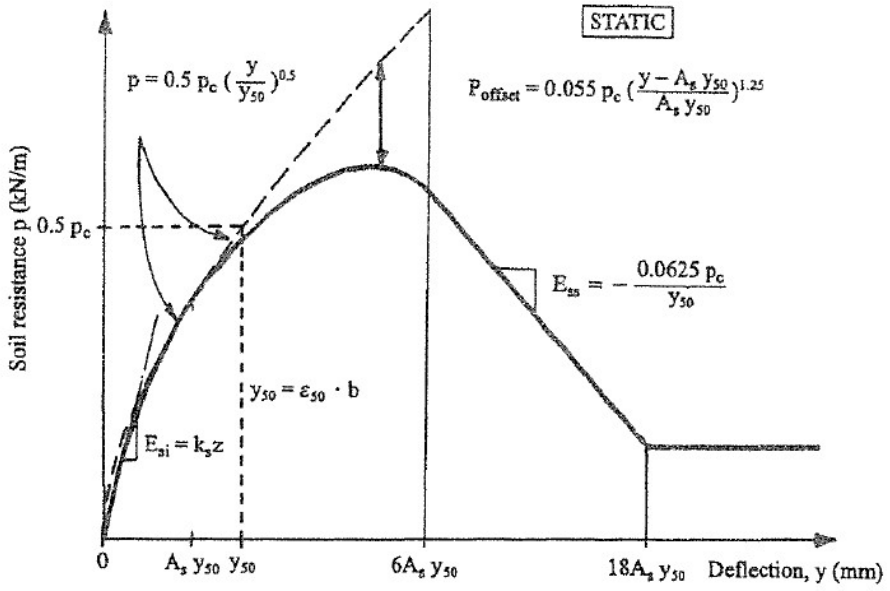

Figure A.4. *p-y* springs under static loading in stiff clay in the presence of free water (Reese and Van Impe, 2001).

A.5 *p-y* Curves for Stiff Clay with Free Water Under Cyclic Loading

Reese and Van Impe (2001) explained the following procedure for stiff clay layers with free water under cyclic loading;

1. Steps 1, 2, 3, 5 and 6 are the same as for the static case.

$$y_p = 4.1\ A_s y_{50}$$

2. Parabolic part of the *p-y* curve is calculated via equation below;

$$p = A_c p_c [1 - \left(\frac{y - 0.45y_p}{0.45y_p}\right)^{2.5}]$$

3. Next straight-line portion of the *p-y* curve is calculated as follows;

$$p = 0.936A_c p_c - \frac{0.085}{y_{50}} p_c (y - 0.6y_p)$$

Part of the curve; where, $y = 0.6y_p$ to $y = 1.8y_p$, is determined with this equation.

4. Final straight-line portion of the *p-y* curve is determined as;

$$p = 0.936A_c p_c - \frac{0.102}{y_{50}} p_c y_p$$

Part of the curve; where, $y = 1.8y_p$ to larger values.is determined with this equation.

p-y springs for cyclic loading in stiff clay in the presence of free water is given in Figure A.5.

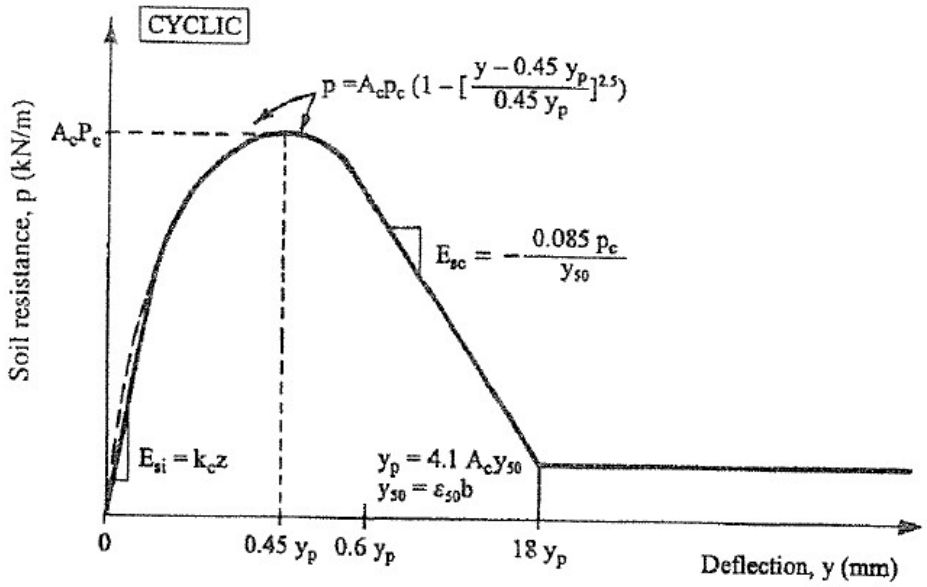

Figure A.5. *p-y* springs under cyclic loading in stiff clay in the presence of free water (Reese and Van Impe, 2001).

A.6 *p-y* Curves for Stiff Clay without Free Water Under Static Loading

As stated by Reese and Van Impe (2001); the following procedure is for stiff clay layers without free water under static loading;

1. Undrained shear strength c_u, submerged soil unit weight γ' and pile diameter b are obtained. ε_{50} should be chosen from the Table A.3.

2. By calculating the ultimate soil resistance, smaller of p from below should be used and J is equal to 0.5;

$$p_{ult} = \left[3 + \frac{\gamma'}{c_u} z + \frac{J}{b} z\right] c_u b$$

$$p_{ult} = 9 c_u b$$

3. Deflection at the half of the ultimate soil resistance should be calculated as follows;

$$y_{50} = 2.5\varepsilon_{50}b$$

4. With the help of below equation, points on the curve is established.

$$\frac{p}{p_{ult}} = 0.5\left(\frac{y}{y_{50}}\right)^{0.25}$$

After $y = 16y_{50}$, $p = p_{ult}$ for all y values.

p-y springs for static loading in stiff clay without free water can be seen in Figure A.6.

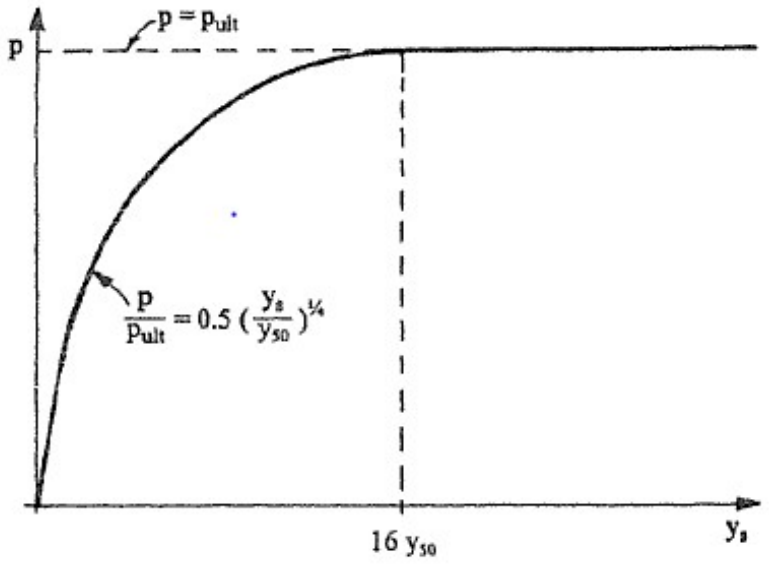

Figure A.6. *p-y* springs under static loading in stiff clay without free water (Reese and Van Impe, 2001).

A.7 *p-y* Curves for Stiff Clay without Free Water Under Cyclic Loading

Reese and Van Impe (2001) defined the following procedure for stiff clay layers without free water under cyclic loading;

1. *p-y* curve is determined as in Appendix A.6.

2. Number of design load application to the pile should be specified.

3. C is obtained via equation below with several values of p/p_{ult};

$$C = 9.6(\frac{p}{p_{ult}})^4$$

4. With selected p/p_{ult} values in the previous step, following equation is performed.

$$y_c = y_s + y_{50}\, C\, logN$$

Where,

y_c = deflection under N-cycles of load

y_s = deflection under short-term static load

y_{50} = deflection under short-term static load at one-half the ultimate resistance

p-y springs for cyclic loading in stiff clay without free water is given in Figure A.7.

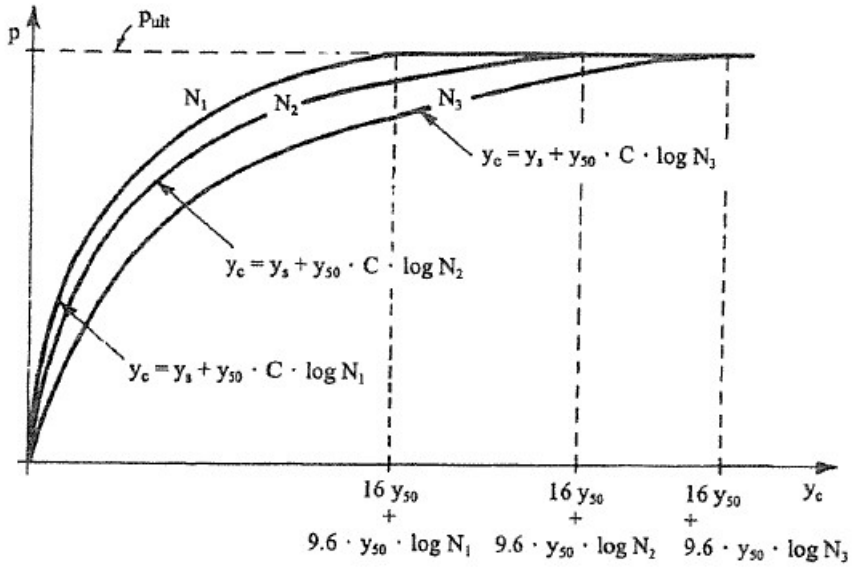

Figure A.7. *p-y* springs for cyclic loading in stiff clay without free water (Reese and Van Impe, 2001).

A.8 Effect of Group Action

Reese et al. (2006) indicated that piles in a group are less efficient than single piles due to pile-soil-pile interaction. Pile-soil-pile interaction in a group of piles can be classified into three categories: side-by-side, line-by-line (leading, trailing), skewed lines

Side-by-side piles:

$$e = 0.64\ (s/b)^{0.34} \quad \text{for} \quad 1 \leq s/b \leq 3.75$$
$$e = 1.0 \quad \text{for} \quad s/b \geq 3.75$$

Leading piles:

$$e = 0.7\ (s/b)^{0.26} \quad \text{for} \quad 1 \leq s/b \leq 4.00$$
$$e = 1.0 \quad \text{for} \quad s/b \geq 4.00$$

Trailing piles:

$$e = 0.48\ (s/b)^{0.38} \qquad \text{for} \quad 1 \leq s/b \leq 7.00$$

$$e = 1.0 \qquad \text{for} \quad s/b \geq 7.00$$

Piles at skewed angle:

$$e = (e_i^2 \cos^2\phi + e_s^2 \sin^2\phi)^{1/2}$$

e_i = efficiency of pile where in line

e_s = efficiency of pile where side-by side

ϕ = angle between piles

Where s and b represent pile spacing and diameter, respectively. Reduction factors for piles in group action are given in Figure A.8.

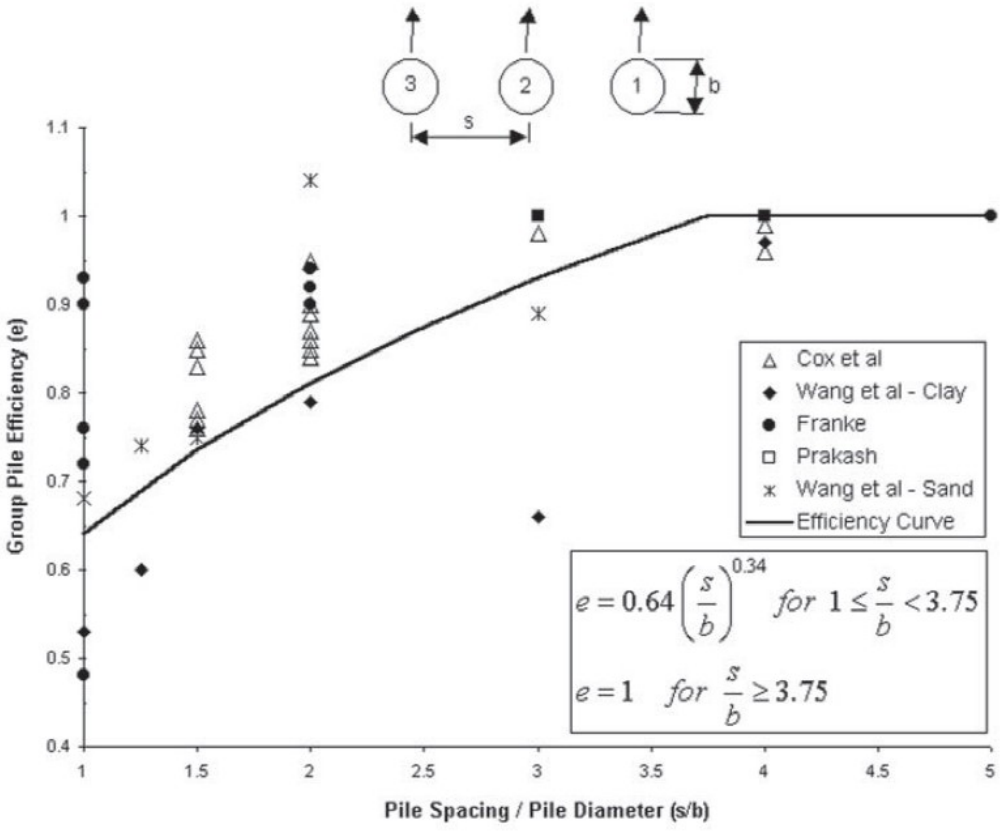

Figure A.8. Reduction factors for piles in group action.